Study of charge ordered materials using polarization dependent x-ray absorption and emission spectroscopy

Steven Richards

A thesis submitted in accordance of the requirements for the degree of Doctor of Philosophy at the University of Kent.

School of Physical Sciences
University of Kent
1st December 2021

Abstract

Transition metal compounds often display a wide range of properties, which are typically caused by strong electron correlations. With magnetic, atomic and electronic transitions leading to novel quantum states, these materials have become the focus of many studies. High temperature superconductivity (SC), Mott states and metal-insulator transitions have all been intensely researched, especially since it is also the case that these states can be tuned by chemical doping, allowing an enhancement of certain properties. The strong interplay between the atomic and electronic structures in many of these materials can led to difficulties in separating the different degrees of freedom. The understanding of how the different states can manifest and the mechanisms which may drive their emergence has become an important research field since many of these properties have important applications.

X-ray absorption and emission spectroscopy (XAS/XES) are element selective techniques which can probe both the electronic state and local structure around the absorbing species. In this thesis conventional XAS, high energy resolution fluorescence detected XAS (HERFD-XAS) and valence-to-core XES (vtc-XES) measurements are the techniques employed to study the transitions in 3 compounds. In all cases, polarization dependent measurements have been used to track changes along different crystallographic planes, since these systems are typically highly anisotropic. Combined with additional simulations of the electronic structure, these techniques are shown to be successful in providing further information regarding the nature of the transitions investigated.

The aim of this thesis is to investigate the atomic and electronic transitions in 3 materials to provide insight into the critical factors that drive the states that can emerge. Measurements have also been conducted once their properties were tuned by chemical doping, to further understand the factors that drive the transitions. Additionally this thesis aims to further develop these techniques. An investigation using the Lβ emission lines with vtc-XES to probe the occupied states is presented. While in recent years the vtc technique has been used in the study of materials with 3d elements with light ligands, very little literature is available on the heavier metals/ligands where the Lβ emission is most applicable. A procedure for providing a correction for the self-absorption effect is also presented. Due to the highly localized nature of the d orbitals in transitions metals, numerical instabilities often affect the standard correction procedures. This issue is successfully addressed by additionally taking into account the background fluorescence intensity.

The role of iridium dimers and the electronic state of this species in the 5d transition metal $IrTe_2$ is investigated in relation to a metal to insulator transition. Robust evidence shows that the Ir dimers are present above and below this transition and that the electronic structure of Ir does not undergo a significant change. The presence of high temperature disordered dimers is inconsistent with the majority of the current literature and these results suggest that changes in the Te species electronic and atomic structure is the most critical factor in the metal to partial insulator transition. Additionally it is known that when the system is doped with platinum, a low temperature SC phase can emerge. This research shows that above this phase, the nature of the material is the same with respect to the parent compound.

Two competing scenarios have been presented for the metal to insulator transition in the 4d transition metal Ca_2RuO_4. While it is clear that a Mott-type mechanism makes the 2/3 filled t_{2g} band insulating, the nature of this transition and the role played by the orbital degree of freedom is unclear. One scenario suggests that the transition is orbital selective and that it only affects the xy band, which becomes metallic. The second scenario suggests that it is not orbital selective and the transition is assisted by the crystal field splitting. The investigation presented in this thesis provides evidence that there is a charge transfer between the non-degenerate t_{2g} bands, where below this transition the xy band become full. While recent studies have suggested that in the metallic phase all 3 bands are conducting, the current investigation shows how the interplay between the atomic and electronic structures is an important factor. These results are further assisted by the study of this material once doped with lanthanum, where the metal to insulator transition is suppressed. The doping has the affect of increasing the t_{2g} bandwidth, and shows how the atomic and electronic transitions are closely linked.

The iron pnictide (NaFeAs) system shows both a structural and magnetic transition along with a orbital/spin nematic state, which once doped can display bulk SC. The original aim of this research was to investigate the nematic state, where the origin of this transition is unclear but theoretically linked to both spin and orbital degrees of freedom. Due to degradation of the samples used, this investigation was not successful in providing information regarding the nematic state. However the results do suggest that the $FeAs_4$ structure is critical for the emergence of the different phases and small distortions are detrimental to the transitions.

Authors declaration

I declare that the work presented in this thesis entitled **"Study of charge ordered materials using polarization dependent x-ray absorption and emission spectroscopy"** is the result of my own research. It has not been submitted for the purpose of a qualification at any other institution or for any other degree. The work carried out has been undertaken at the University of Kent and Diamond Light Source. Where I have consulted the published work of others this has been clearly acknowledged, including all main sources.

Signed: *Steven Richards*

Date: 1/12/2021

Acknowledgements

Over the past 8 years at the University of Kent I have been very lucky to meet an amazing group of people, who have made this PhD possible and I would like to take this opportunity to thank those that have made a lasting impression.

Firstly I would like to thank my supervisor Dr Silvia Ramos, throughout the PhD your support and guidance has been invaluable. When I started this project I had very little knowledge in this field however through the many experiments and discussions, with plenty of coffee, I leave with a true passion for spectroscopy which I hope will continue for many years. I would also like to thank my two Diamond supervisors, Dr Sofia Diaz-Moreno and Dr Shusaku Hayama. My time at Diamond gave me many valuable experiences and your encouragement to question results and leave no stone unturned has contributed significantly towards this work. Additionally I would like to thank you all for your efforts and patience during the many experiments.

I have had the pleasure of working with a large number of people at both Kent and Diamond, with many interesting discussions. Thank you to everyone that I have shared an office with and I must apologies for my continued efforts to slowly spread across the office at Diamond. I would like to thank the entire I20 team and everyone at Diamond in general for the warm welcome I received and for showing me what it is like to work in a large facility. I would like to make a special thanks to everyone that has been a part of the experimental teams throughout the last 4 years. While beamtime is always a big undertaking, it was always a good atmosphere with many laughs and again much coffee.

Outside of academic life there have been many people that have provided support and encouragement, which has kept me going. Firstly I would like to thank my family, especially my parents. While I am sure that they still do not know what I have been doing all this time, their continued support and love through the PhD will never be forgotten. While I can not mention everyone, I would like to say a massive thank you to John, Tarik, James, Sophie, George, Leon, Adrián, Armando and Charlotte (and many more). Through the many pub visits, pool games, caving adventures and motorbike trips, you have all kept me sane and provided some of the best moments of this PhD.

Finally I would like to say an overall thank you to the University of Kent, Diamond Light Source and everyone who I have had the pleasure of meeting. Throughout my undergrad and postgraduate years I have not only been able to pursue my scientific interests but have had the opportunity to explore the U.K. and form lasting friendships. Whether it was above or below ground, in an office or beamline, the pub or coffee shop, this has left an important and lasting impression on my life, which would never have been possible without you all.

Contents

List of Figures

List of Tables

Chapter 1

Introduction

This chapter provides an introduction to the physics of transition metal compounds relevant to this work. Specifically it focuses on some of the important properties that are considered in the 3 materials researched in this thesis: Mott insulators, crystal field splitting, spin-orbit coupling and charge ordering. An introduction to the compounds investigated will also be given, focusing on the underlying properties which have been investigated. This also includes a brief discussion regarding the measurements undertaken and why they are applicable.

1.1 Transition metal compounds

Transition metal (TM) compounds are a unique class of materials, in which a wide range of phenomena can manifest. This family comprises of a large number of materials, with many important applications, including: optics, catalysis, sensors and energy conversion/storage [1, 2, 3]. Transition metals are defined as elements which occupy the central block on the periodic table, where the outer electrons (valence elecreons) are in the d - orbitals. Included in this class are good metals and large-gap insulators. In addition a rich array of magnetic properties can arise, such as multiferroicity or colossal magnetoresistance. It is also the case that transition metal compounds can also show high temperature superconductivity, for example the cuprate and iron pnictide families.

1.1.1 Localization and electron levels

The physics of materials with transition metals often diverge from the standard band theory model [4], and requires the consideration of the strong electron-electron interactions. The rich behaviour of these materials is determined by whether the electrons are localized or delocalized. In the delocalized systems, the electrons can normally be treated with the conventional band theory. The ideal gas model (free electron theory) is a suitable method for describing the behaviour of simple systems, where the electrons move in a uniform background potential which is typically set to 0. A small modification of this theory, known as the nearly free electron theory additionally includes the periodicity of the lattice (includes the cores), but ignores electron-electron interactions. In this scenario forbidden states emerge between the energy bands where the electrons are located. An insulator forms when the highest occupied band is filled and there is a sufficient gap between this band and the nearest unoccupied band. If the bands are only partially filled, and/or overlap, the system is described as a metal.

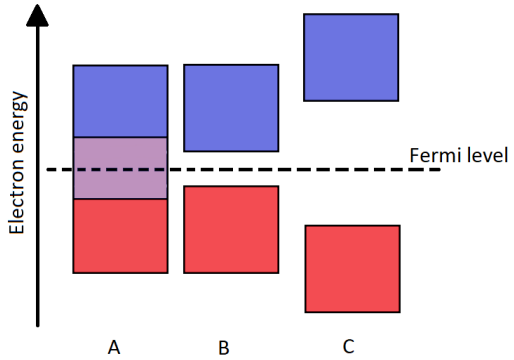

Figure 1.1.1: Schematic diagram of the different states in band theory (blue: conducting band, red: valence band). A) metal, where the valence electrons can move to the conduction band, B) semiconductor, electrons can jump the gap. C) insulator, band gap forbids conduction.

In TM compounds the electrons may need to be considered as localized, where they resemble a state closer to electrons in atoms or ions rather than in a crystal. In this case the important role of the strong electron-electron interactions must be considered and hence a more compressive atomic model must be used to understand the physics. The non-degenerate Hubbard model [5] is a suitable starting position to describe these systems, where the model takes into account electrons located at certain sites, a "hopping" matrix element, t, which describes the ability for these electrons to move to a different site and the on-site Coulomb repulsion, U. In metals, the electrons are able to overcome the Coulomb repulsion and are delocalized which form bands. However in insulators the gap between neighbouring sites is sufficient to lead to small hopping amplitudes with corresponding narrow bandwidths, W, where the electrons prefer to stay localised on one site. This minimises the repulsion energy and hence the total energy of the system is described as its groundstate. If the Coulomb repulsion is greater than the total bandwidth given by W = 2zt, where z is the number of nearest neighbours, it is unfavourable for the electrons to move to a different, occupied site since it would have to overcome the on-site Coulomb interaction but only has the additional kinetic energy from the creation of the electron and hole pair. Figure 1.1.2 a) represents a system where the distance between atoms is large enough that the electrons are localized at each site. Figure 1.1.2 b) represents a system where the kinetic energy gained by the electron and hole allows the electrons to pair on one site. This insulating model can be described by the Mott insulator theory [6] and explains why in systems which would be metallic under the band theory become insulating once strong electron-electron interactions are considered.

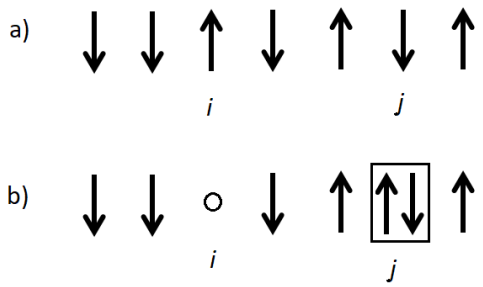

Figure 1.1.2: Creation of charge-carrying excitations (electron and hole) from a state with electrons localized one per site [4]. a) electrons localized to one site, b) movement of an electron and creation of a hole.

In the classical quantum theory of atomic structures [7], electrons form shells, described by the principal quantum number, n = 1, 2, 3 ... . In each shell the electrons can have an orbital moment, l < n, for which there are 2l + 1 states with an associated magnetic quantum number m = l, l - 1, ..., -1. The filling of the shells are governed by Hunds rules and must obey the Pauli exclusion principle i.e. two electrons on each level with different spins. The materials considered in this thesis have either 3d, 4d or 5d "active" orbitals, which for isolated atoms have a fivefold degeneracy with up to 10 electrons. The electrons in the d states can be considered as valence electrons since the binding energy is relatively small. In many cases however the situation becomes complicated due to the fact that the radii (or d states) are such that if the electrons are not participating in chemical bonding they can be treated as localized states and thus the on-site Coulomb interaction may play a critical role in determining the state of the system.

In the simple atomic picture of an isolated atom the energy levels only depend on the principal quantum number and are degenerate, i.e. each state with the same principal quantum number has the same energy. This however is typically not the case in real systems where a number of different interactions result in the states becoming non-degenerate. Which interactions are responsible for this splitting and how the energy levels become arranged is a critical factor in the materials studied in this thesis, since it maybe critical in determining whether the electrons become localized. Two of the important factors that must be considered are the spin-orbit coupling effect and the crystal field splitting effect. The spin-orbit coupling effect becomes important for heavier elements, the effect increases as a function of the atomic number. It originates from the interactions between an electron spin and its orbital moment, which when summed over all electrons in the system forms the total angular momentum, J = L + S. The effect of the spin-orbit coupling is to shift the energy levels and split these into multiplet states depending on their total angular momentum.[1]

[1]Note that in atomic physics there are two schemes used to describe spin-orbit coupling: the j-j coupling and Russell-Saunders coupling [8, 9]. The j-j coupling is applicable to very strong spin-orbit coupling effect, while the Russell-Saunders is generally applicable to lighter elements (3d and 4d TM).

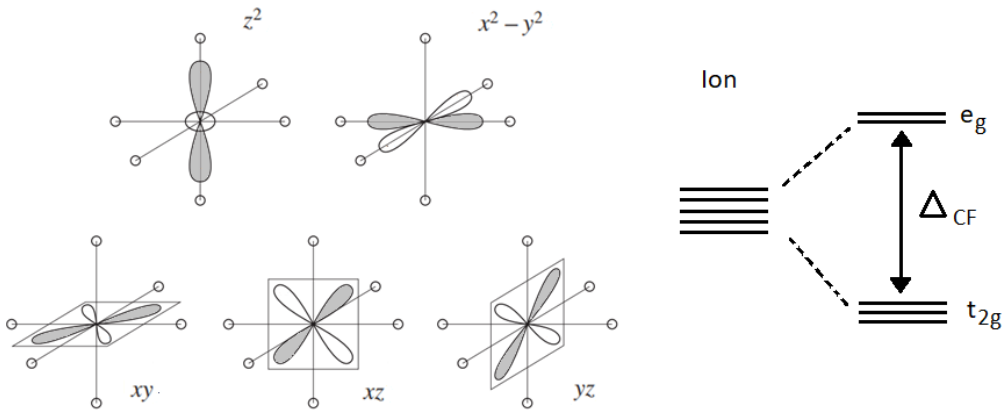

Figure 1.1.3: Left: d orbital shapes, in an octahedral symmetry. Right: splitting of d states due to crystal field.

When transition metal ions are placed within a crystal structure, the single atom symmetry is broken and the symmetry of the system is now determined by the structure of the crystal. The effect of this on the energy levels of the atoms is termed crystal field splitting [10]. As an example, if the transition metal ions are surrounded by a regular octahedron of anions, the d electron energy levels will split into a lower triplet t_{2g} (d_{xy}, d_{xz}, d_{yz}) state and a higher doublet e_g (d_{z^2}, $d_{x^2-y^2}$) state. The d orbital shapes (electron densities) in an octahedral symmetry and splitting due to the crystal field is shown in figure 1.1.3. The origin of this splitting is due to the different electron distributions for the two states. The lobes of the e_g electron wavefunctions are directed towards the negatively charged anions and hence feel a greater Coulomb repulsion, corresponding to an increase in their energy. For the t_{2g} states the lobes are pointed between the anions thus feel weaker Coulomb repulsion and their corresponding energies are lower. An additional effect which modulates the type and strength of the crystal field is the hybridization between the metal d orbitals and the ligand p orbitals, which has a nonzero overlap. When the lobes of the metal d orbitals and ligand p orbitals point directly towards each other, the hybridization will create a strong overlap, which is typically the case for the e_g states. A similar effect will also be present in the t_{2g} orbitals however the overlap will be weaker since due to the form of these orbitals, they will be orthogonal to the p orbitals. An illustration of this overlap for the t_{2g} and e_g orbitals with the ligand p orbitals is shown in figure 1.1.4.

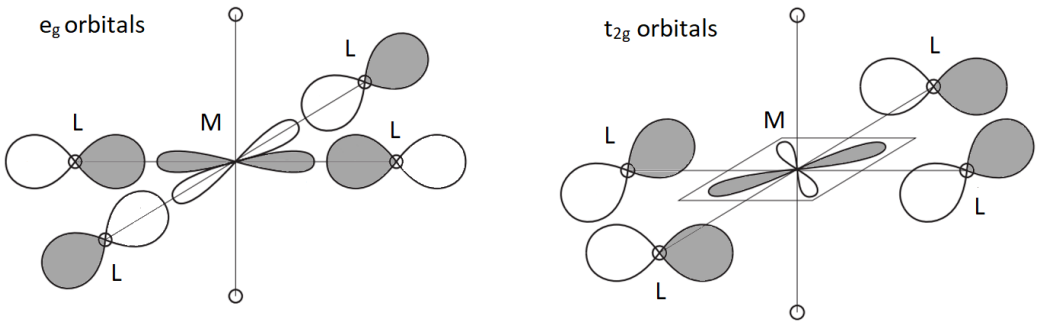

Figure 1.1.4: Possible hybridization between the t_{2g} and e_g orbitals with the ligand p orbitals. Left: e_g hybridization, right: t_{2g} hybridization. Positive lobes are indicated by grey colour. Re-drawn from [10].

1.1.2 Transitions

When considering the different phenomena that can emerge in TM compounds, it is important to consider how the degrees of freedom (spin, charge and orbital) relate to the crystal structure. These compounds often display multiple electronic states linked to transitions caused by changes in temperature, pressure and chemical doping. Due to these considerations, the range of phenomena displayed by these materials is substantial. There are a number of important factors that apply to one or more of the compounds in this thesis and these will be introduced in this section.

One of the most dramatic effects seen in TM compounds are metal to insulator transitions. In the band theory framework the energy levels are separated by an energy gap. If the valence bands

are filled and separated from the conduction band, then the material is insulating. However if it is partially filled or overlapping with another orbital, then the system is a metal. In these scenarios a metal to insulator transition can occur when there is a change in the electron density or a change in the band structure due to, for example, a structural phase transition. The additional type of metal to insulator transition considered in this thesis is the Mott insulator. Based on the localized electron picture, the insulating state is dependent on the electron-electron interaction. If the on-site Coulomb interaction is large enough, then the electron will favour remaining in a localized state and not conducting. By increasing the electron hopping or the bandwidth, the on-site Coulomb interaction can be overcome and a Mott transition will occur. In the case of Mott transitions, these often occur with other changes in the properties of the material, such as structural or magnetic phase transitions. Due to this it can be difficult to determine if the metal to insulator transition is a Mott type or can be explained by band theory.

The crystal structures of the materials investigated in this thesis all undergo changes as a function of temperature, which in the case of the $IrTe_2$ and Ca_2RuO_4 accompany the metal to (partial) insulator transition. In the context of an octahedral local environment, in describing the degeneracy of the d electron levels in both of these materials the Jahn-Teller theorem plays a critical role, which additionally refers to the Jahn-Teller distortion, also linked to orbital ordering. The Jahn-Teller theorem states that the only degeneracy allowed in the groundstate of a system is the spin degeneracy which is connected to invariance with respect to time reversal [11]. All other degenerate states are unstable and would correspond to a maximum of the total energy. An example of this situation is when the d orbitals are filled in such a way that there is one electron in the e_g state. In theory this electron can be in either the z^2 or x^2 - y^2 state and hence degenerate. To overcome this, the structure will distort slightly and lift the degeneracy to ensure a non-degenerate groundstate. A simple description for the Jahn-Teller distortion for an octahedra crystal structure is either a compression or elongation, as shown in figure 1.1.5. In the elongated state the degeneracy is broken by the stabilization of the orbitals with a z component, while the other orbitals become destabilized at a slightly higher energy. This is caused by the fact that the d_{xy} and $d_{x^2-y^2}$ orbitals have greater overlap with the ligand orbitals resulting in these having higher energy. The opposite situation occurs in the compressed state where the orbitals without z components become stabilized. This situation highlights an effect known as orbital ordering, where the electrons now occupy particular orbitals to ensure a minimum total energy.

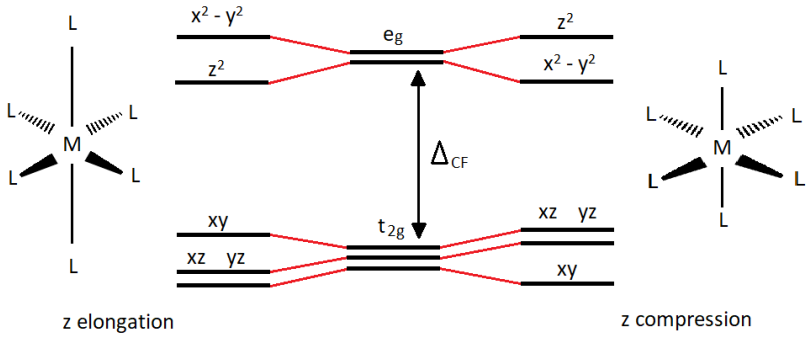

Figure 1.1.5: Orbital configuration due to Jahn-Teller distortion. Left: z elongation with 2 long and 4 short bonds. Right: z compression with 4 long and 2 short bonds.

The final consideration that applies to all the compounds researched in this thesis is the charge ordering transitions [12]. This has already been introduced indirectly, since the Mott insulator transition falls under this category. The charge ordering effect can apply to both non-localized and localized electrons, where the charge modulation in space is the order parameter. In strongly correlated materials (such as TM compounds), the localization effects caused by the strong electron interactions can lead to different sites experiencing a disproportionate distribution of charge. The interactions which emerge from this typically become ordered onto a super-lattice. We refer to this as charge ordering. It is typical to find that the emergence of charge order states occur in close proximity to other transitions and the charge ordering transition itself can be either first or second order. Charge ordering is due to the changes in the electron density and can manifest in a number of situations. For example, in the case of the Mott insulator the redistribution of charge is a consequence of the orbital ordering, to ensure the preservation of a symmetry state. Another typical example are charge density waves (CDW). In these cases, the overall charge density is modulated into a standing wave pattern. The super-lattices that form can come in a variety of patterns, for

example a checker-board like pattern or in stripes. This effect can occur in 1 and 2 dimensional materials. Also in anisotropic materials where the electronic/atomic structures are not the same across different axes.

1.2 Materials and measurements

Three different TM compounds have been studied in this thesis, including in some cases also chemically doped versions. In all 3 cases, research has already been carried out by other groups using a number of different techniques to understand the different properties. However, the nature and/or mechanism which drive the transitions which in turn lead to the different states remains controversial. This is typically related to the fact that there is a strong interplay between the atomic and electronic structures leading to difficulties in separating the different degrees of freedom. In this section a brief introduction is given with relation to the 3 compounds investigated. The aim is to provide an understanding of the key properties and different scenarios which are guiding this research.

1.2.1 $IrTe_2$

The 5d transition metal compound $IrTe_2$ is a perfect example where the interplay between different degrees of freedom create a complex range of phases [13]. The structure is formed of Ir and Te stacked layers which form edge sharing $IrTe_6$ octahedra. At 280K the material experiences a metal to (partial) insulator (MI) transition and further weaker transitions are seen at low temperatures. These transitions are linked to both electronic and atomic structural changes. In terms of the atomic structure, below the transition it is suggested that Ir-Ir dimers form in an ordered state and a small change occurs in the Te octahedra structure [14]. The electronic structure on the other hand has led to several competing scenarios. Initially it was thought that similar to other chalcogenides, in theory the system experienced a CDW type mechanism. However the experimental data could not show the expected band gap opening and the modulation in the structure is highly non-sinusoidal [15, 16, 17]. It was also suggested that the formation of the Ir dimers would cause a Mott-type transition in which the electrons associated with the dimers would become localized [16, 18, 19].

Due to the interplay between the electronic and atomic structures, x-ray absorption and emission spectroscopies are well suited to study this material since they can probe both the local electronic and atomic structures around the target species. In this research, the L_1, L_2 and L_3 edges of the Ir species have been probed with both conventional and high energy resolution fluorescence detected XAS (HERFD-XAS) measurements. Since this material is highly anisotropic, polarization dependent measurements have been carried out in all cases to allow the possibility to track changes across different crystallographic planes. Additionally, valence-to-core x-ray emission spectroscopy has also been used to probe the interactions between the Ir and Te species, since the interaction may also play a critical role in driving the transition.

It has been shown that upon doping the system with Pt, the metal-insulator transition becomes suppressed and a bulk superconducting state emerges [13, 20]. Interestingly it was reported that the dimers seen in the parent material are absent in the doped structures which leads to the possibility of a different symmetry breaking mechanism driving the properties of the system [21]. Due to the success of tracking the evolution of the Ir dimers in the parent compound, additional research was carried out on the doped system to understand if the physics that is driving the properties in the doped compound differ to that of the parent material.

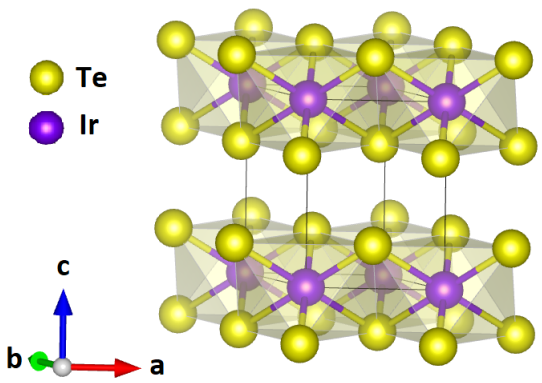

Figure 1.2.1: $IrTe_2$ structure above MI transition.

1.2.2 Ca_2RuO_4

In the case of Ca_2RuO_4, which falls into the complex family of ruthenate compounds, the electronic and atomic interplay creates a metal to insulator transition (360K), followed by a separate magnetic transition at a lower temperature (110K). This system consists of a layered perovskite type structure, in which 6 oxygen atoms form an octahedra around each Ru. Between 400K and 150K there is significant change in this octahedral structure, which goes from an elongated state (along the *c*-axis) to a compressed state [22, 23]. In terms of the electronic transition, while it is clear that a Mott - type transition makes the 2/3 filled t_{2g} band insulating two scenarios have been suggested for the mechanism driving this. One scenario suggests that the transition is orbital selective and it only affects the *xy* band, which becomes metallic [24, 25]. The second scenario suggests that it is not orbital selective and instead is assisted by the crystal field splitting [26]. Understanding which scenario is applicable in this system is critical to further understand its properties.

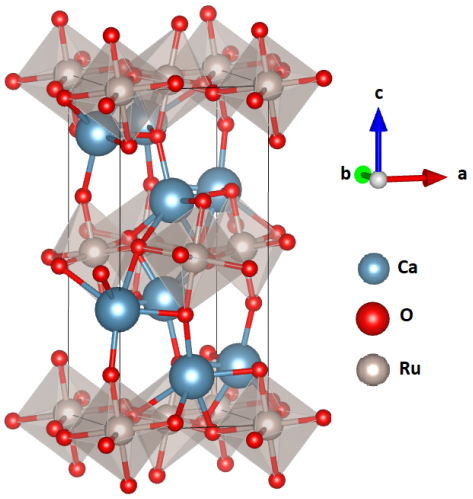

Figure 1.2.2: Ca_2RuO_4 structure above MI transition.

Since the two scenarios proposed have different orbital occupations and there are significant structural changes, polarization dependent XAS measurements are a suitable technique for tracking both the electronic and atomic structures. Since the occupation of certain orbitals change across the transition in the case of the orbital selective scenario and due the strong interaction between the Ru and O structures, by tracking changes in different crystal orientations it might be possible to identify a charge transfer between close lying energy levels. The aim of these measurements was to determine whether the occupation of the different states in the t_{2g} band changes as a function of temperature, whilst also tracking the structural changes in the octahedra.

The substitution of lanthanum on to the calcium sites provides a direct route to explore the interplay between the atomic and electronic structures across the metal to insulator transition. Lanthanum has a slightly larger ionic radius than calcium, and a trivalent oxidation state rather than divalent as for the calcium, which donates an additional electron into the Ru orbitals. This offers the advantage of retaining the original lattice structure and hence the Coulomb interaction is comparable between the two systems [27]. The slight substitution is believed to effectively increase the t_{2g} bandwidth by lowering the highly distorted Ru-O-Ru bond angle (151^o) while simultaneously filling the t_{2g} orbitals with the electron added by the La ion. Upon doping, the MI transition temperature is reduced and eventually suppressed at higher doping levels. While the bandwidth control and filling control are common in perovskite-like oxides [28, 29], the drastic and distinct effects in Ca_2RuO_4 is rarely seen, making a study of the La doping an interesting topic in its own right.

1.2.3 NaFeAs

Iron pnictide compounds have generated significant interest since it was shown that a superconducting phase can emerge. Since these compounds are fundamentally different from the cuprates high temperature superconductors [30], it may lead to a new theory of non-conventional SC. The NaFeAs compounds shows both structural and magnetic transitions along with a filamentary superconducting phase [31, 32]. Once the system is doped with cobalt, the structural and magnetic transitions become suppressed and bulk superconductivity emerges [33]. While the SC phase is still not fully

understood and both the structural and magnetic transitions have been fully resolved, it has been suggested that there is a preceding orbital/spin nematic state. The origin of the transition has been theoretically linked to both the spin and/or orbital degrees of freedom. However it is unclear from experimental results as to what is the critical driving factor and whether this is caused by a static or fluctuating order [34, 35, 36, 37, 38]. It has been suggested that the spin nematicity can be understood as a direct consequence of an orbital ordering on the Fe $d_{xy/yz}$ orbitals.

The aim of this research was to track both the electronic and atomic structural changes across the transitions in this material once doped with Co, using polarization-dependent HERFD-XAS measurements. It is expected that if the nematic phase is dominated by spin nematicity, then the XAS measurements might be sensitive to this change. By providing an overall picture for the atomic and electronic structures in each phase, it may provide further information as to whether the interactions between the different states may be responsible for the emergence of the SC phase.

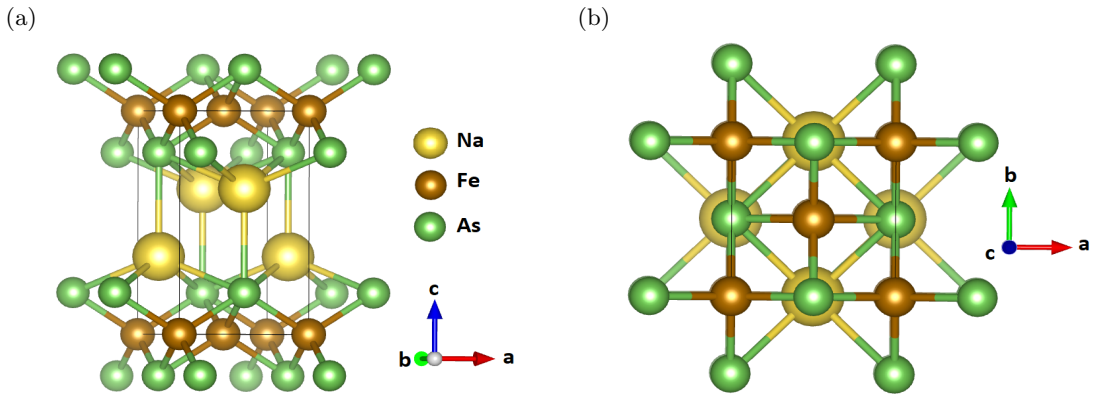

Figure 1.2.3: NaFeAs crystal structure. a) side view, b) top view.

1.3 Chapter summary

This chapter has provided an introduction into the relevant physics of the transition metal compounds researched in this thesis. Specifically the considerations needed to understand how the spin-orbit coupling, crystal field splitting and charge ordering may effect the sample properties have been discussed. Each of the 3 compounds have also been introduced. In each case the scenarios which have been presented in the literature to understand the material properties have been outlined to provide a guide for this research.

Chapter 2

The theory of XAS and XES

In this chapter the basic concepts of x-ray absorption spectroscopy (XAS) and x-ray emission spectroscopy (XES) are discussed. The absorption and electronic transition theories provide the key concepts which govern the origins of the spectra observed. Further details regarding the x-ray absorption near edge structure (XANES) and extended x-ray absorption fine structure (EXAFS) regions are also given, specifically the interactions which provide electronic and structural information. A derivation is given for the single scattering EXAFS equation. The main factors that contribute to the phase and amplitude are given special focus. Additionally, the polarization dependence of these measurements are discussed in relation to the K and L absorption edges. A brief discussion of x-ray emission spectroscopy is given in the context of high energy resolution fluorescence detected XAS (HERFD-XAS).

2.1 Absorption and electronic transition theory

In both XAS and XES measurements a material is bombarded with x-rays and depending on the type of information required, a number of different processes can be recorded. In both cases the creation of a core-hole by the excitation of an electron is needed. Considering the electronic structure of an atom, a core electron must be given enough energy to be excited above the Fermi energy (E_f) for a core-hole excitation to take place, since the Pauli exclusion principle makes transitions to states below this energy impossible as they are already filled [39]. The minimum kinetic energy of a photoelectron (p.e.) emitted (leaving the atom it was generated in) in the final state is thus $\hbar^2 k_F^2/2m_e$, with m_e the mass of an electron. The threshold energy for a photoelecton excitation can then be given in equation 1 and expressed as the wavenumber k:

$$k = \frac{1}{\hbar}\sqrt{2m_e(E_{p.e.} - E_f)} \tag{1}$$

with $E_{p.e.}$ being the energy of the photoelectron emitted from the atom the excited electron is generated in. The system now consist of a photoelectron and a core-hole, which is unstable with a lifetime typically $\tau \approx 10^{-15}$ - 10^{-17}s [40]. This is responsible for the core-hole lifetime broadening effect and is a major limitation in the resolution of conventional XAS/XES measurements.

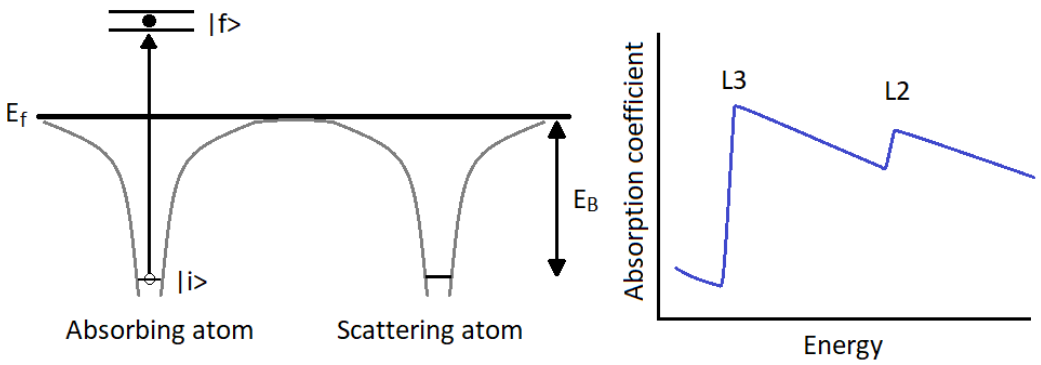

Figure 2.1.1: Left: schematic energy diagram indicating the photon-induced transition, E_B is the binding energy. Right: shows absorption coefficient vs energy, with example edges without scattering effects (isolated atom).

The absorption coefficient μ(E), which describes how far the electromagnetic radiation can penetrate a material before being absorbed, can be derived from Beer-Lambert's law [41]:

$$I(E) = I_0(E)e^{-\mu(E)x} \tag{2}$$

here I(E) is the intensity of the transmitted beam, I_0(E) is the intensity of the incident beam and x is the thickness of the sample. To account for the absorption from all the atoms in the material, μ(E) can be defined as:

$$\mu(E) = \sum_i n_i \sigma_i(E) \tag{3}$$

where n_i is the number of atoms of the same type per unit volume and $\sigma_i(E)$ is the cross-section of each atom i. The energy of the incident photons can be given in terms of their frequency $E = \hbar\omega$, and the cross section is defined by the transition rate, $\Omega(\omega)$, normalized with respect to the flux of the incident x-rays:

$$\sigma(\omega) = \frac{\Omega(\omega)}{nc} \tag{4}$$

with n the number of photons per unit volume of the x-ray beam and c the velocity of light. Using the Fermi's golden rule [42] it can be shown that the probability of an incident x-ray releasing a core-electron per unit time, where the system goes from the initial bound state, $|i>=|i, n_{\overrightarrow{k},\alpha}>$, to a final unbound state, $|f>=|f, n_{\overrightarrow{k},\alpha}>$ is given as:

$$\Omega_{i\to f}(\omega) = \frac{2\pi}{\hbar}|<f|H_I|i>|^2\delta(E_f - E_i - \hbar\omega)\rho(E_f) \tag{5}$$

The interaction Hamiltonian between the x-rays and core electrons is given by H_I, $\rho(E_f)$ is the density of the unoccupied states and $n_{\overrightarrow{k},\alpha}$ is the number of photoelectrons with the wavenumber $\overrightarrow{k}$ and polarization α. By using the single particle Hamiltonian describing the deep core electron and its interaction with the x-ray field, and expanding the matrix term $|<f|H_I|i>|$, the final cross section is given in equation (6) [42, 43], a simple derivation is also given in [44]:

$$\sigma(\omega) = 4\pi^2\alpha_{fs}\hbar\omega|<f|\Im|i>|^2\delta(E_f - E_i - \hbar\omega)\rho(E_f) \tag{6}$$

$$\Im = \epsilon\cdot r(1 + \frac{i}{2}k\cdot r + \cdots) + \frac{1}{2mc}(k\times\epsilon)\cdot(L + \hbar\sigma) + \frac{i\hbar\omega}{4mc^2}\sigma\cdot(\epsilon\times r)$$

The fine structure constant is given by $\alpha_{fs} = e^2/\hbar c$, which governs the strength of the electromagnetic interaction between elementary charged particles. δ is the Dirac delta function which reduces all other energies to zero and ϵ is the polarization of the x-rays. The transition operator, $\Im$, can be given in terms of the largest components and describes the possible interactions and their strength. The first term gives the electronic contributions; $\epsilon\cdot r$ is the dipole and $\frac{i}{2}\epsilon\cdot rk\cdot r$ is the quadrupole transitions. The second term $\frac{1}{2mc}(k\times\epsilon)\cdot(L+\hbar\sigma)$ gives the magnetic dipole transitions, and $\frac{i\hbar\omega}{4mc^2}\sigma\cdot(\epsilon\times r)$ is the dipole spin position operator. In the EXAFS analysis it is typical to only take into account the electronic dipole transitions, as these are the most intense. It is important to also consider the quadrupole transitions when interpreting the XANES pre-edge features.

The equations shown above give the relationships which govern the absorption process of x-rays in a material. For a core electron to be excited, the incoming x-ray must have an energy at least equal to the binding energy. Figure 2.1.1 shows a schematic representation of the absorption coefficient for a generic isolated atom. As the energy of the incident x-rays are varied, there are sharp increases in the absorption and slowly decreasing values after. The inflection point is the absorption edge in which these represent the threshold energies for specific orbitals. The decrease after the edge is due to the fact that the probability of absorption decreases with energy. As the binding energy is specific to the element and orbital, XAS and XES are element specific techniques.

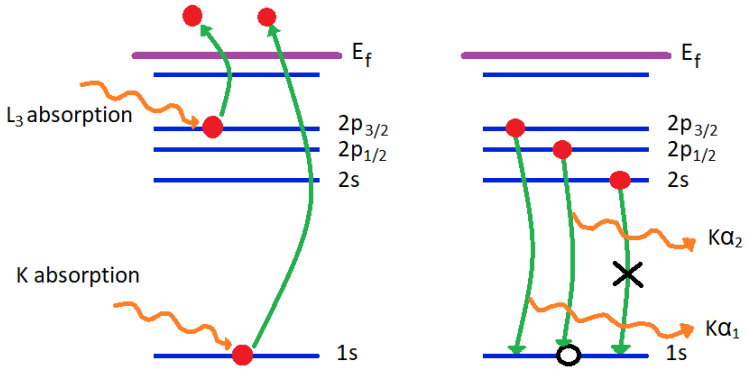

Figure 2.1.2: Schematic energy diagram of the x-ray absorption and K fluorescence. The s-s transition is not allowed.

Both fluorescence detected XAS and XES require the core-hole to be filled by an electron from a higher orbital state, which releases a photoelectron with an energy equivalent of the difference between the initial and final states. Which transitions occur not only depends on the Pauli exclusion principle but also on a set of selection rules. The origins of these selection rules are dependent on the transition moment integral [45]:

$$\int \psi_1^* \upsilon \psi_2 d\tau \tag{7}$$

where two wave functions from two states are given by ψ_1 and ψ_2, and υ is the transition moment operator. The integral gives the probability and magnitude of a transition occurring between two different states. Note that this specifically relates to the electric-dipole electric-field interaction since these are the most intense. While it is not necessary to calculate the value of the integral in this thesis, by understanding the properties of the wavefunctions, including symmetry and angular momentum, it is possible to show whether a transition is allowed or forbidden. This can then be summarised as a series of selection rules which provide the conditions for transitions. If the function is symmetric then in general it is not zero and therefore the transition is allowed. When the function is zero, the interaction energy is zero and no transition can occur between the different states and is termed a forbidden transition. The parity of the wavefunction relates to a symmetry operation, even parity is where the wavefunction does not change under inversion (for example s-type functions) and a wavefunction is consider odd if it does change sign.

Electronic dipole transitions are the most intense and are responsible for the majority of the features observed in XAS and XES. These transitions occur between states of different parity, which gives the main selection rules considered for these transitions:

- The total spin must not change, $\Delta S = 0$
- The total angular momentum can change by: $\Delta J = 0, \pm 1$. However the $0 \rightarrow 0$ transition are not allowed.
- The total orbital angular momentum can change by: $\Delta L = 0, \pm 1$. However the $0 \rightarrow 0$ transition are not allowed.

As the dipole transitions are the dominant decay process it is typical to use the dipole approximation to simplify the interpretation of spectra. For pre-edge features however it is also important to consider quadrupole transitions, in which the parity must be conserved. These transitions are significantly weaker than the dipole allowed transitions as they are coupled to the electric field gradient [46]. However they can provide further information regarding the electronic state of the system. It is also important to note that while the dipole and quadrupole transitions have been treated separately, in reality the geometry of the system under investigation can lead to a mixing of the transitions, i.e. in non-centrosymmetric systems mixing is allowed [47]. The selection rules for quadrupole transitions are given as:

- The total spin must not change, $\Delta S = 0$
- The total angular momentum can change by: $\Delta J = 0, \pm 1, \pm 2$. However $0 \rightarrow 0$, $\frac{1}{2} \rightarrow \frac{1}{2}$, $0 \rightarrow 1$, $1 \rightarrow 0$ transitions are not allowed.
- The total orbital angular momentum can change by: $\Delta L = 0, \pm 1, \pm 2$. However $0 \rightarrow 0$, $0 \rightarrow 1$, $1 \rightarrow 0$ transitions are not allowed.

2.2 X-ray absorption spectroscopy

During an x-ray absorption spectroscopy measurement the energy of the incident beam scans over an absorption edge. The fraction of photons absorbed in this process provides information about the element of interest, where the electronic and local atomic structures can be determined. Figure 2.2.1 shows an schematic diagram of an XAS spectrum, where different regions have been defined. The XANES region which typically extends over a short energy range originates from the photoelectrons reaching the conduction band and provides information regarding the electronic state of the element of interest and the local chemical environment. The final extended region (EXAFS) results from the scattering of photoelectrons which have been ejected to the continuum and provides local structural information. There are 3 different modes which are used in collecting the resultant spectra, which all include measuring the incident intensity (typically with an ion chamber).

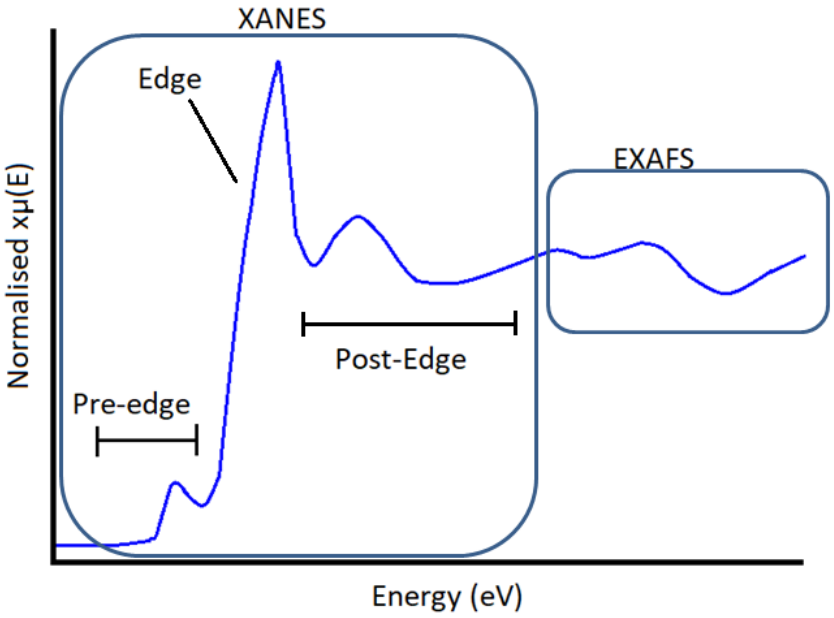

Figure 2.2.1: Schematic diagram of an XAS spectra, XANES (pre-edge, edge, post-edge) and EXAFS regions have be identified

Transmission mode is the most direct route where the intensity downstream of the sample at a given energy is compared to the incident intensity, as shown in equation (8) where x is the sample thickness and I_t is the intensity of the transmitted photoelectrons. As this is a direct route this method does not suffer from self-absorption effects however it requires careful consideration with regards to the sample thickness since the x-rays need to be transmitted by the sample. The attenuation coefficent, which descibes the distance over which the x-ray beam is absorbed, is given by Beer-Lambert law (equation 2). If a sample is too thick (typically taken as 2 absorption lenghts), then a significant proportion of the x-rays are absorbed and not enough pass through to measure the spectra. If on the otherhand the sample is too thin, then the majority of x-rays pass through and this can be detrimental to the signal to noise ratio. In fluorescence mode, when the core-hole created by the incident x-rays is filled by an electron in a higher energy orbital, an photoelectron is released. This is given in equation (9) where I_f, the intensity of the fluorescence x-rays, is proportional to the absorption coefficient. While this technique can suffer from significant self-absorption, it doesn't have the same limitation with respect to the sample thickness when compared to transmission measurements.

$$\mu(E)x = ln(\frac{I_0}{I_t}) \tag{8}$$

$$\mu(E) \approx \frac{I_f}{I_0} \tag{9}$$

An additional limitation comes from the core-hole lifetime broadening which in conventional XAS limits the achievable resolution. To over come this HERFD-XAS has been used [48]. This technique uses a XES spectrometer to select specific fluorescence lines with greater resolution than the core-hole broadening. The experiments presented in this thesis are almost exclusively measured in fluorescence mode, due to the need of single crystal samples which are highly concentrated hence the absorption length is typically small.

2.2.1 X-ray absorption near edge structure (XANES)

The XANES region typically covers an energy range of approximately 50eV below and 100eV above the main absorption edge, shown in figure 2.2.1, and can be defined by three regions: pre-edge, edge and post-edge. These regions are sensitive to the formal oxidation state, coordination environment and geometry of the absorbing atom. Different interactions contribute to each region and provide specific information:

- **Pre-edge**: This region is typically defined by 50eV below the rising edge, and within a simple approximation involves quadrupole transitions to empty bound states. This region can provide information regarding the local coordination environment, the oxidation states and bonding [47]. These features are typically more intense with non-local and *pd* orbital mixing.
- **Edge**: This is the threshold for continuum states. The energy position can be defined in a number of ways. For this thesis it is taken as the first peak (after the pre-edge region) in the first derivative. The edge position is dependent on the oxidation state of the absorbing atom. When a neutral atom gains or loses an electron the effective charge of the nucleus changes and the remaining electrons either feel a greater or a weaker binding force, hence the energy to excite a core electron in to the continuum will also change [49, 50].
- **Post-edge**: This region can extend up to 100eV after the absorption edge and is dominated by multiple-scattering (MS) resonance of the photoelectrons with low kinetic energy. The features typically show dependence on the atomic position of neighbouring atoms and information can be obtained regarding distances and bond angles.

While XANES measurements have the advantage that the Debye-Waller factor is negligible, there is no simple equation that can be used to interpret the results since the low kinetic photoelectrons have long mean free paths and MS dominates. The features in this region are effected by the core-hole broadening. The core-hole created is in an unstable state and will decay in a short amount of time. The energy width of this state is proportional to its lifetime hence as higher atomic number elements have shorter lifetimes, the broadening is greater. This effects limits the resolution of features in the XANES measurements. It is possible however to make some analysis of the features by either fingerprint analysis or using quantum chemistry modelling codes to simulate the XANES spectra [51]. The fingerprint analysis requires comparison to known reference compounds where information regarding the local coordination chemistry, molecular orbitals and oxidation states is known. In this thesis the XANES have been analysed by simulating the groundstate electronic structure using density-functional theory/multiple-scattering theory calculations and tracking changes in features across the studied transitions.

2.2.2 Extended x-ray absorption fine structure (EXAFS)

When an electron gains enough energy to be excited to the continuum, the interactions with neighbouring atoms will cause a modulation to the measured absorption coefficient after the edge. This region provides information about the local environment around the absorbing atom, including the number and type of neighbours, distances and disorder in the structure. Starting from a simplified model of the interaction, a single scattering event consists of a released photoelectron travelling a distance r to a neighbouring atom (the scatterer) and returning to the original absorber. As the photoelectron can be treated as a wave, the interference between the outgoing and incoming waves will either be constructive or destructive. This can be modelled as a sinusoidal function which will be modulated by the total scattering path between the interacting atoms and the wavenumber (equation (1)). Equation (10) gives the simplified expression for the modulation in the absorption coefficient:

$$\mu(k) = \mu_0(k)(1 + \chi(k)) \quad \text{where} \quad \chi(k) \propto cos(2kr) \tag{10}$$

here $\mu_0(k)$ is the absorption coefficient for an isolated atom. Since the discussion will be in terms of the photoelectron, the energy dependence has been translated into the photoelectron wavenumber via equation (1). In order to be able to analyse the modulation to provide information regarding the local structure around the absorbing atom it is necessary to take into account a series of effects, which can lead to modifications to the amplitude and phase of $\chi(k)$. Here only single scattering events will be considered, within the harmonic approximation for lattice vibrations. The final expression for the EXAFS equation based on the IUCr (2011) definition is given in equation (11) [52, 53, 54, 55, 56, 57]. In this equation the terms are defined as: S_o^2 is the amplitude reduction factor, N_j is the degeneracy of the scattering path, $f_j(k, \pi)$ is the backscattering amplitude, r_j is the

distance between the absorbing atom and scatter, $\lambda(k)$ is the mean free path, σ_j^2 is the Debye-Waller factor and δ_j is the phase shift of the wavefunction dependent on the species of the absorbing and scattering atoms. It is useful to separate the phase (Φ_j) [58] and amplitude (A_j) [59] components, which are given in equations (12):

$$\chi(k) = S_0^2 \sum_j N_j \frac{f_j(k,\pi)}{kr_j^2} e^{-\frac{2r_j}{\lambda(k)}} e^{-2k^2\sigma_j^2} sin(2kr_j + \delta_j(k,r_j)) \tag{11}$$

$$\chi(k) = \sum_j \chi_j(k) = \sum_j A_j(k,r_j) sin(\Phi_i(k,r_j)) \tag{12}$$

$$A_j(k,r_j) = S_0^2 N_j \frac{f_j(k,\pi)}{kr_j^2} e^{-\frac{2r_j}{\lambda(k)}} e^{-2k^2\sigma_j^2}, \qquad \Phi_j(k,r_j) = 2kr_j + \delta_j(k,r_j)$$

The summation represents the fact that contributions from all scattering atoms will be considered. The N_j term is the degeneracy of the scattering paths. Since there may be multiple atoms of the same species at the same average distance, the EXAFS can provide information regarding the number of scattering atoms. The phase of the EXAFS modulations arises from the optical path, $2kr_j$ and a phase shift. The optical path is the phase of the photoelectron travelling to the scattering atom and returning to the original absorber and varied with the interatomic distance. The additional phase in the sine function is introduced to account for phase shifts in the photoelectron which can severely affect the simplified model of the optical path and depends on the atomic species involved in the scattering process [56]. When considering what contributions account for it, it is useful to treat the system semiclassically. The wavefronts of the photoelectron will not have a constant k value due to the atomic potential created by the atoms. For both the absorbing and scattering atoms, due to the conservation of energy the photoelectron will be travelling faster in the centre of the potential. It is typical to combine all phase shift effects into one parameter, δ_j, and this is normally calculated by software, for example FEFF [60, 61].

The main contribution to the EXAFS amplitude comes from the backscattering amplitude, $f_j(k,\pi)$ [56]. This takes into account the probability of the scattering event occurring elastically towards the absorber. The k-dependence of this factor is different for different elements and it is typical for large atoms with many electrons to have a higher probability of scattering when compared to small atoms with few electrons. An additional factor that needs to be considered is that the photoelectron is not a planewave, but is better approximated by a spherical wave that travels out isotropically ($\psi(k,r) = e^{ikr}/kr$) [62]. Since EXAFS measurements are proportional to the value of the backscattered wave at the origin, the backscattering amplitude must also be modulated by the fact that waves spread out and therefore the scattering probability will decrease as the square of the distance between the origin and scatterer, this is introduced into the EXAFS equation by the $1/kr^2$ term.

Once a photoelectron has been created, the final state of the absorbing atom will be different to the initial state due to the core-hole. The orbitals will adjust to the fact that all the other electrons will feel an additional force from the nucleus and will lead to a reduction in amplitude of the EXAFS oscillations [63]. The overlap between the initial and final state [63], $|<\psi^f|\psi^i>|$ will be reduced by this effect and therefore also a reduction in the transition strength. The amplitude reduction factor, S_0^2, is an element-dependent constant used to model this factor. This also takes into account the measurement errors and is typically fitted as a parameter.

The mean free path, $\lambda(k)$, takes into account the contributions to the reduction in the amplitude of the EXAFS modulations and is related to the fact that scattering effects are not instantaneous. The first contribution comes from the core-hole left by the photoelectron. After a period of time ($\tau_{c.h.}$) this will be filled by an electron from a higher orbital, hence the initial and final states of the absorbing atom will not be the same and the overlap used in equation (6) will again reduce the amplitude. The second contribution originates from the inelastic scattering of the photoelectron, which can be considered in terms of a lifetime ($\tau_{p.e.}$) since the further it is travelling the more likely inelastic losses become. The total lifetime therefore is $1/\tau = 1/\tau_{c.h.} + 1/\tau_{p.e.}$ and the consequence of this is an energy broadening, $\Delta E \approx \hbar/\tau$. This term is the main reason why EXAFS is a local probe, since it reduces the modulations by $\approx 90\%$ at a distance of $\approx 10\mathring{A}$.

The final term considered at this stage is the mean square radial displacement (Debye-Waller) factor, $e^{-2k^2\sigma_j^2}$. The EXAFS measurements typically consist of $\approx 10^8$ absorption events at each energy point. Since the lifetime of the photoelectron ($\approx 10^{-15}$s) is shorter than the characteristic time for lattice vibrations ($\approx 10^{-13}$s), this technique gives a snapshot of the local structure in the area covered by the focus spot of the beam. There are two effects that need to be considered due to the averaging of the EXAFS measurements. Firstly static disorder can arise when there are differences in the position of the absorbing atom which are randomly distributed throughout the

sample, for example defects in the crystal structure. The second effect is the thermal disorder. Since all chemical bonds will show a vibration, the distance between the absorber and scatter will vary over time and there will be a contribution to the EXAFS from the different lengths.

While this is a simplified model (e.g. no multiple scattering or polarization dependence) equation (11) gives an acceptable overview of the different effects which need to be considered when analysing the EXAFS signal. The methods for treating the different factors when fitting the experimental data to theory will be introduced in section 4.5.

2.2.3 Multiple scattering

Single scattering (SS) events typically dominate the EXAFS signal, but in certain cases multiple scattering (MS) events need to be considered too. These events result from the photoelectron wave scattering from more than one neighbouring atom before returning to the original absorber. This can be defined by the "path length", r_{tot}, which gives the sum of each "leg" involved in the scattering path and the effective half path length as $r_{eff} = r_{tot}/2$. Here a "leg" is defined as the distance between two scattering atoms. The majority of the systems in this thesis can be described by single scattering events, however it is important to also note that in the $Ca_{2-x}La_xRuO_4$ analysis MS paths have been considered to obtain a reasonable fitting result.

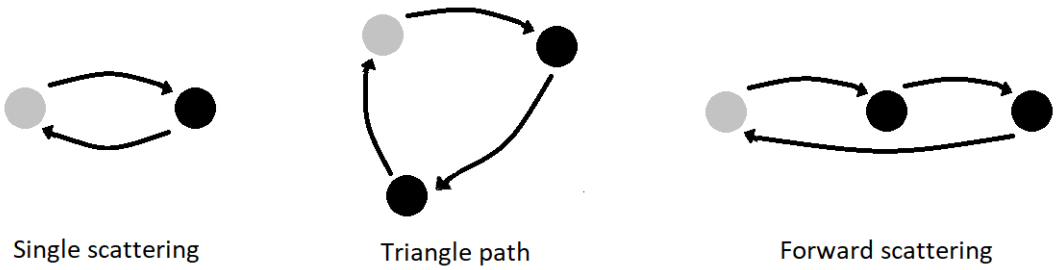

Figure 2.2.2: Possible multiple scattering events considered. Grey atom represents the absorbing atom.

The mathematics needed to include the MS paths is significantly more complex [54, 55, 64, 65, 66] than SS event. FEFF has been used to include these paths correctly via the implementation of the Rehr-Albers scattering-matrix algorithm [55]. While the polarization effects discussed in section 2.2.4 apply to the first event in a MS path, the effect on additional scattering events are difficult to calculate since the scattering events become isotropic. Using the orientation of the sample relative to the x-ray beam, the MS paths including the polarization dependency have been calculated in FEFF6 [67, 68] when needed.

The single scattering equation (11) can be modified to account for MS events:

$$\chi(k) = S_0^2 \sum_j N_j \frac{|F^j_{eff}(k)|}{kr^2_{eff}} sin(2kr_{eff} + \phi^j(k) + 2\delta_c(k)) e^{-2k^2\sigma_j^2} e^{-2r_{eff}/\lambda(k)} \quad (13)$$

here N_j is the degeneracy of path j and $\sigma^2_{eff} =< (r_i - r_{eff})^2 >_i$ is the mean square deviation in the half path length, where r_i is the instantaneous half path length. The term r^2_{eff} is introduced to the denominator to allow this equation to resemble the SS equation. For an N-leg path, the scattering amplitude, F^j_{eff}, is given by the product of (N-1) curved-wave effective scattering matrices, $F^{(N-1)} \cdots F^2 F^1$. The scattering matrix depends on the photoelectron energy, the scattering angle $\beta_i = cos^{-1}(\hat{r}_i \cdot \hat{r}_{i+1})$ which is the angle between the incoming and outgoing legs at site i, and the distance to site $(i-1)$, $|r_i - r_{i-1}|$ due to the curve wave effects [55]. The optical path length is given by $e^{ik(\rho_1+\rho_2+\cdots+\rho_N)}$ where $\rho_i = |r_i - r_{i-1}|$. δ_c is the phase shift from the central atom. As the F^j scattering matrices are complex the effective scattering phase, $\phi^j(k)$ also depend on the inter-site distance and angles.

2.2.4 Polarization dependent XAS - single crystal samples

Both the phase and amplitude of the EXAFS are dependent on the polarization of the x-rays. The excitations are highly preferential in the plane of the electric field and since the x-rays generated from a synchrotron are highly polarized in the plane of the ring, the analysis of spectra collected on single crystal samples can provide a wealth of orientation dependent information [69]. As all of

the samples in this thesis (apart from the references) are single crystals, the polarization analysis can give information along different crystallographic planes due to the periodic structure. In cubic crystals the electric dipole transition probability is isotropic, however in lower symmetry groups the probability become anisotropic [70]. In the case of K and L_1 measurements with initial s states, the polarization dependence on the EXAFS amplitude is simple to analyse since it only involves final states with p symmetry. The situation becomes more complicated for the L_2- and L_3-edges as the final states involve both s and d symmetry. While the d transitions are the most intense interactions, the contribution from the s states is still not fully understood [69, 70, 71, 72, 73]. The samples used in this thesis are highly anisotropic and in single crystal form, so a careful consideration of the dependency of both the XANES and EXAFS regions with respect to the polarization is discussed below.

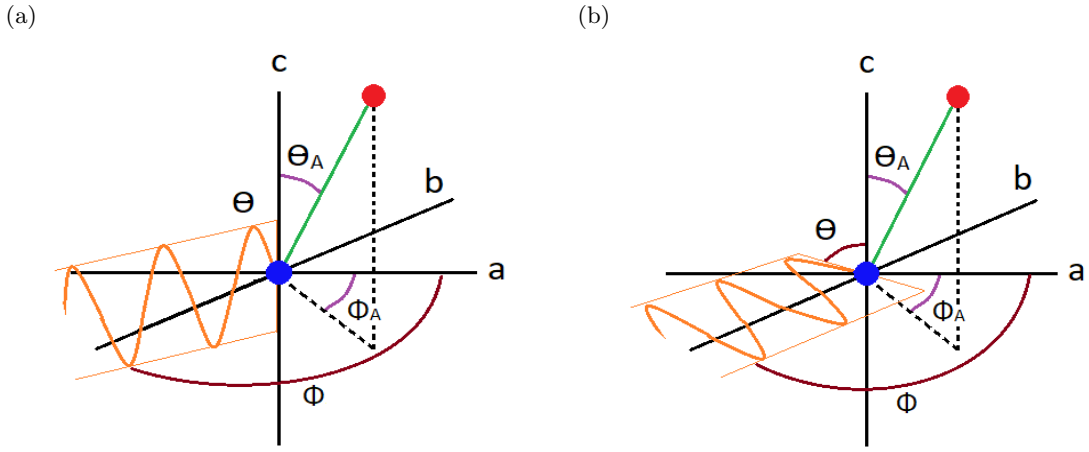

Figure 2.2.3: Representation of the relative angles between the scattering paths and electric field, considered for the polarization dependent calculations. It is assumed that the central atom is at the origin. a) electric field parallel to c-axis, b) electric field perpendicular to c-axis

XANES

Due to the multiple scattering events and possible mixing of dipole and quadrupole transitions, analysis of the polarization dependence is complicated, especially since no formal equation can be used in this region. The focus of the XANES analysis in this thesis is on the changes in features across transitions, since the anisotropic nature may provide information regarding the directionality and orbital selectively of the transitions [74, 75, 76]. By measuring the XANES at different orientations it has been shown that the orbital occupancy ratio can be calculated in certain situations [77, 78, 79]. Since the pre-edge features are dependent on the quadrupole transitions, which are dependent on the local symmetry of the absorption atom, differences across angles becomes difficult to interpret in this region. Additionally the hybridization between the metal and ligand orbitals also has an effect on the intensities of features in the pre-edge region. Recent work has shown how it is possible to directly image the active orbitals in real space, using non-resonant inelastic x-ray scattering since the method has non-vanishing matrix elements beyond the dipole limit showing that polarization dependent measurements are sensitive to orbital orientation [80]. While XAS can not provide this level information, it can show how different crystallographic planes can be linked to certain orbitals and hence changes across transitions can be mapped. Using knowledge of the electronic structure and simulations of the systems, an understanding of the angular dependence of the XANES for each material will be discussed in the relevant sections.

K (and L_1) edge EXAFS

Since the K and L_1 absorption edges (initial s state) within the dipole approximation, only consider p symmetry orbitals for the final state, the polarization dependence on the EXAFS is introduced by:

$$\chi_A \propto < (\hat{E} \cdot \hat{r})^2 >_{\theta,\phi} \tag{14}$$

The polarization vector (electric field) is given as $\overrightarrow{E} = E(sin\theta cos\phi, sin\theta sin\phi, cos\theta)$ and the scattering atom A is at a distance $\overrightarrow{r}_A = r(sin\theta_A cos\phi_A, sin\theta_A sin\phi_A, cos\theta_A)$. While during the experiment the electric field is fixed and the sample is rotated, it is simpler for the derivation if it is considered that the sample is fixed and the electric field is changing (both cases are equivalent). Figure 2.2.3 shows the experimental set up for the extreme cases (0^o and 90^o), representing the different angles considered. For conventional XAS using powdered samples the polarization dependence is effectively averaged over all orientations:

$$\chi_{Ran} \propto < (\hat{E} \cdot \hat{r})^2 >_{\theta,\phi} \tag{15}$$

$$= < (sin\theta cos\phi sin\theta_A cos\phi_A + sin\theta sin\phi sin\theta_A sin\phi_A + cos\theta cos\theta_A)^2 >_{\theta,\phi}$$

$$= < (sin\theta sin\theta_A cos(\phi - \phi_A) + cos\theta cos\theta_A)^2 >_{\theta,\phi}$$

where $cos(\alpha - \beta) = cos\alpha cos\beta + sin\alpha sin\beta$ has been used. Integrating over all directions and using the trigonometric relation $sin(2\theta) = 2sin\theta cos\theta$:

$$\chi_{Ran} \propto \frac{1}{4\pi}[sin^2\theta_A \int_0^{2\pi}\int_0^{\pi} sin\theta d\theta d\phi sin^2\theta cos^2(\phi - \phi_A) + \tag{16}$$
$$\int_0^{2\pi}\int_0^{\pi} sin\theta d\theta d\phi sin(2\theta)\frac{sin(2\theta_A)}{2} cos(\phi - \phi_A) +$$
$$cos^2\theta_A \int_0^{2\pi}\int_0^{\pi} sin\theta d\theta d\phi cos^2\theta]$$

Using the following relations:

$$\int_{\pi}^{0} dcos\theta(1 - cos^2\theta) = \frac{4}{3}; \int_{-\phi_A}^{2\pi-\phi_A} cos^2\phi' d\phi' = \pi; \int_{-\phi_A}^{2\pi-\phi_A} cos\phi' d\phi' = 0 \tag{17}$$

the final expression becomes:

$$\chi_{Ran} \propto \frac{1}{4\pi}[\frac{4\pi}{3}sin^2\theta_A + 0 + \frac{4\pi}{3}cos^2\theta_A] = \frac{1}{3} \tag{18}$$

This gives the angular dependence of the EXAFS signal when the incident beam is polarized in the plane of the synchrotron on a powdered sample. Since the only component which will change between powdered and single crystal samples will be the angular dependence term, a generalized equation can be formed to give the weighting factor to the EXAFS signal when single crystal samples are measured:

$$\chi_{Ran} \approx \frac{1}{3}\chi(k) \tag{19}$$

$$\chi_{Pol} \approx (sin\theta sin\theta_A cos(\phi - \phi_A) + cos\theta cos\theta_A)^2\chi(k) \tag{20}$$

Where $\chi(k)$ represents the measured EXAFS signal. By expressing χ_{Pol} in terms of χ_{Ran} the final weighting factor becomes:

$$\chi_{Pol} \approx 3(sin\theta sin\theta_A cos(\phi - \phi_A) + cos\theta cos\theta_A)^2\chi_{Ran} \tag{21}$$

This derivation has been based of *D. Haskel's* thesis [44], with concepts taken from [42]. The positions of the atoms can be calculated and the relative angles to the axes are determined for the model used in the fit for a given material. The ARTEMIS fitting program uses FEFF to calculate single scattering paths for randomly oriented samples. Using equation (21), a weighting factor can be calculated for each path which allows the polarization dependence to be taken into account. In these measurements the samples are rotated around one axis, i.e. the *c*-axis is rotated from being parallel to perpendicular to the polarization of the beam, and the angles for the equation is defined by this scenario. The *ab*-plane orientation is not characterized and is left as the only fitting parameter for the weighting factor. This factor is introduced into the fitting process via a global parameter, the amplitude reduction factor S_o^2, which takes into account all contributions to the amplitude reduction when fitting a model to experimental data.

L_2 and L_3 edge EXAFS

For the L_2 and L_3 absorption edges, the polarization dependence is complicated because it involves two final states. It was suggested that neglecting the *s-d* cross term can lead to significant errors in both the bond lengths and amplitudes [71]. However the literature is inconclusive in providing a universal explanation for how much the additional term actually contributes to the EXAFS signal. It has been shown that the crystal structure, experimental set-up and analysis technique can all affect the final result [72]. For this thesis the $IrTe_2$ L_3 data has been fitted with the assumption that the *d* contribution is significantly greater than the *s*. While this approach appears to work for this system, it is important to understand the different effects that need to be considered and why the simplification is valid.

The simplified expression for the EXAFS equation for the L_2/L_3-edges is shown in equation (22), a number of varying versions have appeared in the literature [71, 72, 73, 81]. This equation is taken from *P. H. Citrin* [72], which gives a in depth derivation, including the assumptions used.

$$\chi_{k,\theta} \approx A_j(k) n_d(\theta) sin[2kR + \delta_{2b}(k)] + n_{sd}(\theta) sin[2kR + \delta_{2b}(k) + \Delta_a(k)] \tag{22}$$

with A_j defining all other amplitude related effects, δ_{2b} is the total phase shift of the photoelectron, $\Delta_a(k)$ is the cross term correction for the phase shift for purely *d* final state scattering and:

$$n_d(\theta) \approx 0.5 \sum_{j=1}^{N} (1 + 3|\hat{\epsilon} \cdot \hat{r}_j|^2) \tag{23}$$

$$n_{sd}(\theta) \approx 0.2 \sum_{j=1}^{N} (1 - 3|\hat{\epsilon} \cdot \hat{r}_j|^2) \tag{24}$$

the quantities n_d and n_{sd} can be considered as effective partial coordination numbers and importantly it should be noted that there is no contribution from the *s* final state on it own. The reason for this is because as the *s* state is isotropic it can be shown that compared to the *d* and coupled *sd* states, the contribution vanishes [72, 73]. For an isotropic absorber the *s-d* cross term vanishes by angular averaging, however for anisotropic absorbers this is not the case. The initial analysis shown in the literature suggested that in the worst case scenario the effect on the bond lengths is up to ±0.05Å and the amplitude can be modified up to a factor of 2. On the other hand it has been suggested that the *d* contribution is approximately a factor of 50 greater than the *s* contribution in all cases and therefore the one final state approximation (effectively the same as the K-edge approximation) is suitable [82, 83]. The errors introduced are also dependent on angle, shown in figure 2.2.4, with a "magic angle" 54.7^o where any angular dependence is extinguished. Since there is a range of literature with differing results, the effect on the EXAFS will be limited to a discussion with respect to $IrTe_2$.

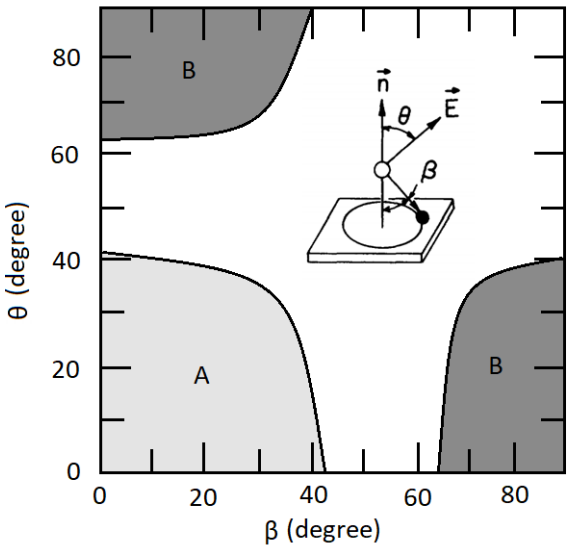

Figure 2.2.4: Ratio of the amplitude factors n_{sd} and n_d as a function of absorption geometry and polarization, re-drawn from [71]. Unshaded areas indicate n_{sd} <10%, section A: n_{sd} up to 20% and section B: up to 40%.

The effect on the bond lengths has been reported to be between 0.05-0.01Å [72] and arises from the relative phase shifts between the *s* and *d* states waves. In the case for $IrTe_2$ the average error in this thesis associated with the fitted bond lengths is ±0.03Å, shown in section 6.4.3. This suggests that the additional error from neglecting the *s* contributions is not significant enough to affect the results in a detrimental way, since the error from the fits is comparable. It is also important to note that since the research focuses on changes in the bond length across a transition, it is less important to accurately determine the individual bond lengths values. The difference introduced from the polarization dependence will be consistent across each angle and therefore the results will still provide valuable information.

The EXAFS amplitude has been shown to be modified by up to a factor of 2 [72]. The analysis from the $IrTe_2$ data however shows reasonable amplitude correction values. This discrepancy may arise from two factors. Firstly these studies were carried out using HERFD-XAS measurements which unlike previous studies, have a greater ability in selecting the energy of the fluorescence that is measured. The higher resolution may reduced the contributions to the EXAFS from the *s* final state transitions. The second factor may arise from the angles measured. It was shown that there are certain combination of angles which reduces the angular dependence. The experimental set-up requires for the angle with respect to the *ab*-plane to be a fitting parameter which affects the amplitude reduction factor. By having this as a variable parameter the fitting program may pick a value that provides a reasonable reduction factor. While there isn't sufficient data to assess if these factors play a crucial role, understanding that these factors need to be considered allows for a reasonable interpretation of the results presented.

2.3 Non-resonant X-ray emission spectroscopy (XES)

Non-resonant X-ray emission spectroscopy measurements observe the radiative decay of electrons after the creation of a core-hole. Unlike XAS, the incident energy is set well above an absorption edge and it is the detectors that sweep over the emitted energy. XES data has also been collected for the HERFD-XAS (high energy resolution fluorescence detected - x-ray absorption spectroscopy) to select the energy of the fluorescence x-rays which are monitored in this technique. While core-to-core XES is not a technique that has used in this thesis, valence-to-core XES (based on the same principles) has been used. A detailed review of the applications and experimental considerations for vtc-XES is given in chapter 5.

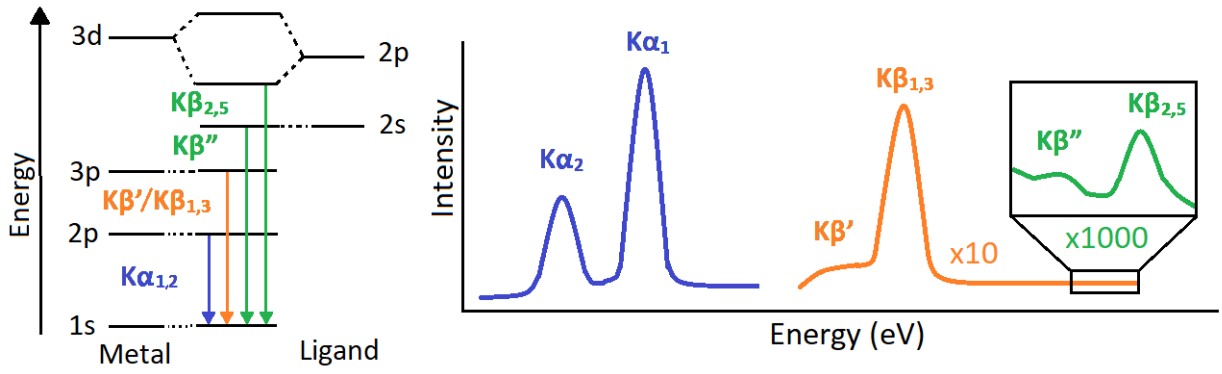

Figure 2.3.1: Origins of XES transitions for K-edge with respect to the materials in this thesis (metal with light ligand) and representation of the spectra obtained for each.

In general, XES can provide information on both the absorbing atoms, the ligand chemical environment and covalency. Specifically it is sensitive to the spin state, oxidation state, chemical environment, ligand ionization state and metal-ligand bond length [84]. A schematic diagram of the transitions typically involved in K emission spectra is given in figure 2.3.1. Similar transitions can be identified for the L-edges with final states in the 2p orbitals, however due to an increase in the number of initial states that have reasonable transition probabilities the description become more complicated [85, 86, 87, 88].

Unlike conventional fluorescence XAS, HERFD-XAS [48, 87] uses the XES measurements to select a specific transition to monitor as the incident energy is changed. This is a fluorescence measurement since it is monitoring a decay process and it is also suitable for single crystal samples that are needed for the polarization dependent measurements. By using the maximum of the related XES, this technique reduces the core-hole lifetime broadening effects and gives greater selectivity with respect to the fluorescence transition of interest.

2.4 Chapter summary

This chapter has covered the basic theory and mathematical formulation of the absorption and electronic transition processes in the XAS and XES experiments. Specifically the origins of the absorption edge and the allowed transitions are discussed. An introduction to the structural information obtained from the XANES and EXAFS regions is given, with emphasis placed on the EXAFS equation and the effects that contribute to the amplitude and phase for the EXAFS modulations. Special consideration is given to the polarization dependence term in the EXAFS equation. While the L_2- and L_3-edge measurements are more complicated due to 2 final states, it is shown that for the experiments in this thesis an approximation to a single final state (the same as K/L_1 edges) is suitable. A brief discussion about XES spectroscopy is given in relation to its uses in the HERFD-XAS.

Chapter 3

Experimental setup and theoretical calculations

This chapter will cover the critical concepts involved in the spectroscopy measurements and electronic simulations. The basic principles of synchrotron sources will be discussed and details regarding the 3 beamlines used to collect the experimental data will be presented. Additionally, the SEM/EDX and magnetic susceptibility characterization measurements will be discussed with relation to their use in this thesis. Finally the fundamental mathematics of the density functional theory (DFT) used to simulated the experimental data are given, along with the differences with multiple scattering theory and the 2 packages used (FDMNES, Exciting) will be described.

3.1 Synchrotron radiation

The primary measurements presented in this thesis have been carried out using synchrotron radiation from both Diamond Light Source (DLS) in the U.K. and the European Synchrotron Radiation Facility (ESRF) in Grenoble, France. It was first observed in 1947 that when electrons travelling near the speed of light have their paths bent by a magnetic field, due to the conservation of energy, a broad-spectrum of radiation termed "synchrotron radiation" is produced [89, 90, 91, 92]. Storage-ring synchrotron x-ray sources generally fall into one of three different classes. The first generation were originally built for different purposes, typically for particle physics research. The second generation were built for the sole purpose of producing synchrotron radiation and x-rays were generated by bending magnets. The third generation use additional insertion devices in the straight sections of the ring to produce further sources and typically feature beams with significant improved collimation. Some third generation machines are also being upgraded to take advantage of new technologies. An additional source of tunable x-rays are free electron lasers (FEL) which provide significantly more intense x-rays in short pulses [93].

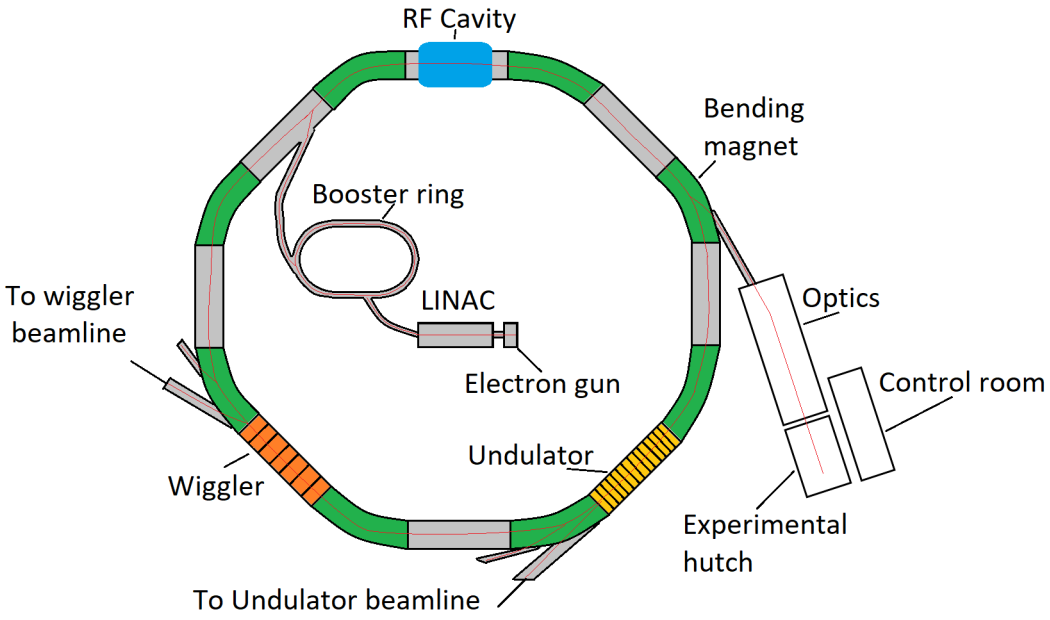

Figure 3.1.1: Schematic diagram of typical 3^{rd} generation synchrotron, including the main components.

The capabilities of a synchrotron can be defined by a number of factors, however the three most critical things to consider are the brilliance, the optics in the beamline of interest and experimental end stations. The beamline optics have the ability to manipulate the beam to optimise it for a specific experiment, using for example focusing mirror, slits and an appropriate monochromator. The experimental endpoints determine what type of measurements are performed, by having a range of detectors and sample environments.

$$Brillance = \frac{Photons\ per\ second}{Source\ area \times Source\ divergence \times Bandwidth} \tag{25}$$

The brilliance [94, 95], is defined by equation (25) which shows that greater brilliance results in more photons of a given wavelength and direction focused per second. This quantity takes into account the number of photons produced per second, the divergence of the photons, the cross-section of the beam and the photons which are within a bandwidth of 0.1% of the central wavelength.

The main components of a third generation synchrotron facility, shown in figure 3.1.1 are an electron gun, linear accelerator, booster ring, radio-frequency (RF) cavity, storage ring and the beamlines [96]. Electrons are initially inserted into the system via the electron gun, which are then passed to the linear accelerator, where a series of oscillating electric potentials accelerate the electrons to an energy of several 100MeV. The electrons are then injected into a booster ring formed of two straight sections joined by semicircular curves. Using a radio frequency voltage source the electrons are further accelerated up to the required energy of the synchrotron. Finally they are delivered to the storage ring, which is comprised of a series of straight and bent sections where synchrotron radiation can be produced to feed the different beamlines. As the electrons travel around this ring, they lose energy when passing through the bending magnets and insertion devices, to compensate during each rotation they pass through a RF cavity which provides an energy boost [97].

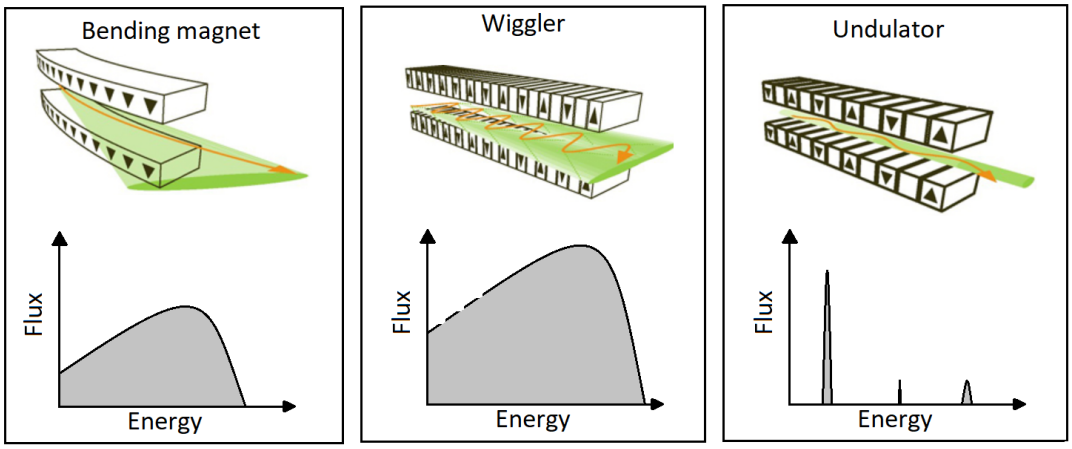

Figure 3.1.2: 3 types of x-ray sources with the associated characteristic radiation. Images reused from [98]

To produce synchrotron radiation, three main sources are typically used. Shown in figure 3.1.2 are the simplified diagrams and spectral profiles of each device. The basic principle of operation for all three devices is that when a charged particle passes through a magnetic field it is accelerated radially. This change in trajectory causes a release of radiation [99].

- **Bending magnets**: are used to keep the beam within the circle pattern of the storage ring. Formed of a single pair of dipole magnets calibrated to the specific needs of individual synchrotrons, the change in the velocity of the electrons will result in an short period of acceleration and thus the release of radiation. This source produces a white beam, which consists of a broad range of energies.
- **Wigglers**: Placed in the straight sections of the storage ring, wigglers are made of a series of alternating magnetic poles. As the beam passes through the device it oscillates back and forth, producing radiation. The x-rays from this source are used in a similar way to the bending magnets. However as the radiation emitted at each bend will superimpose each other the net brilliance can be significantly greater than the bending magnets.

- **Undulators**: Based of the same principles as a wiggler, the magnetic poles in an undulator are less powerful and produces smaller deflections. This results in the x-rays interfering, producing a coherent beam. The wavelengths can be tuned by adjusting the gap between the magnets and the brilliance of this devices can be up to four order of magnitude greater compared to the bending magnets. The undulators produce concentrated narrow energy bands rather than a broad spectrum.

The x-ray beam will pass through an "optics hutch" before reaching the sample, in which the beam can be modified to suit the specific requirements of the experiments. While the range of optical components is large, for XAS/XES beamlines the typically required optics include [51, 99]:

- **Collimating mirror**: When the source of the x-rays gives large divergence, a collimator mirror is used to maximise the intensity to reach the monochromator and reduces the divergence of the beam. Additionally collimators are used to ensure that the resolution of the monochromator is maintained.

- **Monochromator**: To select the specific energy required (technically a small range of energies) a double crystal monochromator (DCM) is typically used. Different sets of crystals can be used to selected specific energies (E_γ) by orientating to an angle which satisfies the Bragg condition:

$$2d_{hkl}sin\theta = n\lambda_\gamma = n\frac{hc}{E_\gamma} \tag{26}$$

  With n the harmonic number and d_{hkl} the distance between planes. In the beamlines used for this thesis, the monochromator crystals come in pairs to ensure that the transmitted beam is returned to the original direction towards the sample. The I20 beamline uses an in-house designed 4 bounce device which gives further advantages such as high stability and reproducibility [100].

- **Focusing mirrors**: Set between the monochromator and sample, these mirrors further refine the x-ray beam to a required focus spot size.

- **Harmonic rejection mirrors (HRM)**: Bragg's law allows for undesired harmonics to pass the monochromator, which can degrade the signal-to-noise ratio and create difficulties in the normalization processes. Harmonic rejection mirrors serve as low-pass filters which can be orientated in such a way as to stop harmonics without affecting the required energy, since the undesired harmonics are at least twice the energy. The HRM can have different coatings which can additional reject certain energies.

3.2 Beamlines

Determining which beamline is suitable for a specific experiment requires the consideration of several factors, which include the sample environment, energy range and type of measurement. For the spectroscopy measurements presented in this thesis the requirements included: tunable energy range covering the absorption edges of the elements of interest, a focused beam, stages with a rotational degree of freedom, cryogenic sample environments and fluorescence detection. The XMas instrument (BM28) at the ESRF and I20 and B18 beamlines at Diamond have been used for the thesis, with the specific capabilities outlined in the following sections. Diamond light source is a third generation synchrotron with a target energy of 3GeV, while the ESRF operates at 6GeV. It should be noted that the measurements at the ESRF were carried out before a significant upgrade took place in 2018 and the following discussion is related to before the upgrade.

3.2.1 XMas

Using a bending magnet as a source, the XMas beamline has an available energy range of 2.035 to 15keV, a beam size at the sample of approximately 70 (V) x 60 (H) μm FWHM and an energy resolution of $\Delta E/E = 1.7x10^{-4}$ at 10 keV [101]. A schematic diagram of the optical configuration is given in figure 3.2.1. The set up consists of a water cooled double crystal monochromator, toroidal focussing mirrors, harmonic rejection mirrors and 4 slits.

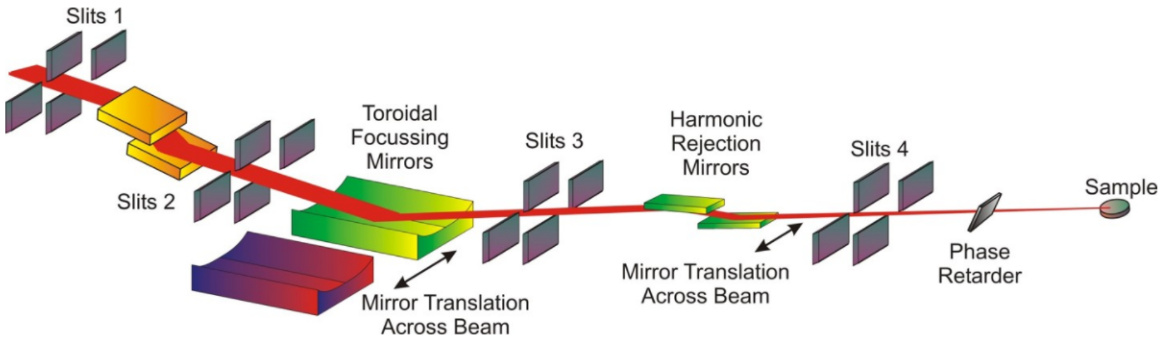

Figure 3.2.1: Schematic diagram of the XMas beamline optical components [102]

This beamline was only used for the $Ca_{2-x}La_xRuO_4$ XANES measurements. A Vortex Si Drift Diode detector was used, with a typical energy resolution of <136eV FWHM at Mn Kα. Set at 45^o to the sample within the plane of the synchrotron, the detector has a single element active area of approximately $50mm^2$. These measurements required a sample environment with a temperature range between 400K - 55K, hence a ARS DE202G cryofurnace with an operation range of 600K - 10K has been used. To allow angular dependent measurements, the cryofurnace has been mounted directly onto the phi circle of a Huber diffractometer allowing the samples to be oriented in any direction at base temperature.

3.2.2 B18

The general purpose XAS B18 beamline uses a bending magnetic source, with an available energy range of 2.05 - 35keV and focused beam spot at sample of approximately 200 (V) x 250 (H) μm FWHM [103]. The main optical components include: a collimating mirror, double bounce monochromator (Si (111) or Si (311)), a double toroidal focusing mirror and a pair of harmonic rejection mirrors. A schematic diagram is given in figure 3.2.2. Two sets of measurements have been performed on this beamline to collect EXAFS data for the $Ca_{2-x}La_xRuO_4$ samples. In both cases the monochromator used the Si (311) crystals and a 36 element Ge fluorescence detector, set perpendicular to the direction of the beam within the plane of the synchrotron. A helium pulse tube cryostat (400K - 50K) and a cryo-jet system (300K - 50K) have been used to give a temperature range of 400K - 50K. In each case the samples have been mounted such that they could be rotated within the plane of the synchrotron in order to take angular dependent measurements.

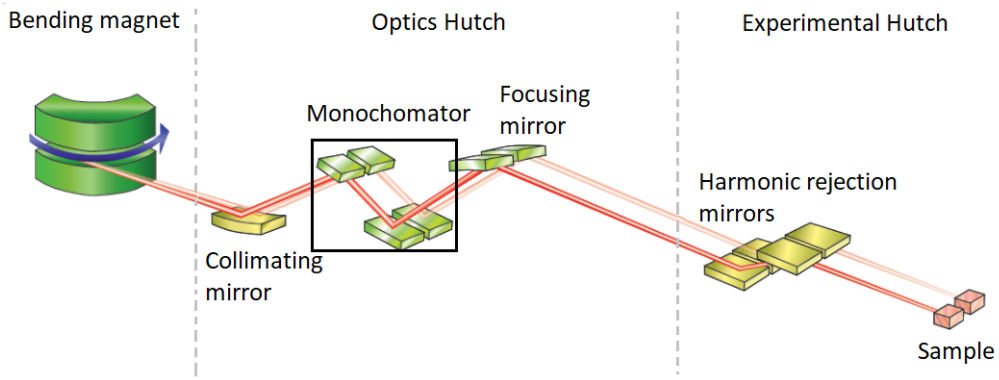

Figure 3.2.2: Schematic diagram of the B18 beamline optical components, reproduced from [104]

3.2.3 I20

I20 is the versatile x-ray spectroscopy beamline at Diamond Light Source and uses a wiggler as the source. The operational energy range for the scanning branch is 4 - 20keV, with a beam size of approximately 400 (V) x 300 (H) μm FWHM [105]. A schematic diagram is given in figure 3.2.3, showing the major optical components: a collimating mirror, deflecting mirror, a four bounce monochromator (Si (111) available crystals), two focusing mirrors and a pair of harmonic rejection mirrors.

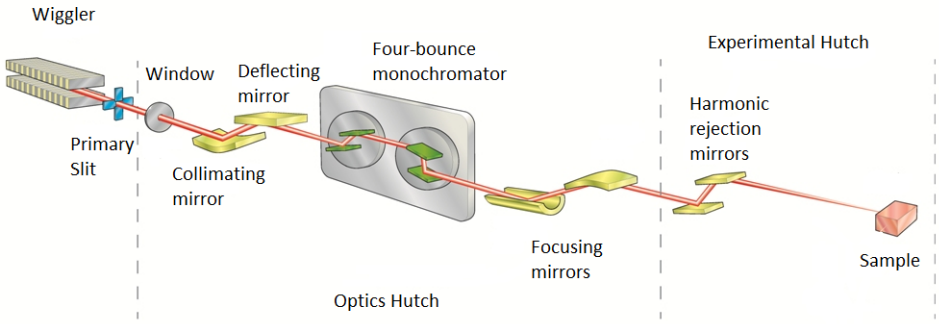

Figure 3.2.3: Schematic diagram of the I20 beamline optical components [105]

All of the $IrTe_2$ and NaFeAs measurements, which include conventional XAS, HERFD-XAS and vtc-XES, have been carried out on this beamline. Two different cyrostats have been used. A nitrogen cooled Linkam stage with an operational temperature range of 350K-78K and a closed-cycle He cyrostat (Stinger). The Linkam uses one kapton window and has an angular range of approximately 120^o. The stinger was developed[2] specifically for angular dependent measurements with the spectrometer and covers a temperature range between 300K-5K. There are three layers on the stinger cryostat. An outer layer which provides a vacuum space, a radiation shield which reduces low energy x-ray scatters reaching the detector and a inner shield which defines the cooling area. There are two kapton windows (with the additional radiation shield) over 180^o, however the practical angular range is approximately 160^o. In both cases the samples could be rotated with respect to the polarization of the beam at base temperature in order to collect angular dependent measurements. For the conventional XAS measurements a 64 element monolithic Ge detector was used, placed perpendicular to the direction of the beam within the plane of the synchrotron. The HERFD-XAS and vtc-XES measurements were carried out using a three-analyser XES spectrometer equipped with a 2d pixel (medipix) detector. Further information is given in section 3.3.3.

3.3 Detectors

In spectroscopy, a range of different detectors are used, depending on the conditions of the measurements. The following were used in this thesis.

3.3.1 Ion chambers

To measure the incident intensity, a ion chamber is placed between the beamline optics and sample. These detectors are filled with either pure or a mixture of inert gases (i.e. Ar, He, N_2, Kr). The incident x-rays ionize the gases and the electron-ion pairs are collected on the plates between which there is a voltage difference. This produces a current proportional to the incident intensity. An accelerating electric field between the collector plates is needed to avoid pair recombination. It is typical to select a combination of gases so that approximately 10-15% of the incoming intensity is absorbed in the ion chamber. The remaining photons reach the sample. The incident intensity, I_0, is given by $I_0 = \xi(I_0)I_{inc}(1 - e^{-\mu_{I0}x_0})$, where x_0 is the length of the chamber, μ_{I0} is the absorption coefficient, $\xi(I_0)$ is the gain in the current amplifier and I_{inc} is the incident intensity [51, 106].

3.3.2 Solid state detectors

3 solid state detectors have been used: Vortex Si drift diode, 36 element Ge detector and 64 element Ge detector. Their operation is based on similar physics. Based on semiconducting materials, the ionizing radiation creates charge carries, under the influence of an electric field the electrons and holes travel to the electrodes. Variations in the ionization produces varying charge and this is measured [107]. The XMas Si drift diode is a single element detector and the Ge detectors are monolithic, which means both have no dead space between elements. The I20 detector has an additional Te mask in front of the Ge. This type of detector is energy discriminating which allows for the selection of specific emission lines.

[2]The Stinger was commissioned by the author for this project

3.3.3 XES spectrometer

Both the HERFD-XAS and XES measurements have been carried out using a point-to-point scanning x-ray emission spectrometer in place at the I20 beamline [108] at Diamond Light Source. The spectrometer consists of a 1 meter Rowland circle (Johann-type geometer [84]), 3x100mm diameter analysing crystals and a medipix detector, which is shown in figure 3.3.1. A He environment (bag) is used in the space between the sample, analysers and detector to minimise the air path that the photons travel through (the sample, analysers and detector are not enclosed). The analysing crystals collect and focus the photons on to the detector, which has enough resolution to allow a step size of 0.1eV (however this is dependent on energy). By varying the angle of the analysing crystals relative to the sample, the bragg angle changes and hence the selected wavelength also changes. There is a range of analyser crystals available which are changed depending on the emission line of interest.

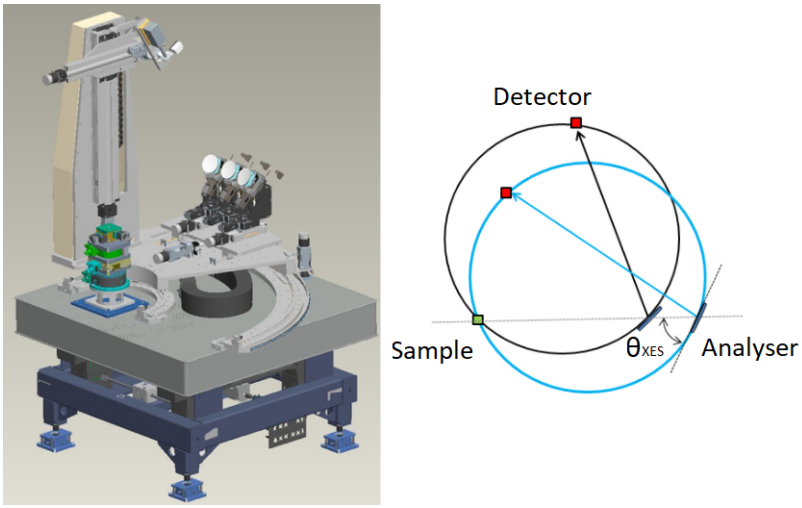

Figure 3.3.1: Schematic diagram of the I20 XES spectrometer [108]. Emitted photons are focused and collected by the analysers onto the detector.

The system can be operated in two different modes to either collect HERFD-XAS or XES measurements. The HERFD-XAS uses the spectrometer to select the maximum of the emission line of interest. The incident energy is scanned through the absorption edge (and EXAFS), which allows the intensity variation of the emitted line to be recorder as a function of the incident energy. The advantage of using the spectrometer to collect XAS data is to reduce the background noise (no contamination of an elastic peak) and to overcome the effect of the core-hole broadening [48], by selecting a much narrower energy band than the solid state detectors. The improvement in the resolution is highlighted in figure 3.3.2.

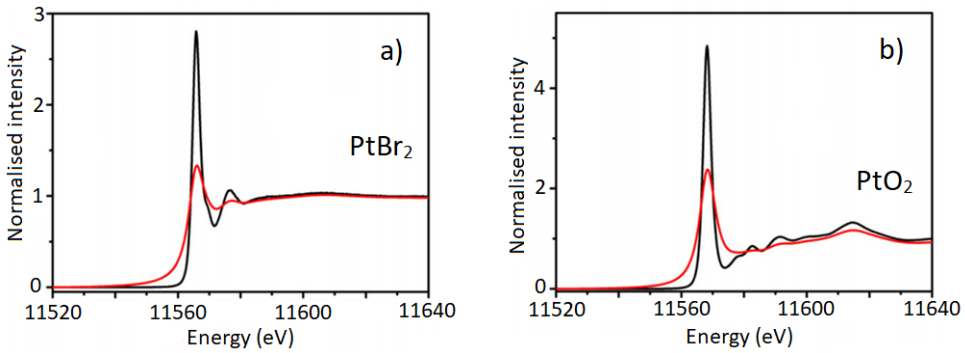

Figure 3.3.2: A comparison between the normalised HERFD-XANES (black line - emission) and normalised conventional XANES spectra (red line - absorption) for $PtBR_2$ and PtO_2 [108]

Non-resonant x-ray emission spectroscopy (XES) is measured by setting the incident energy well above the absorption edge and scanning the spectrometer over the emission line of interest. In this thesis the XES data has been collected for the valence-to-core emissions, which can provide information regarding the metal-ligand interaction, oxidation states, ligand identification and valence levels of the absorbing centre, as discussed in chapter 5.

3.4 Characterization techniques

The phase transitions that this project focuses on are highly sensitive to the geometric structure of the crystals, which in turn are sensitive to a number of parameters, for example growth method, dopant level and environmental contamination. In addition, polarization dependent spectroscopy techniques require single phase, single crystal samples. To confirm the samples are suitable, scanning electron microscope (SEM), energy-dispersive x-ray (EDX) and magnetic susceptibility (SQUID) measurements have been carried out. These measurements have been performed at the University of Kent, Diamond Light Source and the ISIS Neutron and Muon Source characterization lab [3].

3.4.1 Scanning electron microscope and energy-dispersive x-rays

SEM and EDX analysis has been used to check the quality of the single crystals (no impurities, homogeneous composition). These techniques are seen as complementary, since they use the same experimental set-up but differ in what they detect. A simple schematic diagram of the set-up is given in figure 3.4.1, which highlights the typical components.

In both cases a beam of electrons is focused on to the sample and it is the interactions of these electrons with the atoms in the sample that are measured. To produce the beam, which typically has an energy ranging between 0.5 keV - 40 keV, an electron gun is used. A series of condenser lenses and deflection coils are used to convert the divergent beam from the electron gun into a convergent beam and to deflect the beam to allow for raster scanning [109].

To collect an image of the sample surface, both secondary and backscattered electron detection systems can be used. The origins of the secondary electrons are inelastic scattering interactions of low energy electrons. As a result this detection method probes the surface of the samples. A grey scale image is produced by comparing the incident intensity of the beam with the detected secondary or backscattered electrons. The image shows brighter features at the edges and steep surfaces and thus provides information regarding the surface topography. Backscattered electrons are high-energy electrons scattered by elastic interactions just below the surface of the sample. Since this scattering has a strong dependence on the atomic number of the scatterer, it can be used to map areas of the sample with different chemical compositions [110]. The magnification of the SEM is generally dependent on focal spot size and the size of the raster area.

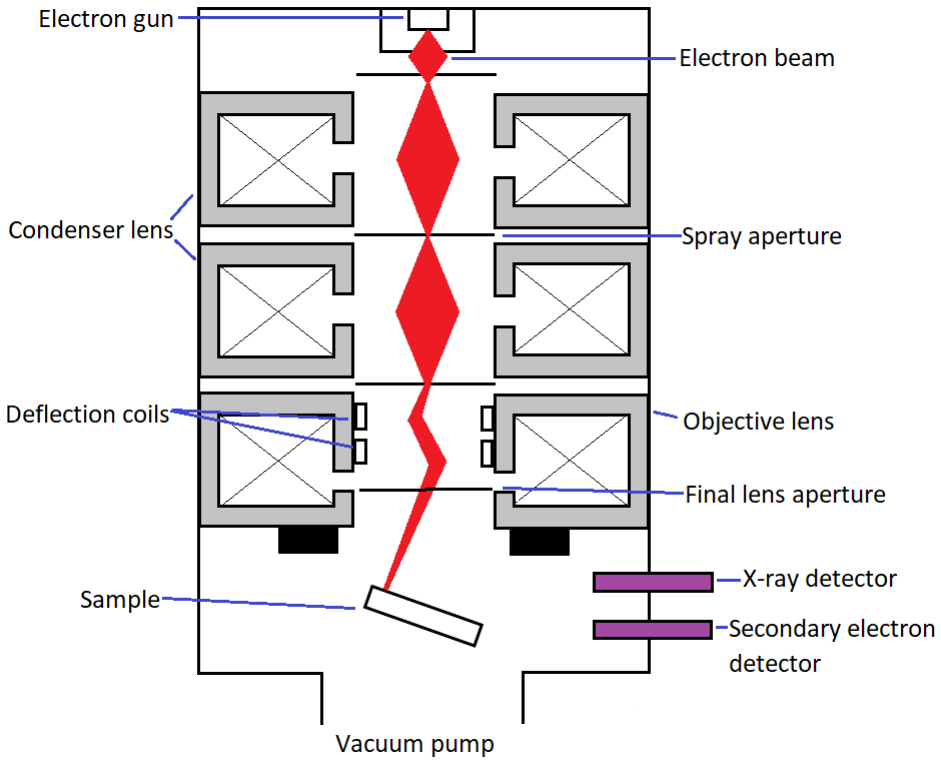

Figure 3.4.1: Schematic diagram of the SEM/EDX microscope. [109]

The EDX measurements uses electrons to generate x-rays, which are detected, to determine the chemical composition of a sample. When an atom is bombarded by the beam, inner electrons can

[3] ISIS Materials Characterisation Laboratory, Harwell. (Dr Gavin Stenning)

be excited and ejected from the atom which creates a core-hole. In the process of an electron from a higher orbital decaying to fill this hole, an x-ray can be released. The energy of these x-ray photons is dependent on the energy difference between the initial and final state and is element selective. By measuring the intensity and energy of the x-rays emitted, the stoichiometry of the sample is analysed [110].

3.4.2 Magnetic susceptibility

A schematic diagram of the typical superconducting quantum interference device (SQUID) is shown in figure 3.4.2. Commercial SQUID magnetometers typically work by detecting the change in the magnetic flux created when a sample is moving through a superconducting pick-up coil, which is then converted to a voltage (v_{squid}). The samples are placed at the end of a mechanical rod either in a gel capsule or on a quartz sample holder. Initially a long scan is conducted over the sample rod to identify the centre of the sample. Figure 3.4.2(insert) shows a SQUID response versus the sample position. The measurements shown in this thesis have been carried out in a sweep mode, in which data is collected as the temperature is changed but the temperature is not stabilized at each point. This allows for reduced scan times but does introduce some errors in determining the exact temperature of the transitions. An applied field is used to assist in aligning the individual magnetic moments to produce the largest possible signal, the size of the field applied for these measurements is based on the values used in the literature for a given material to allow a comparison. The samples are rapidly moved in the x-position as the temperature is changed and the change in magnetic flux is measured [111].

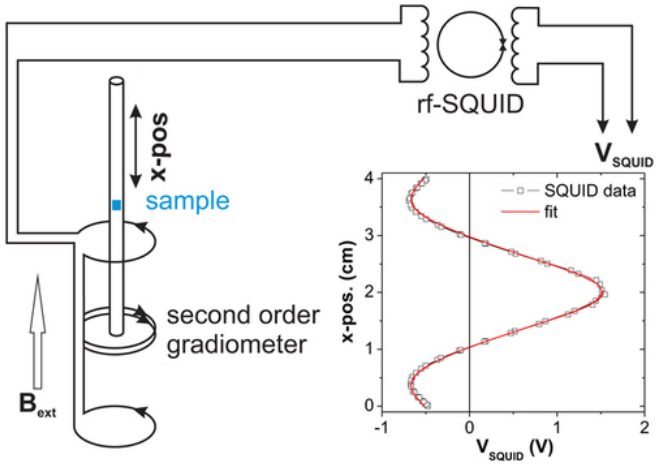

Figure 3.4.2: Schematic setup for a SQUID with a 2^{nd} order gradiometer, insert shows squid response verse sample position [111].

To be able to confirm that the samples in this research show the expected transition at the correct temperatures, magnetic susceptibility measurements have been carried out. This technique is capable of providing a significant amount of information about the samples, however for the work in this thesis it has only been used to determine the temperature of the magnentic transitions. This has bene done as it confirms if the samples are of a high enough quality. While this technique will only show the magnetic transitions, all the compounds under investigation show a magnetic transition that can give information with regards to the state of the compound. [4].

3.5 Simulations - Density functional theory (DFT) and multiple scattering theory

Understanding the electronic structure of the materials has been key for this work, since it plays a critical role in driving the transitions. In some cases it is important to simulate the experimental spectra to give further insight into how the electronic structure may change with the structural transitions. By gaining an understanding of the orbitals contribution to specific features in the XAS/XES spectra and how these change across the transitions it is possible to obtain a better understanding of the mechanisms involved. Where needed in this thesis, simulations have been carried out to produce XAS/XES spectra, band structure and density of states. There are a number

[4]Note: due to difficulties with access to a SQUID during the COVID-19 pandemic, only $IrTe_2$ measurements have been carried out.

of different methods used for calculating the electronic structure of materials and in this thesis both density functional theory (DFT) and multiple scattering theory (MST) have been used. There are key similarities between the two methods and for this thesis the DFT method will be the focus of the discussion. While it is not appropriate to give a full derivation of the mathematics that govern DFT in this thesis, a brief overview of the key concepts is given (a detailed overview of DFT is given by *U. V. Barth in reference* [112]). Two software packages have been used in this thesis: FDMNES [113, 114] and Exciting [115]. While both use DFT as a foundation, the treatment of the Kohn-Sham wavefunctions and the methods to calculate the required properties differ. Key characteristics of the software packages are given in the following sections.

Using the Born-Oppenheimer approximation [116], which treats the nuclei as point charges and treats nuclei and electrons independently, the energy of a many-body system can be calculated using the time-independent non-relativistic Schrödinger equation:

$$\hat{H}\Psi = [\hat{T} + \hat{V} + \hat{U}]\Psi = [\sum_{i=1}^{N}(-\frac{\hbar^2}{2m_i}\nabla_i^2) + \sum_{i=1}^{N} V(r_i) + \sum_{i<j}^{N} U(r_i, r_j)]\Psi = E\Psi \tag{27}$$

here $\hat{H}$ is the Hamiltonian, E is the total energy, $\hat{T}$ is the kinetic energy, $\hat{V}$ is the potential energy from an external field due to the nuclei and $\hat{U}$ is the electron-electron interaction energy. Ideally if this equation is solved, all the properties of the material can be obtained. However, due to the interaction term $\hat{U}$, it is not possible to separate the many particle equation into a series of single-particle equations. This makes this equation effectively impossible to solve for most systems. The simulation packages avoid solving the Schrödinger equation directly and calculates the ground state of a system using a set of single particle equations, reducing the problem to a mono-electronic simulation. The basic principle comes from the Hohenberg-Kohn theorems [117]:

- The potential energy and hence the total energy of an interacting system of electrons is a unique functional of the electron density:

  $$V(r) \Rightarrow \Psi_i(r) \Rightarrow n(r) \Rightarrow V(r)$$

  where $V(r)$ is the potential energy, $\Psi_i(r)$ is the wavefunction of the system and $n(r)$ is the electron density.

- The total energy of a system is variational, the energy takes its minimum at the ground state electron density i.e.

  $$E[n] \geq E[n_{GS}]$$

In principle all properties of a system are exact functionals of the ground state density, hence Hohenberg and Kohn proved that there is a one-to-one mapping between the external potential and the ground state density, which comes from the first theorem. The internal electronic energy of a system, F[n], can be defined as the total energy of the system minus an external potential, υ_{ext}, acting on the system, with each term a functional of the density. The second theorem then says that effectively through the variation principle, equation (28) will only be minimised with an input density that corresponds to the true ground state density. While this still technically requires the evaluation of F[n] via the many-body Schrödinger equation, if a suitable approximation for F[n] is determined then the Hohenberg-Kohn theorems says that the ground state energy and density can be evaluated for a system.

$$E[n(r)] = F[n(r)] + \int \upsilon_{ext}(r)n(r)dr \tag{28}$$

To find a suitable approximation to $F[n(r)]$, a practical approach was developed by Kohn and Sham [118]. It was shown that the ground-state density of interacting particles can be calculated from the ground-state density of an auxiliary system of non-interacting particles, effectively an auxiliary system of particles identical to electrons, with the exemption that the interaction term is neglected. These particles can then be treated as single particles moving through some external potential, υ_{ext} (Kohn-Sham potential), from which the density can be calculated. The expression for the auxiliary system can be determined by a set of component energies, which are given below in terms of the density.

$$E[n] = T_0[n(r)] + \int drn(r)\upsilon_{ext}(r) + E_H[n(r)] + E_{xc}(r) \tag{29}$$

$$T_0 = -\frac{1}{2}\sum_i \int dr \phi_i^*(r)\nabla^2\phi_i(r)$$
$$n(r) = \sum_i \phi_i^*(r)\phi_i(r)$$
$$\upsilon_{ext} = -\sum_n \frac{Z_n}{r - R_i}$$
$$E_H[n(r)] = \frac{1}{2}\int\int dr dr' \frac{n(r)n(r')}{|r - r'|}$$
$$E_{xc}[n(r)] = \int dr n(r)\varepsilon_{xc}[n(r)]$$

where T_0 is the kinetic energy of non-interacting particles, $E_H[n]$ is the classical Coulomb energy, $E_{xc}[n]$ is the exchange and correlation function and the Kohn-Sham (KS) orbitals are given as $\phi_i(r)$ (spatial form only). The single particle Kohn-Sham orbital equations can then be given as:

$$(-\frac{1}{2}\nabla^2 + \upsilon_{KS}(r))\psi_i(r) = \epsilon_i\psi_i(r) \tag{30}$$
$$\upsilon_{KS}(r) = \upsilon_n(r) + \upsilon_h(r) + \upsilon_{XC}(r) \tag{31}$$

where $\upsilon_n(r)$ is the potential due to the nuclei, $\upsilon_h(r)$ is the potential due to the electron repulsion and $\upsilon_{XC}(r)$ is the exchange-correlation potential. There are a number of different simulation packages that each use different methods to calculate the density of the auxiliary system (hence the real system). However, the essential aim is to represent the system of interest in terms of its density via an auxiliary system, calculate a series of component energies to describe the Schrödinger like equation, by requiring that the potential of this system converges (within a set of constrains). While there are different methods to calculate the density of electrons, they are all based on self-consistent calculations used to minimise equation (28) to find the true electronic state of the system.

In this thesis two software packages have been used. The Exciting package is a DFT based code which solves the Kohn-Sham equation to calculate the groundstate electronic structure, from which the properties can be derived. Exciting also uses a two particle Green function to calculate the excited properties. The second package, FDMNES, uses the multiple scattering theory to effectively calculate the absorption cross-section. The multiple scattering theory rewrites the Kohn-Sham equation (30) in terms of the Green function to solve the wave equation. While an overview of these packages will be discussed in the following sections, there are a number of factors that need to be considered and which apply to both.

The only true approximation comes in the form of the exchange and correlation functions [119]. The exchange function accounts for the quantised nature of the charge and the anti-symmetric nature of the wavefunctions. The correlation function takes into account that in the real system the electrons tend to avoid each other. While the exchange function is possible to solve, it is computationally expensive. The correlation function describes a many-body problem and hence can not be solved with a single particle method. These two terms are then taken together and approximation functions are used. There is a large range of functionals available, typically grouped into empirical (or semi-empirical) functions, which use some experimentally determined results to define them, and non-empirical functionals, which are defined by first principle calculations. In this thesis the two non-empirical functional families used are the local density approximation (LDA) [120] and generalized gradient approximation (GGA) [121]. The LDA approach is derived from a homogeneous electron gas model, which has a uniform density in its ground state and therefore can be uniquely defined by its density alone. The GGA approach is an extension of the LDA which not only considers the local density at each point but also its gradient. The determination of which functional should be used is dependent on the system under investigation and computation expense. The LDA approach is applicable to many systems and has relatively low computation cost, however it typically fails to calculate the correct binding energies. GGA on the other hand is a more accurate approach for calculating the binding energies however has higher demands on computation cost. Additionally, GGA functional have the disadvantage that unlike LDA there is no single universal form so it can prove difficult picking the most suitable version.

In any method a suitable description of the potential and wavefunctions must be made with respect to the different areas in the crystal (i.e. interstitial and muffin-tin regions). In a typical system the wavefunctions are smooth and vary slowly in the space between the atoms, however close to the nuclei they exhibit strong variations due to the potential for the nuclei. Basis sets are formed of a set of basis functions which describe the wavefunctions. Three approaches are used to take this into account. One option is to represent the total wavefunction as a linear combination of atomic orbitals. This is computationally efficient, since an extremely small basis is typically used. However

it suffers from numerical instabilities in the basis-set superposition [122]. One of the most widely used approaches is to introduce pseudopotentials [123]. The pseudopotential replaces the strong nuclei potential with a weaker potential which allows the wavefunctions for the core electrons to be frozen and replaced with pseudo-wavefunction. The pseudo-wavefunctions aim to replace the fast varying core functions with smooth wavefunctions, which reduces the number of nodes close to the nuclei. The valence states can then be obtained by a planewave basis set. This method significantly reduces the number plane waves required to expand the wavefunctions and eliminates the numerical difficulties in the core region. However since the pseudopotentials are approximations, it can lead to an over-simplified model for some systems. The final approach explicitly partitions the system into interstitial and muffin-tin regions, where the wavefunctions are then described differently [124]. In the interstitial region the wavefunctions are represented by a set of planewaves. In the muffin-tin region the potential is treated as spherical and wavefunctions are defined by a set of functions, which are expanded in terms of spherical harmonics, radial functions and a set of coefficients to ensure the wavefunctions are continuos at the sphere boundary. This method in the simplest form is termed the augmented wavefunction (APW) method and allows for a complete description of the system and is seen as the "gold standard".

Finally it is also important to introduce periodic boundary conditions for the basis sets and the KS orbitals to remove the problem of infinitely large systems (and integrals). This is done by using Bloch's theorem and requires that the Bloch wave vector always lies within the Brillouin zone. This however introduces one of the main issues with these simulation packages when it comes to accuracy: incorrect determination of the number of sampling points within these regions (and how to properly account for the edge of each region) can lead to an inaccurate description of the system, especially in metals since sharp changes in the orbitals may be missed.

3.5.1 Exciting

Exciting is a full-potential all-electron package which calculates the groundstate properties via DFT and the excited state system via the many-body perturbation theory. A full review of Exciting is given in reference [115]. In this section only a brief overview of the key concepts of Exciting is given, specifically focusing on the basis set employed, method for the self-consistent solution of the KS equation and the method to model an excited system (appropriate for XAS experiments).

In treating the wavefunctions, Exciting uses a full potential method where the interstitial and muffin-tin region are defined separately. One of the key advantages of this package is that it calculates an all-electron system rather than approximating the core electrons in one function. The core and valence electrons are treated differently. This can be done as the core electrons are well localized and typically do not hybridize with other electrons. The linearized augmented planewave method ((L)APW) [125, 126] is used in Exciting. In this method a variation parameter is added to the solutions in the muffin-tin radius which additionally includes the energy derivative of the basis function. This allows the radial basis functions to be solved at a fixed energy and thus equation (32) can be solved with a set of linear equations. There are a number of additional methods to improved the treatment of the valence, core and semi-core orbitals in Exciting. These include the APW [127], LAPW(+LO) [125, 128], APW+lo [129] and super-LAPW [128]. These methods either improve the efficiency or accuracy of the calculations and their use depends on the system being investigated.

The process for finding the self-consistent solution for the KS equation in Exciting is shown in figure 3.5.1. The procedure starts by making an initial guess for the KS potential, calculated from the superposition of atomic densities. Exciting then calculates the core wavefunctions and the basis functions, which have been described above. Since the basis is completely defined, equation (30) can be transformed into a generalized-eigenvalue problem:

$$H^k C^k = \epsilon^k S^k C^k \tag{32}$$

Here H^k is the Hamiltonian matrix, S^k is the overlap matrix, C^k contains the coefficients which are used to expand the KS wavefunctions and ϵ^k corresponds to a set of eigenvalue energies. Exciting constructs these matrices and solves equation (32) for KS eigenvalues and wavefunctions. From this solution the density and potential are calculated. The electron density is solved via equation (33) where ω_k is the weight of the k-points, both regions are treated slightly differently but result in a summation of electron densities on a real-space grid. The KS potential is then calculated via equation (31). This procedure is then repeated until the new potential converges with the previous step within a set of constraints, where the potential is updated on each iteration via: $\upsilon_{KS}^{new} = \hat{M}\upsilon_{KS}^{old}$ with $\hat{M}$ a non-linear operator.

$$n(r) = \sum_k \omega_k \sum_i f_{ik} |\psi_i k(r)|^2 \tag{33}$$

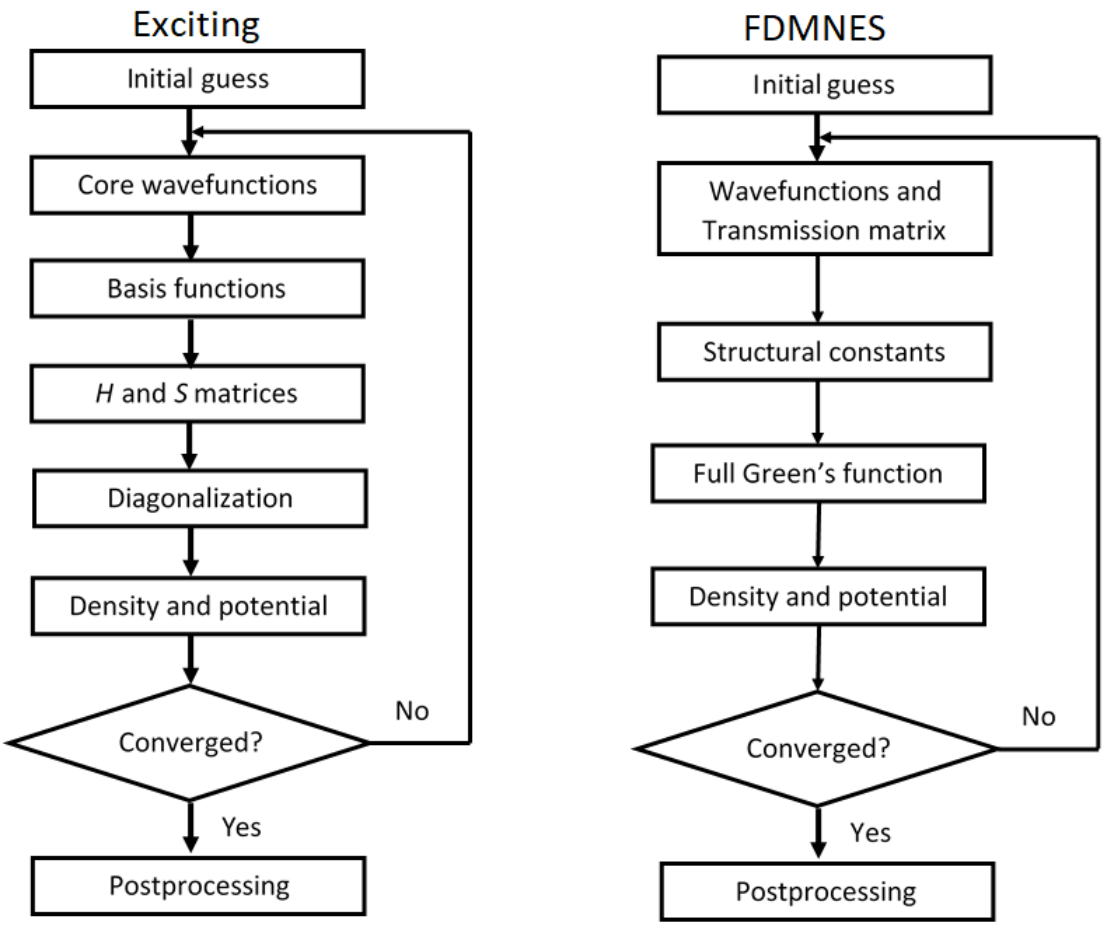

Figure 3.5.1: Flow diagrams of the self-consistent method in both Exciting and FDMNES

In spectroscopy measurements a core-hole is created, the interaction between the core-hole and the rest of the system can cause significant differences between the measured and simulated spectra. To account for this, two methods are available in Exciting, time-dependent density functional theory (TDDFT) [130, 131, 132] and the Many-body perturbation theory (MBPT) [133]. The MBPT involves solving the Bethe-Salpeter equations [134, 135, 136]. It is this method that is applied in this thesis since it is more appropriate for electron-hole excitations. The BSE calculation involves solving the ground state properties (DFT), calculating the quasi-particle bands and finally solving the 2 particle Green's function (BSE). The quasi-particle eigenvalues are formed by using the one-particle Green's function which is obtained from the DFT KS states. A full derivation of these corrections (including the two-particle Green's function later used) are given in [137]. The one-particle Green's function models the propagation of an additional particle (non-interacting electron-hole pairs) in the system and takes into account the dynamically screened Coulomb potential. With the corrected energies, the final step in calculating the absorption spectrum can be performed. With the corrected quasi-particle bands, a two-particle Green's function is then applied to take in to account the electron-hole interaction. The interacting two-particle correlation function is given schematically in equation (34), where S_0 is the non-interacting electron-hole pairs and K is the electron-hole interaction kernel. The correlation function can be obtained by solving an effective eigenvalue problem, which importantly includes the effective Hamiltonian (equation (35)). The Hamiltonian is given by the diagonal part orientating from the independent particle transitions, H^{diag}, the repulsive exchange term, H^x, caused by the unscreened Coulomb interaction and the attractive term, H^c for the particle-hole correlations from the screened Coulomb interaction. The terms Υ_x and Υ_c determine the level of approximation applied, i.e. either spin-singlet (Υ_x=1, Υ_c=1) or spin-triplet (Υ_x=0, Υ_c=1). It is important to note that the resultant absorption spectrum is derived from taking into account the diagonalization of this Hamiltonian in which the macroscopic dielectric function of the interacting system is obtained, its implementation is give in [115].

$$S = S_0 + S_0 K S \tag{34}$$

$$H^{eff} = H^{diag} + 2\Upsilon_x H^x + \Upsilon_c H^c \tag{35}$$

It is important to also take into account the spin-orbit (SO) coupling in these systems. The previous discussions have focused on a spin-independent Hamiltonian consideration of the KS equation, defined by the first variation. By also considering the electron spin interaction (second variation), the spin-orbit coupling can be introduced. This is done by adding an additional approximation into the expansion of the spherical harmonics [138], where the SO is not considered in the interstitial and vacuum regions (considered as vanishingly small).

Exciting has been used in this thesis to simulate the absorption spectra (XANES only) and its associated properties. Since this package gives significant control over the type of calculations preformed and the parameters used, it is important to note the general parameters that have be considered in each simulation set. The generalized gradient approximation, using the Perdew-Burke-Ernzerhof corrections [121], exchange-correlation functional has been used in all calculations. While the LDA approach was attempted (since it is less computational expensive) it was unable to reproduce the correct band separation around the Fermi energy. It is important to converge the total energy of the system with respect to both the K-grid and $R_{MT}G_{max}$. The K-grid determines the size of the sampling within the Brillouin zone, while the $R_{MT}G_{max}$ parameter determines the number of augmented planewaves. To ensure an accurate groundstate the total energy, charge distance and effective potential have been converged within the limits of 1×10^{-4}, 1×10^{-4} and 1×10^{-5} respectively. Additionally the calculations have been performed with consideration of the spin-orbit.

3.5.2 FDMNES

The finite difference method near-edge structure (FDMNES) is a real-space symmetrized code using the full potential muffin-tin approximation to calculate the XANES and XES spectra, where additional properties can also be extracted including the density of states and orbital overlap. For this thesis the package has been set to use multiple scattering theory (MST), utilizing Green functions rather than the finite difference method which has significantly higher computational demands. A full description of the MST can be found here [139, 140, 141], a derivation of the Green's functions in this approach are given in reference [142] and an FDMNES package overview can be found here in references [113, 114]. In this section a brief summary of key components of the method is given, specifically the steps involved in the self-consistent calculations and the MST method.

FDMNES uses the muffin-tin approximation, where the potential has spherical symmetry around the atom within the muffin tin and the potential is constant in all other areas. The radial Schrödinger equation is solved within each sphere and planewaves are used to represent the other regions. The multiple scattering approach uses the Green's functions as an alternative to solving the Schrödinger equation for an electron moving in a potential. Equation (36) gives the Green's function used, where the multiple scattering amplitude (transmission matrix), Λ, is calculated using the optical theorem and projected on to the spherical harmonics basis. The transmission matrix is related to the full Green's function and gives a complete description of the interacting system. The wavefunctions are expanded, as shown in equation (37), where $Y_l^m(\hat{r})$ are the spherical harmonics, $\phi_l(r;E) = rb_l(r,E)$ is the solution to the radial SE at energy E and $a^f_{l,m}(E)$ are the energy dependent atomic amplitudes.

$$\text{Ģ}(r,r';E) = \sum_{l,l'}\sum_{m,m'} \Psi *_{l',m'} (r';E)\Lambda^{l'm';(j)}_{l,m}(E)\Psi_{l,m}(r;E) \tag{36}$$

$$\Psi_f(r;E) = \sum_{l,m} a^f_{l,m}(E)b_l(r,E)Y^m_l(\hat{r}) \tag{37}$$

By considering a cluster of atoms, all the scattering processes from one atom to any other atom can be calculated via the transmission matrix, which contains all the atoms individual expansion in spherical harmonics. The diagonal of this matrix gives the atomic scattering amplitudes and the off diagonal terms are the propagation terms. The density related quantities can be expressed in terms of the transmission matrix and the radial solutions. The spectra are obtained via the real part of the Green's function when substituted in the cross section term (equation (6)) [143].

The procedure for the calculations is shown in figure 3.5.1. Initially a guess is made for the potential. It is assumed for the absorption spectra that the system is in an excited state in which a core electron is placed in the first available unoccupied level. The wavefunctions and transmission matrix are then solved, the structural constants are also applied which gives all the information regarding the crystal structure. Once the potentials have been calculated (FDMNES uses the LDA approach) the full Green's function can then be solved. In the self-consistent method [113] the treatment is similar to the Kohn-Sham method where the potential calculated is then used to converge the system to a stable total energy given by equation (29).

FDMNES gives less user control, for example the exchange-correlation function is limited to LDA[5] and the wavefunctions are fixed. However it has the advantage that the methods used are less computationally costly and the XES spectra can be calculated using the same scheme. The most important parameter defined by the user is the atomic radius, which needs to be converged to ensure a suitable representation of the electronic structure.

3.6 Chapter summary

This chapter has introduced the experimental set up and theoretical considerations applied in this thesis. The main elements of a synchrotron, specifically the sources of radiation are discussed. The 3 beamlines used to perform the experiments have been outlined with consideration of the different optical components needed to create a monochromatic focused beam. Additionally the types of detectors used to monitor the incident and outgoing intensities of the radiation are given with respect to the type of measurements carried out. To characterize the sample before the main experiments both SEM/EDX and magnetic susceptibility measurements have been used. The basic concepts and considerations have been outlined in this chapter. Finally the fundamental mathematics needed to produce simulations are given, with special focus on the procedure to solve the Schrödinger like equation in a one particle approximation. The two packages (FDMNES and Exciting) have been outlined.

[5] using either the Perdew-Wang [120], Hedin-Lundquist [144], X-alpha [145] approximations

Chapter 4

Data processing

This chapter provides the information regarding the data processing techniques used to analyse the spectroscopy data. From the raw data several steps are taken to de-glitch the spectra and a consistent normalization procedure allows for comparison between data sets. Since the majority of these measurements have been taken in fluorescence mode from highly concentrated samples, details of the self-absorption procedure are given, which include a method to account for numerical instabilities that can affect standard programs. The techniques used to extract atomic and electronic structural information are given. Specifically the branching ratio is discussed in relation to the electronic structure. The beat effect and fitting to theoretical model procedures show how local structural information is extracted from the EXAFS.

4.1 Processing, background subtraction and normalization

Before any analysis of the absorption spectra can take place, several processing steps are taken. All the data presented in this thesis, as a minimum have had a self-absorption correction applied and have been normalized. A background subtraction has also been carried out on the EXAFS data. Apart from the self-absorption correction; the normalization, background subtraction and fitting procedure later described have been carried out using the DEMETER: ATHENA and ARTEMIS programs [146]. Certain effects caused by the incident beam, beamline optics and detector setup can make comparison between spectra impossible. For example most synchrotrons operate in a "top-up" cycle where the beam decay over time is counteracted by a periodic top-up. While this ensures that the optics are stable, it leads to jumps in the intensity of the beam. To eliminate these types of features the measured signal is normalized with respect to the incident beam (I_0) which is collected simultaneously, as the absorption is relative to the total intensity. It can not be assumed that the monochromators will remain at a perfect energy over a course of multiple measurements and that this energy is calibrated to the true energy. Either a steady drift in the energy or occasional jumps can lead to incorrect comparisons between different spectra, where the edge position can provide significant information regarding the oxidation state of the species. To account for this, measurements are taken on reference samples with known absorption edge energies before and after the experiments to determine the extent of the drift, the edge position can then be aligned with respect to the references. Finally as spectroscopy experiments are probabilistic, random unbiased variations in the measurements (referred on the whole as noise) must be averaged out by taking sufficient data at each energy point to improve the quality of the data/signal to noise. This is achieved by measuring the same conditions several times and merging the resultant spectra. Additionally, multiple scans give the advantage of being able to check for radiation damage and minimises the total acquisition time per spectrum.

The experimental absorption spectra, specifically the edge jump in fluorescence, is not only dependent on the absorption coefficient of the spectra but is also dependent on many other factors including the solid angle covered by the detector, sample properties (e.g. thickness) and use of filters. Any analysis of spectra including peak fitting, linear combination and fitting to theoretical models require comparison between different spectra and therefore it is necessary to attempt to remove these additional factors. Within a simplified view of the effects that contribute to measured spectra, the following terms can be used [51, 147]:

- **Intrinsic background**: The course atomic-like (single atom) structure of the element of interest. This is formed of the featureless pre-edge, a rising absorption edge, and the post-edge curve.

- **Extrinsic background**: The slow varying background function which has contributions from the detector response and non-atomic like background.
- **Scaling factor**: Difference between spectra caused by the samples physical properties, for example the thickness and concentration.
- **Fine structure**: This is the useful structure that gives information regarding the electronic and atomic structures, defined as χ(E). This is given as the oscillatory components of μ given in equation (11).

The normalization procedure is carried out to normalize the data to the absorption of one absorber. The edge step should be consistent across all spectra for a given element present in a sample and therefore can be normalized to the same value, which is typically taken as 1. The first step is to determine the E_0 position, which defines the energy of the edge. The E_0 position can be selected in a number of different ways, for the data in this thesis the position of the first inflection point in the spectra (after any pre-edge features) is used, which is determined by the first peak in the first derivative. It is necessary to remove the slow variation before and after the edge. This is prominently formed from the absorption coefficient response across the energy range and the detector response. Figure 4.1.1 shows a typical spectra before and after the normalization steps, also shown is the pre- and post edge functions. The pre-edge function is normally a straight line due to the short range typically collected, while the post-edge can be fitted with a 1^{st}, 2^{nd} or 3^{rd} polynomial and the choice is dependent of the data. The pre- and post-edge functions are extrapolated to the E_0 position and the difference between these is used as the scaling factor. This scaling factor is used to apply the normalization consistently across all data sets.

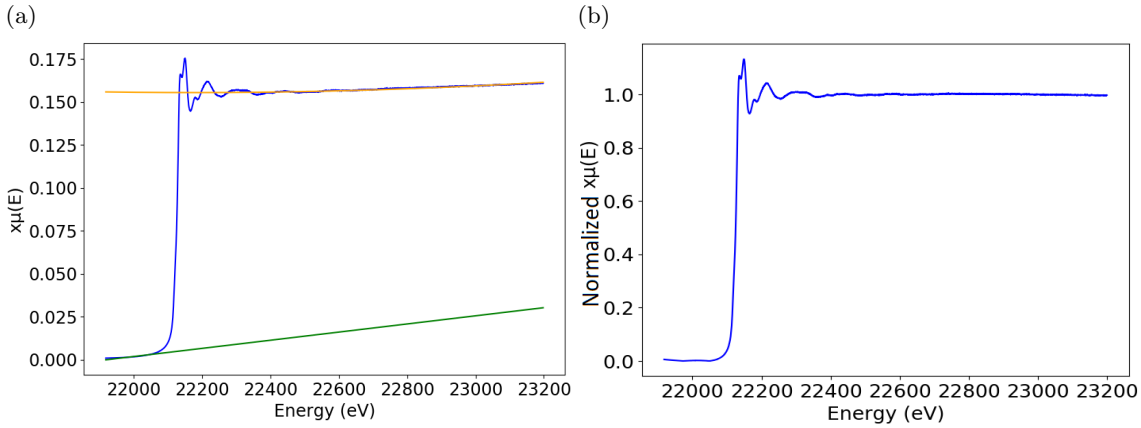

Figure 4.1.1: Normalization steps: a) Pre- and post- edge functions on uncorrected data, b) edge-step corrected data

At this stage apart from a self-absorption correction, detailed in section 4.2, the XANES reduction is complete. The next step for the EXAFS analysis is a background subtraction [148]. While the normalization process takes into account some of the background contributions, it is necessary to further account for non-atomic like contributions and statistical noise, which occurs as oscillatory features. The extrinsic background can only be approximated as accurate modelling of non-atomic background is currently not possible. The background function is applied in ATHENA where the E_0 position determines the start of the function. To account for the oscillatory background, a background parameter (Rbkg) is also applied. In this case it is assumed that the oscillation in the Fourier transform EXAFS (FT-EXAFS) should be suppressed before at least the diameter of the absorbing atom. It is typical to use a Rbkg value which suppresses oscillations before the first peak in the FT-EXAFS while ensuring that the features from the scattering paths are not significantly effected. Examples of background corrections applied to the data with varying Rbkg values are shown in figure 4.1.2, where it can be seen that care must be taken to ensure a consistent correction. When Rbkg is 0.5 there are significant features below 1Å. Where Rbkg is set to 1, below 1Å the features are suppressed and there are very little changes in the remaining features. At a value of 1.8 Rbkg, while the features below 1Å are suppressed, there is also a significant suppression of the first major feature.

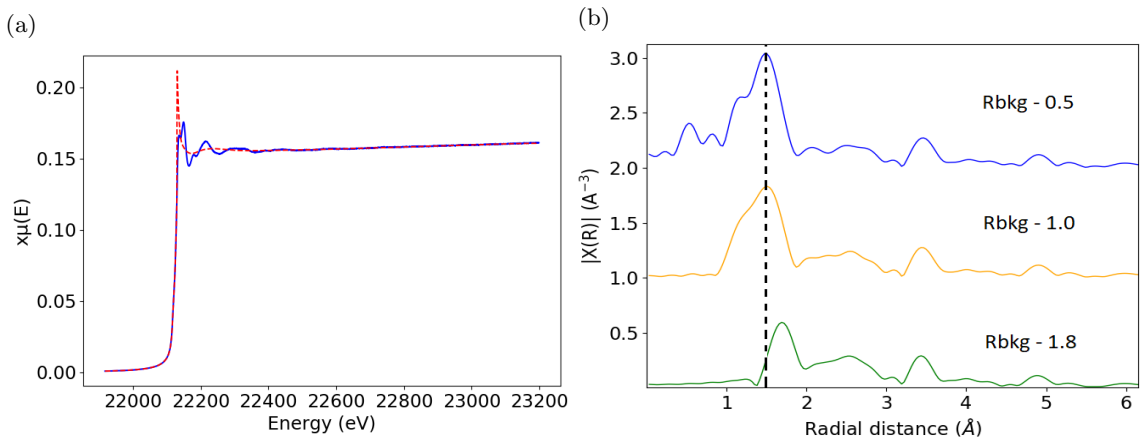

Figure 4.1.2: Background function: a) typically Rbkg function on spectra (dashed red line), b) 3 examples of applied corrections: 0.5 too little, 1.0 reasonable, 1.8 too much. Plotted in R-space.

4.2 Self-absorption

In the limit of dilute samples and thin films, the x-ray fluorescence signal to a good approximation is directly proportional to the atomic sub-shell absorption coefficient of the element of interest. For concentrated and thick samples, self-absorption effects can lead to a severe suppression of the XANES and EXAFS amplitudes making it difficult to carry out a full analysis. In particular and critical for the data presented in this thesis, *Tan el. al.* [149] have shown how these effects can lead to differences in coordination numbers and Debye-Waller factors when modelling the experimental data. In this section a brief overview of the current techniques used to correct for self-absorption is given [150, 151], and a new procedure is presented where a numerical instability in many of the available codes is taken into account.

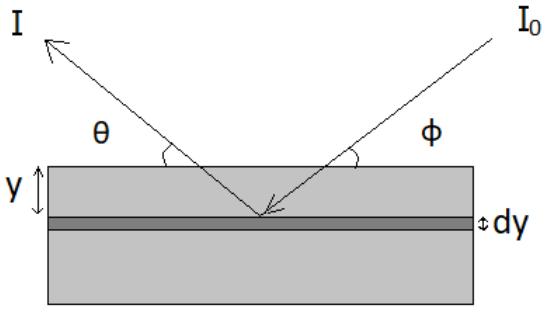

Figure 4.2.1: Typical fluorescence geometry

4.2.1 Theory and standard correction procedure

In general, self-absorption corrections are derived from an expression for the experimental XAS given by *Goulon et al* [152], where different approximations are made to correct data in a number of given situations. The total fluorescence intensity from an edge of interest, *I(E)*, originating from a slice of sample, *dy*, at a depth of y can be expressed as:

$$dI(E,y) \propto \frac{A}{r^2} I_0(E)\epsilon_0(E)\mu_0(E)e^{[-\mu_{tot}(E)y-\mu_{tot}(E_f)z]}dy \tag{38}$$

The intensity of the outgoing photons is proportional to a number of factors; i) the incident photon beam I_0, ii) the area, A, of the fluorescence detector at a distance r, iii) the absorption coefficients, where μ_{tot} is a combination of the element of interest, μ_0, and all other elements, μ_b, and iv) $\epsilon_0(E)$ the probability that the core-hole will decay through a radiative process. The exponential term takes into account the path of the photon while travelling through the sample. To calculate the total yield from entire an sample of thickness d:

$$\frac{I(E)}{I_0(E)} \propto \frac{A}{r^2}\epsilon_0(E)\mu_0(E)\frac{1}{sin\phi}\int_0^d e^{[-[\frac{\mu_{tot}(E)}{sin\phi}+\frac{\mu_{tot}(E_f)}{sin\theta}]x]}dx \tag{39}$$

Figure 4.2.1 shows a simple diagram of a typical fluorescence set up, here for simplicity the depth is calculated perpendicular to the sample surface where $x = ysin\phi = zsin\theta$.

$$\begin{aligned}\frac{I(E)}{I_0(E)} &\propto \frac{A}{r^2}\epsilon_0(E)\frac{\mu_0(E)}{sin\phi}\frac{e^{-(\frac{\mu_{tot}(E)}{sin\phi}+\frac{\mu_{tot}(E_f)}{sin\theta})x}}{-(\frac{\mu_{tot}(E)}{sin\phi}+\frac{\mu_{tot}(E_f)}{sin\theta})}\Bigg|_0^d \\ &\propto \frac{A}{r^2}\epsilon_0(E)\frac{\mu_0(E)}{\mu_{tot}(E)+\mu_{tot}(E_f)\frac{sin\phi}{sin\theta}}[1-e^{[-[\frac{\mu_{tot}(E)}{sin\phi}+\frac{\mu_{tot}(E_f)}{sin\theta}]d]}]\end{aligned} \tag{40}$$

It is from equation (40) where most of the corrections deviate with different approximations, however this restricts the corrections to specific situations. The early corrections [149, 152, 153] were only applicable to the EXAFS region due to a discontinuity at the edge making it unsuitable for XANES data. The first corrections that applied to the entire spectra came from *S. Eisebitt 1993* [154], which estimate two unknowns (μ_{tot}, μ_0) from independent fluorescence measurements and *A. Iida, T. Noma 1993* [155] using tabulated data to estimate the background absorption coefficient. There have been a number of further strategies implemented to extend the corrections [156, 157, 158, 159] to account for different experimental considerations, including within the thickness limit and for finite detector areas.

Given the range of corrections available, the two most applicable methods for the data presented in this thesis are discussed in further detail [150, 151]. However it is shown neither provided a suitable correction due to a numerical instability at the absorption edge. It is this instability that is accounted for so that the data can be processed in a sensible manner.

Fluo [150] is one of four [153, 159, 160] correction methods implemented in the *Demeter: Athena* software [146], which is widely used for XAS processing and analysis. The Fluo code is applicable for XANES correction only (where as the other three apply to EXAFS) however as a significant proportion of the data for this thesis is focused on this region, it provides a suitable starting point for the corrections and has the added advantage of only needing the chemical formula and incident/detector angles to provide a correction. Following on from equation (40), a simplification is made by neglecting the exponential term in the limit of "infinitely" thick samples where $\mu_{tot} \gg d^{-1}$ and since $0 \leq (\phi, \theta) \leq 90^o$ which leads to:

$$[\frac{\mu_{tot}(E)}{sin\phi}+\frac{\mu_{tot}(E_f)}{sin\theta}] \gg d \tag{41}$$

$$\frac{I(E)}{I_0(E)} \propto \frac{A}{r^2}\epsilon_0(E)\frac{\mu_0(E)}{\mu_{tot}(E)+\mu_{tot}(E_f)\frac{sin\phi}{sin\theta}} \tag{42}$$

Equation (42) represents pre-edge subtracted data where it is assumed that over the small energy range considered before the edge I_0 is constant. An edge-step normalization is then added, giving a normalized signal (N):

$$N = \frac{\frac{I}{I_0}(E)}{\frac{I}{I_0}(E^+)} = \left[\frac{\epsilon_0(E)\mu_0(E)}{\epsilon_0(E^+)\mu_0(E^+)}\right]\left[\frac{\mu_{tot}(E_f)\frac{sin\phi}{sin\theta}+\mu_b(E^+)+\mu_0(E^+)}{\mu_{tot}(E_f)\frac{sin\phi}{sin\theta}+\mu_b(E)+\mu_0(E)}\right] \tag{43}$$

Here E^+ indicates an energy above the absorption edge. To simplify, the numerator and denominator are divided by $\mu_0(E^+)$:

$$N = \frac{\mu_0(E)}{\mu_0(E^+)}\frac{\epsilon(E)}{\epsilon(E^+)}\left[\frac{\frac{\mu_{tot}(E_f)}{\mu_0(E^+)}\frac{sin\phi}{sin\theta}+\frac{\mu_b(E^+)}{\mu_0(E^+)}+\frac{\mu_0(E^+)}{\mu_0(E^+)}}{\frac{\mu_{tot}(E_f)}{\mu_0(E^+)}\frac{sin\phi}{sin\theta}+\frac{\mu_b(E)}{\mu_0(E^+)}+\frac{\mu_0(E)}{\mu_0(E^+)}}\right] \tag{44}$$

Finally by using the approximation that $\frac{\epsilon(E)}{\epsilon(E^+)} \approx 1$ and defining $\beta = \frac{\mu_{tot}(E_f)}{\mu_0(E^+)}$, $\gamma = \frac{\mu_b(E)}{\mu_0(E^+)}$, $\gamma' = \frac{\mu_b(E^+)}{\mu_0(E^+)}$, the edge-step normalized absorption coefficient $\frac{\mu_0(E)}{\mu_0(E^+)}$ can be calculated:

$$\frac{\mu_0(E)}{\mu_0(E^+)} = \frac{N(\beta\frac{sin\phi}{sin\theta}+\gamma)}{(\beta\frac{sin\phi}{sin\theta}+\gamma'+1)-N} \tag{45}$$

Using tabulated absorption coefficients, *Fluo* solves equation (45) to find the correction. In figure 4.2.2 an example is given where this method has been applied to IrO_2 data collected at 300K

with the sample surface at 45^o with respect to the polarization of the incident beam. At the absorption edge the correction breaks down and becomes asymptotic and then negative. Mathematically this occurs due to the denominator of equation (45) approaching zero, where the measured absorption coefficient approaches and then becomes larger than the theoretical total absorption coefficient. Physically the reason for this comes from two factors. Firstly when considering the type of orbitals investigated, the K-edge has non-localised final states which creates a broad whiteline feature since the orbitals can have a wide range of energies. On the other hand the L-edge measurements involve localised final states which results in a very sharp increase in the measured signal since there is less variation in the allowed energies. The second reason is also related to this and is due to the improvement of the achievable resolution in recent years (measurements below the core-hole lifetime limit). This further increases the ability to detect transitions at specific energies. The overall result from these effects is not modelled well by the existing codes, which use tabulated absorption coefficients calculated from a mono-electronic approach, most applicable for non-localized states.

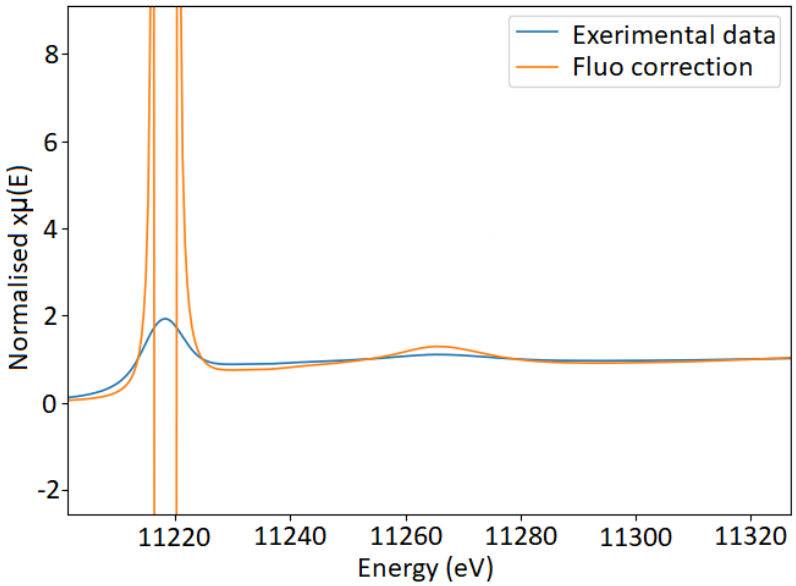

Figure 4.2.2: Example of a self-absorption correction by Fluo program on the IrO_2 data (300K, 45^o)

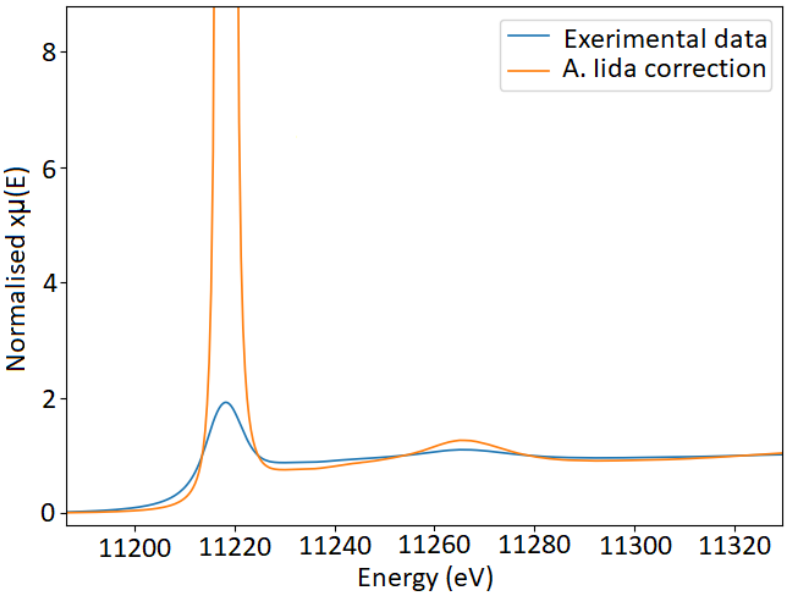

Figure 4.2.3: Example of a self-absorption correction by the procedure presented by A. Iida and T. Noma (1993) on the IrO_2 data (300K, 45^o)

The second correction method is derived from *A. Iida, T. Noma 1993* [155], and implemented with small variations in *XANES dactyloscope* [161]. The advantage of this method is that it can be applied to the entire spectrum however it does require a very carefully pre-edge subtraction and normalization. The method was re-invented by *J. M. Ablett, et. al. 2005* [151] where detailed examples have been given. Starting from equation (40), a calibration constant is introduced to take in to account certain factors that are assumed to be constant across the entire spectra, leading to:

$$\frac{I(E)}{I_0(E)} = K\frac{\mu_0(E)}{[\mu_{tot}(E) + \frac{\mu_{tot}(E_f)sin\phi}{sin\theta cos\tau}]}(1 - e^{-[\frac{\mu_{tot}(E)}{sin\phi} + \frac{\mu_{tot}(E_f)}{sin\theta cos\tau}]d}) \tag{46}$$

It is from equation (46) that the calibration constant can be estimated at a point away from the edge in which the EXAFS oscillations are minimal and the absorption coefficient for the element of interest can be calculated. Note that the additional term $cos\tau$ can be used with $sin\theta$ to take into account corrections using a large detector area. The procedure is as follows: i) an accurate measurement of the incident x-ray intensity is important so that a correct normalization and background subtraction can take place. ii) once the background has been determined it can be normalized and subtracted from the normalized fluorescence intensity and equation (46) can be applied. iii) taking the assumption that $\mu_b(E)$ is constant throughout the energy range, tabulated absorption coefficients for $\mu_{tot}(E_f)$, $\mu_b(E)$ and $\mu_0(E)$ at a point far from the edge where oscillations from the EXAFS signal are minimal can be inserted in the equation (46) and the calibration constant can be estimated. iv) The sub-shell absorption coefficient can then be obtained at each energy point. This is done by inputting trial values for μ_{tot} and comparing the output with the measured background-subtracted fluorescence intensity until agreement is made within a pre-set limit.
Figure 4.2.3 shows an example correction from the procedure described above on IrO_2 (300K, 45^o) with the follow absorption coefficients used: $\mu_{tot}(E_f) = 3065.8\text{cm}^{-1}$, $\mu_b(E) = 0.03\text{cm}^{-1}$, $\mu_0(12.0keV) = 3545.93\text{cm}^{-1}$. Similar to *Fluo* the correction fails at the edge, becoming asymptotic. The reason for this due to the pre-edge normalization step and calibration constant. The background absorption is removed by the pre-edge step however when calculating the calibration constant this is not accounted for, leading to an unrealistic correction in the data which displays a dramatically varying absorption coefficient at the edge.

4.2.2 New correction procedure

For the worked carried out in this thesis an accurate correction is needed for the EXAFS region in order to produce reliable fitting and a reasonable correction in the XANES region so that a comparison between the different angles can be undertaken. The procedure outlined by *A. Iida, T. Noma 1993* [155] has been reproduced to give control over the correction parameters and absorption coefficients used (the code used is shown in appendix A). The critical difference in the implementation of the code used in this thesis compared to *A. Iida, T. Noma 1993* code comes from the $\mu_0(E)$ value used to determine the calibration constant far from the edge. When carrying out the normalisation step and pre-edge correction, the data effectively represents the absorption coefficient with the background fluorescence subtracted. In the method presented by *A. Iida, T. Noma 1993* [155] it is assumed that the background fluorescence can be accounted for in the calibration constant however it is not the case for all elements and edges where the background fluorescence is significant. To correct for this, an approximation of the background fluorescence from the element of interest is calculated before the edge ($\mu_0(E^*)$)and then subtracted from the μ_0 used to calculate the calibration constant. Figure 4.2.4 and 4.2.5 shows the edge-step normalised transmission and fluorescence data, along with the correction, for IrO_2 (300K, 45^o). The absorption coefficients used to calculate the calibration constant were: $\mu_{tot}(E_f) = 3065.8\text{cm}^{-1}$, $\mu_b(E) = 0.03\text{cm}^{-1}$, $\mu_0(12.0keV) = 3545.93\text{cm}^{-1}$ and $\mu_0(E^*) = 1932\text{cm}^{-1}$. There is excellent agreement in both the XANES and EXAFS (represented by the k-space data) between the corrected fluorescence and transmission data, indicating that this method is applicable for the data in this thesis.

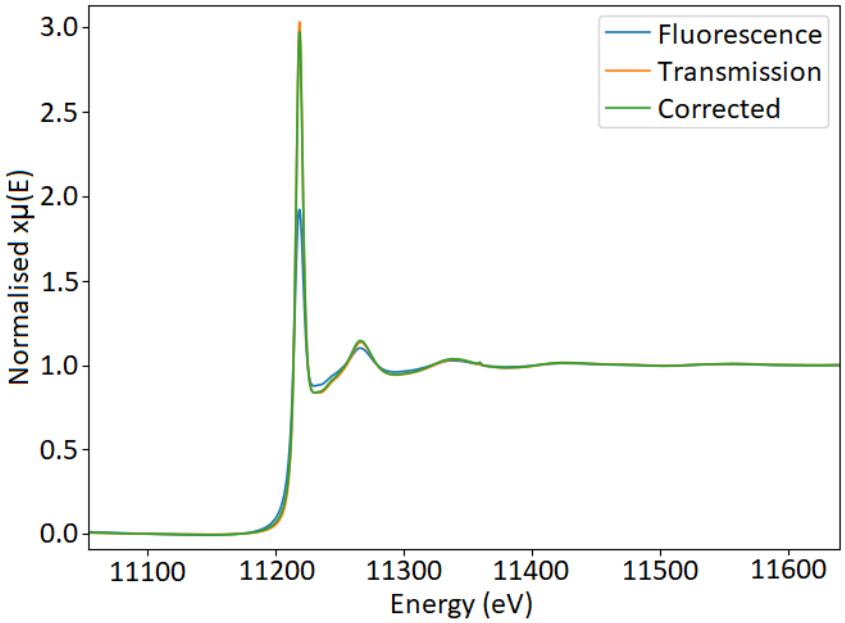

Figure 4.2.4: Example of the new self-absorption correction, comparing the correction on Fluorescence to transmission data on the IrO_2 data (300K, 45^o)

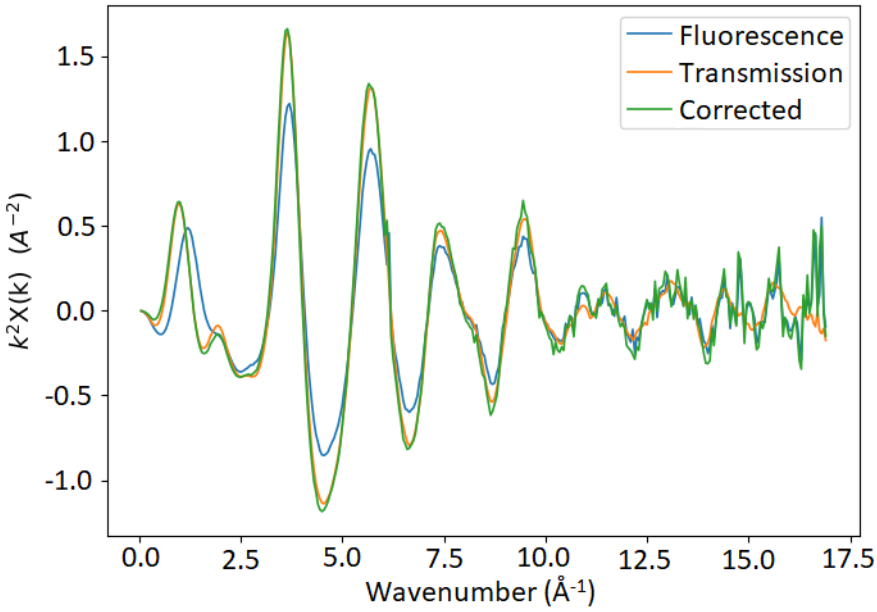

Figure 4.2.5: Example of the new self-absorption correction, comparing the correction on Fluorescence to transmission data, in k-space, on the IrO_2 data (300K, 45^o)

4.3 Data extraction

Once a correction for the self-absorption and the background contribution has been applied, the $\chi(k)$ can be extracted. Using equation (47), k is extracted from E by ATHENA.

$$k = \frac{1}{h}\sqrt{2m_e(E - E_0)} \tag{47}$$

Where m_e is the mass of an electron. As $\chi(k)$ decreases in amplitude at high values of k, it is typical to apply a weighting for analysis. ARTEMIS allows either k-weightings of 1,2 and 3 ($k\chi(k)$, $k^2\chi(k)$ and $k^3\chi(k)$ respectively), or a combination of all three to allow an evaluation of the best fit. The aim is to make $\chi(k)$ a constant amplitude, where different weightings can fit low-z or high-z scattering elements better. High frequency oscillations and incomplete ranges can introduce additional artefacts, to ensure that only atomic-like data is considered a spline clamp is applied to the data. This effectively adds the structure outside this range to the background and hence these oscillations will be set to zero.

The fits in this thesis have been carried out in R-space, which gives greater control over the range of data used and can be fitted peak by peak. The Fourier transform (equation (48)) allows the extraction of periodic frequencies from the data, where k^w is the k-weighting applied.

$$\chi(R) = \frac{1}{\sqrt{2\pi}}\int_{k_{min}}^{k_{max}} k^w\chi(k)\epsilon^{2ikR}dk \tag{48}$$

Analysis of the peak position, intensity and broadness can provide information regarding the local structure. As the Fourier transform is finite, a reasonable range selection is needed in k. A window function is applied to the $\chi(k)$, to avoid sharp discontinuities. A Hanning function has been used in this thesis (other examples of fitting windows included Kaiser-Bessel and Gaussian) which smoothly reduces the paths at the end of the window close to zero [51].

A final extraction of data can be performed by a back-Fourier transform. While by definition, the inverse Fourier transition of a Fourier transform will reproduce to the original data, if modified to only take the real parts of the original Fourier transform then the back Fourier transform can provide information relating the phase and amplitude effects. If a small range is selected then specific information regarding one or more paths can be extracted. In this thesis, this technique is used in the beat effect section 4.6.

4.4 Electronic structure: Branching Ratio (BR)

As already mentioned in previous sections, the electronic structure information obtained during these experiments has been analysed by using simulated groundstate structures and tracking changes in features across the transitions investigated. The materials in this thesis contain transition metals with d electrons which can lead to significant effects caused by the spin-orbit coupling. Using a simple atomic picture the L_3-edge represents dipole transitions $2p_{3/2} \rightarrow d_{3/2}$ and $2p_{3/2} \rightarrow d_{5/2}$. However at the L_2-edge, the J selection rules only allow the $2p_{1/2} \rightarrow d_{3/2}$ transitions. It was shown on the basis of a 2j+1 degeneracy of the initial core states and in a one electron model, that the L_2/L_3 branching ratio is 2:1 [162, 163]. Without spin-orbit coupling this is a statistical value. Since the materials investigated in this thesis include 3d, 4d and 5d transition metals, spin-orbit coupling can not be neglected and has been shown that the BR varies significantly depending on its strength. It has been shown that for deep core levels there are systematic changes in the BR with changing ground-state spin-orbit energy in the atom and that changes in the crystal field splitting can also have an influence on the BR value [162, 163, 164, 165, 166, 167]. The BR is very sensitive to a number of factors, which makes it difficult to compare values obtained in different experiments and compounds as it can vary dramatically. There have been attempts to create a set of generalized rules to understand the relationship between the BR's and interactions, where a comprehensive overview is given in *B. T. Thole, et. al. 1988* [163]. While it is difficult to apply these rules in all situations, it has been shown that comparison of BR's across transitions can show if changes occur in the electronic structure of the absorbing atom, as long as the interaction that makes the two final state manifolds different (either spin-orbit coupling or electrostatic core-valence interactions) is also present in the initial state. To express the BR two values are typically quoted in the literature:

$$BR = \frac{L_3}{L_2} \tag{49}$$

$$BR_N = \frac{L_3}{L_3 + L_2} \tag{50}$$

where BR is the branching ratio and BR_N is the normalized value. To calculate the intensity under the whiteline a standard Gaussian or Lorentzian function is fitted. The whiteline feature is a result of well confined electrons which produces a peak in the near-edge region. It is the interaction of these electrons with the spin-orbit coupling and crystal field which defines the BR. It is also necessary to add an additional step function since the tail end of the whiteline will have a small overlap with other orbitals. This is fitted with an arctangent function. The area considered is shown in figure 4.4.1. Here the red line shows the best fit of the Gaussian-arctangent function, the black line is the arctangent function, the orange area is the intensity considered and the green area represents the overlap from the other orbitals. In this thesis the BR is used to understand if there are significant changes in the spin-orbit and crystal field effects across the transitions investigated.

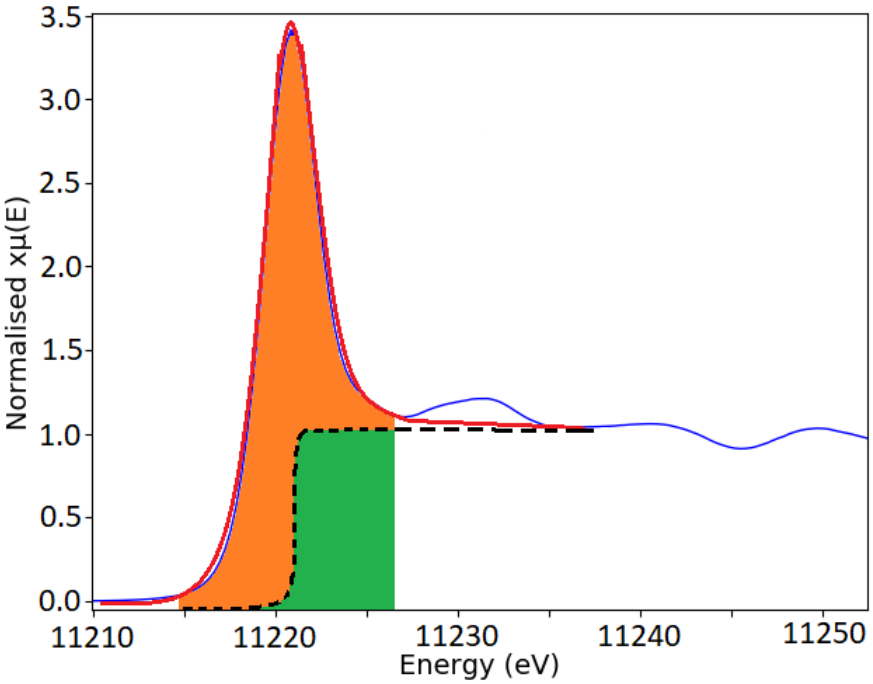

Figure 4.4.1: Branching ratio normalized peak area. The orange area represents the intensity from the L_2/L_3-edge that is considered and the green area represents the overlap from other orbitals that is removed.

4.5 Fitting to theoretical models

A quantitative analysis of the extracted EXAFS signal provides information regarding bond lengths, degeneracies and disorder. This is achieved by fitting a theoretical EXAFS signal to the measured signal, an analysis of the fitting parameters that modulate the theoretical model provides the required information. There are a number of different programs which can fit theoretical EXAFS to the experimental data, in this thesis ARTEMIS is used [146]. This program used FEFF6 to produce the theoretical EXAFS based on known structures of the parent compounds in a well characterized high temperature phase. Using the atom positions from a given structure, FEFF6 calculates the scattering paths and their contribution is weighted. These individual paths are then compared to the experimental data and using equation (11) the model EXAFS signal is built.

$$\chi(k) = S_0^2 \sum_j N_j \frac{f_j(k,\pi)}{kr_j^2} e^{-\frac{2r_j}{\lambda(k)}} e^{-2k^2\sigma_j^2} sin(2kr_j + \delta_j(k))$$

For each individual path FEFF calculates certain parameters: the scattering amplitude $f_j(k,\pi)$, the mean free path of the photoelectron $\lambda(k)$ and the phase shift $\delta_j(k)$. The remaining parameters are either fixed or refined by fitting the theoretical to the measured EXAFS and can be manipulated to provide the most suitable fit. This is achieved by minimizing the difference between the theoretical model and experimental data in the region of interest using a least-squared method:

$$[\sum_{j=1}^{N} |\overline{\chi}_{data}(r_j) - \overline{\chi}_{model}(r_j)|^2]; r_{min} \leq r_j \leq r_{max} \quad (51)$$

The fitting parameters used in this thesis are:

- **Degeneracy, N_j**: often referred to as the coordination number, this parameter identifies the number of identical scattering paths from the same absorber. With polarization dependent measurements, the degeneracy is also constrained by paths that will give the same contributions to the EXAFS signal with a given polarization (i.e. the same vectors). This parameter is fixed in the fitting process.
- **Threshold energy, ΔE_0**: determines the energy used to calculate the momentum of the photoelectron and effectively gives the shift between the theoretical and measured signals. In these fits the ΔE_0 parameter is allowed to vary for each spectrum, since large changes may suggest an incorrect normalization. The obtained value should be reasonably consistent across spectra and with a value between ±10eV when compared to the theoretical ΔE_0.
- **Amplitude reduction factor, S_0^2**: This is treated as a global parameter that in principle takes into account intrinsic losses, that are not dependent on k and r. However this factor is sensitive to a number of effects, including self-absorption, harmonics, sample inhomogeneity and detector non-linearity, hence is seen as a useful variable to determine if a fitting is realistic. The values should fall between 0.7 and 1.05. As a general rule, a value outside this range suggests that the model is incorrect, however some solids can come with values of 0.6 hence the value is dependent on the material. The same S_0^2 value is fitted to all paths contributing to the EXAFS but is an independent variable across different angles. The independences across different angles is used to check if the self-absorption correction is consistent across data sets.
- **Debye-Waller factor, σ_j^2**: This is the mean square relative displacement which describes the static and thermal disorder. Each path in practice will have its own value, however the parameter is normally fitted with the same value for similar path lengths for the same atomic species. This is to minimize the number of fitting parameters used. The value should be positive since it is the squared value of the deviation and typically ranges between 0.002Å^2 and 0.03Å^2, with values larger than this suggesting that the path is so disordered it does not contribute to the signal. The values should decrease with decreasing temperature and deviation from this may indicate a change in its properties.
- **Half path length, dr_j**: the average deviation from the reference path length defined by FEFF.

While ARTEMIS can perform the fits in both R and k-space, the fits in this thesis are carried out in real space with ARTEMIS automatically fitting all k-weightings at the same time. Each path is fitted on a peak by peak basis which allows greater control over the different parameters used. The final fit is a combination of several data sets taken under the same conditions with different orientations relative to the beam. Temperature dependent measurements are not fitted in the same sets as this allows for different fitting parameters to be tracked across the temperatures. ARTEMIS calculates the EXAFS signal by default using the powder average equation. To take into account the polarization dependence the S_0^2 is replaced with $S_0^2 * W_j$ with $W_j = 3(sin\theta sin\theta_j cos(\phi - \phi_j) + cos\theta cos\theta_j)^2$ which is the weighting factor that gives the contributions relative to the polarization of the x-rays (Section 2.2.4). By fitting multiple orientations during the same fit the ϕ parameter (ab orientation) can be calculated correctly. The aim of the fitting is to monitor the different parameters across temperature to track changes in the local atomic structure.

It is important to evaluate the fits within a physical framework to ensure that the parameters and overall theoretical EXAFS make physical sense. As already outlined the parameters have well defined conditions, when the values range outside these constraints it suggests that the model may be incorrect or there are properties which have not been taken into account. In addition, the "goodness" of the fit is evaluated by two numbers, χ^2 and R-factor. The statistic χ^2 is defined as [168]:

$$\chi^2 = \frac{N_I}{N_G} \sum_{j=1}^{N} \left| \frac{\overline{\chi}_{data}(r_j) - \overline{\chi}_{model}(r_j)}{\epsilon_j} \right|^2 \tag{52}$$

which gives a quantitative value for the mismatch between the experiment and model by defining it as a statistical value. In this equation N_I is the number of independent parameters available defined by $(2\Delta k \Delta R)/\pi$ and N_G is the number of guess parameters used in the fits. $\overline{\chi}$ is both the real and imaginary parts of the Fourier transform and ϵ is the estimated uncertainty of the data. The sum is performed over the range of data points included in the fit, which when multiple data sets are included (polarization dependent fitting) the sum includes all data points in all data sets.

The uncertainty in the fitting parameters calculated in ARTEMIS is defined as the amount by which the parameters can vary without causing the fit to become significantly worst. The estimate in the uncertainty (ϵ) is not always reliable so it is typically to calculate the reduced χ^2_v:

$$\chi^2_V = \frac{\chi^2}{V} \tag{53}$$

where V is the number of guess parameters which are unused in the fits. Effectively χ^2_v takes into account the amount of information used in the fit and the total amount available. It should be noted that it is typical for ARTEMIS to underestimate the uncertainty in the fits since the statistical errors rarely dominate systematic errors.

The additional parameter to check the accuracy of the fits is given by the R-factor:

$$R = \frac{\sum_{j=1}^{N} |\overline{\chi}_{data}(r_j) - \overline{\chi}_{model}(r_j)|^2}{\sum_{j=1}^{N} |\overline{\chi}_{data}(r_j)|^2} \tag{54}$$

this is a measure of the agreement between the experimental data and the model. R should be much smaller the 1.

4.6 Beat effect

There are several methods that can be used to extract structural information for EXAFS. The fitting to theoretical models method is used in this thesis as the main fitting process. However it does have some limitations. Due to the limited k-range in which EXAFS with sufficient amplitudes can be observed, the data represented in R-space suffers from broadening effects. The resolution is determined by the width of these features, which in the case of close lying shells can affect the ability to resolve different scattering path with similar lengths. When two paths are similar in length and amplitude, the fitting parameters applied, especially the Debye-Waller factor, may treat one of the paths as noise. *G. Martens et. al.* [169] presented an extended Fourier transform method with significantly improved resolution, which can be used to determine differences in bond lengths for identical atoms. This method has been used in this thesis to determine if two paths of similar lengths are present in a data set before a fit is attempted.

If two shells of identical atoms are positioned at a distance of R_1 and R_2 from the absorption atom, the backscattering amplitudes, $f_i(k, \pi)$, and phases, $\delta_j(k)$, can be considered the same. In this case, the sum over both shells from the EXAFS equation (11) describing the modulating part of the absorption coefficient can be written as:

$$\chi(k) = -k^{-1}\bar{A}(k)sin[2k\bar{R} + \bar{\varphi}(k)] \tag{55}$$

The average distance of the two shells from the absorbing atoms is given by $\bar{R} = (R_1 + R_2)/2$. The envelope function, $\bar{A}(k)$ which gives the amplitude related effects, then becomes:

$$\bar{A}(k) = A_1(k)[1 + C^2 + 2Ccos(2k\Delta R)]^{1/2} \tag{56}$$

$$C = \frac{A_2}{A_1} = \left(\frac{N_2}{N_1}\right)\left(\frac{R_1^2}{R_2^2}\right) \times e^{[-2(\sigma_2^2 - \sigma_1^2)k^2 - \Delta R/\lambda]} \tag{57}$$

Where $A_1(k)$ is the envelope function of the first shell, C is the ratio of the envelope functions of the second and first shell and the relative distance is $\Delta R = R_2 - R_1$. From equation (56) it can be seen that the envelope function for shell 1 is modulated by the presence of shell 2. There will be beats determined by the relative separation of the two shells, in k-space. The term under the square root of $\bar{A}(k)$ will show minima and maxima when:

$$k_E = \frac{n\pi}{2\Delta R}, n = 1, 2, ... \tag{58}$$

It is assumed that there are only small differences between the shells in terms of the mean-square displacement (σ_i^2) and that the mean free path (λ) is k-independent.

Figure 4.6.1 shows an example of the beat effect on $IrTe_2$ data. In this system it has been proposed that there are two close lying shells of Ir atoms, as a result of dimerization. The reported bond lengths relative to the absorbing Ir atom are $R_1 = 3.98 \pm 0.005$Å and $R_2 = 3.82 \pm 0.005$Å and the contributions from both paths will range from 3.3-4.3Å. Using equation (58), the position of the minima should be between 9.23-10.47Å^{-1} and as shown in figure 4.6.1 b) this is confirmed.

(a)

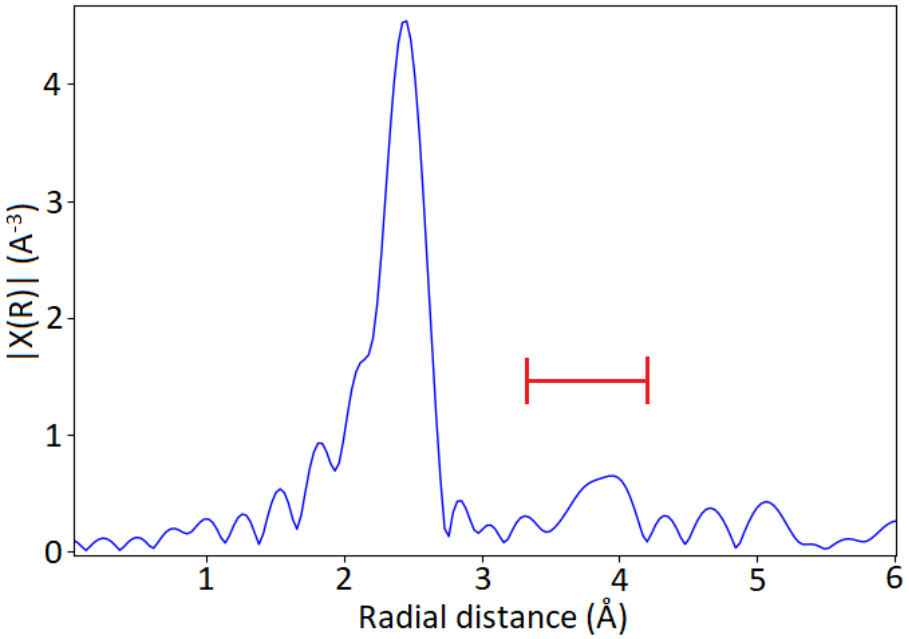

(b)

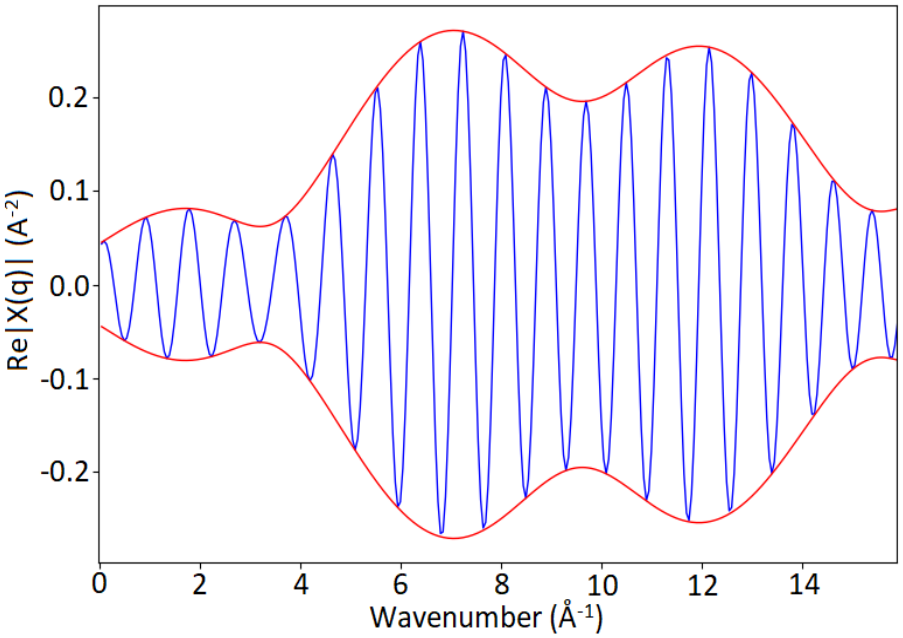

Figure 4.6.1: EXAFS Beat analysis example on $IrTe_2$ sample (225K, 15^o). a) Fourier transform, range shown for two similar length Ir-Ir paths from two shells, b) Resultant back Fourier transform (q-space) with envelope function showing a beat at 9.8Å^{-1}.

4.7 Chapter summary

This chapter has given details regarding the data processing techniques used in this thesis. The processing, background subtracting and normalization steps remove glitches from the data and adjust the spectra so that a comparison can be made between different data sets. The self-absorption correction applied to all data sets presented in this thesis is given. Details are provided with respect to some of the existing correction methods and a new procedure is introduced to allow for reasonable corrections to XANES and EXAFS data. The procedure used to extract the branching ratio information is given and allows comparison of the spin-orbit coupling and crystal field across transitions. To extract local structural information from EXAFS, both the beat effect and the method to fit theoretical models to the experimental data have been discussed. The former allows for the determination of the relative separation of similar length scattering paths from the same scattering species. The latter provides significant information regarding the nature of the local structure including: bond lengths, degeneracy and disorder. The methods discussed in this chapter have been used to extract the relevant information required to give a deeper understanding of the materials investigated.

Chapter 5

Valence-to-core x-ray emission spectroscopy

In this chapter an investigation into the use of valence-to-core XES measurements is presented. While this technique has been used in many studies, its use for investigating materials with heavy metal/ligands and specifically the L-edge emission lines is not well understood. A study of the K-edge emission features is presented, which provides a suitable reference point for the analysis. Using tungsten reference samples, the L-edge emission lines are investigated. With the additional use of simulations, the different features are identified and discussed with relation to the electronic structure of the materials.

5.1 Introduction

X-ray emission spectroscopy is often seen as a complementary technique to absorption spectroscopy, which involves a core electron being exited to the continuum. The emission process occurs when this core-hole is filled by an electron from a donor orbital and a fluorescence photon is emitted. The technique can provide significant information from the occupied molecular orbitals (OMO) regarding the local charge, spin-density and the chemical environment of the species being probed [85, 170]. One area of XES which has seen rapid advancements in recent years in its interpretation and analysis is the so called valence-to-core measurements. While this high energy region has been observed since at least the 1930's [171, 172], it is only recently that the applications of the technique in material studies have been made possible due to improvements in high-energy beamlines, with higher flux and multi-element XAS spectrometers, and computational simulations. The technique directly probes the valence orbitals, where analysis of these features indicate that they originate from transitions involving the filled ligand valence *ns* and *np* orbitals [48, 173, 174]. As shown in figure 5.1.1, the combination of vtc-XES and HERFD-XANES can provide a wealth of information around the Fermi energy levels, where HERFD probes the lowest unoccupied molecular orbitals (LUMO) and vtc probes the highest occupied molecular orbitals (HOMO) [48]. While valence band photoemission spectroscopy (PES) measurements can provide similar information with a higher spectral resolution, vtc has the advantage that it is a element selective, bulk technique and has less requirements with regards to the sample environment (i.e. PES requires ultra-high vacuum (UHV)). It has been shown that it is sensitive to the metal spin and oxidation state as well as ligand identification, hybridization, protonation state and metal-ligand bond lengths [175, 176, 177].

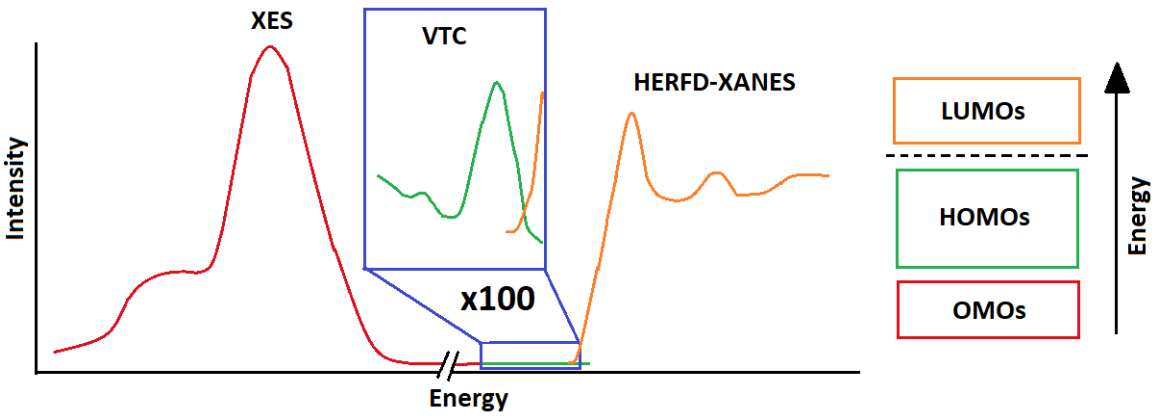

Figure 5.1.1: Left: Representation of the XES, vtc and HERFD-XANES regions. Right: depiction of the type of molecular orbital which contribute to each region.

Experimentally the incident x-ray photons are set at an energy well above the metal K/L absorption edge and the XES analyser crystals scan fluorescence photons at energies just below the Fermi energy. Compared to the main emission line, the vtc region is at least 100 times less intense (for example the Kβ), making these measurements significantly more difficult than traditional XES. Further details of the experimental set-up are given in section 3.3.3. In recent years a large range of literature has shown the successes of this technique for a wide range of applications, specifically focused on the Kβ emission line for 3d elements with light ligands [178, 179, 180, 181, 182, 183, 184]. The interpretation, including DFT simulations have shown very good agreement with the theory and that for these systems a simple molecular orbital description is suitable for understanding the origin of the features. However, only preliminary measurements have been published regarding the use of L-edge emission lines for vtc in material studies. While studies had shown that vtc features are detectable for heavy elements [185, 186, 187, 188, 189], the current level of interpretation has not as yet fully explained the origins of the observed features in this region. Furthermore it has been suggested that the level of the DFT theory typically used may not be appropriate for vtc with heavy elements and/or heavy ligands. Using a range of reference samples and calculations performed using FDMNES, an overview of K- and L-edge valence-to-core emission spectra will be discussed (sections 5.3 and 5.4) and later used to interpret results on the $IrTe_2$ and NaFeAs compounds.

5.2 Background removal and FDMNES simulations

The importance of the intensities of different features when comparing vtc-XES spectra taken from different samples requires careful and consistent normalization. There are several different techniques employed to process the data, with the most reliable based on the normalisation with respect to the area of the entire Kβ region (main emission and vtc area). Using the assumption that the integrated intensity of this region is chemically invariant [173, 190], an estimate can be achieved by either summing every energy point or by interpolation of the XES data and integrating the obtained function. A detailed review of these procedures and potential sources of error is given by *E. Gallo et al. 2014* [174]. As the vtc-XES data forms the tail end of a strong emission line, subtraction of the background tail intensity allows comparison between experiment and DFT calculations. The main source of error using this method arises from the selection of data points used for the interpolation at the high energy side of the vtc region, which may show multi-electron features [191, 192] difficult to separate from the background emission. A two step correction process has been applied to the data presented in this thesis. Firstly the XES data has been interpolated across the vtc region and the background intensity has been subtracted, the regions considered are shown in figure 5.2.1. Due to the relatively large energy gap between the Lβ_5 emission lines and vtc region in the 5d compounds, sufficient data points have not been collected to cover the whole energy range. To take into account differences between spectra introduced by the beamline optics and/or small changes in the sample position, the data has been normalized with respect to the maximum intensity of the main emission line (Lβ_5). Here the assumption has been that the ratio of this emission line will be stable across temperature related transitions. This approach however may produce significant errors when comparing spectra for different samples, so caution is needed.

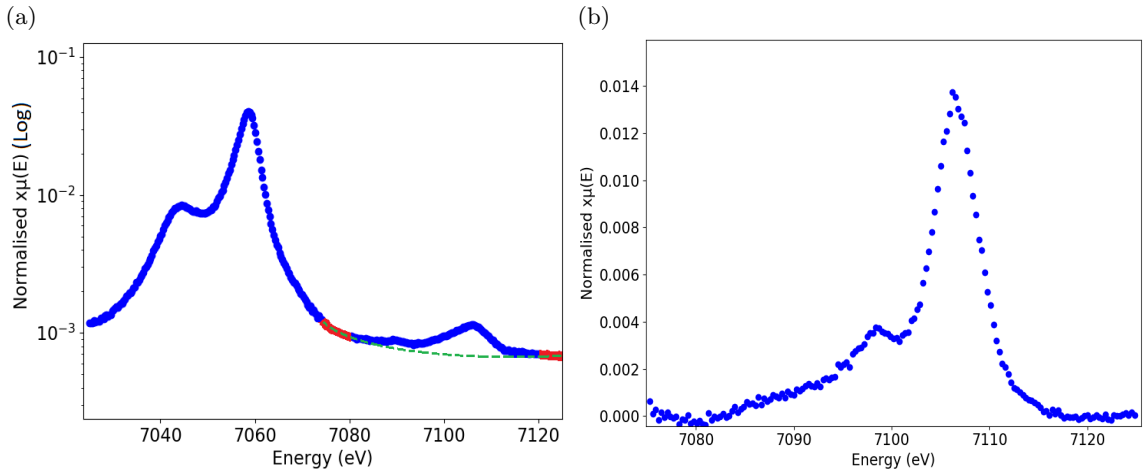

Figure 5.2.1: vtc normalization step. a) red markers indicate selected points for curve fitting, b) background subtracted data.

To interpret the origin of each feature resolved in the vtc-XES spectra, simulations have been carried out using the FDMNES package [193]. This software implements a self-consistent *ab initio* multiple scattering calculation using a muffin-tin approximation. XES spectra, the density of state and orbital overlap have been simulated for all vtc data sets in this thesis. A detailed review of the FDMNES package including the theoretical considerations has been given in section 3.5.2. To solve the electronic structure these calculations have been performed using a multiple scattering method, based on Green's functions. Taking into account a core-hole and spin-orbit coupling, a fully self-consistent method ensures a sufficient level of theory to model the compounds presented in this work.

5.3 Kβ" and K$\beta_{2,5}$ transitions for K emission

Figure 5.3.1 shows a schematic representation of the x-ray emission from Kβ and a simplified molecular orbital diagram showing the origins of the different features in the spectra. The feature defined at K$\beta_{1,3}$ originates from the 3*p*-1*s* transitions and provides information regarding the metal local charge and spin-density [85, 194]. For historical reasons the two higher energies features are defined as Kβ" and K$\beta_{2,5}$. The Kβ" emission involves contributions from the *ns* ligand orbitals while the K$\beta_{2,5}$ emission represents the *np* ligand orbitals, the tail end of this feature also has contributions directly from the 3d metal orbitals [173, 195]. The intensity of the features is modulated by the degree of overlap between the ligand and metal molecular orbitals and the associated symmetries. Analysis of the transitions involved reveal that while contributions from electric dipole, magnetic dipole and electric quadrupole mechanisms have been considered, approximately 99.5% derives exclusively from the electric dipole-allowed character [178, 194, 196]. Interestingly it has been determined that it is the metal *p* orbital participation in the bonding that introduces the electric dipole-allowed *p*-*s* character and it is the extent of the 4p mixing rather than the 3p mixing that fully defines the intensity [178, 194, 196]. The charge on the metal stabilizes the ligand orbitals and therefore determines the energy of the transitions. However the metal-ligand bond length also directly influences the relative separation between the Kβ" and K$\beta_{2,5}$ features [182]. It should be noted that there has been significant efforts in the literature to further determine the character of the molecular orbitals [48, 174]. For example it has been shown how the various phase combinations of the lone pairs of the *d* orbitals from difference symmetries can affect the shape of the K$\beta_{2,5}$ feature [178]. In addition, one of the most successful applications of this technique is the identification of ligands. The identification of elements with similar atomic numbers can be difficult with spectroscopy techniques however vtc-XES has been shown to be very sensitive to this [197, 198, 199]. This is due to the energy positions of the different possible features being very sensitive to the ligands. Note that for the purpose of this thesis that type of discussion has not been included. The metal oxidation state and the character of the ligand orbitals is all that will be needed to study the transitions in the materials discussed in this work.

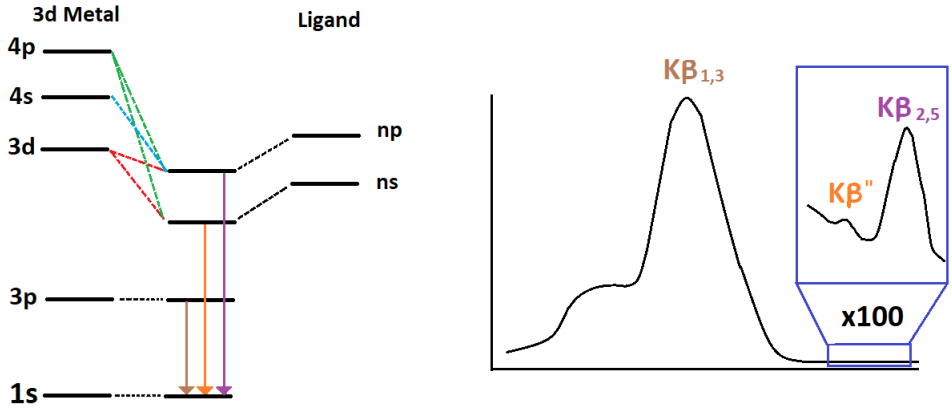

Figure 5.3.1: Fe Kβ XES spectrum and simplified molecular orbital (MO) diagram

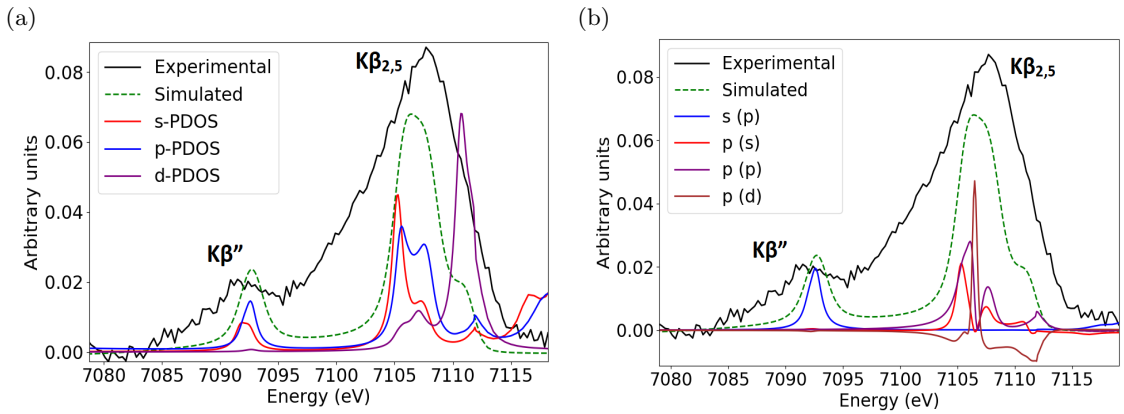

Figure 5.3.2: Fe K-edge: Fe_2O_3 vtc. a) experiment vs simulated DOS, b) experiment vs simulated orbital overlap. Legend indicates (Ligand(Metal)) orbital overlap.

To illustrate the explanation given above for Kβ vtc emission, an example of the Fe_2O_3 is given in figure 5.3.2, with the associated DOS and orbital overlap calculations from FDMNES. This data was collected as part of the work on the NaFeAs system presented in this thesis and further detials of the experimental set up are given in chapter 8. The data was collected on the I20 beamline at Diamond light source, at room temperature. This example has been chosen as this technique/emission line is commonly used for Fe compounds, hence it provides a useful validation of the approach and reproduced literatutre results. The simulated spectra shows that there are two well defined features within the energy range, which are labelled Kβ" centred at 7093eV and K$\beta_{2,5}$ at 7107eV. Both peak positions and the relative intensities are well reproduced, the comparison suggests significant spectral broadening in the experimental data due to life-time broadening. The DOS indicate that both features are centred around s and p orbitals, where the tail end of K$\beta_{2,5}$ feature also shows significant d character. The orbital overlap confirms that the simplified molecular orbital interpretation is appropriate. The Kβ" feature shows overlap with only ligand s orbitals, while K$\beta_{2,5}$ only shows contributions from orbitals with ligand p character. While further analysis is provided in a later section (8.4.2) along with other Fe compounds, the current result shows how the level of theory used by the DFT simulations is sufficient for the 3d vtc.

5.4 Lβ transitions for L emission

Due to the lack of literature regarding vtc-XES using Lβ emission, a study of well known tungsten reference compounds has been carried out to assist the research in this thesis by identify the origin of certain features. The aim of these experiments was to determine how different oxidation states and chemical environments can affect the features seen in the region of interest. These measurements have been carried out by *S. Hayama* (Diamond Light Source). 4 reference samples have been used for this work: WC, W_2C, WO_2, WO_3. The hexagonal tungsten (IV) carbide (WC) is formed by a tungsten W^{+4} cation and a carbon C^{-4} anion, where the atoms form a triple bond. The lesser studied Tungsten carbide (W_2C) is a highly distorted system with several different bonding types, providing a rich chemical environment. Tungsten(IV) dioxide crystallizes into a monoclinic cell. The Tungsten trioxide in which the tungsten shows a +6 oxidation state and at room temperature is also a monoclinic structure. Both WO_2 and WO_3 have octahedral coordination of oxide around but show diffent linkages between the WO_6 units. The metal-ligand bond lengths for WC, W_2C, WO_2, WO_3 are: 2.212Å, 2.135Å, 2.039Å, 1.929Å respectively.

Both vtc-XES and HERFD-XANES have been carried out using the L_3 W edge - Lβ_5 fluorescence line, which are shown in figure 5.4.1. The energy of the incident x-rays for the vtc measurements was set at 10700eV. The monochromator was set up for Zn K-edge, with the spectrometer calibrated with the elastic peak, suggesting that the spectra should be shifted by approximately +4.4eV. There is a small energy difference between the unoccupied orbitals probed by the HERFD-XANES $2p \rightarrow 5d$ transitions and occupied orbitals probed by the vtc-XES $5d \rightarrow 2p$ transitions. A comparison of the HERFD spectra from the 4 samples shows some differences. Notably there is an edge position shift between the WO_2 and WO_3 spectra consistent with the oxidation state change from +4 to +6 respectively. Interestingly there is also a double peak feature that appears only in the WO_3 compound indicating a significant difference in the d orbital configurations compared to the other compounds. Both carbide structures show similar edge positions, with W_2C shifted very slightly left. Intensity differences and a more defined shoulder feature at 10208eV in W_2C are also seen.

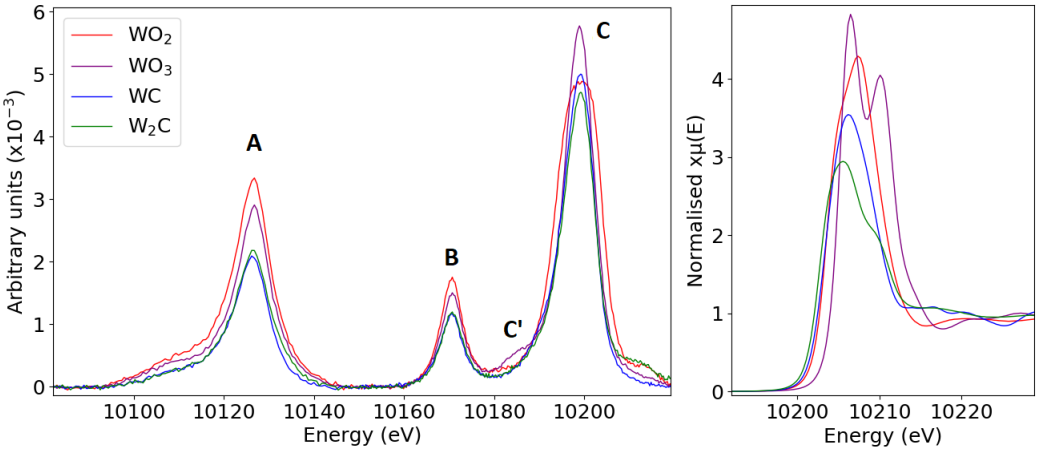

Figure 5.4.1: W L_3-edge: Tungsten HERFD-XANES and vtc-XES reference measurement on WO_2, WO_3, WC, W_2C. 4 areas of interest have been marked.

As shown in figure 5.4.1, 4 features have been defined in the valence-to-core spectra. These can be defined as feature A at 10125eV, B at 10170eV, C at 10187eV and C' at 10200eV. Due to the method used to normalize this data, there is potentially a large error with the absolute values of the intensities, however comparison between the relative intensities within each spectra, peak position and peak structures is possible. It is important to note that while the HERFD spectra indicates shifts in the edge position, this is not replicated in any of the vtc features. Comparison between the carbide compounds shows very little difference apart from the high energy tail of feature C, which is most likely due to multi-electron features. The differences between the WO_2 and WO_3 compounds are more striking. The relative difference between the intensities of features A and B, where WO_2 shows greater intensity, is opposite to that observed in feature C, where WO_3 is more intense. The WO_2 C features shows greater broadening compared to the other compounds, however as tungsten is in the same oxidation state as the WC system it suggests that this change is not related to the oxidation state of the metal. Interestingly the 3 compounds with similar oxidation states (WC, W_2C, WO_2) all show comparable intensities for feature C however WO_3 is significantly more intense. Also defined is feature C' where the WO_3 spectra displays an addition feature when compared to the other systems.

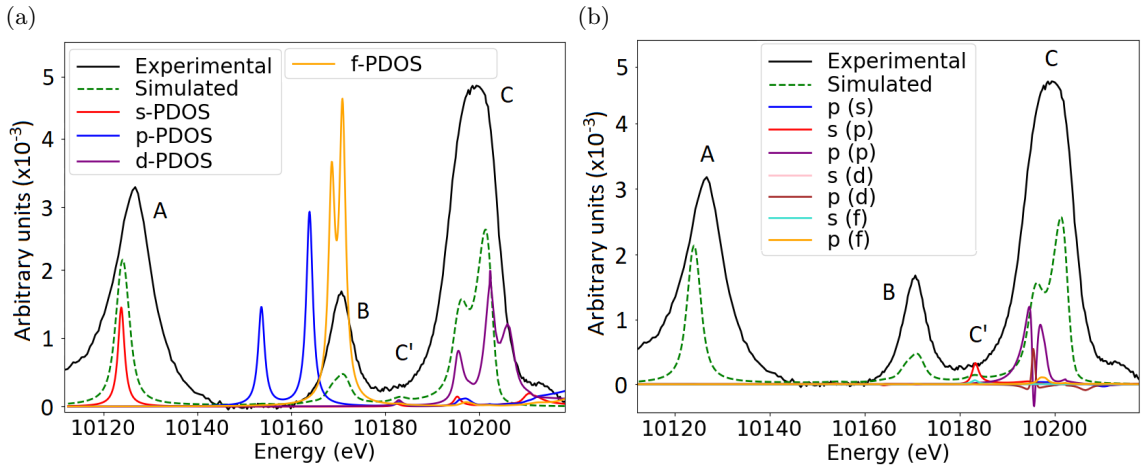

Figure 5.4.2: W Lβ: WO_2 vtc. a) experiment vs simulated DOS, b) experiment vs simulated orbital overlap. Legend indicates (Ligand(Metal)) orbital overlap.

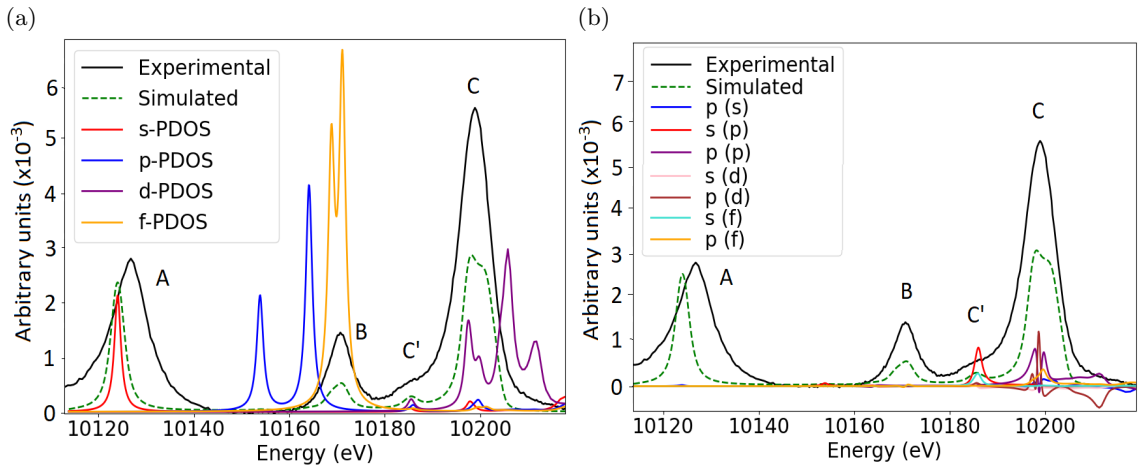

Figure 5.4.3: W Lβ: WO_3 vtc. a) experiment vs simulated DOS, b) experiment vs simulated orbital overlap. Legend indicates (Ligand(Metal)) orbital overlap.

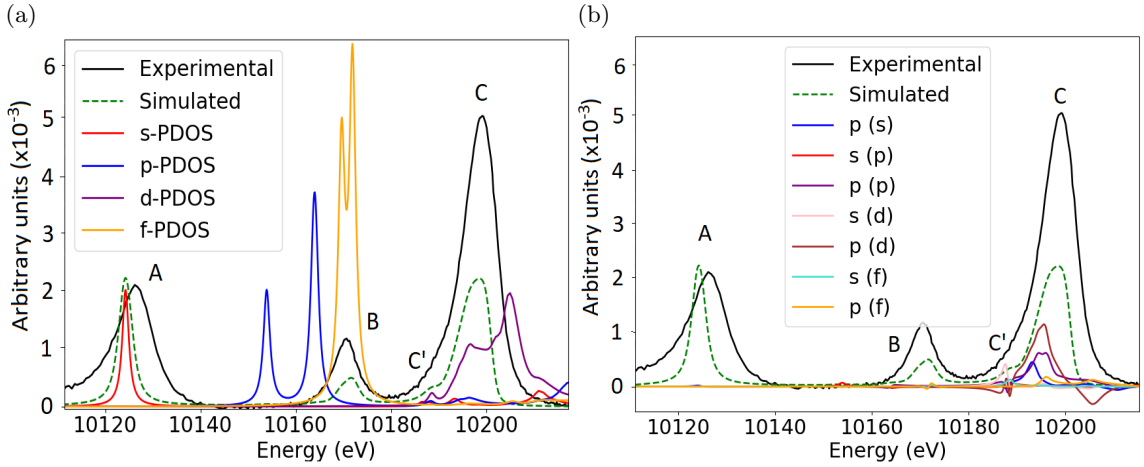

Figure 5.4.4: W Lβ: WC vtc. a) experiment vs simulated DOS, b) experiment vs simulated orbital overlap. Legend indicates (Ligand(Metal)) orbital overlap.

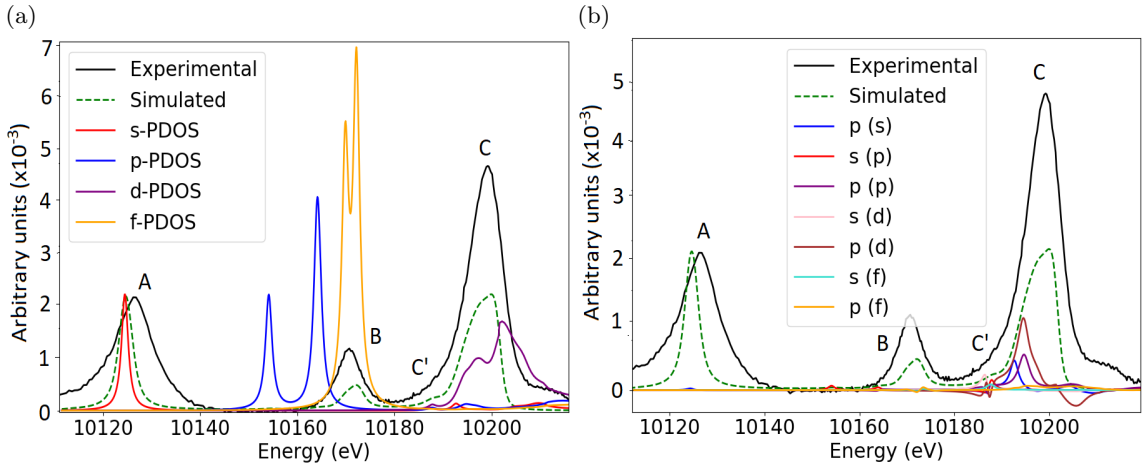

Figure 5.4.5: W Lβ: W_2C vtc. a) experiment vs simulated DOS, b) experiment vs simulated orbital overlap. Legend indicates (Ligand(Metal)) orbital overlap.

To be able to determine the origin of the features in the valence-to-core spectra, partial density of states and orbital overlap simulations have been calculated using FDMNES and are shown for each compound in figures 5.4.2- 5.4.5. Note that the simulations have been shifted to align feature C to

the experimental data and have been scaled to get similar intensities to the experimental data. This has been carried out to allow a consistent interpretation between the different compounds, since the alignment and scaling has been applied by the same amount. The simulated spectra for each compound shows fairly good agreement with the experiment. The position and relative intensities for features B and C are comparable, however in all cases the position of feature A is offset by approximately 3eV and greater relative intensity compared to the other 2 features. The origin of this disagreement may arise from the treatment of the orbitals which contribute to this feature. Typically the simulation codes apply different treatments to core and valence orbitals to allow for reasonable calculation times, as discussed in section 3.5. As these features arise from deep core states, approximations used in the simulations may not be appropriate. The DOS calculations for all samples show similar characteristics. Feature A is shown to be exclusively *s* character, feature B is mostly *f* character and feature C has contributions for mostly *d* orbitals however also small contributions for *s* and *p*. It is interesting to note that the DOS indicates significant *p* character just below feature B however this is not reproduced in either simulated or experimental spectra. It shows that emission from these orbitals are not allowed under the symmetry conditions. While there is a significant *f* orbital density in feature B, these transitions are significantly weaker than the other features indicated by the relatively weak intensity. The C' feature is very weak however the density of states indicates a shift between the samples. As the metal-ligand bond lengths increase, the relative separation between C and C' decreases. Comparison of the *d* orbital contributions in each system shows little change between the carbides but significant differences with respect to the oxides. The dispersion in the *d* orbital is more significant in the W^{+6} compound which has empty 5d orbitals.

The orbital overlap for each compound reveals how both features A and B do not have any overlap with the ligand orbitals, indicating that these features arise from emission directly from the metal, suggesting these are not valence states. Focusing on the C and C' features, there is significant overlap from both ligand *ns* and *np* orbitals. The oxide compounds display a clear separation between the two features whereas this is not the case in the carbides. The C' feature shows overlap involving the ligand *ns* orbitals while the C feature only shows overlap with the ligand *np* orbitals. This suggests similar mechanisms to that of the Kβ vtc emission. The broadening of feature C in the WO_2 can be seen not to derive directly from the orbital overlap where even though the overlap is more intense and at a slightly lower energy it in itself is not significantly broader.

The investigation of the Lβ vtc with tungsten samples provides an insight into the origins of the features in the spectra. Using the analysis above a suggested simple molecular orbital diagram is given in figure 5.4.6 highlighting the origins of each feature. The two lower energy features defined by A and B directly result from deeper metal orbitals, not valence states. The result confirms that the area covered by the C and C' features shows strong ligand character and similar to the Kβ emission it is over a range of approximately 20eV. While the simulations on C' *ns* ligand contribution reveals it is sensitive to metal-ligand bond lengths, due to the very weak intensity it is difficult to confirm with the experimental data. The intensity difference shown in feature C indicates that the vtc is sensitive to changes in the oxidation states of the metal. While the simulations show that the Lβ emission is sensitive to changes in the oxidation state, metal-ligand bond length and chemical environment, the spectral resolution is a limiting factor. In general, these results show that for heavier atoms the vtc-XES spectra show similar interaction between the metal and ligands, when compared to the light ligands. The lower energy features arise from deep-core orbitals, while the higher energy features come from the ligand *ns* and *np* orbitals. The broadening of the features in the higher energy region significantly suppresses the transitions from the ligand *ns* orbitals. This reduces the amount of information that can be extracted regarding the metal-ligand bond length and oxidation states.

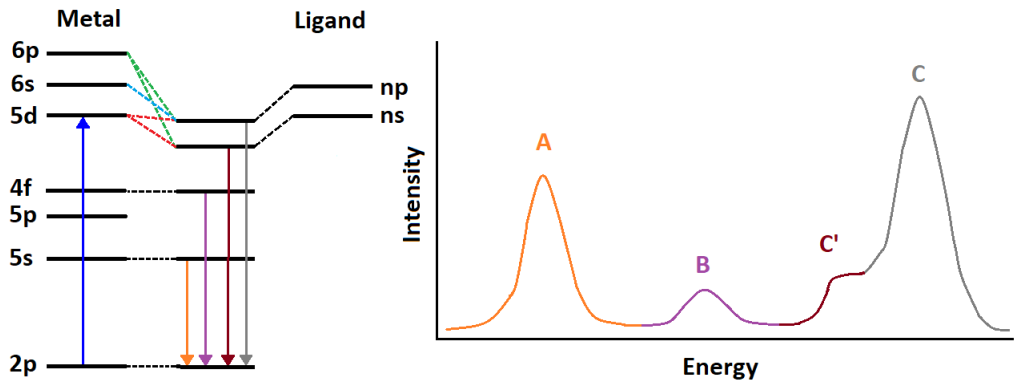

Figure 5.4.6: Suggested simplified molecular orbital diagram indicating the origins of the different features for Lβ vtc-emission. The HERFD-XANES transition is also indicated with a blue arrow.

5.5 Chapter summary

This chapter has covered the theory and interpretation of the valence-to-core XES technique. The data acquisition and normalization steps for the vtc-XES spectra have been outlined. For both the K- and L-edge emission lines, the different features and their origins have been identified. Additionally, FDMNES has been used to further understand the spectra and it has been shown to reproduce the features correctly. The results show how both K- and L-edge valence-to-core XES can provide information regarding the oxidation state, metal-ligand bond length and chemical environment surrounding the absorbing atom.

Chapter 6

$IrTe_2$: Study of the atomic and electronic role played by Ir species in the first order transition

---

The role of iridium (Ir) dimers and their electronic state in the 5d transition metal dichalcogenide (TMD) $IrTe_2$ with relation to the first order transition (FOT) has been debated with no consensus so far. Using polarization-dependent HERFD x-ray absorption spectroscopy, including measurements on the $L_1/L_2/L_3$ Ir edges, a detailed study of the electronic state and local structure around the Ir species across the FOT is presented. Robust evidence shows that Ir dimers are present above and below the transition and that there is no signature of an electronic change on this species. Furthermore an investigation into the nature of the system once the FOT is suppressed by Ir-site doping is carried out. The results indicate that above the superconducting phase the nature of the Ir species and dimers remains the same with respect to the pure system.

6.1 Introduction

5d transition-metal compounds have been intensely researched for many years as they can display a wide range of interesting phenomena. Due to large atomic numbers (Z) the spin-orbit coupling in these materials can be significant and along with electron-electron interactions, these systems often show multiple orbital degeneracy which when coupled to spin, charge and lattice degrees of freedom lead to intriguing electronic phases [200]. Unique quantum states can also be realised such as the $J_{eff} = 1/2$ Mott insulator Sr_2IrO_4 where spin and orbital degrees of freedom are strongly entangled [201] or topological insulators like Bi_2Se_3 and Bi_2Te_3 [202, 203]. Interestingly many systems also show a cascade of states when external conditions are applied such as temperature, chemical doping and pressure [19, 204, 205, 206].

Layered dichalcogenides that form CdI_2 structures have been shown to exhibit a diverse range of physical properties. Systems like 1T-TaS_2 [206] and 1T-$TiSe_2$ [204] show charge density waves (CDW) along with structural modulations. When the CDW are suppressed by applied pressure or chemical doping, superconductivity can emerge. Furthermore compounds with iridium have attracted interest, for example the metal-insulator transition in $CuIr_2S_4$ [207] and the frustrated magnetic state in Na_2IrO_4 [205].

$IrTe_2$ is a perfect example of the interplay between different degrees of freedom and how they create a complex range of phases, dependent of external parameters. At standard room temperature and pressure, $IrTe_2$ is in a $P\bar{3}m1$ symmetry as shown in figure 6.1.1, made of Ir and Te layers which form edge sharing $IrTe_6$ octahedra. In its formal state Ir is 3+ where the 5d electrons are arranged into t_{2g} orbitals. The tellurium is in a 1.5+ state where the 5p orbitals are suggested to be non-degenerate. At 300K the lattice parameters [208] are $a/b = 3.93$Å and $c = 5.39$Å, with a c/a ratio of 1.37, which is significantly less than similar dichalcogenides with values reported between 1.6-1.8 [209]. Rather than weak Van der Waals ($2R_{VdW} = 4.12$Å) bonding seen in other dichalcogenides, the layers in $IrTe_2$ are bonded by strong "Te-Te bonding" [210]. When cooling, $IrTe_2$ undergoes a first order transition at 280K (T_1), then a further transition at 180K (T_2), shown in figure 6.2.4 as two consecutive susceptibility drops. On heating the transition at 180K is not seen and the low temperature (LT) phase directly transits in to the high temperature (HT) phase at 280K. This result is consistent with resistivity measurements as shown in [19]. Below 280K there is a change to a lower P1 triclinic symmetry group which is accompanied with a lattice modulation with a wave vector $Q_{1/5} = (1/5, 0, 1/5)$ [13]. The physical consequence of this is the appearance of Ir-Ir ordered dimers along the a-axis, as shown with x-ray diffraction measurement [13, 14], with a small compression of the $IrTe_6$ octahedra. At 180K there is a further modulation of the ordered dimers in to a $Q_{1/8} = (1/8, 0, 1/8)$ state [14].

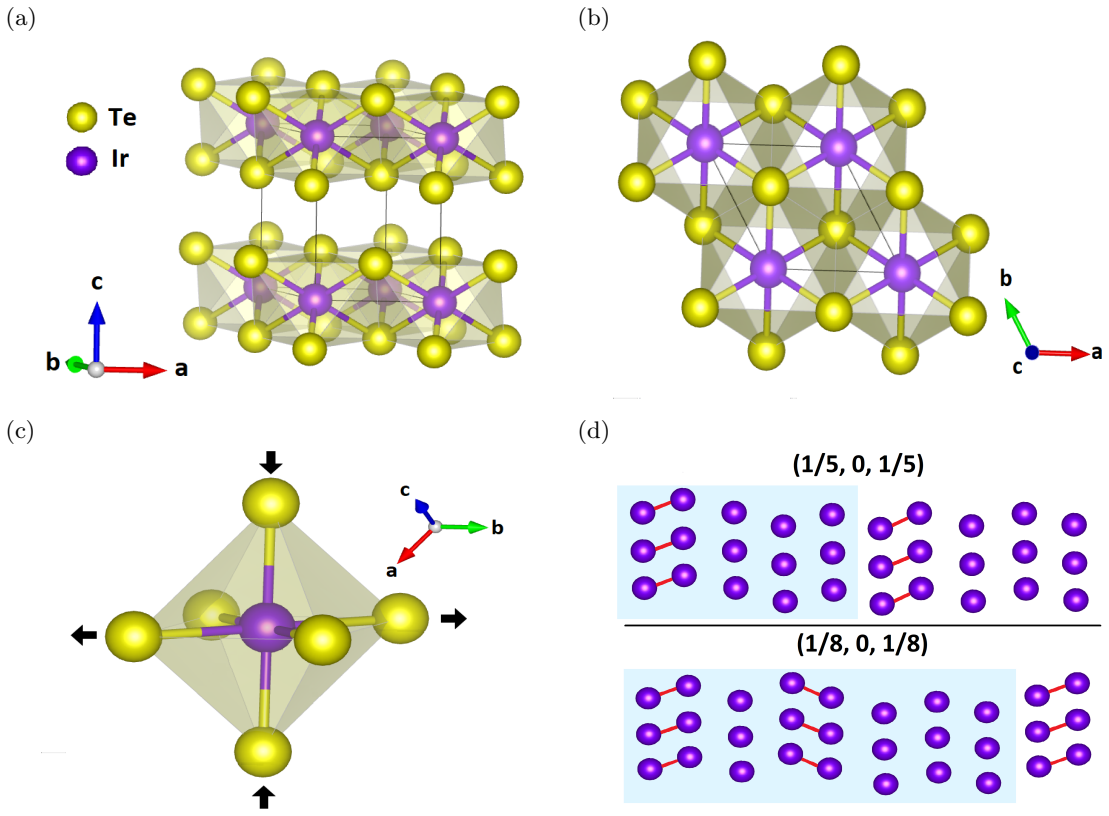

Figure 6.1.1: $IrTe_2$ crystal structure. a) Side view, b) Top view, c) $IrTe_6$ octahedra - arrows indicate the suggested compression direction, d) Top view - Dimer states $Q_{1/5}$, $Q_{1/8}$.

While the low temperature dimer structure is well characterized, the mechanism for the formation of the Ir-Ir dimers and the loss of metallic behaviour is still widely debated. Diffraction studies have determined that the high temperature phase does not contain Ir-Ir dimers [211, 212, 213], however *B. Joseph, et. al. 2013* [214] suggested this was not the case and dimers may be present above the transition. Given that many systems with t_{2g} orbital degeneracy display a range of intriguing electronic states which are accompanied by different types of dimerization [215] (stripe-type dimers, complicated octamer), understanding the specific role of the Ir-Ir dimers in $IrTe_2$ is critical. Similar to other chalcogenides, the initial conclusion from early experiments on this compound suggested a CDW type mechanism [13, 216] however this has been shown to be incompatible with many recent experiments. For example, the expected band gap opening for the mechanism has not been observed in angle-resolved photoemission spectroscopy (ARPES) [15] or in optical spectra [16], and the modulation in the structure is highly non-sinusoidal [17]. The formation of the Ir dimers has been suggested to cause a Ir^{3+}/Ir^{4+} charge ordering, where the dimers become more positively charged. This in turn results in the nearby Te atoms being pushed away causing a Jahn-Teller like distortion [16, 18]. While photoemission studies have shown a split of the Ir-4f spectrum below the transition attributed to the formation of the Ir^{4+} state [19], further studies have not produced consistent results with respect to the final state of Ir [17, 18, 20, 213]. Furthermore, due to a strong hybridization between the Ir 5d and Te 5p orbitals it has been shown that the nominal ionic models may not be appropriate for this system [217]. This has also lead to debates suggesting that the Te species plays a significant role in the transition, including a Van Hove singularity at the Fermi level (E_F) related to the Te orbital ($p_x + p_y$) [218]. It has also been proposed that the in-plane intralayer Te-Te bond formation and interlayer depolymerization play a critical role in the formation of the Ir dimers [16, 17, 219]. This however has been ruled out by chemical bond analysis [220] which has shown that dimers are favoured in isolated layers.

Interest in this compound in recent years has been motivated by the discovery that both intercalation (M_yIrTe_2) and Ir-site doping ($Ir_{1-x}M_xTe_2$) with M = Pt (similar effects when doped with Pd) results in low temperature superconductivity [13, 20]. As the level of dopant is increased the first order transition at 280K is suppressed and eventually completely lost at the point where the SC temperature is at its highest (3.2K), this is shown in figure 6.1.2. Upon Ir-site doping the lattice parameters undergo a small linear change where the a-axis increases and the c-axis decreases (at x=0.05: a=3.936Å, c=5.386Å) [221] causing the c/a ratio to slightly decrease. In the case of doping with Pt, an additional electron leads to a slight electron doping on the Ir and Te sites [222].

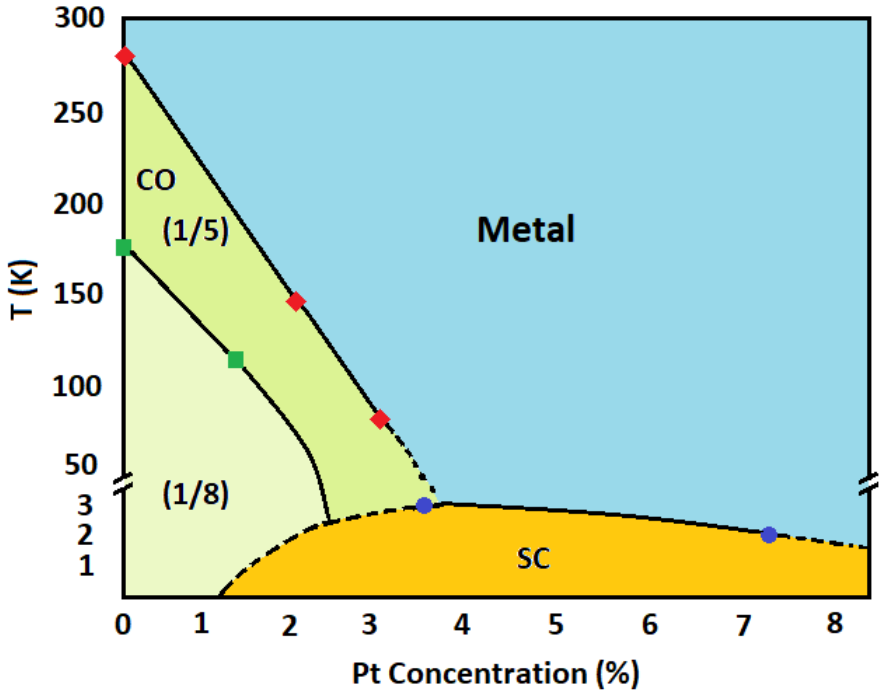

Figure 6.1.2: $Ir_{1-x}Pt_xTe_2$ phase diagram. Red diamonds - first order transition, green squares - second transition, purple circle - SC phase transition. Combination from 2 sources [13, 223]

The full nature of the superconductivity phase has not so far been determined. The experimentally determined gap size, vortex states, coherence length and band structures suggests a fully gapped weak-coupling BCS *s*-wave like state [224, 225]. However the driving force for the formation of this state is still in question. While the SC phase is not the focus of the research presented in the chapter, determining the state of the system before this phase is important in understanding why a SC phase can emerge. It has been proposed that upon doping, the Ir-Ir dimers are absent in the structure [21] and therefore can not be involved in the SC phase. However the reason for the lack of a dimerized state is still unclear and the consideration of an dimer/SC entanglement is an intriguing topic.

The research presented here can be divided into two sections. Firstly, it aims to provide further evidence regarding the formation of the Ir dimers and importantly to understand how the electronic structure of the Ir species may change across the transitions at 280K and 180K. Secondly to investigate how the Ir-site doping with Pt affects the atomic and electronic structures and whether this differs from the pure compound. Using polarization-dependent HERFD-XAS measurements along with DFT simulations, evidence is given to show that Ir dimers are present above and below the transitions in both the pure and doped systems. Analysis of the electronic structure indicates that the Ir species does not undergo an oxidation state change. Furthermore these results are discussed in relation to a scenario in which the Te (5p orbitals) are the dominant species that drives the transition [16].

6.2 Sample preparation and characterization

To track the structural modulations across different crystallographic planes, single crystal samples of suitable size (at least $1mm^2$) have been grown by Dr R.Perry (University College London, ISIS Pulsed Neutron and Muon Source), using a self-flux method. High purity (99.9%) Ir (Pt) powder and Te pieces, washed in ethanol, were mixed together in an atomic ratio of 0.18:0.82 respectively. The mixture was then placed in to a Al_3O_3 crucible and sealed with a SiO_2 plug, flushed with argon. Literature shows that the second transition at T_2 is sensitive to the crystal quality and the cooling rate of the growth method, where this transition is not observed in batches which have been fast cooled [13]. For this reason multiple batches have been grown with varying cooling procedures to prepare samples with both transitions and of a suitable size. The most successful growths occur when the mixture is heated to 1180^oC for 6hrs, then cooled to 920^oC at a rate of 0.75^oC/hr and finally cooled to room temperature at a rate of 20^oC/hr. The resultant mixture was then extracted from the crucible and washed in a dilute HCl + HNO_3 to partially dissolve the Te flux. This was then dried and suitable size crystals were extracted and characterized.

6.2.1 Characterization measurements (SEM/EDX, SQUID)

To ensure that suitable samples were used during the experiments, characterization measurements have been carried out. SEM images and EDX measurements have been taken to ensure that the samples were single crystals with the correct composition. The methods used for the characterization are detailed in section 3.4. These measurements have been carried out at the University of Kent. Figures 6.2.1- 6.2.3 shows the SEM/EDX results for samples used in the experiments when $x = 0$, 0.02 and 0.05. In all 3 cases the SEM images show a flat homogeneous sample surface, indicated by the consist contrast across the images. The parent compound shows a change in contrast between different sections. It was shown that this is a result of a thin layer of oil on the surface left from the extraction process, however this is not expected to affect the spectroscopy results. The $x = 0.05$ sample shows small cracks in the surface, however due to the relative size between the beam and sample, this again should not have a large impact on the results.

The EDX measurements indicate that all compounds show the correct molecular weighting of the Ir to Te species suggesting a successful growth, with no measurable contaminants. The doped compounds show the presence of the Pt element. However due to limitations of the technique, it is difficult to extract an accurate value for the molecular weighting, especially since the Ir and Pt emission lines are close in energy. Still, it was possible to determine that the $x = 0.02$ samples contained less Pt than the $x = 0.05$, sample therefore providing confidence that transition temperature would be different in these samples.

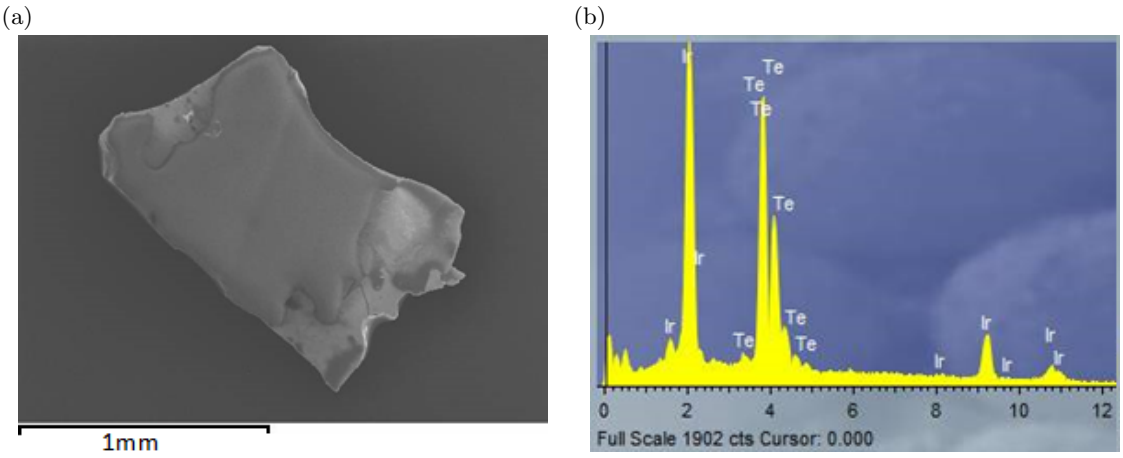

Figure 6.2.1: a) SEM images and b) EDX measurements on $IrTe_2$.

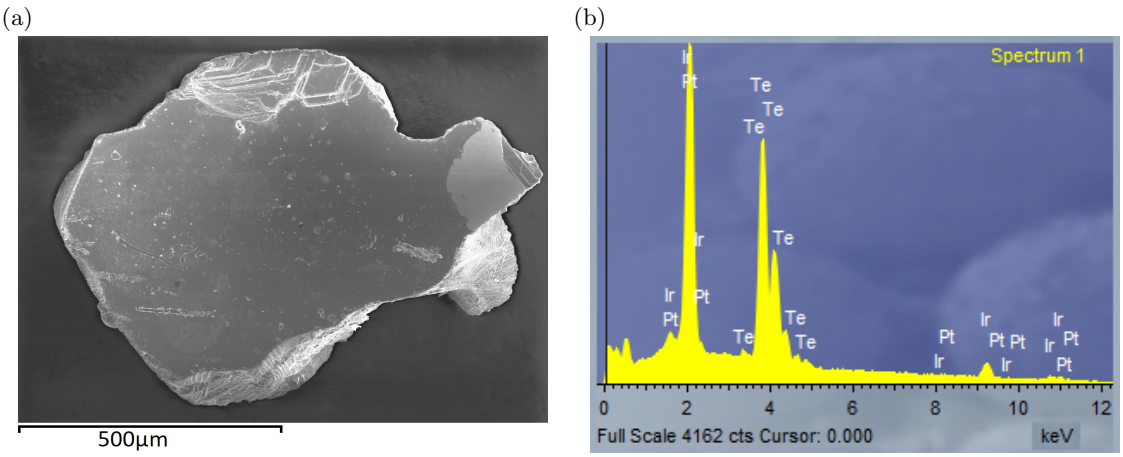

Figure 6.2.2: a) SEM images and b) EDX measurements on $Ir_{1-x}Pt_xTe_2$ ($x = 0.02$).

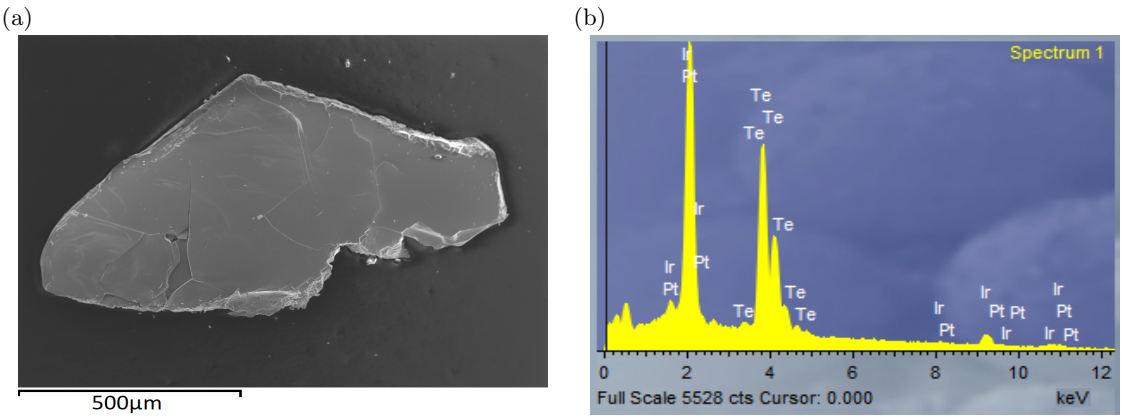

Figure 6.2.3: a) SEM images and b) EDX measurements on $Ir_{1-x}Pt_xTe_2$ ($x = 0.05$).

To check the presence and temperature of both transitions in the parent compound, magnetic susceptibility measurements have been carried out. The measurements have been carried out at the ISIS Neutron and Muon Source characterization lab, with the assistance of Dr G. Stenning. The results for the susceptibility measurements are shown in figure 6.2.4. Both transitions are present at the correct temperatures when the sample is cooled. On heating only the transition at 280K is seen. Due to a calibration issue with the SQUID used for these measurements, the absolute values of the susceptibility were incorrect, where some showed negative values. While this makes it difficult to compare to the literatue, the aim of these measurements were to identify the temperature of the transitions, hence still provide valuable information. It should be noted that while it would also be appropriate to perform resistivity measurements, due to the size of the crystals obtained and that crystals from the same growth batch may show different results, resistivity measurements would not be practical as larger crystals would be needed.

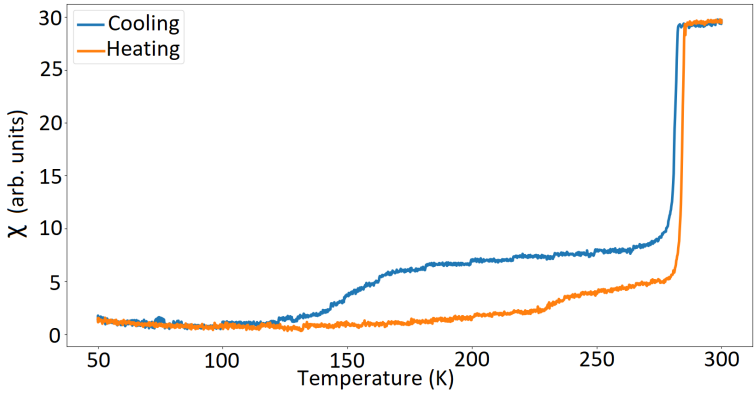

Figure 6.2.4: Magnetic susceptibility results for $IrTe_2$

6.3 Experimental set up

Due to the very subtle nature of the expected changes across the transitions in this compound a comprehensive set of experiments has been carried out. The aim of the XAS experiments is two fold: firstly to track any structural changes across the transitions focusing on the Ir-Ir paths and secondly to investigate the Ir electronic structure. All measurements presented here have been carried out at the I20 (scanning) beamline, Diamond Light source (U.K.), details of the beamline are given in section 3.2.3.

6.3.1 Sample environment and geometry

For these experiments two cryogenic sample environments have been used. Initially a nitrogen cooled Linkam stage with a temperature range of 600K-78K, was utilised for the XAS L_1 and HERFD-XAS L_3 measurements, shown in figure 6.3.1(a). Due to the long time duration of these experiments and low temperatures required, it was necessary for dry nitrogen gas to be flowed over the stage window to prevent ice build-up. It should also be noted that due to the sample being set back from the front of the stage the L_3 measurements where restricted in the angular range (approximately 120°). The

remaining experiments used a closed-cycle He cryostat (Stinger), with an operational range between 300K-5K and angular range of approximately 150^o, specifically built for polarization dependent measurements utilising the XES spectrometer, shown in figure 6.3.1(b). This allowed measurements to be carried out without such strong restrictions in angular range and at lower temperatures, as specifically needed for doped compounds .

To be able to carry out polarization dependent measurements and analysis, the samples used were cleaved between the Ir layers. This allowed them to be fixed with the c-axis parallel with the direction of the beam, as shown in figure 6.3.1(c), with the ab-plane in an unknown orientation. The samples where then rotated between the c-axis and ab-plane to build measurements along different crystallographic planes. For all data sets in this section, 0^o refers to the beam polarization being parallel with the ab-plane, where 90^o indicates the beam polarization being parallel with c-axis.

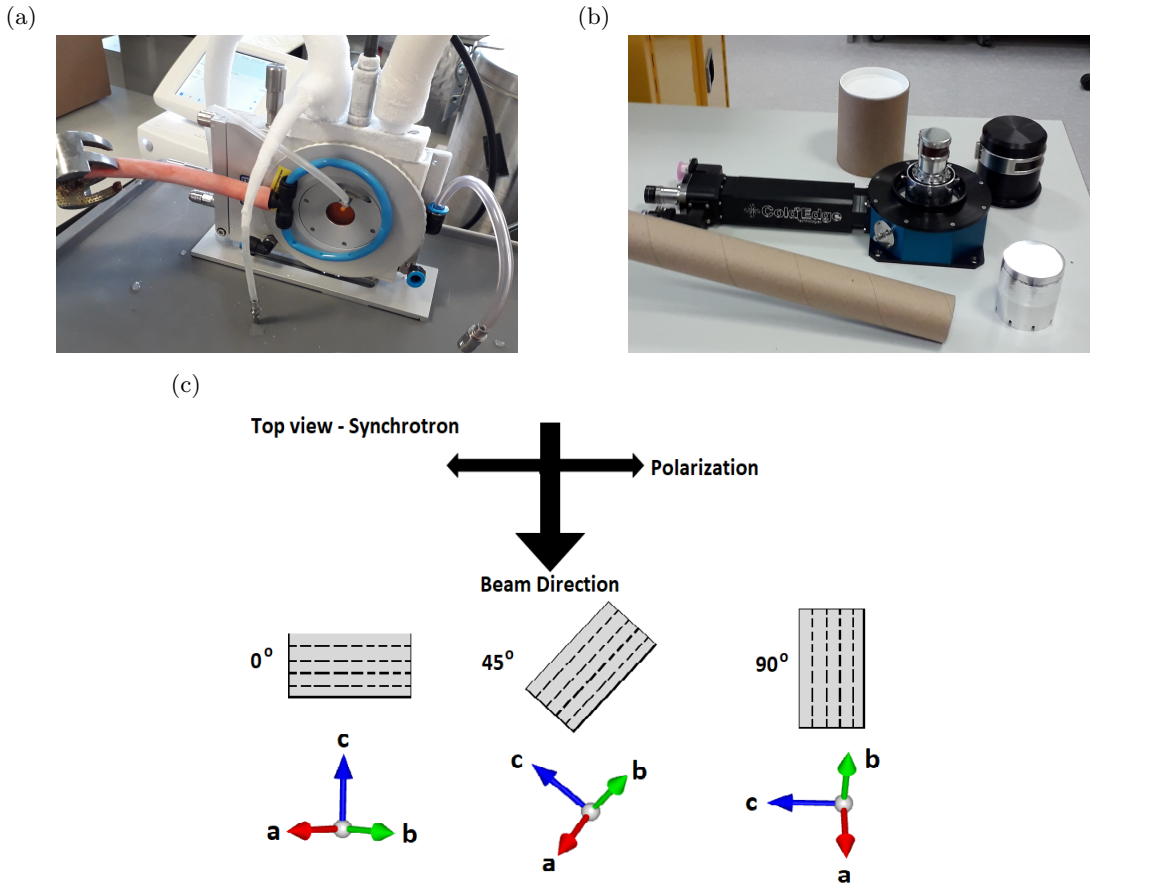

Figure 6.3.1: $Ir_{1-x}Pt_xTe_2$ sample environments and alignment. a) Linkam stage b) Stinger stage c) sample alignment, top view - dash line indicate Ir layers.

6.3.2 Measurements

Conventional XAS, HERFD-XAS and vtc-XES measurements have been used to collect a wide range of data for this investigation. These measurements were carried out in fluorescence mode on single crystal samples and the full details of these techniques are given in chapter 3. For each of the experiments, the following co-workers assisted with the running of the beamlines and collecting data: Dr Silvia Ramos (University of Kent), Dr Shusaku Hayama (Diamond light source) and Dr Sofia Diaz-Moreno (Diamond light source). Table 6.3.1 shows the scan parameters for each set of measurements and further details and justification for each measurement is given below.

	Pre-edge		**Edge**		**Post-edge**	
	Step (eV)	**Time (s)**	**Step (eV)**	**Time (s)**	**Step (eV)**	**Time (s)**
XAS - L_1	5	1	0.4	2	1-5	2-6
HERFD - L_2 ($L\beta_1$)	5	1	0.3	3	0.5-5	1
HERFD - L_3 ($L\alpha_1$)	5	1	0.4	2	1-5	2-6
HERFD - L_3 ($L\beta_5$)	5	1	0.3	6	2-4	3
VTC* - L_3	-	-	0.5	10	-	-

Table 6.3.1: Scan parameters for $Ir_{1-x}Pt_xTe_2$ absorption spectroscopy measurements. * Note that while the term "edge" does not apply to the VTC, for simplicity it has been included in this table.

Conventional x-ray absorption spectroscopy (XAS) in fluorescence mode has been carried out on $IrTe_2$ samples. The Ir L_1 (13.419keV) edge was recorded with the fluorescence window over a range of 12.72keV - 13.10keV ($L\gamma_2$ and $L\gamma_3$ emission lines). These measurements probe the s to p transitions. If there is a strong angular dependence in the XANES region, these measurements have the advantage that the p-orbital symmetry is simpler to analyse than the d-orbitals measured later. The aim of this is to track the Ir electronic structure across the transitions while understanding if certain orbital directions are involved in the change of properties. Using the Linkam stage and a 64-element germanium detector, measurements were taken at 4 angles (15^o, 30^o, 60^o, 75^o) and 4 temperatures (300K, 230K, 150K, 100K). These measurements were repeated 3 times under the same conditions to improve the statistics of the data.

Polarization-dependent HERFD-XAS measurements have been carried out on the L_2 and L_3 Ir edges, probing the 5d unoccupied states. Using the XES spectrometer, specific emission lines can be selected giving the advantage of reducing the core-hole lifetime broadening effects which can greatly enhance the sensitivity within the XANES region. Ir L_2 (12.824keV) HERFD-XAS data has been collected using the $L\beta_1$ (10.708keV) emission line. This emission line measures the $3d_{3/2}$ - $2p_{1/2}$ transitions. Using the Stinger cryostat $IrTe_2$ samples were measured at 4 angles (15^o, 30^o, 60^o, 75^o) and a range of temperatures (300K, 290K, 280K, 270K, 250K, 200K, 180K, 160K, 150K). If Ir^{4+} is formed, it is expected that the $J_{eff} = 1/2$ state will change from full to half-filled and this is best probed by the L_2-edge. This data set, along with the L_3 measurements also allows the branching ratio to be investigated giving further information on the state of the Ir species across the transitions. Ir L_3 (11.215keV) HERFD-XAS measurements have been performed using the $L\alpha_1$ (9.175keV) emission line which measures the $3d_{5/2,3/2}$ to $2p_{3/2}$ transitions. Using the Linkam cryostat $IrTe_2$ samples have been measured at 4 angles (15^o, 30^o, 60^o, 70^o). The following temperatures have been measured: $x = 0$: 320K, 310K, 300K, 290K, 280K, 270K, 250K, 225K, 200K, 190K, 180K, 170K, 160K, 150K.

The $Ir_{1-x}Pt_xTe_2$ ($x = 0.02, 0.05$) samples have been measured at 4 angles (15^o, 30^o, 60^o, 75^o) using the Stinger cryostat. The temperature at which the transitions should occur in each sample is expected to be different, so the following temperatures were measured to track any changes. $x = 0.02$: 300K, 250K, 200K, 100K, 55K. $x = 0.05$: 300K, 250K, 200K, 55K. To ensure good statistics each data set was repeated twice under the same conditions.

The changes across the transitions could be very subtle, depending on which scenario is realised. To be able to rule out the possibility that these measurements did not have the sensitivity required to detect these changes, HERFD-XAS Ir L_3 (11.215keV) data was collected using the $L\beta_5$ emission line. While these measurements are considerably more challenging due to the relative strength of this emission line being approximately two orders of magnitude weaker than the $L\alpha_1$, it has the advantage that it probes the 5d orbitals directly, giving greater sensitivity to changes in the energy levels. The 5d hole has a smaller core-hole lifetime than the 3d hole, hence the spectral resolution of the XANES will be further enhanced. Data was taken using the Stinger cryostat sample environment; 4 angles (15^o, 30^o, 60^o, 75^o) have been measured at the following temperatures: 300K, 270K, 190K, 160K and 120K. Due to the weak signal of this emission line, 5 repeats have been taken under each condition.

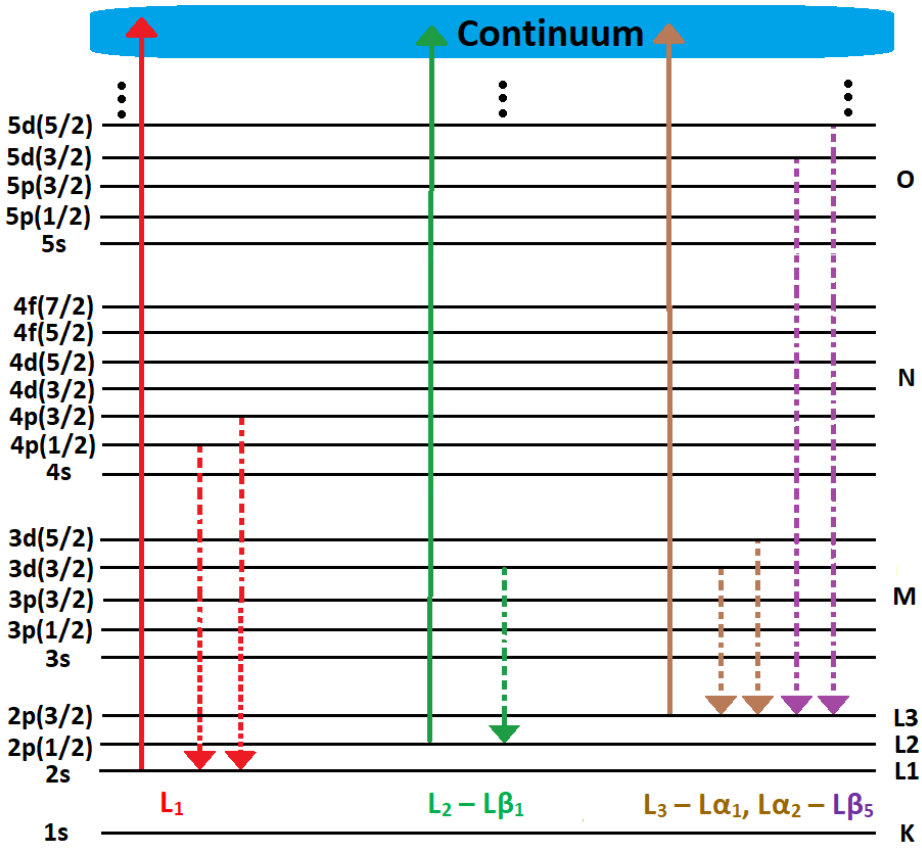

Figure 6.3.2: Electronic transitions considered for $Ir_{1-x}Pt_xTe_2$ measurements. Dashed line indicate fluorescence and solid line indicate absorption.

Valence-to-core XES measurements have been carried out just below the Fermi energy using the L_3 absorption edge using the Lβ emission lines. These measurements not only probe the occupied valence bands of the Ir species but, due to hybridization, also probe the Te 5s/5p orbitals. This technique should be sensitive to an oxidation state change in the Ir and will give information regarding the Ir-Te orbital interactions. The incident x-ray energy was set at 11350eV while the analysing crystals sweep the emission energies over approximately 100eV just below the Fermi energy. Measurements were taken at the same angles and temperatures as the Lβ_5. Due to the absence of publications regarding this emission line, in addition to the Ir reference samples a range of well known tungsten samples have also been measured and detailed results are given in section 5.1. This allows for a further understanding of the features observed in the Ir spectra and how certain changes affect the relative position and intensity of the related features.

6.4 Data analysis and Results

The full analysis of the experiments carried out on $Ir_{1-x}Pt_xTe_2$ ($x = 0, 0.02, 0.05$) single crystals has been separated into the XANES and EXAFS regions. In all cases measurements have been taken above and below the first order transition, with measurements also carried out over the second transition when observed. For each data set a self-absorption correction has been applied, with the parameters for each edge shown in table 6.4.1. A correction has not been applied to the L_1-edge measurements, where significant distortion near the edge made a correction unreliable. Without the correction, comparison between angles becomes unreliable for this edge, especially when identify changes in the intensities of the features.

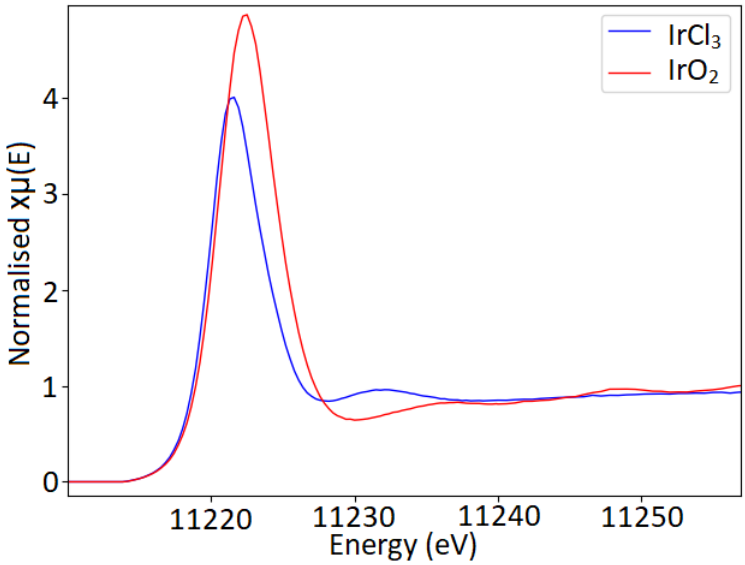

Figure 6.4.1: Ir L_3 ($L\beta_5$) reference sample measurements, carried out at 300K, 45^o on $IrCl_3$ and IrO_2

	$\mu_{tot}(E_f)$	$\mu_b(E)$	$\mu_0(E_{ae})$	$\mu_0(E_{be})$
$L_2(L\beta_1)$ $x = 0.0$	3708.66	886.54	3701.82	2983.16
$L_3(L\alpha_1)$ $x = 0.0$	5539.85	1170.86	3545.92	1825.16
$L_3(L\beta_5)$ $x = 0.0$	3597.85	1244.89	3720.28	1828.16
$L_3(L\alpha_1)$ $x = 0.02$	5517.60	1187.67	3474.99	1791.60
$L_3(L\alpha_1)$ $x = 0.05$	5479.72	1212.89	3368.61	1736.75

Table 6.4.1: Self-absorption correction parameters for $Ir_{1-x}Pt_xTe_2$ for all edges. All values in cm^{-1}.

The data processing methods used for these results are described in section 4. A pre-edge subtraction, post-edge normalization and background subtraction have been applied to all data sets, with the ranges used shown in table 6.4.2. Further information specific to the XANES and EXAFS regions are given in the relevant sections. To be sure that the position of each edge is a true value each data set has been calibrated to Ir reference samples. Figure 6.4.1 shows an example of the references taken on the L_3-edge of IrO_2 and $IrCl_3$. The differences in edge position and intensity of the white lines for the reference samples suggest that if Ir does undergo even a partial oxidation state change across the transition this should be visible in the XANES.

	E0 (eV)	**Pre-edge (eV)**		**Post-edge (eV)**		**Rbkg (Å)**
		Min	Max	Min	Max	
L_1 $x = 0.0$	13422.6±0.5	-150.0	-45.0	123.1	547.49	1.5
$L_2(L\beta_1)$ $x = 0.0$	12824.3±0.4	-119.3	-45.0	150.0	375.7	1.6
$L_3(L\alpha_1)$ $x = 0.0$	11219.7±0.5	-150.0	-30.0	150.0	1080.4	1.5
$L_3(L\beta_5)$ $x = 0.0$	11219.6±0.9	-114.2	-30.0	150.0	274.1	1.5
$L_3(L\alpha_1)$ $x = 0.02$	11219.9±0.5	-114.8	-30.0	150.0	880.2	1.6
$L_3(L\alpha_1)$ $x = 0.05$	11219.9±0.5	-114.8	-30.0	150.0	880.2	1.6

Table 6.4.2: Data processing parameters for $Ir_{1-x}Pt_xTe_2$. Pre-edge and post-edge values relative to E_0.

6.4.1 XANES

$IrTe_2$ - Parent compound

Figure 6.4.2 shows the L_1 spectra and first derivative for $IrTe_2$ sample between 300K - 100K at the 2 most extreme angles measured. The E_0 position has been determined from the first derivative, as the energy of the first peak, marked by the dashed line. At 13422.6±0.5eV the edge position is consistent across all data sets and when compared to the reference $IrCl_3$ edge position at 13422.1eV, it suggests Ir is in a +3 state. The angular dependence of the measurements should reflect the p orbital symmetry, but the analysis does not explore this aspect of the data. There are small differences between the angles, for example at 13.45keV there is an additional shoulder in the 75^o data. However there are no changes in any of the features across the transitions. It should be noted that there is a suppression of the edge intensity in the 15^o data. It was shown after the measurements were taken that there was significant shadowing of the detector at this orientation. This made it very difficult to normalize the data in the XANES region in a consistent way.

The L_2 XANES spectra for the $IrTe_2$ sample is shown in figure 6.4.3, along side the first derivative. The data is shown for both the 15^o and 75^o angles across both transitions. The edge position is again stable across all measurements at 12824.3±0.4eV and is consistent with the $IrCl_3$ reference at 12824.89eV. There is a small increase in the first peak intensity which is angular dependent. For example at 300K the intensity is approximately 3.42 (arb. units) for 15^o, after the first transition it increases to 3.51 (arb. units) and after the second transition it reaches 3.56 (arb. units), however at 75^o no consistent change is seen. The magnitude of this increase, along with no peak shift, is not consistent with an oxidation state change on the Ir species. However is it also unlikely that this is simply a thermal effect. Given that the intensity increase is more significant at the angles closest to the ab-plane, this could be an effect from the ordering of the Ir-Ir dimers below the transition. After the edge there are two changes at approximately 12.836keV and 12.855keV, where across the first transition the features decrease in intensity. These changes will be discussed in a later section (6.4.4) as DTF simulations are required to understand how they relate to changes in the electronic and atomic structures. It will be shown that these changes are potentially related to the change in the Te octahedra structure.

Two sets of measurements have been carried out on the L_3-edge. Initially the spectrometer was aligned to the $L\alpha_1$ emission line with results shown in figure 6.4.4, where a Pb foil was used for calibrating the monochromator. To eliminate the possibility that the Ir species undergoes very subtle changes, the $L\beta_5$ emission line has also been measured and results are shown in figure 6.4.5. The $L\beta_5$ emission line has the advantage that it probes the 5d orbitals directly, giving greater sensitivity to changes in the energy levels. Additionally, the 5d hole has a smaller core-hole lifetime than the 3d hole, hence the spectral resolution of the XANES will be further enhanced. All measurements show a consistent edge position at 11219.7±0.5eV for $L\alpha_1$ and at 11219.6±0.9eV for $L\beta_5$. This is consistent with the $IrCl_3$ edge position at 11220.39eV. The larger error associated with the $L\beta_5$ E_0 position is a reflection of the fact that this emission line is approximately two orders of magnitude less intense that the α line. There is no pre-edge feature in the L_3 data and the post-edge structure shows the same changes across the transition as the L_2 data. The first peak intensity change is consistent for the $L\alpha_1$ emission line when compared to the L_2-edge data, however no consistent change is seen in the $L\beta_5$. The reason that the change is not consistent is most likely due to the less intense signal from this emission line making the measurements more difficult. The L_3-edge measurements clearly show no obvious change in the valence state of Ir across the transitions.

(a)

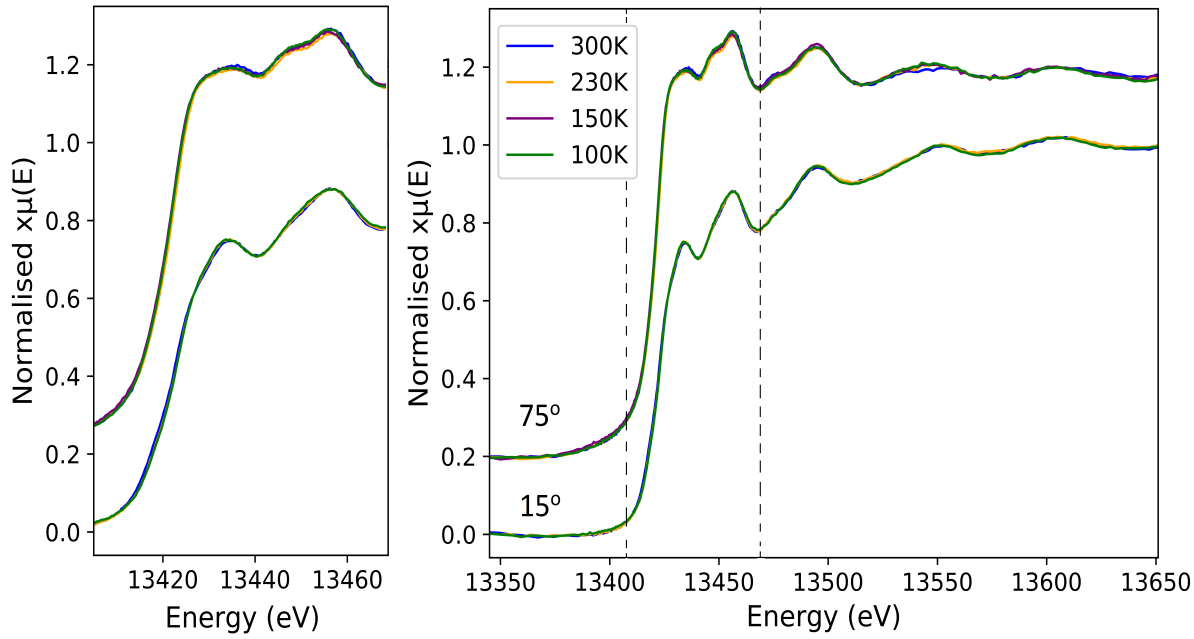

(b)

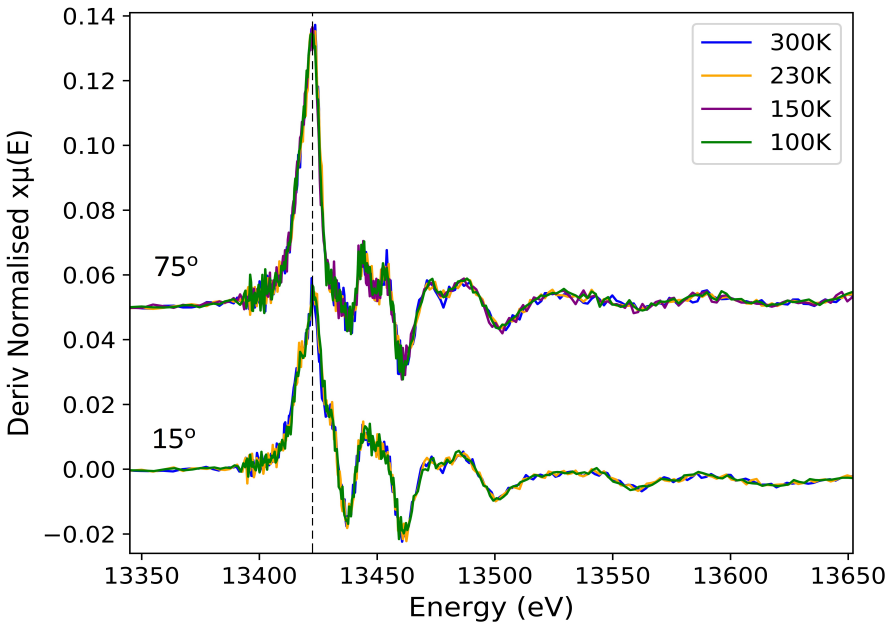

Figure 6.4.2: XANES: a) normalized spectra and b) normalized first derivative for the Ir L_1 fluorescence on $IrTe_2$ samples. Data is shown for 15^o and 75^o angle, across both transitions.

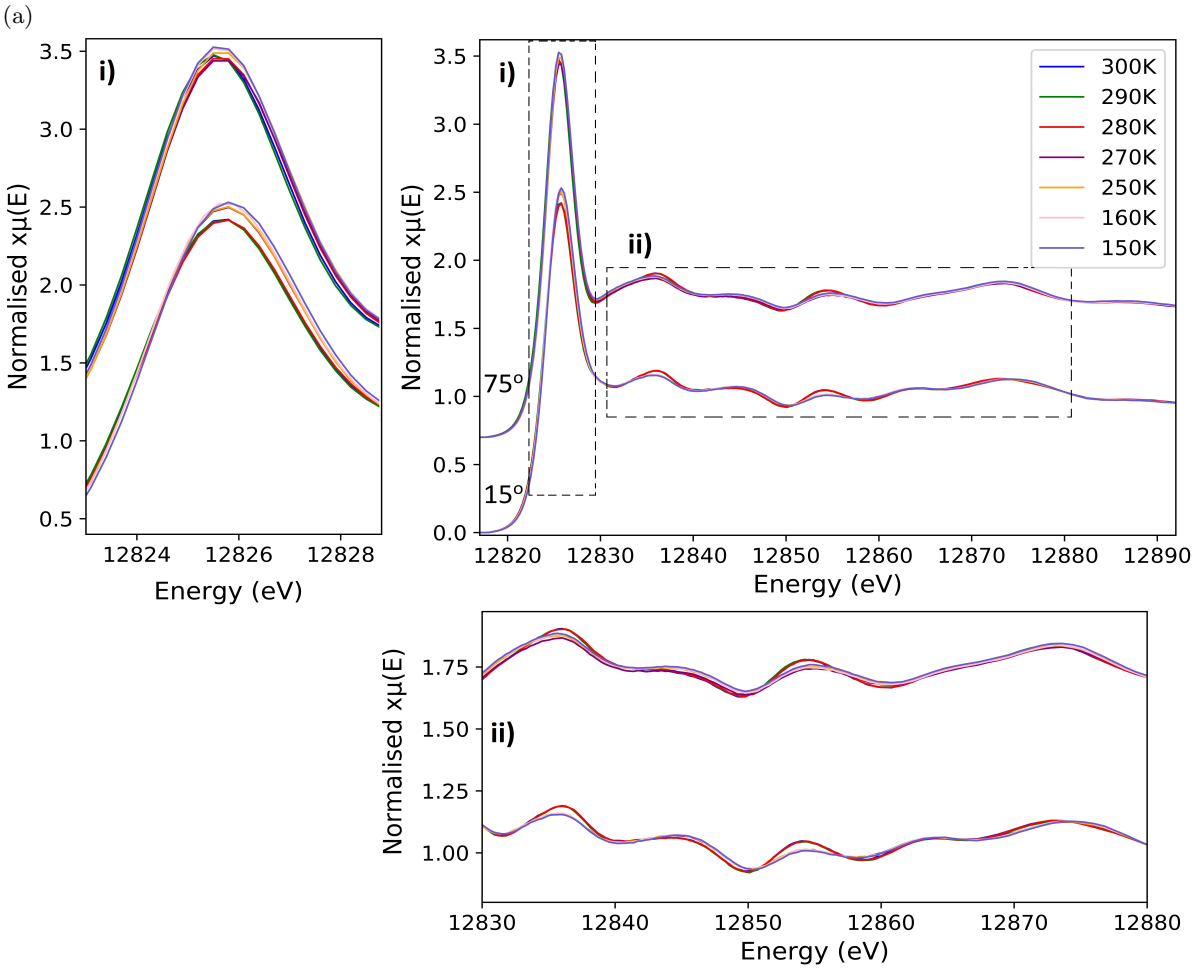

Figure 6.4.3: XANES: a) normalized spectra and b) normalized first derivative for the Ir L_2 ($L\beta_1$) fluorescence on $IrTe_2$ samples. Data is shown for 15^o and 75^o angle, across both transitions.

(a)

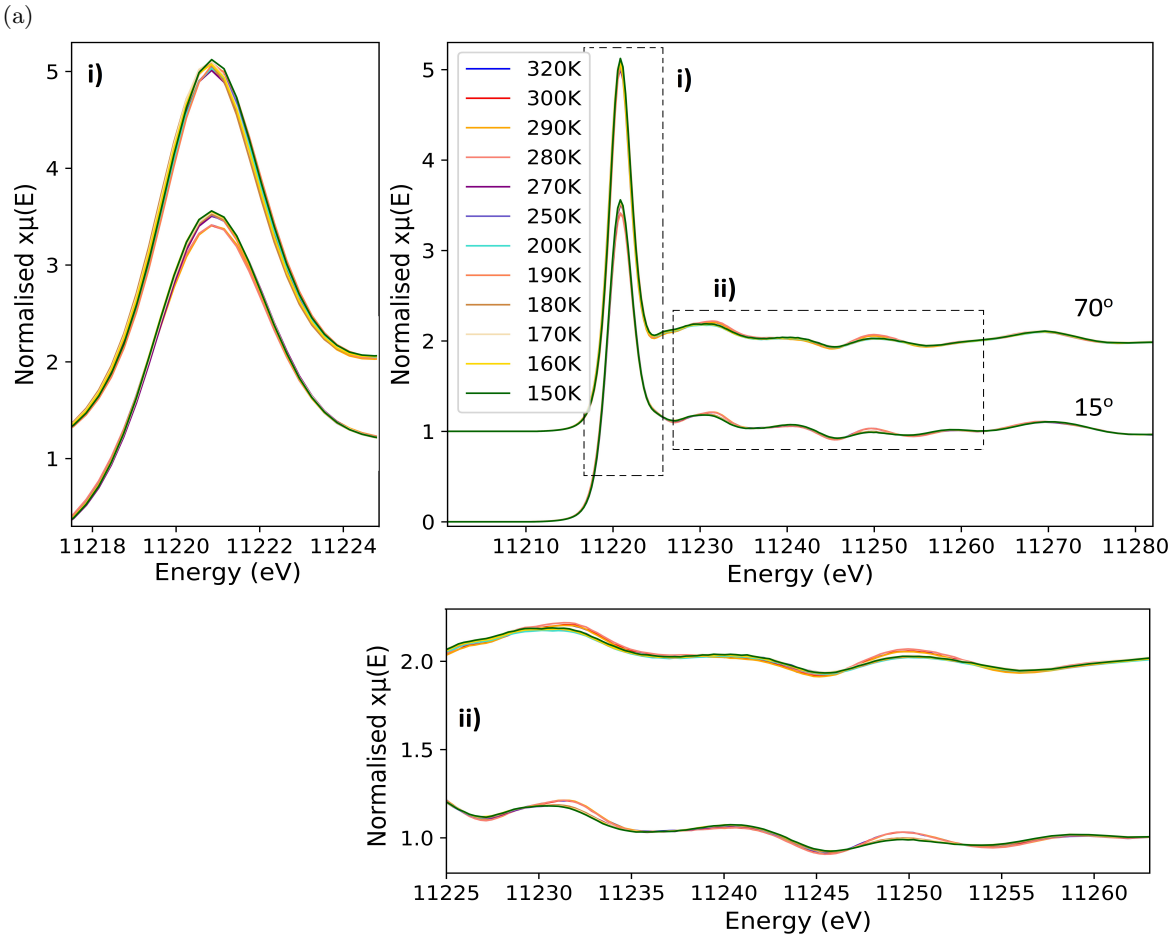

(b)

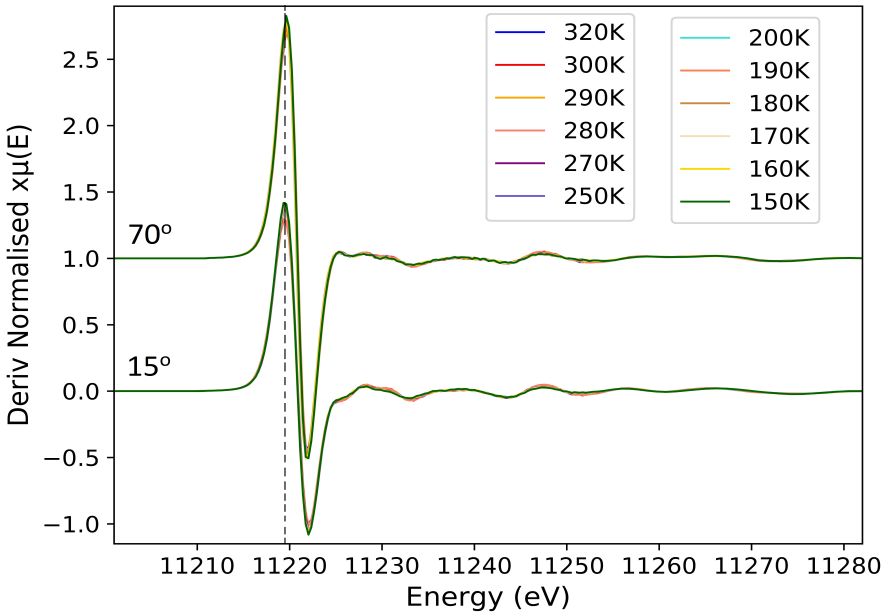

Figure 6.4.4: XANES: a) normalized spectra and b) normalized first derivative for the Ir L_3 ($L\alpha_1$) fluorescence on $IrTe_2$ samples. Data is shown for 15^o and 70^o angle, across both transitions.

(a)

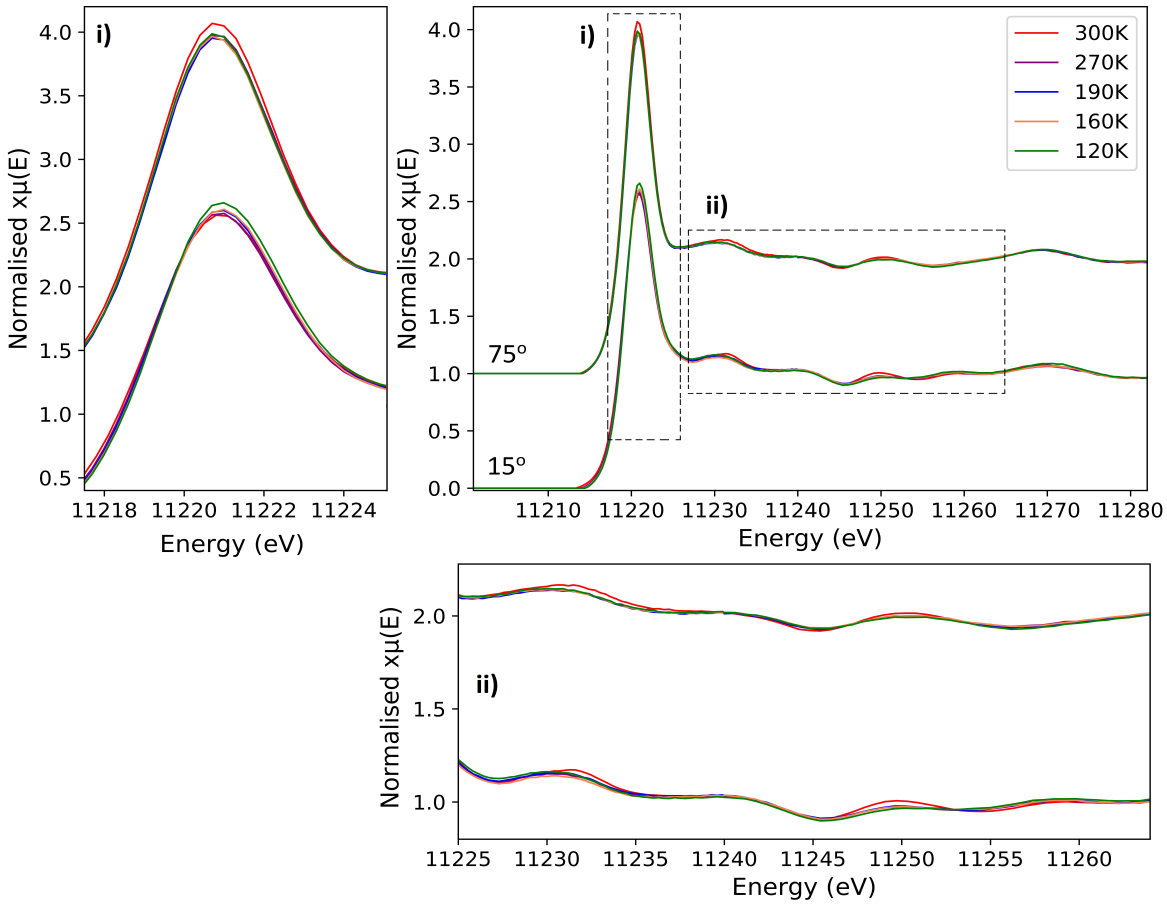

(b)

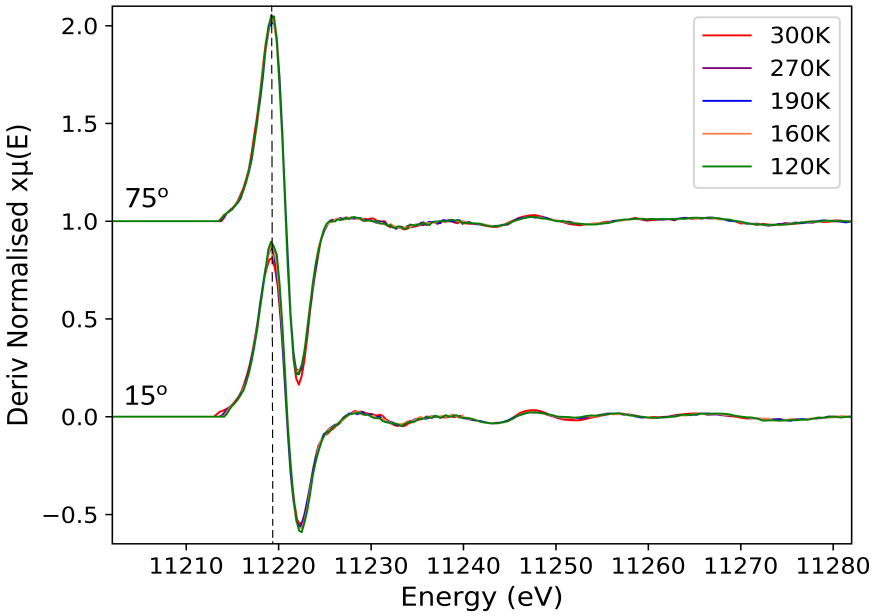

Figure 6.4.5: XANES: a) normalized spectra and b) normalized first derivative for the Ir L_3 ($L\beta_5$) fluorescence on $IrTe_2$ samples. Data is shown for 15^o and 75^o angle, across both transitions.

Branching ratio (BR)

The strong spin-orbit coupling in the system, along with a suggested redistribution of charge across the transition makes analysis of the branching ratio a suitable method to understand if the Ir ion undergoes any change. Nominally, in a simple atomic picture the BR can be used to assess the spin state and spin-orbit splitting in transition metal compounds. This becomes complicated for 5d transition metal systems with large spin-orbit coupling (SOC), which deviates from the expected 2:1 ratio. However, it has been shown in the literature [226] that as long as the SOC and crystal field is present in the initial and final states, then comparing the BR can reveal if changes occur. Further details on the theory of the BR and the method for extracting the data are given in section 4.4. Figure 6.4.6 shows the results for the $L_3(L\alpha_1)/L_2(L\beta_1)$ ratios for comparable angles, with suitable error bars shown related to the error in fitting the standard Gaussian. Note that the values here are the normalized BR's, the non-normalized values are give in brackets. The average value obtained for $IrTe_2$ is 0.729±0.01 (2.74) and no significant changes are seen across either transition or angles. As noted in section 4.4, comparing BR ratios from literature can prove difficult due to different techniques used and a lack of data regarding the effect caused by the bonding atom. A study of the BR in Ir compounds [227] found values of 3.6, 7.1 and 6.9 for Ir, $IrCl_3$ and IrO_2 respectively. The BR calculated for $IrCl_3$ and IrO_2 for this research are approximately 0.718 (2.47) and 0.686 (2.19) respectively. The most likely cause for the large discrepancy is due to these measurements being taken using HERFD. However without more data it is difficult to come to any conclusions. The edge position calculated from the XANES analysis suggests the Ir is in a +3 state. However the BR value for $IrTe_2$ is slightly larger than the +3 reference. This may be a result of the Ir being bonded to a heavy element with its own spin-orbit affecting the Ir BR.

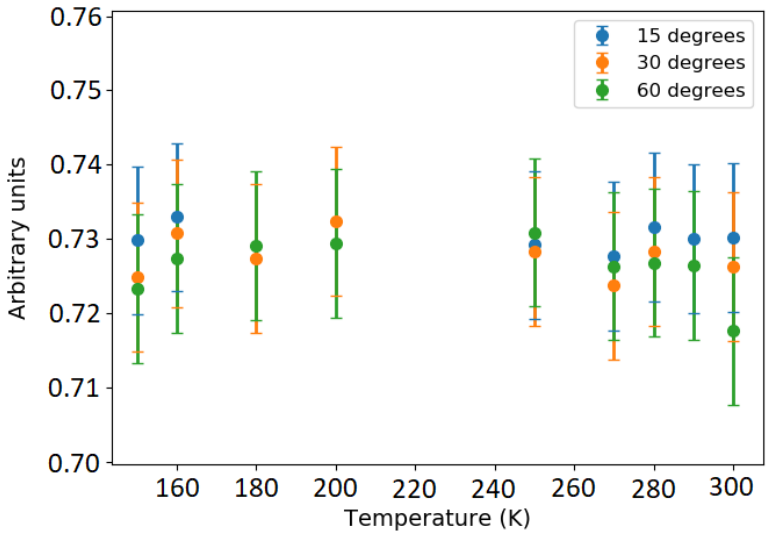

Figure 6.4.6: L_3/L_2 normalized branching ratio's for $IrTe_2$ across 3 angles.

$Ir_{1-x}Pt_xTe_2$, $x = 0.02$, 0.05

Figures 6.4.7 and 6.4.8 show the L_3 ($L\alpha_1$) XANES spectra and first derivative for both $Ir_{1-x}Pt_xTe_2$, $x = 0.02$, 0.05 between 300K - 55K, at the two most extreme angles measured. In the case of $x = 0.02$, the FOT is expected at approximately 140K, where as in $x = 0.05$ the transition is fully suppressed. In both cases the E_0 position calculated from the first derivative is stable across measurements at 11219.9±0.5eV. The $IrCl_3$ reference E_0 position is 11220.39eV, suggesting that in the doped system the Ir species remains close to a +3 state. There are no differences between the doped spectra when compared to the pure system except for the temperature of the transition. The $x = 0.02$ systems shows no pre-edge features and similar small intensity changes after the peak, which will be discussed in a later section. Similar to the parent compound, there is an intensity increase in the edge peak which is strongest in the angles closest to the *ab*-plane. The results from the system where the transition has been completely suppressed show no changes in any part of the spectra throughout the temperature range measured. Interestingly this suggests that the changes in the intensity of the first peak are not simply temperature related. It further confirms that while this is unlikely to be an oxidation state change, it could be related to a potential small redistribution or localization effect on the Ir orbitals which may be a consequence of the Ir-Ir dimers ordering. This result builds upon information later discussed, and will be expanded in the discussion section in this chapter.

(a)

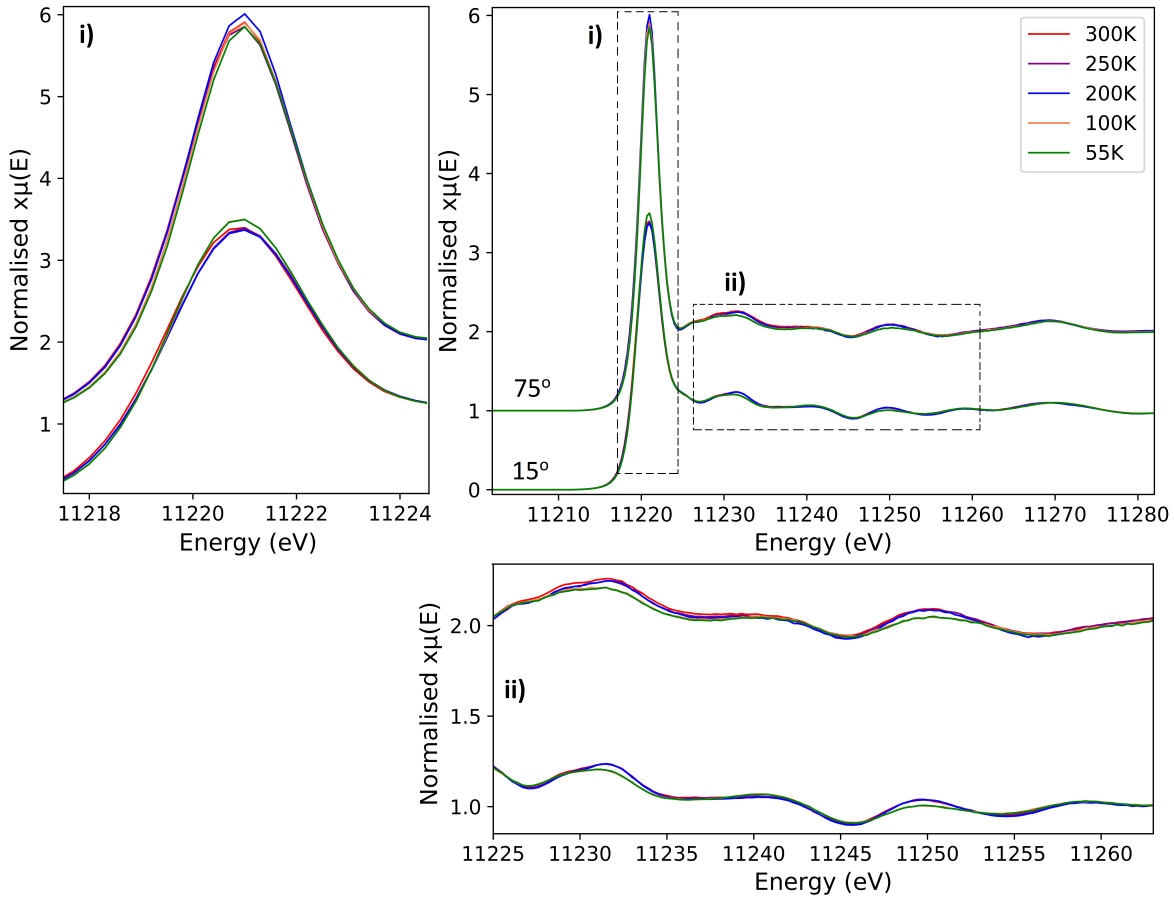

(b)

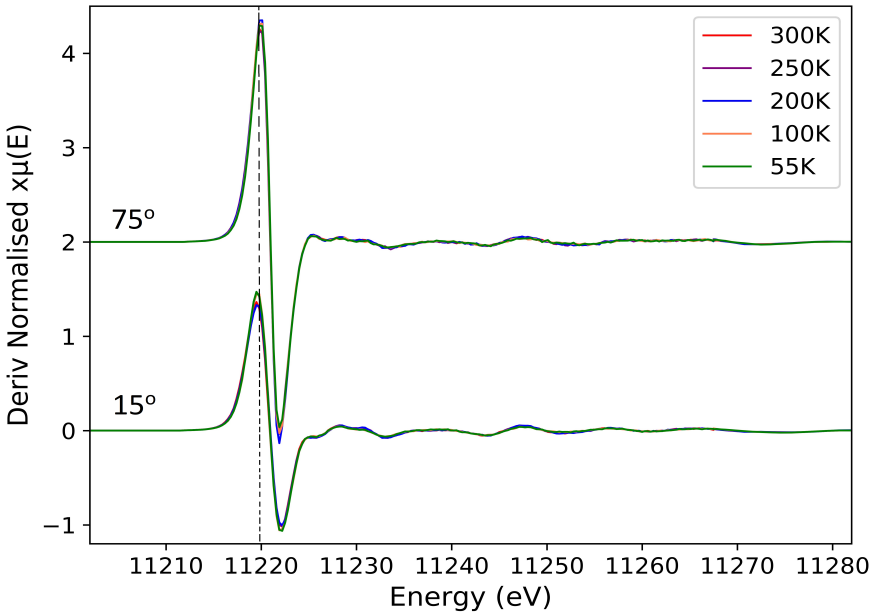

Figure 6.4.7: XANES: a) normalized spectra and b) normalized first derivative for the Ir L_3 ($L\alpha_1$) fluorescence on $Ir_{1-x}Pt_xTe_2$, $x = 0.02$ samples. Data is shown for 15^o and 75^o angle, across both transitions.

(a)

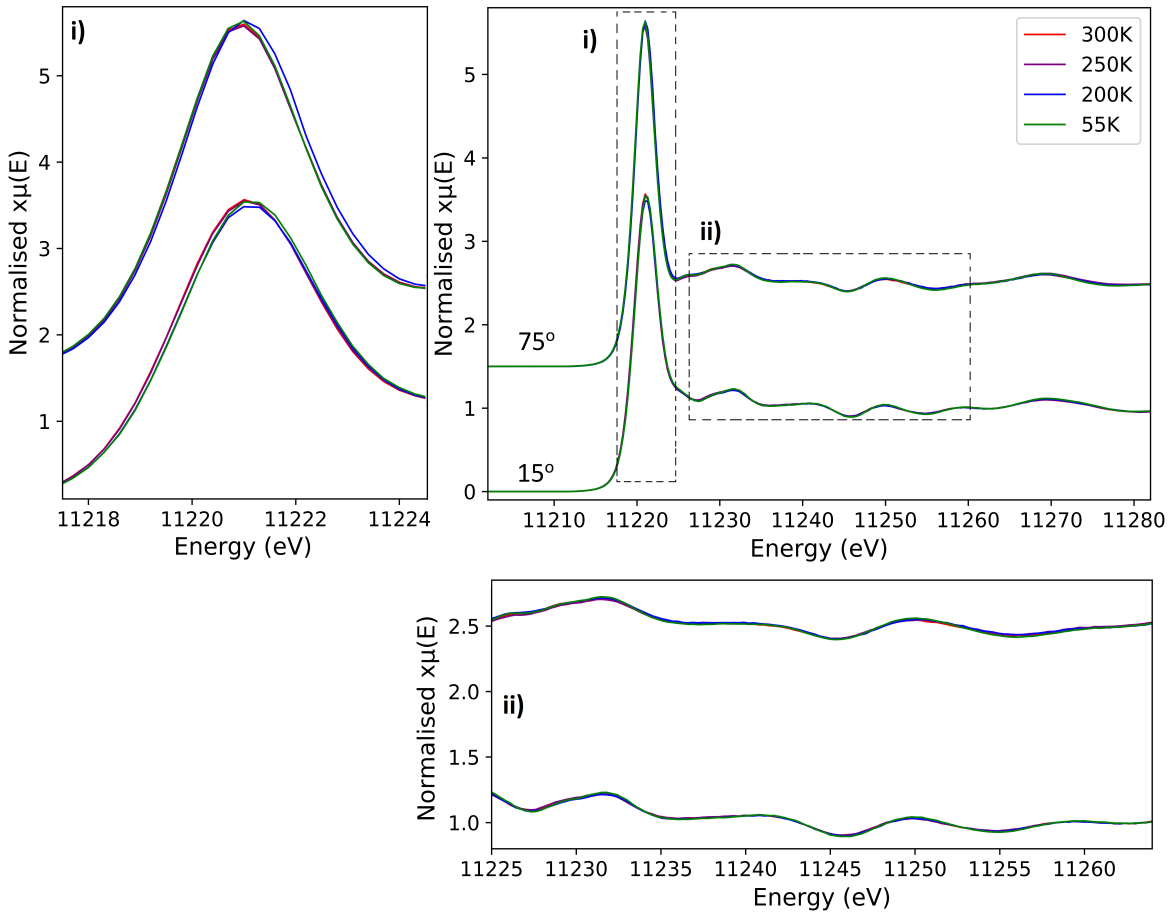

(b)

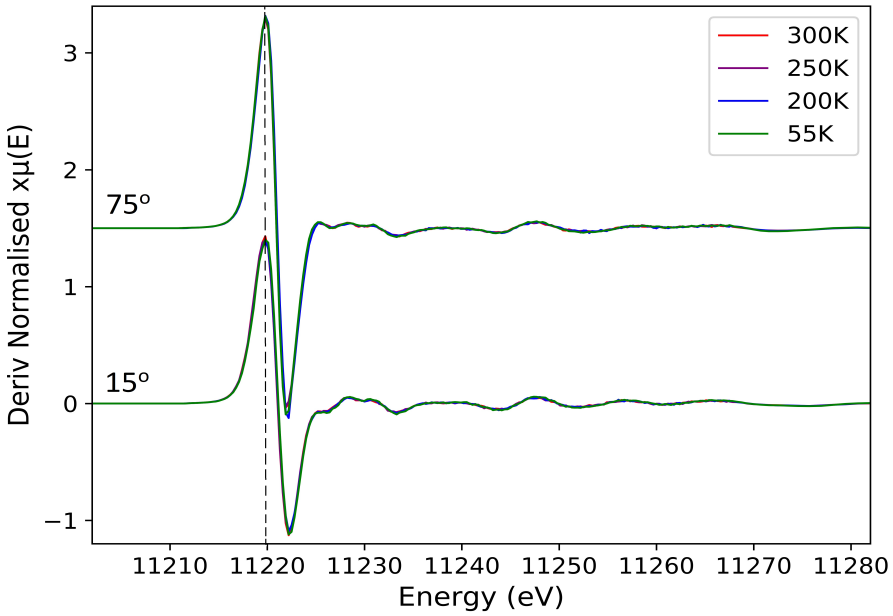

Figure 6.4.8: XANES: a) normalized spectra and b) normalized first derivative for the Ir L_3 ($L\alpha_1$) fluorescence on $Ir_{1-x}Pt_xTe_2$, $x = 0.05$ samples. Data is shown for 15^o and 60^o angle, across both transitions.

6.4.2 Valence-to-core XES

The HERFD-XANES data shows very little changes across both transitions. However the subtle intensity change seen in the absorption edge suggests that vtc-XES may provide further information from the valence band regarding the role of the Ir species. It may also reveal changes in the Te species. Measurements have been carried out using the Ir Lβ emission lines on IrO_2, $IrCl_3$ and $IrTe_2$. Shown in figure 6.4.9 the vtc spectra for $IrTe_2$ is shown across both transitions at the 2 extreme angles. Also shown is the comparison between the two reference samples at 45^o. The normalization procedure outlined in section 5.2 has been applied.

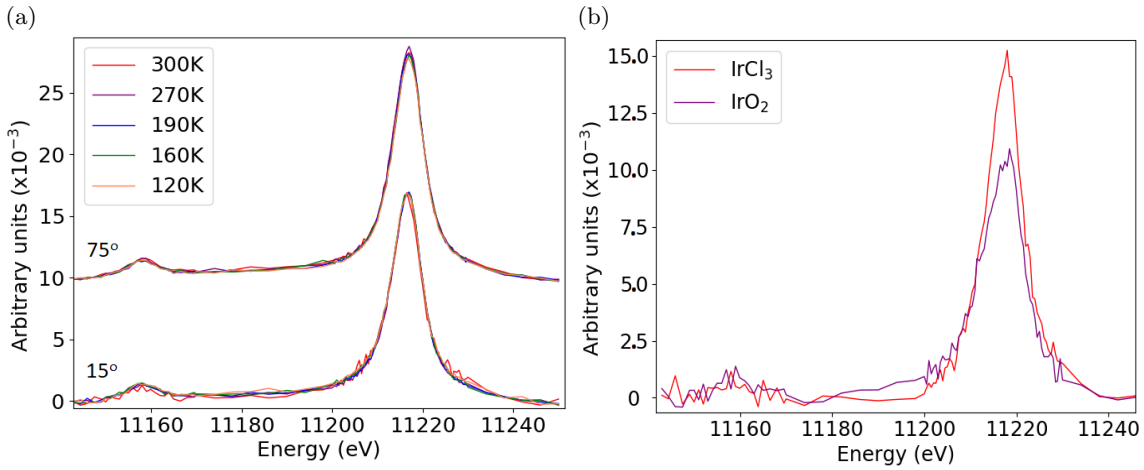

Figure 6.4.9: Ir Lβ: vtc spectra for a) $IrTe_2$ for 15^o and 75^o and b) Ir reference samples, IrO_2 and $IrCl_3$

The two reference samples allow comparison between the Ir +3 and +4 oxidation states. At approximately 11160eV there is a very subtle feature in both spectra. However due to the quality of the data it is not possible to resolve any information from this area. The main feature at 11217eV shows a significant intensity difference, however no peak shift is seen. While it is not possible to make a complete comparison between the intensities due to the issues involved in the normalization steps, the size of the difference does suggest a link with the oxidation state change. Along with the tungsten reference samples, these results show that the Lβ (for heavier elements) does not undergo a peak shift upon an oxidation state change but an intensity difference is seen. There is also a shallow feature that appears in the IrO_2 sample at approximately 11190eV which is not resolved in $IrCl_3$. The $IrTe_2$ spectra show no measurable differences across either temperature or angle. The feature at 11160eV is resolved but shows no changes either. The intensity of the main feature is effectively the same as the $IrCl_3$ sample. While the intensity comparison may involve significant errors, this again suggests that the Ir in the $IrTe_2$ compound is in a +3 state across both transitions. Based on the analysis of the tungsten reference samples and simulations, figure 6.4.10 shows the simplified molecular orbital diagram used to understand the origins of each feature.

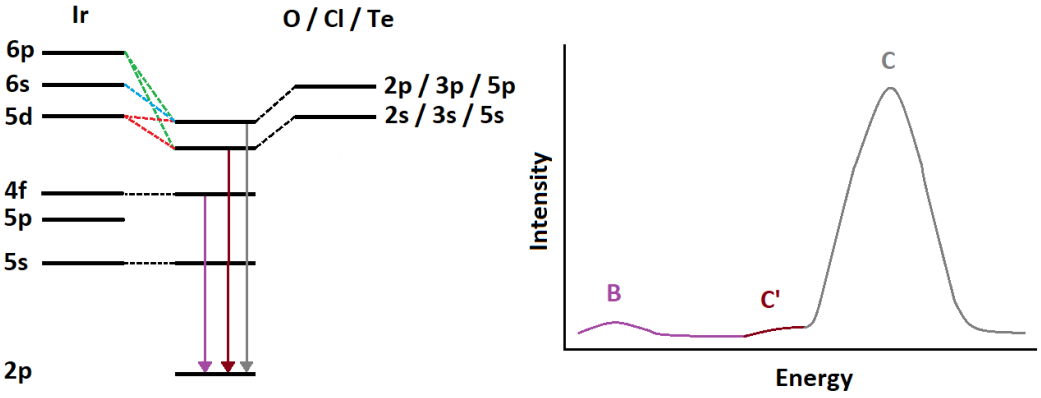

Figure 6.4.10: Ir simplified molecular orbital (MO) diagram indicating potential transitions in vtc-XES

FDMNES simulations have been carried out on all 3 samples at room temperature. The resultant spectra, DOS and orbital overlap are shown in figures 6.4.11-6.4.13. Note that feature C has been aligned with the experimental data and has been scaled to allow a reasonable comparison. The simulated spectra peak intensity and positions are in good agreement with the experiment for all samples. The DOS shows that feature B is centred around the f orbitals, but also shows a wide p orbital density in a similar region. Feature B shows that the p-PDOS and f-PDOS intensity is much larger than the experiment, which is mostly likely due to this feature arising from deep states. The weaker intensity reflects that it is less probable for a core-hole to be filled by electrons from these orbitals. Taking the analysis from the tungsten references into consideration, these results suggest that the emission involving the metal $5p$ orbitals is not allowed (confirmation of the dipole selection rules) and therefore feature B is formed of contributions for the f character. Feature C shows mostly d character but also a small contribution from s and p orbital mixing from the ligands. Interestingly there is a small feature in the region defined by C'. Comparison between the three samples shows that this feature undergoes a shift in energy between the different oxidation states. However the analysis of the metal-ligand bond lengths for the tungsten reference samples (section 5.4) may indicate a different origin of this shift. The bond lengths for IrO_2, $IrCl_3$ and $IrTe_2$ are: 2.015Å, 2.371Å and 2.639Å respectively. Both the metal-ligand bond length and oxidation state appear to have a role in determining the energy position of this feature. The orbital overlap is shown along side the DOS to give an understanding of the interactions between the metal and ligands. The features in the vtc-XES have been shown to directly probe the ligand orbitals (section 5.4). The orbital overlap shows very little ligand character in feature B as expected. Feature C' indicates overlap with only ligand ns orbitals while feature C has contribution from only ligand np orbitals. This result is consistent across all samples. While there are some striking differences in the character of the overlap, what is interesting to note is that separation between the ns and np features in the $IrTe_2$ sample. The simulations suggest that due to the separation of features C' and C, it is difficult to resolve the individual features and therefore the subtle changes in the Ir-Te path length may not be determined. This again highlights that the limiting factor of these measurements is the core-hole lifetime broadening effects.

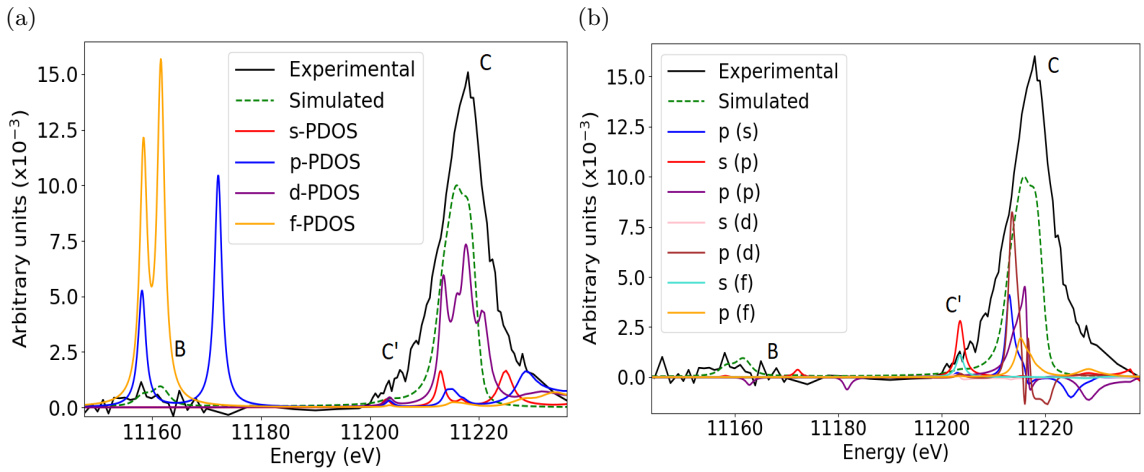

Figure 6.4.11: Ir Lβ: $IrCl_3$ vtc-XES. a) experiment vs simulated DOS, b) experiment vs simulated orbital overlap. Legend indicates (Ligand(Metal)) orbital overlap.

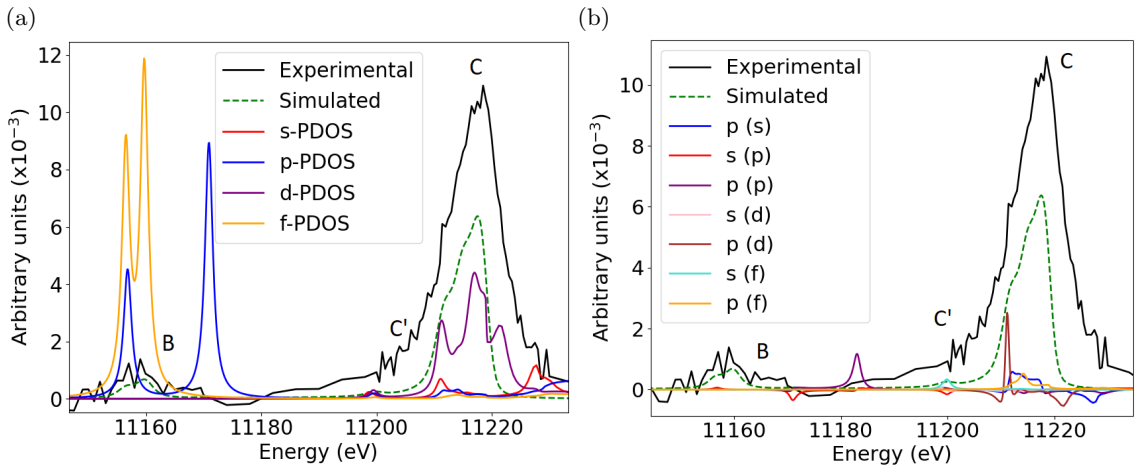

Figure 6.4.12: Ir Lβ: IrO_2 vtc-XES. a) experiment vs simulated DOS, b) experiment vs simulated orbital overlap. Legend indicates (Ligand(Metal)) orbital overlap.

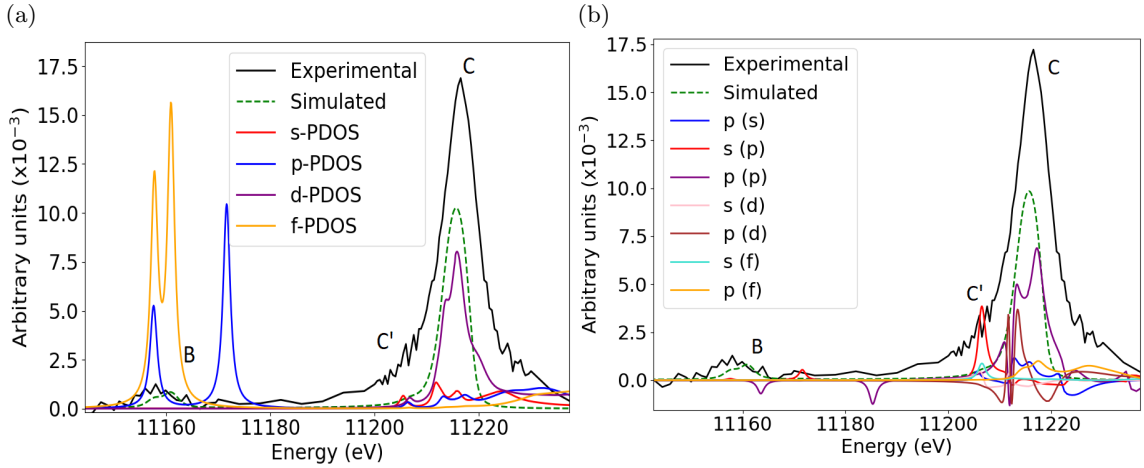

Figure 6.4.13: Ir Lβ: $IrTe_2$ vtc-XES. a) experiment vs simulated DOS, b) experiment vs simulated orbital overlap. Legend indicates (Ligand(Metal)) orbital overlap.

6.4.3 EXAFS analysis

For each compound the EXAFS and FT-EXAFS have been plotted with a comparison between the 4 angles measured and across the temperature range. The relative position of the first 4 single scattering paths with respect to the excited Ir atom are shown in figure 6.4.14, along with an example of the experimental data. The first contribution comes from the Ir - Te paths at 2.65$\mathring{A}$ with a degeneracy of 6. It is suggested that there is a split in this path below the 280K transition where 2 paths becomes shorter and 4 become longer, however the difference is too small to separate the paths in the data. The next contribution comes from the Ir - Ir paths. This is split into the undistorted path (Ir_L) at 3.939$\mathring{A}$ and the dimerized path (Ir_S) at 3.800$\mathring{A}$. In total these paths have a degeneracy of 6 but the split in the contributions will be determined separately for each phase. Finally the single scattering contributions for the second Ir - Te path at 4.623$\mathring{A}$ is considered. Table 6.4.4 shows the path lengths, degeneracies and relative angles of the paths with respect to the ab-plane (ϕ_A) and c-axis (θ_A).

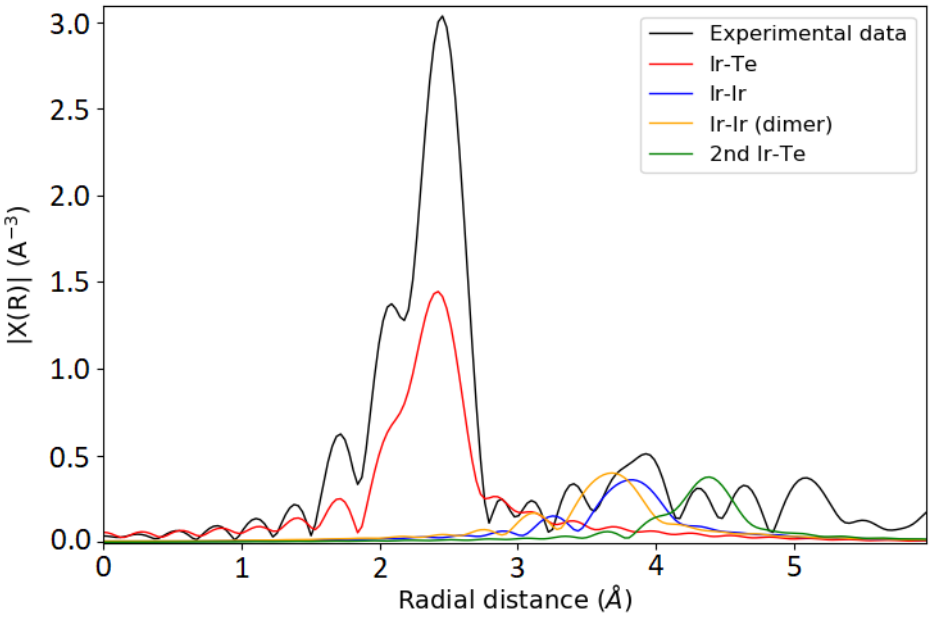

Figure 6.4.14: $IrTe_2$ single scattering path contributions, plotted in R-space. $IrTe_2$ spectra (300K, 30^o) shown for reference.

$IrTe_2$ - Parent compound

Figure 6.4.15 shows the comparison across angles for both the EXAFS and FT-EXAFS taken on the $IrTe_2$ samples. The data and fits shown here have been carried out on data collected from the L_3 Ir edge ($L\alpha_1$). The EXAFS have been plotted using a k-weight of 2 and the Fourier transform has been performed used a k-range between 3$\mathring{A}^{-1}$ - 13.2$\mathring{A}^{-1}$. The EXAFS shows reasonable signal to noise ratio up until at least 13.5$\mathring{A}^{-1}$, with strong EXAFS oscillations. The data has been cut at 13.2$\mathring{A}^{-1}$ as systematic errors start to appear, with this range sufficient for interpretation of the data. There are some very small differences between the angles, for example at 4.0$\mathring{A}^{-1}$ and 7.4$\mathring{A}^{-1}$. These changes are seen more clearly in the Fourier transform. Firstly, it is clear there is more noise in the higher temperature data, shown just below 2$\mathring{A}$ and less defined features after the Ir-Te path. The features that represent the contributions for the two Ir-Ir paths do show some significant changes in the range of 3.6$\mathring{A}$ - 4.2$\mathring{A}$. While it is difficult to conclude an angular dependence in 300K data due to distortions caused by systematic errors, the 160K shows a clear difference between the $15^o/30^o$ and $60^o/70^o$, with the Ir-Ir feature becoming less intense and less broad. This data shows how the angular dependence can affect the contributions to the data from specific paths, where the $15^o/30^o$ angles are more sensitive to the Ir-Ir paths in the ab-plane. Figure 6.4.16 shows the data collected at the 15^o angle across both transitions, which has been separated into the high and low temperature phases. While there is some small thermal effects, the biggest change is seen for the Ir-Ir paths. Below the first order transition, the feature becomes more defined and greater intensity is seen at 4$\mathring{A}$.

(a)

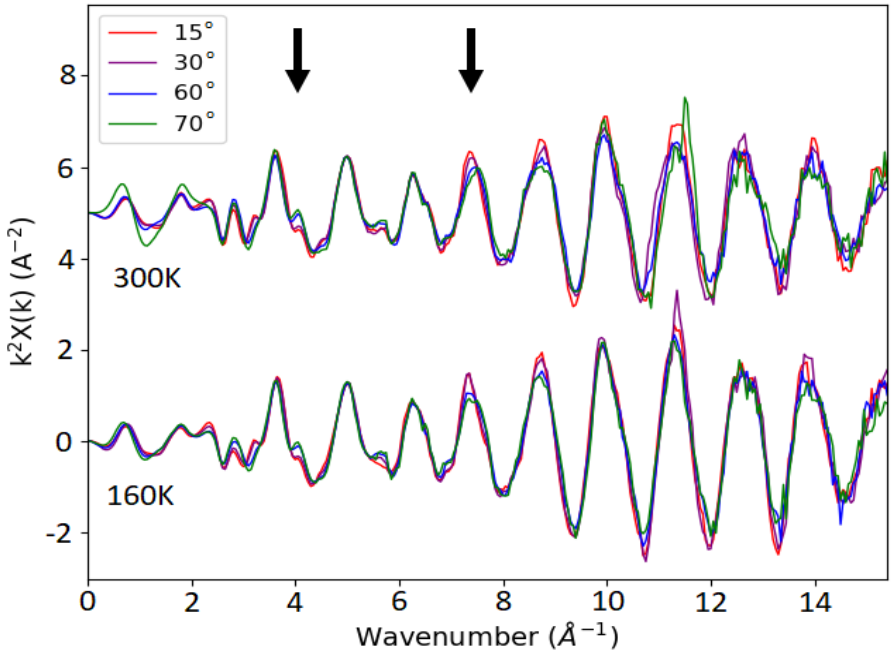

(b)

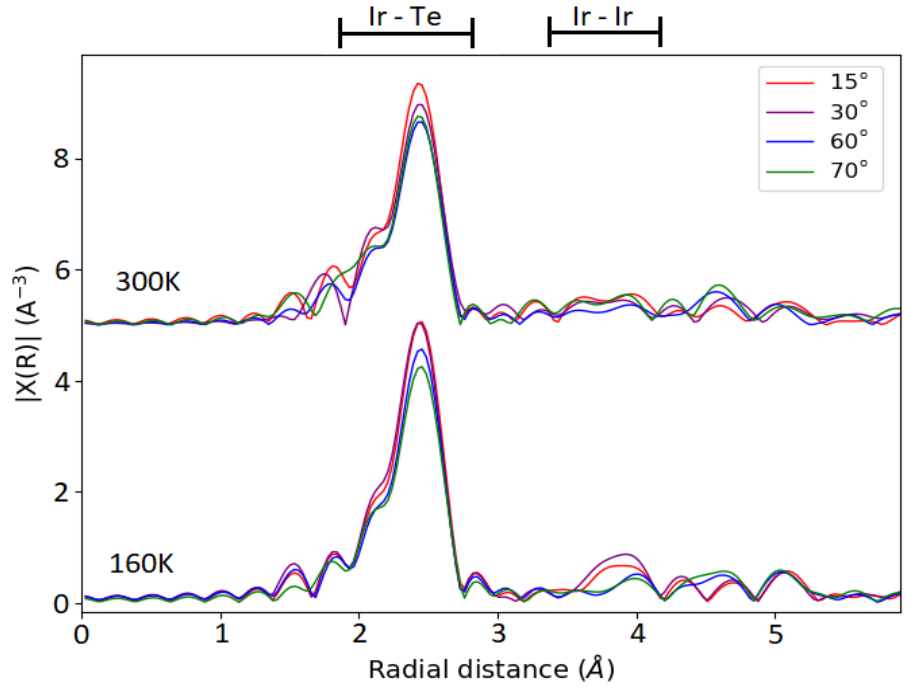

Figure 6.4.15: a) EXAFS and b) FT-EXAFS for $IrTe_2$ (Ir L_3-edge) sample. Showing the angular dependence of these measurements at both 300K and 160K. Also indicated are the two regions of interest, identifying the Ir-Te and Ir-Ir contributions in the FT-EXAFS.

(a)

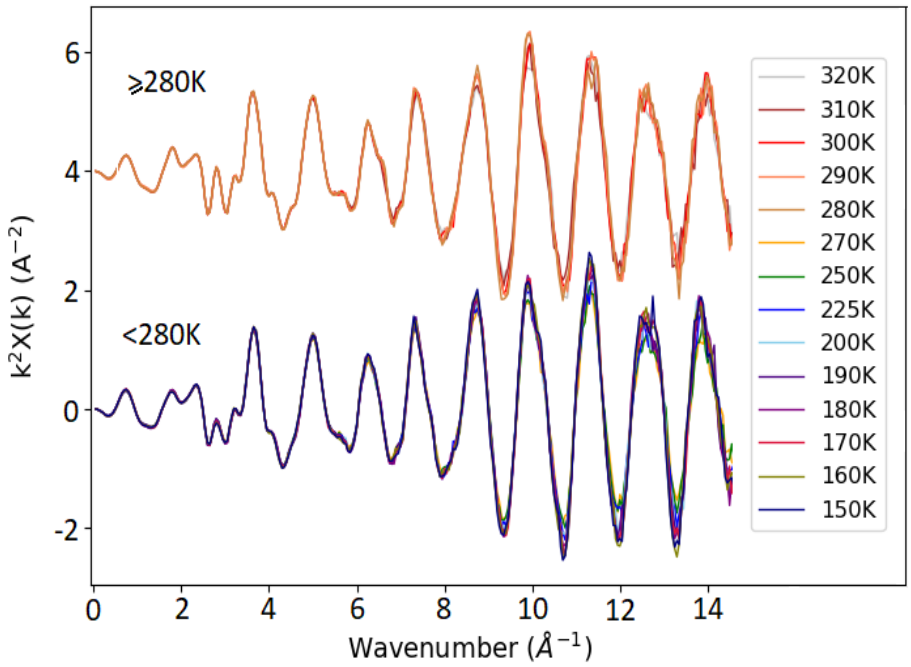

(b)

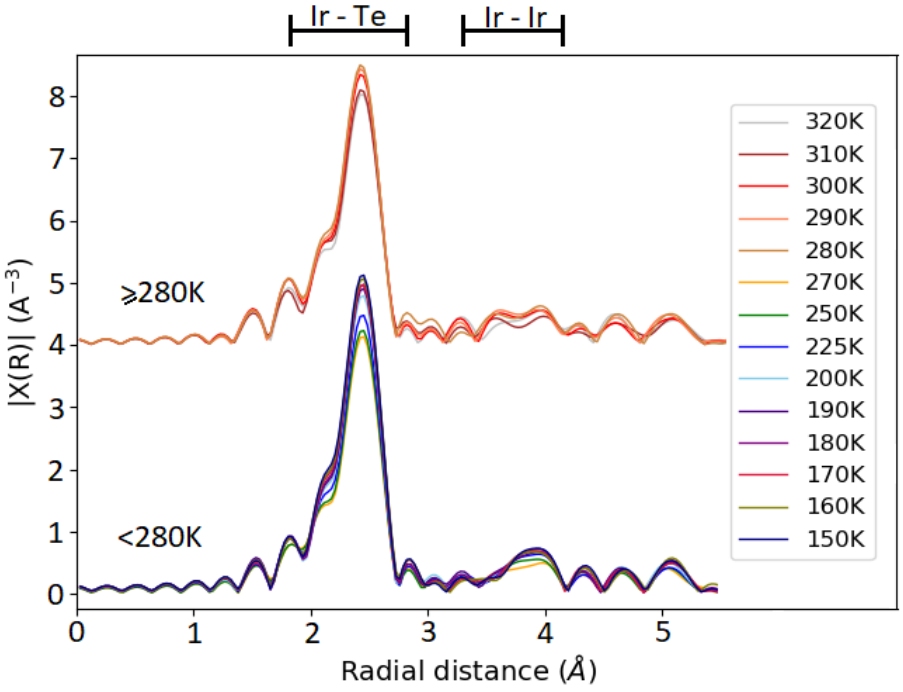

Figure 6.4.16: a) EXAFS and b) FT-EXAFS for $IrTe_2$ (Ir L_3-edge) sample. Showing data for the 15^o angle across both transitions at 280K and 180K. Also indicated are the two regions of interest, identifying the Ir-Te and Ir-Ir contributions in the FT-EXAFS.

Beat effect

The small difference between the two Ir path lengths and the relative difference in the contributions make the standard fitting procedure difficult to apply. The fitting parameters may treat the shorter Ir path as noise, which would be reflected in the Debye-Waller factor. Before attempting to fit a model to the data it is necessary to determine if both paths are present. To this end, an analysis of the Fourier transform known as the beat effect has been carried out, with further details of the methodology given in section 4.6. Taking the average lengths of the undistorted (Ir_L) and dimerized (Ir_S) Ir-Ir paths as $Ir_L = 3.97$Å and $Ir_S = 3.82$Å we expect to see a minimum in the range of 8-10Å in q-space (back Fourier transform), using equation (58).

Table 6.4.3 shows the minima of the beat effect for each temperature and angle for the $IrTe_2$ sample. Examples of this effect are shown for temperatures above and below the transition in figure 6.4.17. There is a clear effect seen above and below the transitions in all angles for this sample. Hence both the Ir_L and Ir_S paths are present for the full temperature range studied here. While it can not be determined if there is any change in the nature of paths, this shows that a model fitting both paths is appropriate in this situation.

	Angle			
Temperature (K)	**15^o**	**30^o**	**60^o**	**70^o**
320	9.4±0.3	9.8±0.3	9.8±0.3	9.8±0.3
310	9.8±0.3	9.6±0.3	9.7±0.3	9.6±0.3
300	9.6±0.3	10.1±0.3	9.7±0.3	9.5±0.3
290	9.7±0.3	10.1±0.3	9.8±0.3	9.6±0.3
280	9.9±0.3	10.1±0.3	9.8±0.3	9.5±0.3
270	9.4±0.3	9.5±0.3	9.6±0.3	9.5±0.3
250	9.4±0.3	9.6±0.3	9.6±0.3	9.5±0.3
225	9.4±0.3	9.6±0.3	9.7±0.3	9.6±0.3
200	9.4±0.3	9.4±0.3	9.6±0.3	9.6±0.3
190	9.4±0.3	9.6±0.3	9.7±0.3	9.6±0.3
180	9.4±0.3	9.4±0.3	9.6±0.3	9.5±0.3
170	9.4±0.3	9.4±0.3	9.6±0.3	9.6±0.3
160	9.3±0.3	9.4±0.3	9.3±0.3	9.7±0.3

Table 6.4.3: $IrTe_2$ (Ir L_3-edge) beat effect: minimum for the beat with relation to the Ir_L and Ir_S.

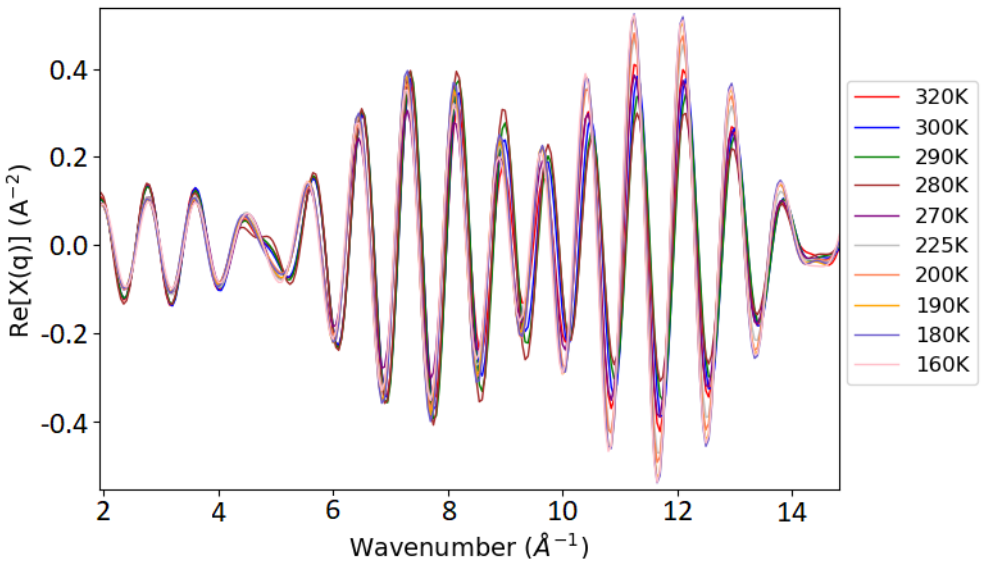

Figure 6.4.17: $IrTe_2$ beat effect example for 15^o from all temperatures measured on L_3-edge ($L\alpha_1$).

Fitting

To further understand how the nature of the Ir-Ir paths may change across the transitions, the EXAFS data has been fitted. The structure used is shown in table 6.4.4 and the method for this is described in section 4.5.

Path	**Path length (Å)**	**Degeneracy**	$\theta_A(^o)$	$\phi_A(^o)$
Ir-Te	2.650	2	59.14	35.10
	””	2	59.14	94.43
	””	2	59.14	144.90
Ir-Ir (Ir_L)	3.939	*	90.00	0.00
	””	*	90.00	60.00
	””	*	90.00	120.00
Ir-Ir (Dimer - Ir_S)	3.800	*	90.00	0.00
	””	*	90.00	60.00
	””	*	90.00	120.00
2nd Ir-Te	4.623	2	29.47	35.10
	””	2	29.47	94.43
	””	2	29.47	144.90

Table 6.4.4: $Ir_{1-x}Pt_xTe_2$ Scattering paths. The asterisk indicates that the degeneracy of these paths is a variable in the different models (formally the degeneracy is 2).

The beat effect analysis for this composition shows that both the undistorted and dimerized Ir paths are present above and below the transitions. The literature shows that below 280K the dimerized paths are in an ordered state along the a-axis. However no information is given for these paths above 280K. To study this further, two separate models have been applied to all the data sets. Model 1 represents a system where the dimerized paths can be fitted in all directions within the ab-plane. As the ratio between the Ir_L and Ir_S is unknown in the high temperature phase, this model assumes that they have equal weighting. While different ratios of Ir_L and Ir_S paths have been tested, due to the highly distorted structure above the 280K transition, it is difficult to determine specific ratios. Model 2 is based on the reported low temperature structure. The dimerized paths are only considered along the a-axis, with only 1 in 5 Ir-Ir paths dimerized. Below the second transition at 180K a 3^{rd} model was tested to determine if it was possible to fit the $Q_{1/8}$ dimer structure. However no significant improvement was made to the fitting parameters. The 3rd model has not been included in the remainder of the chapter.

All fitting parameters for both models are shown in tables 6.4.5- 6.4.6 and examples of the fits are shown in figures 6.4.18- 6.4.19 for 300K and 160K for all angles measured. The fits were done in R-space using a range of 2.1Å-4.3Å, extracted from k-space between $3Å^{-1}$-$12.5Å^{-1}$, with k-weightings of 1, 2 and 3. While the EXAFS oscillations are strong beyond this range, this was chosen as the most consistent range across all data sets and limits the systematic errors in the data sets. For each data set the number of independent points is between 45-88 and the number of variables used is between 14-17, apart from 320K where the background has also been fitted which increases the number of variables to 59. The R-factors for each model range between 0.008 and 0.017. The E_0 position for each data has been allowed to vary, but it shows a consistent value within the error which reflects the stable edge position in the XANES data. This parameter was left as a fitting parameter across all temperatures to track any chances in E_0 position. The value for S_0^2 is a global factor in these fits that takes into account a number of factors that affect the amplitude value when comparing the experimental data to the theoretical data. Across all fits this value is between 0.9-1.05, which suggests a reasonable match between the model and data. The example fits for the 300K data using model 1 shows very good agreement with the model for both the Ir-Te and both Ir-Ir paths. There is a small difference at 3Å, but is most likely caused by systematic errors in the data, as it is between two scattering paths. The 160K fits using model 2 also show very good agreement in the fitting range. There is a small intensity difference from the contribution for the Ir_L scattering path, but the agreements still suggests that both Ir-Ir paths are present. The path lengths and Debye-Waller factors are plotted in figures 6.4.20- 6.4.21. The Ir-Te scattering paths are consistent across both models and show a small change across both transitions, which is also reflected in the Debye-Waller factor. The Ir-Ir paths show a clear difference between the

models across the first transition. Model 1 shows reasonable path lengths and Debye-Waller factors above the transition. However, below this transition the Debye-Waller factor values for the Ir_S become unreasonably large compared to the undistorted paths. Model 2 on the other hand is more appropriate below transition, with positive Debye-Waller factors. While the error for the Debye-Waller factor for the Ir_S paths is large compared to the Ir_L paths, this is a reflection of the relatively small contribution to the spectra. The Debye-Waller parameters used in these fits are adjustments to the model which take into account thermal distortions. Typically if the value is significantly large (including errors) it suggests that the contribution for the path is larger in the model than the experimental data and the opposite is seen for a negative value. Appling model 1 below the transition gives large Debye-Waller factor values, suggesting that the contribution for the Ir_S paths is too large in the model due to fitting these paths in all directions rather than just one. Applying model 2 above the transition however gives negative Debye-Waller factor values suggesting that the model is under estimating the contribution for the Ir_S paths, which again comes from the model only fitting these path in one direction. Combining model 1 and 2 where they are most appropriate to the scenarios being tested, shown in figures 6.4.21(a, d), show firstly that it is reasonable to fit two similar path lengths for Ir-Ir above and below both transitions. Secondly, that there is a change in the ordering of the short paths across at least the first transition (T_1). It is important to notice that some of the Debye-Waller values can be negative within the error, which typically suggests that there is an issue with these paths. The reason for these values may be related to several factors. Firstly, the contribution to the signal is significantly less for the Ir_S compared to the Ir_L paths, which makes it more difficult to fit these paths. Secondly it may be a consequence of fitting the angular dependence of these paths, where in section 2.2.4 it is shown that the *ab* orientation is left as a fitting parameter. This introduces an additional degree of uncertainly in these fits.

(a)

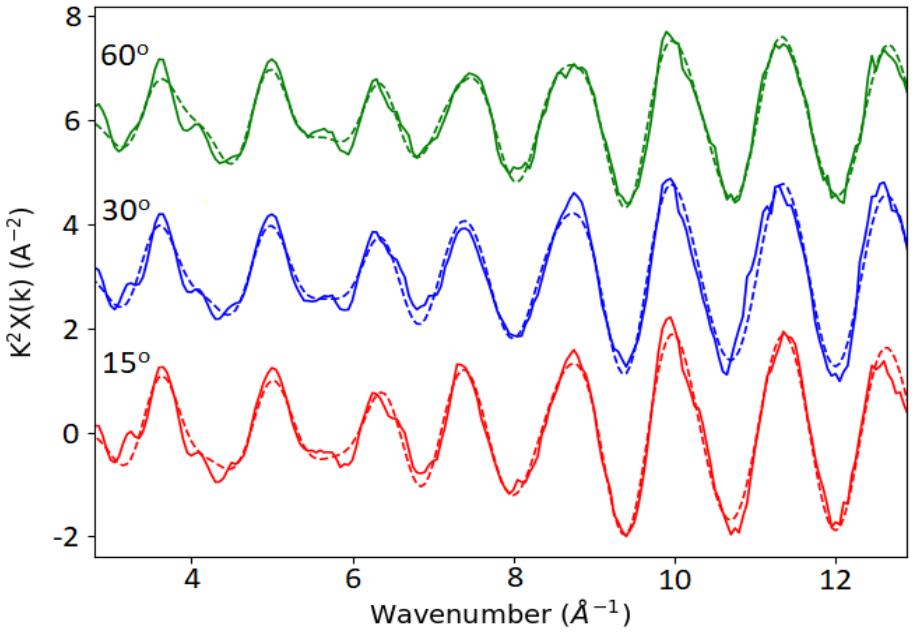

(b)

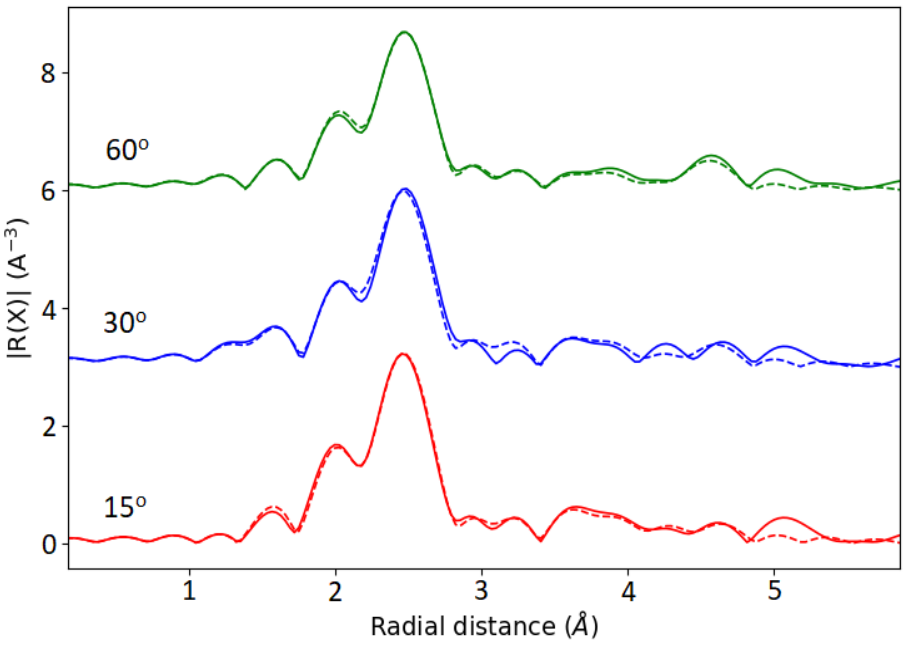

Figure 6.4.18: a) EXAFS and b) FT-EXAFS fitting examples for $IrTe_2$ (Ir L_3-edge) at 300K using 3 angles. The dashed lines indicate the fitting result.

(a)

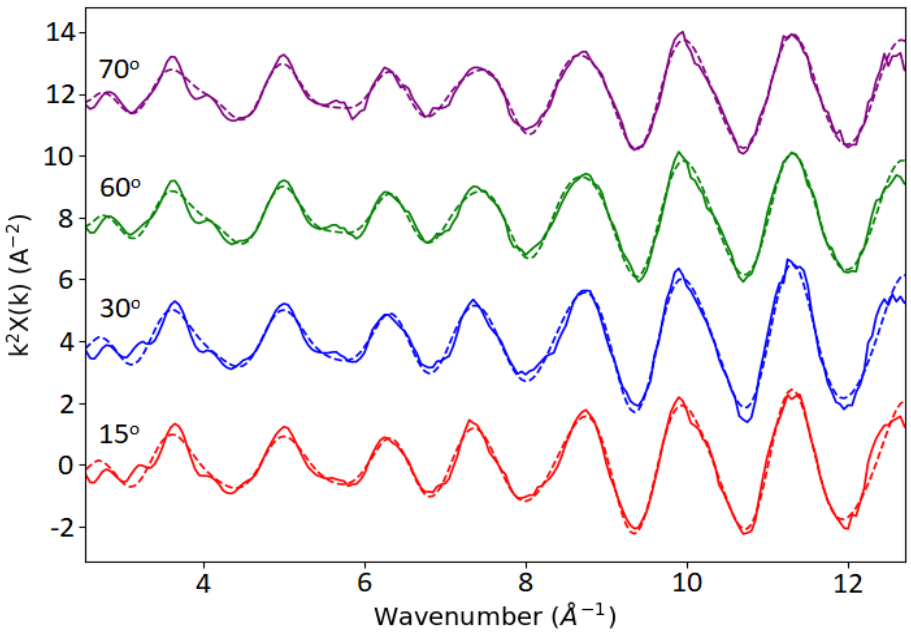

(b)

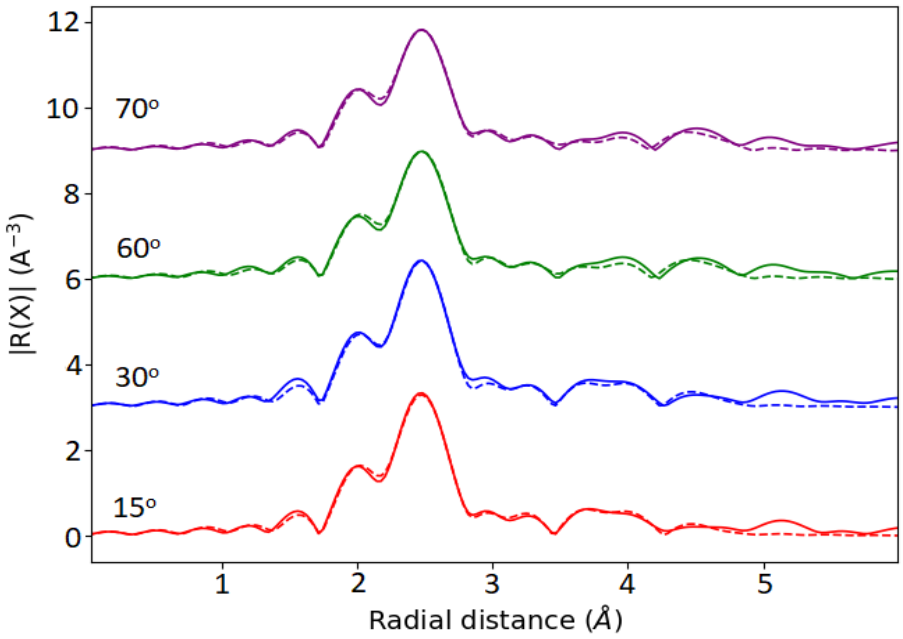

Figure 6.4.19: a) EXAFS and b) FT-EXAFS fitting examples for $IrTe_2$ (Ir L_3-edge) at 160K using 4 angles. The dashed lines indicate the fitting result.

Parameters	320K	310K	300K	290K	280K	270K	250K	225K	200K	190K	180K	170K	160K
ΔE_0 (eV)	6.3±0.5	6.4±0.5	6.3±0.6	6.3±0.6	6.0±0.6	6.2±0.5	5.9±0.5	6.3±0.5	6.3±0.5	6.2±0.5	6.2±0.5	6.1±0.5	6.1±0.5
S_o^2 - (15^o)	0.99±0.08	0.96±0.05	0.98±0.06	0.95±0.05	0.99±0.05	0.95±0.07	0.77±0.03	0.7±0.2	0.92±0.04	0.94±0.04	0.94±0.04	0.91±0.05	0.95±0.04
S_o^2 - (30^o)	0.99±0.08	1.00±0.05	0.98±0.06	0.98±0.06	0.95±0.05	1.01±0.06	0.84±0.06	0.8±0.3	1.01±0.04	1.03±0.04	1.03±0.04	1.03±0.05	1.01±0.05
S_o^2 - (60^o)	1.03±0.09	1.00±0.05	0.99±0.06	0.99±0.06	1.04±0.05	0.99±0.05	0.92±0.09	0.9±0.1	0.97±0.05	0.99±0.05	1.00±0.04	0.98±0.05	1.00±0.05
S_o^2 - (70^o)	-	-	-	-	-	1.01±0.05	1.00±0.08	1.0±0.1	0.95±0.06	0.96±0.06	0.97±0.05	0.94±0.05	0.96±0.06
1^{st} Ir-Te R ($\AA$)	2.644±0.002	2.644±0.002	2.643±0.002	2.642±0.002	2.640±0.001	2.644±0.001	2.643±0.001	2.656±0.001	2.644±0.001	2.643±0.001	2.643±0.001	2.643±0.001	2.643±0.001
1^{st} Ir-Te σ^2 ($\AA^2$)	0.0030±0.0004	0.0029±0.0003	0.0027±0.0003	0.0026±0.0003	0.0028±0.0002	0.0028±0.0002	0.0026±0.0002	0.0026±0.0002	0.0019±0.0002	0.0019±0.0002	0.0019±0.0002	0.0017±0.0002	0.0018±0.0002
Ir-Ir Dimer (Ir_S) R ($\AA$)	3.86±0.02	3.85±0.01	3.86±0.02	3.878±0.001	3.86±0.02	3.89±0.02	3.89±0.01	3.92±0.04	3.89±0.02	3.89±0.02	3.89±0.02	3.90±0.04	3.89±0.02
Ir-Ir Dimer (Ir_S) σ^2 ($\AA^2$)	0.003±0.002	0.001±0.001	0.002±0.002	0.001±0.001	0.003±0.002	0.007±0.004	0.002±0.002	0.01±0.01	0.005±0.004	0.005±0.004	0.006±0.005	0.009±0.007	0.010±0.008
Ir-Ir (Ir_L) R ($\AA$)	3.99±0.02	3.99±0.01	3.99±0.02	4.01±0.02	3.97±0.01	3.99±0.01	4.01±0.01	3.97±0.02	3.99±0.01	3.99±0.02	3.99±0.02	3.98±0.02	3.99±0.02
Ir-Ir (Ir_L) σ^2 ($\AA^2$)	0.002±0.002	0.001±0.001	0.002±0.002	0.002±0.002	0.002±0.002	0.002±0.001	0.001±0.002	0.003±0.001	0.001±0.002	0.001±0.002	0.002±0.002	0.002±0.001	0.003±0.001
2^{nd} Ir-Te R ($\AA$)	4.63±0.03	4.64±0.01	4.63±0.01	4.62±0.02	4.62±0.01	4.62±0.01	4.62±0.01	4.63±0.01	4.63±0.01	4.63±0.01	4.63±0.01	4.63±0.01	4.62±0.01
2^{nd} Ir-Te σ^2 ($\AA^2$)	0.014±0.003	0.011±0.002	0.012±0.002	0.011±0.002	0.012±0.002	0.015±0.004	0.016±0.003	0.016±0.002	0.01±0.01	0.011±0.003	0.010±0.002	0.01±0.01	0.011±0.002
R-Factor	0.019	0.014	0.017	0.015	0.016	0.012	0.010	0.012	0.009	0.010	0.008	0.012	0.010
Independent points	88.5	46.6	46.6	49.7	55.8	63.6	63.6	74.4	60.0	60.1	60.1	60.1	60.1
Variables	59	14	14	14	14	17	17	17	17	17	17	17	17

Table 6.4.5: $IrTe_2$ EXAFS fitting parameters for data between 320K-160K. Model 1: Ir-Ir dimers fitted along all Ir-Ir paths. Note that (-) indicates the data set was not usable.

Parameters	320K	310K	300K	290K	280K	270K	250K	225K	200K	190K	180K	170K	160K
ΔE_0 (eV)	6.3±0.7	6.4±0.4	6.3±0.5	6.2±0.5	6.3±0.6	6.1±0.4	5.9±0.5	6.3±0.4	6.3±0.5	6.3±0.5	6.2±0.5	6.1±0.5	6.1±0.5
S_o^2 - (15^o)	0.99±0.08	0.96±0.05	0.98±0.06	0.95±0.05	0.99±0.07	0.97±0.04	0.96±0.06	0.94±0.06	0.92±0.04	0.94±0.04	0.94±0.03	0.91±0.04	0.96±0.03
S_o^2 - (30^o)	0.99±0.08	1.00±0.05	0.99±0.06	0.95±0.05	0.95±0.07	1.02±0.04	1.02±0.06	1.02±0.06	1.01±0.04	1.03±0.04	1.03±0.04	1.04±0.04	1.01±0.05
S_o^2 - (60^o)	1.0±0.1	1.01±0.05	0.99±0.06	0.98±0.06	1.02±0.07	1.00±0.05	1.01±0.04	1.00±0.04	0.98±0.04	0.99±0.04	1.01±0.04	1.00±0.05	1.01±0.04
S_o^2 - (70^o)	-	-	-	-	-	1.01±0.05	1.04±0.05	0.99±0.04	0.97±0.05	0.96±0.05	0.97±0.04	0.96±0.05	0.98±0.05
1^{st} Ir-Te R ($\AA$)	2.644±0.003	2.643±0.002	2.643±0.002	2.642±0.002	2.642±0.002	2.644±0.001	2.643±0.001	2.644±0.001	2.645±0.001	2.644±0.001	2.643±0.001	2.643±0.001	2.643±0.001
1^{st} Ir-Te σ^2 ($\AA^2$)	0.0030±0.0004	0.0029±0.0003	0.0028±0.0003	0.0025±0.0003	0.0027±0.0003	0.0028±0.0002	0.0027±0.0002	0.0024±0.0002	0.0020±0.0002	0.0019±0.0002	0.0019±0.0002	0.0018±0.0002	0.0019±0.0002
Ir-Ir Dimer (Ir_S) R ($\AA$)	3.79±0.03	3.79±0.02	3.82±0.04	3.84±0.02	3.80±0.02	3.80±0.03	3.81±0.05	3.80±0.05	3.81±0.05	3.81±0.04	3.82±0.03	3.79±0.05	3.80±0.04
Ir-Ir Dimer (Ir_S) σ^2 ($\AA^2$)	-0.001±0.003	-0.003±0.002	-0.001±0.004	-0.003±0.002	-0.001±0.003	0.0002±0.0002	0.002±0.004	0.001±0.005	0.002±0.004	0.001±0.004	0.001±0.003	0.001±0.004	0.001±0.004
Ir-Ir (Ir_L) R ($\AA$)	3.95±0.02	3.95±0.01	3.95±0.02	3.96±0.01	3.94±0.01	3.97±0.01	3.97±0.01	3.97±0.01	3.97±0.01	3.97±0.01	3.98±0.01	3.97±0.01	3.97±0.01
Ir-Ir (Ir_L) σ^2 ($\AA^2$)	0.006±0.002	0.005±0.001	0.005±0.002	0.006±0.002	0.004±0.001	0.005±0.001	0.005±0.001	0.005±0.001	0.004±0.001	0.004±0.001	0.003±0.001	0.003±0.001	0.004±0.001
2^{nd} Ir-Te R ($\AA$)	4.63±0.03	4.64±0.01	4.63±0.02	4.62±0.02	4.63±0.02	4.62±0.01	4.62±0.01	4.63±0.01	4.63±0.01	4.64±0.01	4.629±0.009	4.62±0.01	4.62±0.01
2^{nd} Ir-Te σ^2 ($\AA^2$)	0.015±0.004	0.011±0.002	0.012±0.002	0.011±0.002	0.012±0.002	0.014±0.003	0.014±0.003	0.013±0.002	0.012±0.003	0.011±0.002	0.010±0.002	0.011±0.002	0.011±0.002
R-Factor	0.019	0.014	0.017	0.016	0.018	0.011	0.010	0.010	0.009	0.010	0.008	0.010	0.010
Independent points	88.5	46.6	46.6	48.2	99.4	62.2	63.6	63.5	62.9	62.2	61.5	59.5	59.5
Variables	59	14	14	14	65	17	17	17	17	17	17	17	17

Table 6.4.6: $IrTe_2$ EXAFS fitting parameters for data between 320K-160K. Model 2: Ir-Ir dimers fitted along one Ir-Ir path (a-axis). Note that (-) indicates the data set was not usable.

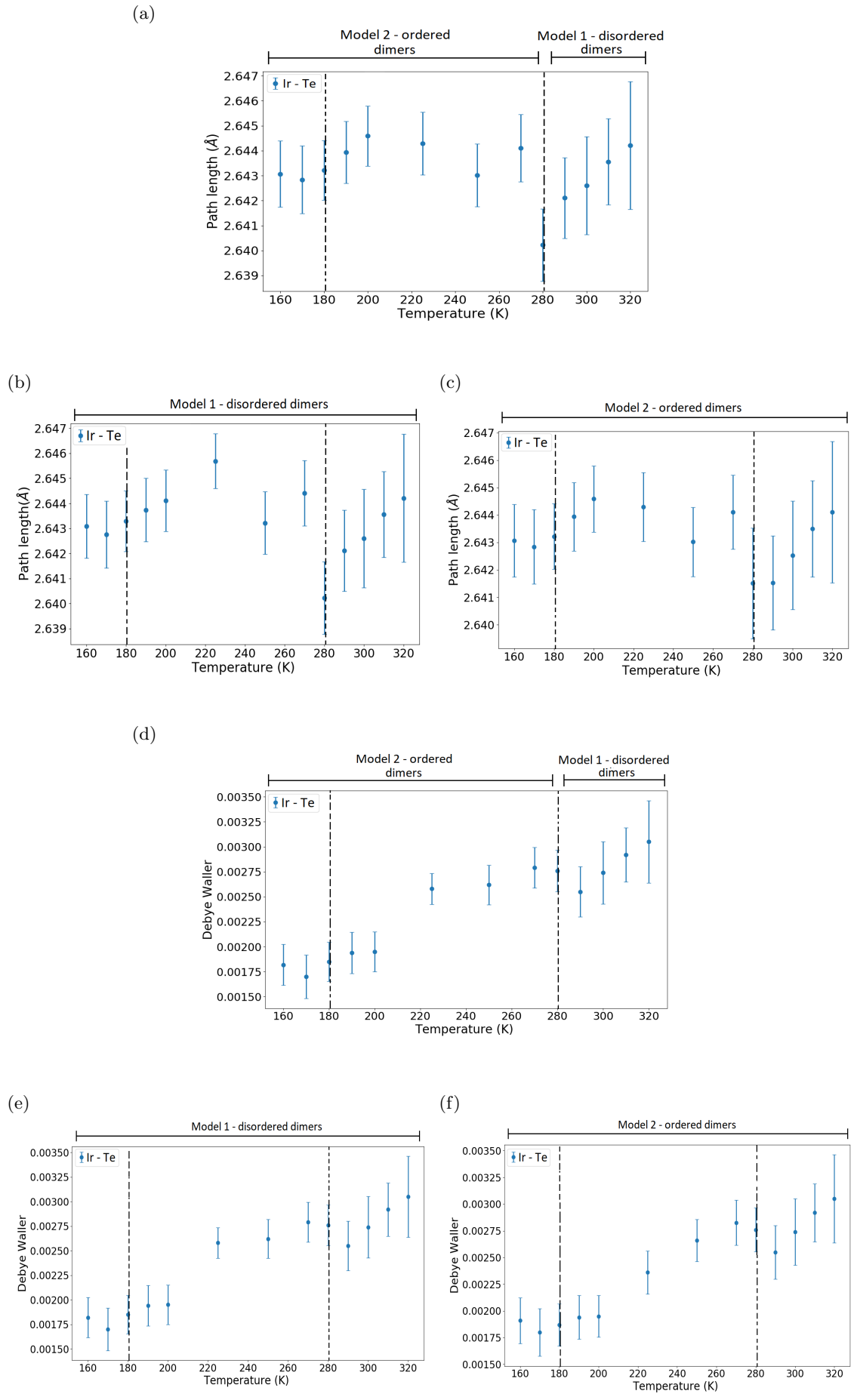

Figure 6.4.20: Fitting parameters for Ir-Te paths for $IrTe_2$. (a)-(c) Path lengths, (d)-(f) Debye-Waller factors. (a)/(d) - model 1 applied to 280K and above, model 2 applied to below 280K. (b)/(e) - model 1 only, (c)/(f) - model 2 only. Dashed lines indicate transitions.

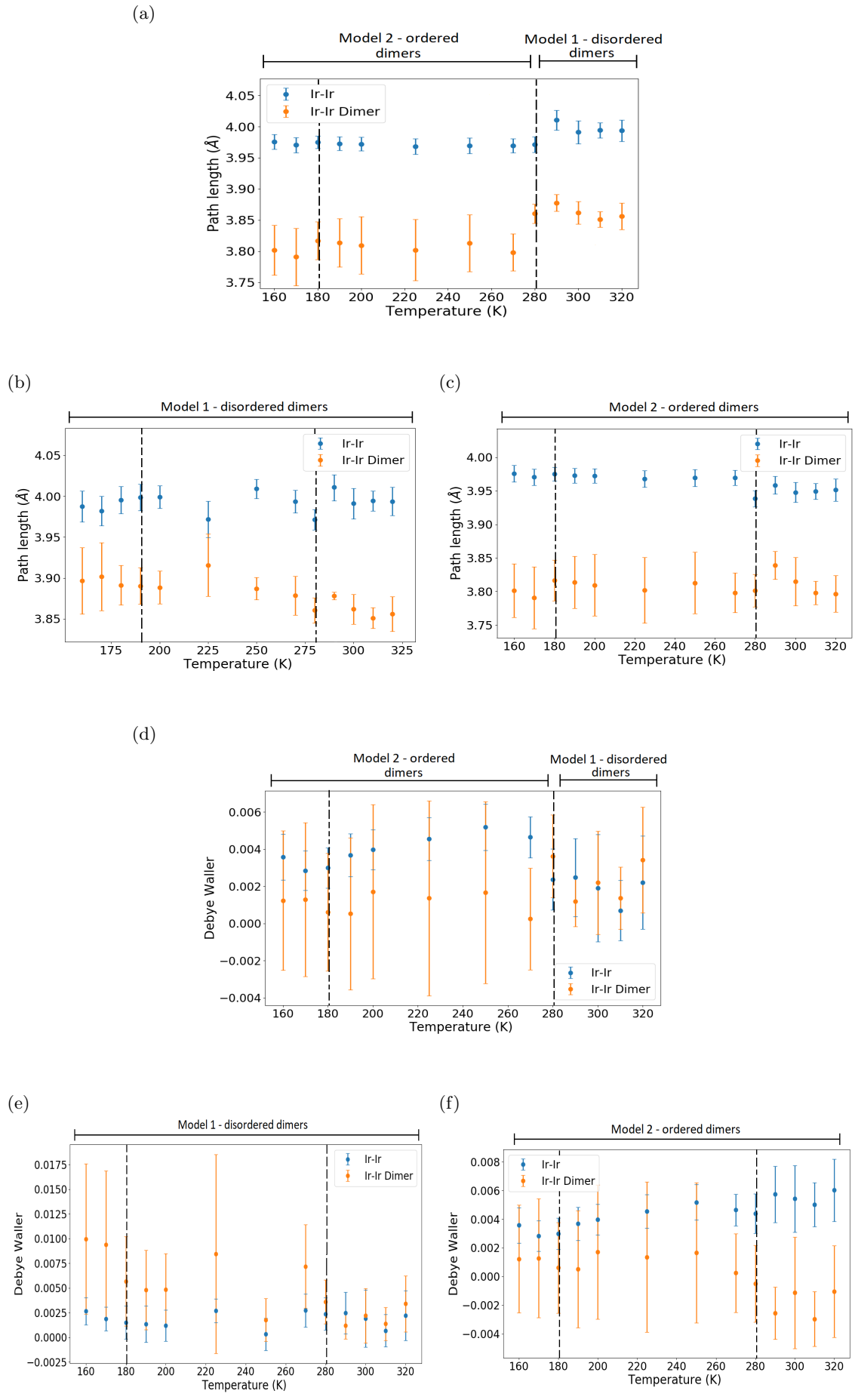

Figure 6.4.21: Fitting parameters for Ir-Ir (Ir_L - blue, Ir_S - orange) paths for $IrTe_2$. (a)-(c) Path lengths, (d)-(f) Debye-Waller factors. (a)/(d) - model 1 applied to 280K and above, model 2 applied to below 280K. (b)/(e) - model 1 only, (c)/(f) - model 2 only. Dashed lines indicate transitions.

$Ir_{1-x}Pt_xTe_2$, x = 0.02, 0.05

The EXAFS and FT-EXAFS for both doped compositions have been plotted in figures 6.4.22-6.4.25. The EXAFS have been plotted use a k-weighting of 2, and a k-range of 3Å-13Å has been used for the Fourier transform. For $x = 0.02$, the angular dependence has been shown in figure 6.4.22. The EXAFS oscillations are strong up until at least 14Å. The differences between the angles are similar to the pure system, where there is a change in the $15^o/30^o$ and $60^o/75^o$, shown for example in the EXAFS at 7.5Å^{-1}, indicated by the arrow. The FT-EXAFS indicate that the features for the Ir-Ir paths have a strong angular dependence, where as the Ir-Te do not. It is interesting to note that the Ir-Ir structure at 300K is more defined in these measurements than in the pure compound. For comparison, the 15^o data across all temperatures has been plotted in figure 6.4.23. Due to the extended temperature range measured, there is a clear thermal effect on the amplitude of the signal. The most significant structural change is seen at 3.7Å, representing the Ir_S paths. Across the transition at 140K, the lower end of this feature becomes more rounded in the low temperature phase. This suggests that the dimerized Ir paths either becomes more defined or contributes more to the signal, indicating that there is a change associated with these paths.

The angular dependence on the signal for the $x = 0.05$ composition is shown in figure 6.4.24, plotted in both EXAFS and FT-EXAFS. The quality of the data appears slightly worst than the other compositions, where distortions in the data appear from approximately 9Å^{-1}. A k-range of 3Å - 12.5Å has been used for all data sets. Again the changes seen across the angles are consistent with the $x = 0.00$ and 0.02 data, where the largest changes are seen for the Ir-Ir paths. All temperatures measured for the 15^o angle for comparison are shown in figure 6.4.25. There is a clear thermal effect in the overall amplitude of the signal, seen as an increase in the amplitude at lower temperatures. This composition should not show the metal-insulator transition, which is reflected in the data. There is no clear structural change seen in the EXAFS data. A small difference between the 300K and 250K data in the FT-EXAFS in the Ir region (3-4Å) is most likely a thermal effect rather than structural.

Beat effect

To verify that both the undistorted and dimerized Ir-Ir paths are present in both compositions, an analysis of the back Fourier transform has been carried out to check if a beat effect is seen for these paths. Table 6.4.7 shows the position of the minimum for both compositions, across all angles and temperatures. The values obtained are comparable to that from the pure sample (table 6.4.3) suggesting firstly that both paths are present in all data sets and secondly that the difference between these paths are similar across all compositions. This gives confidence in applying a fitting model which considers Ir-Ir dimers.

$Ir_{1-x}Pt_xTe_2$, x = 0.02

	Angle			
Temperature (K)	**15^o**	**30^o**	**60^o**	**75^o**
300	9.6±0.3	9.7±0.3	9.7±0.3	9.6±0.3
250	9.8±0.3	9.6±0.3	9.8±0.3	9.7±0.3
200	9.9±0.3	9.7±0.3	9.7±0.3	9.7±0.3
100	9.5±0.3	9.6±0.3	9.6±0.3	9.4±0.3
55	9.4±0.3	9.4±0.3	9.6±0.3	9.5±0.3
$Ir_{1-x}Pt_xTe_2$, x = 0.05				
300	9.6±0.3	10.0±0.3	9.8±0.3	9.8±0.3
250	9.4±0.3	-	9.7±0.3	-
200	9.6±0.3	-	9.5±0.3	-
55	9.6±0.3	9.8±0.3	9.8±0.3	9.8±0.3

Table 6.4.7: $Ir_{1-x}Pt_xTe_2$ (Ir L_3-edge), $x = 0.02$, 0.05 beat effect: minimum for the beat with relation to the Ir_L and Ir_S. The dash mark (-) indicates no data available for the temperature/angle.

(a)

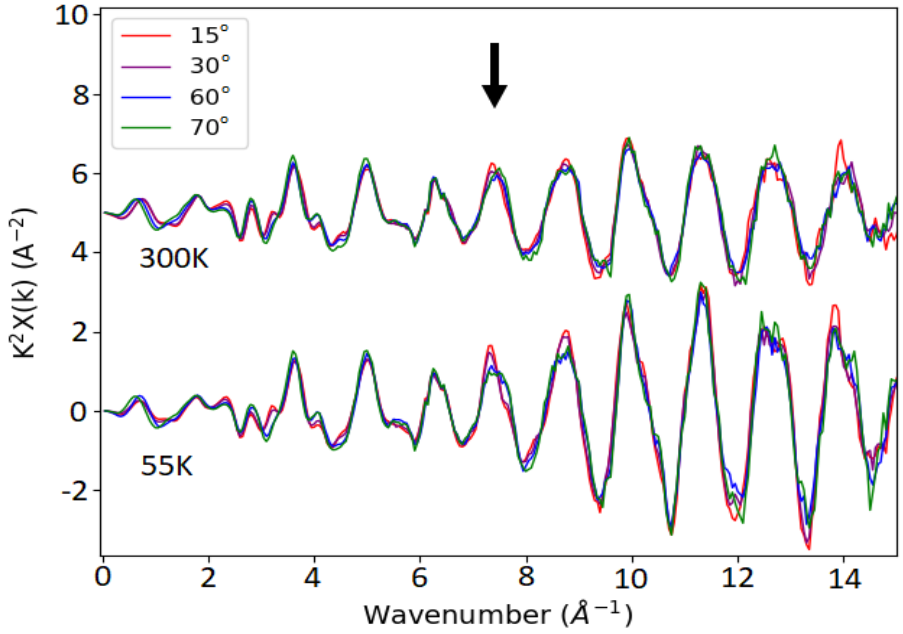

(b)

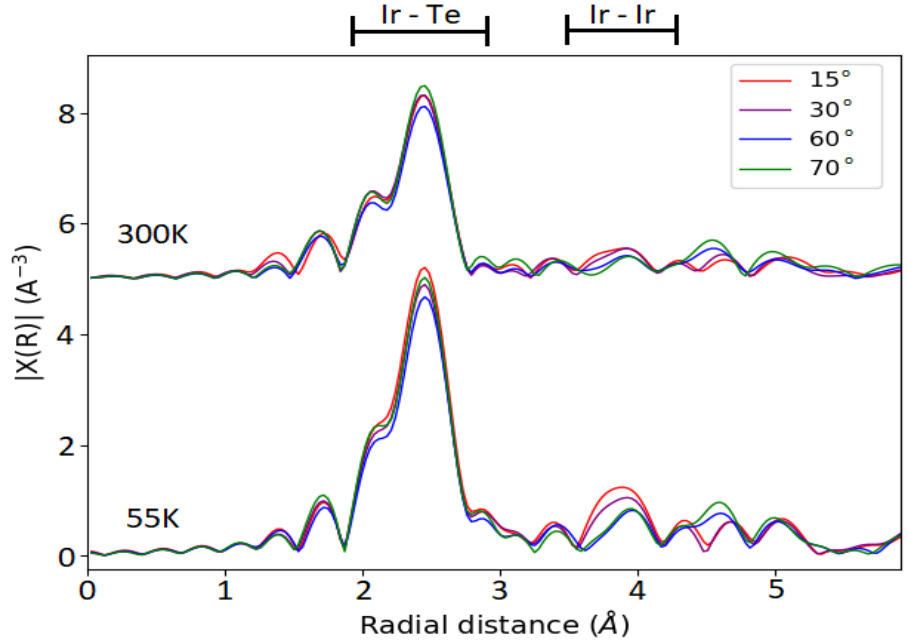

Figure 6.4.22: a) EXAFS and b) FT-EXAFS for $Ir_{1-x}Pt_xTe_2$ (Ir L_3-edge), $x = 0.02$ sample. Showing the angular dependence of these measurements at both 300K and 55K. Also indicated are the two regions of interest, identifying the Ir-Te and Ir-Ir contributions in the FT-EXAFS.

(a)

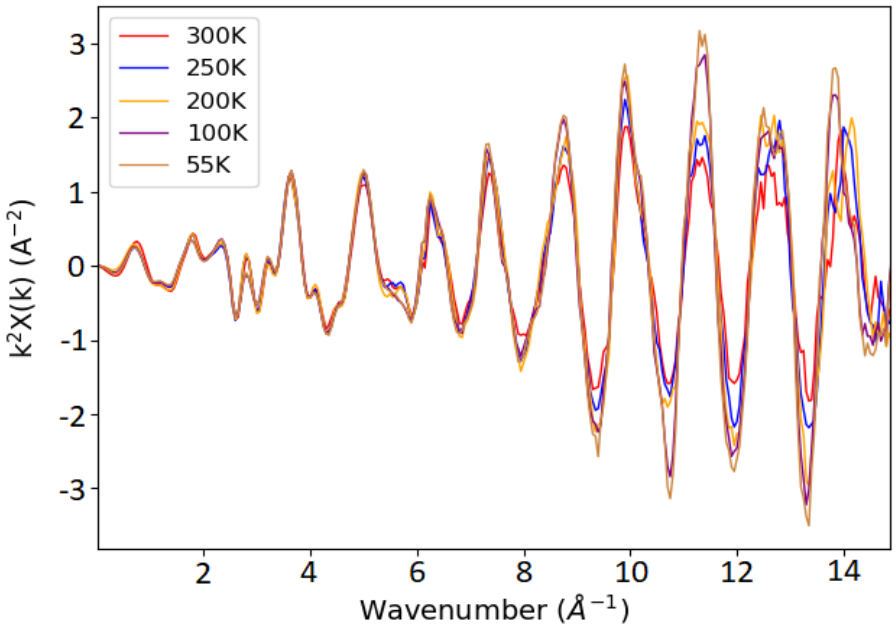

(b)

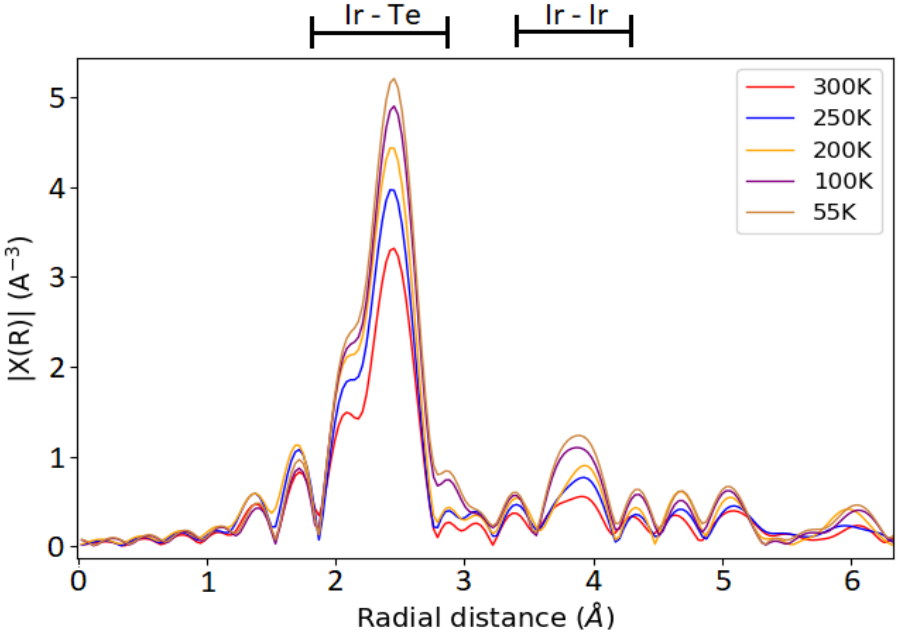

Figure 6.4.23: a) EXAFS and b) FT-EXAFS for $Ir_{1-x}Pt_xTe_2$ (Ir L_3-edge), $x = 0.02$ sample. Showing data for the 15^o angle across the transition at 140K. Also indicated are the two regions of interest, identifying the Ir-Te and Ir-Ir contributions in the FT-EXAFS.

(a)

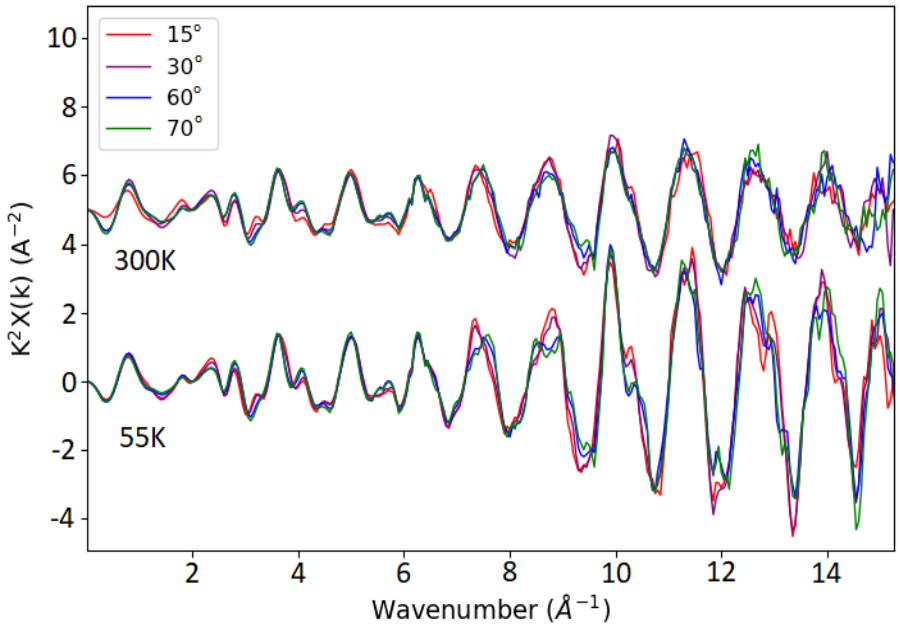

(b)

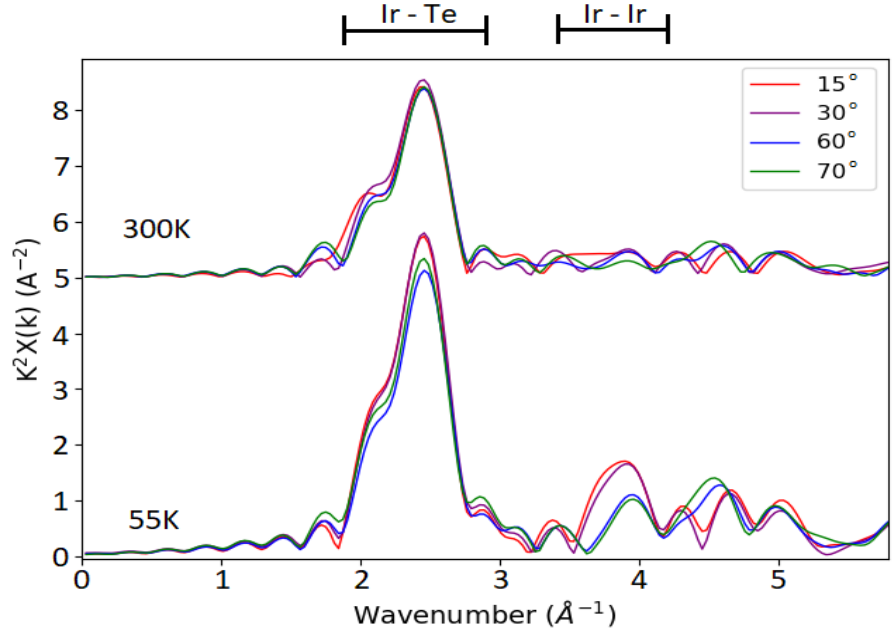

Figure 6.4.24: a) EXAFS and b) FT-EXAFS for $Ir_{1-x}Pt_xTe_2$ (Ir L_3-edge), $x = 0.05$ sample. Showing the angular dependence of these measurements at both 300K and 55K. Also indicated are the two regions of interest, identifying the Ir-Te and Ir-Ir contributions in the FT-EXAFS.

(a)

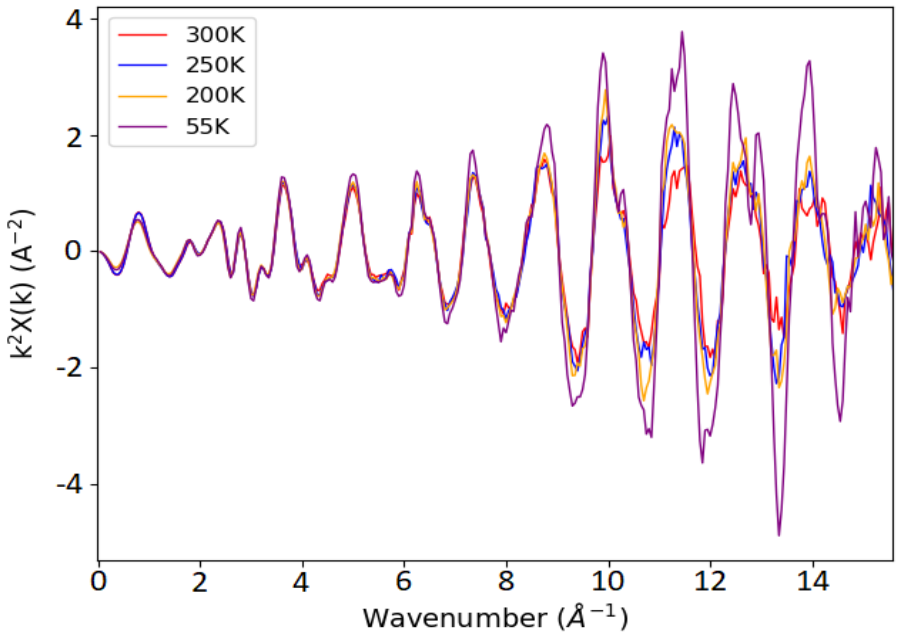

(b)

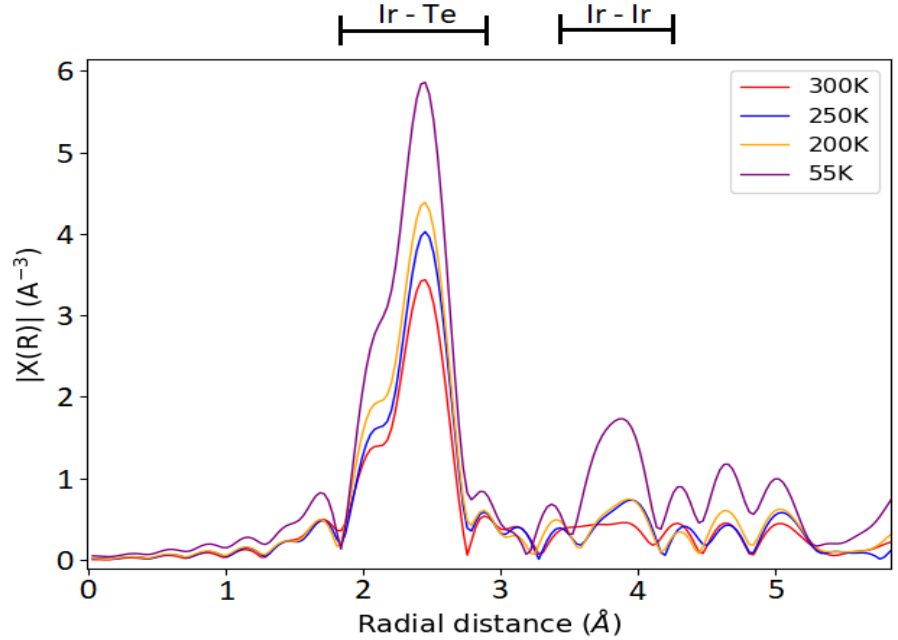

Figure 6.4.25: a) EXAFS and b) FT-EXAFS for $Ir_{1-x}Pt_xTe_2$ (Ir L_3-edge), $x = 0.05$ sample. Showing data for the 15^o angle. Also indicated are the two regions of interest, identifying the Ir-Te and Ir-Ir contributions in the FT-EXAFS.

Fitting

To understand how the structures of the doped compounds differ from the pure, the same fitting procedure and models have been applied (table 6.4.4). While it is expected that the Pt dopant will affect the structure, due to the relatively small amounts considered it has been assumed that the distortions will be taken into account by the fitting parameters. Given that from the beat analysis it has been shown that both Ir_L and Ir_S paths are present, the same two models for the Ir structure used for the pure compound have been applied to the $x = 0.02$ sample. The transition has been fully suppressed in the $x = 0.05$ sample, so only model 1 for the HT phase has been applied. The second transition seen in the pure sample is expected to be suppressed in both compositions.

The results from the fits on the $x = 0.02$ compound for both models are shown in tables 6.4.8-6.4.9 and example fits are shown in figures 6.4.26-6.4.27. The $x = 0.05$ compound fitting results and example fits are shown in table 6.4.10 and figures 6.4.28- 6.4.29. Data have been extracted from a k-range of 3Å^{-1} - 12.8Å^{-1} and the fitting has been carried out in R-space using a range of 2.1Å - 4.3Å with k-weightings of 1, 2 and 3. The number of independent statistical points available range between 56 - 71 and the number of variables used is 16 (apart from the 250K, 200K $x = 0.05$ fitting, due to having only 2 angles available). The R-factor ranges between 0.007-0.016, but the average is slightly larger than in the pure compound, which may suggest higher disorder in these samples. The E_0 values have been allowed to vary for all data sets and show a reasonably stable position, which is consistent with the XANES analysis. The global S_0^2 value takes into account amplitude reduction factors. This value varies between 0.86-1.02, with a general increase seen across the angles.

The Ir-Te and Ir-Ir path lengths and Debye-Waller factors from each model for the $x = 0.02$ and 0.05 have been plotted in figures 6.4.30 - 6.4.31 and 6.4.32. The Ir-Te path lengths and Debye-Waller factors are consistent across the two models. There is a small change across the transition at 140K in the path lengths, reflecting a similar change when compared to the pure compound and the Debye-Waller factor shows a general decrease as a function of temperature consistent with thermal effects. This path for the $x = 0.05$ compound is consistent in all measurements which reflects that no transition is present in this system and further confirms that the changes in this path are directly related to the transition.

The Ir-Ir paths for the $x = 0.05$ compound show consistent values for both Ir_L and Ir_S paths and reasonable Debye-Waller factors when using model 1. This confirms that without a transition both paths are present and the most likely scenario for the dimerized paths is that they are in a disordered state. Both models have been tested for the $x = 0.02$ compound. Model 1, representing disordered Ir_S paths, shows reasonable values for the path lengths and Debye-Waller values above the transition but these values become large below 140K, with a significant error associated with the values. Modelling an ordered dimer system, model 2 shows reasonable values below the transition. These fits show again that there is a change in the nature of the structure across the transition and similar to the pure compound it suggest an order-disorder like transition (consistent with the observations in the pure material). Similar to the pure compound it is important to note that some of the Debye-Waller factors can be negative with the error bars. While this typically suggests that there is an issue with fitting these paths, it is most likely due to fitting the angular dependence of the paths with the *ab*-plane orientation as a fitting parameter and the contribution to the signal is significantly less for the Ir_S compared to the Ir_L paths.

(a)

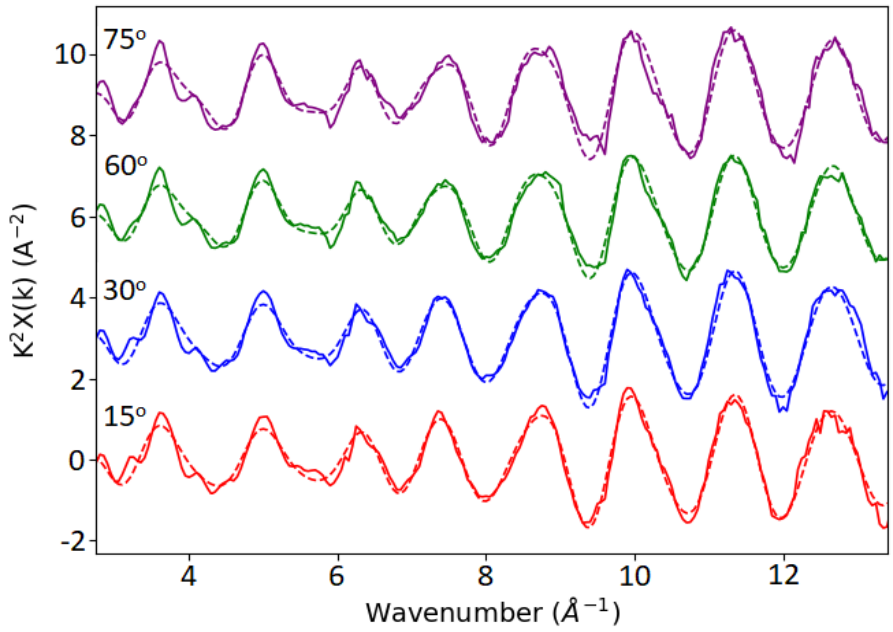

(b)

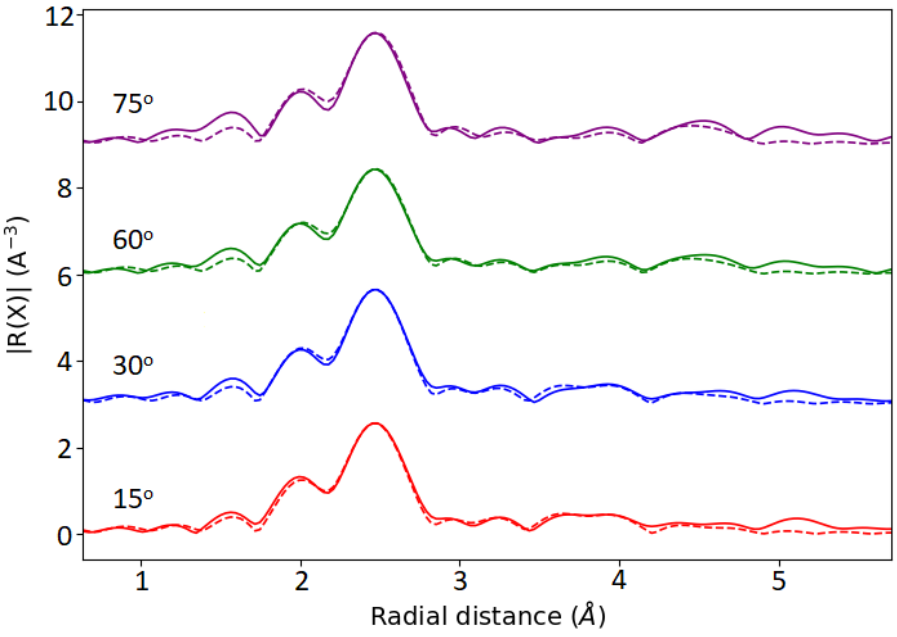

Figure 6.4.26: a) EXAFS and b) FT-EXAFS fitting examples for $Ir_{1-x}Pt_xTe_2$ (Ir L_3-edge), $x = 0.02$ at 300K using 4 angles. The dashed lines indicate the fitting result.

(a)

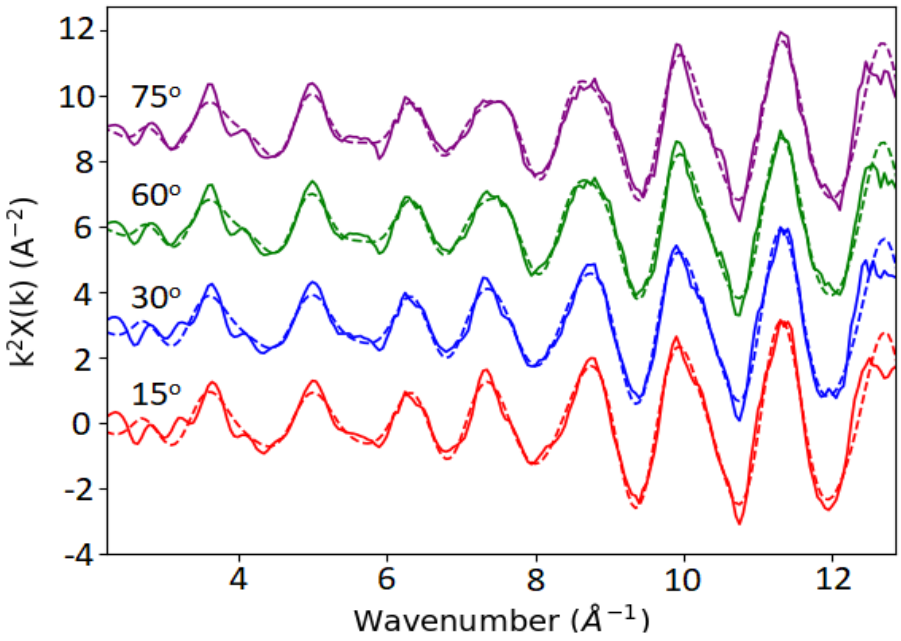

(b)

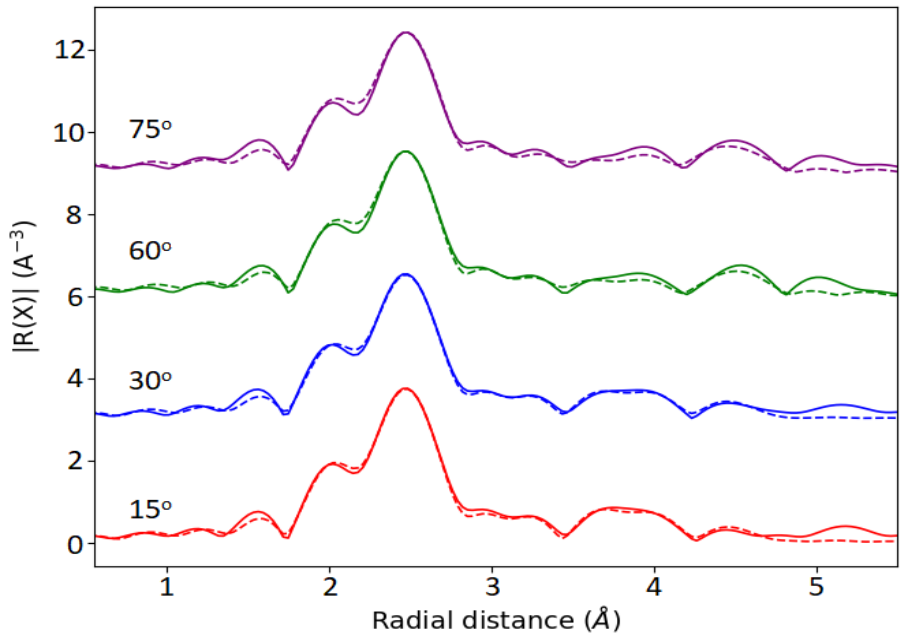

Figure 6.4.27: a) EXAFS and b) FT-EXAFS fitting examples for $Ir_{1-x}Pt_xTe_2$ (Ir L_3-edge), $x = 0.02$ at 55K using 4 angles. The dashed lines indicate the fitting result.

(a)

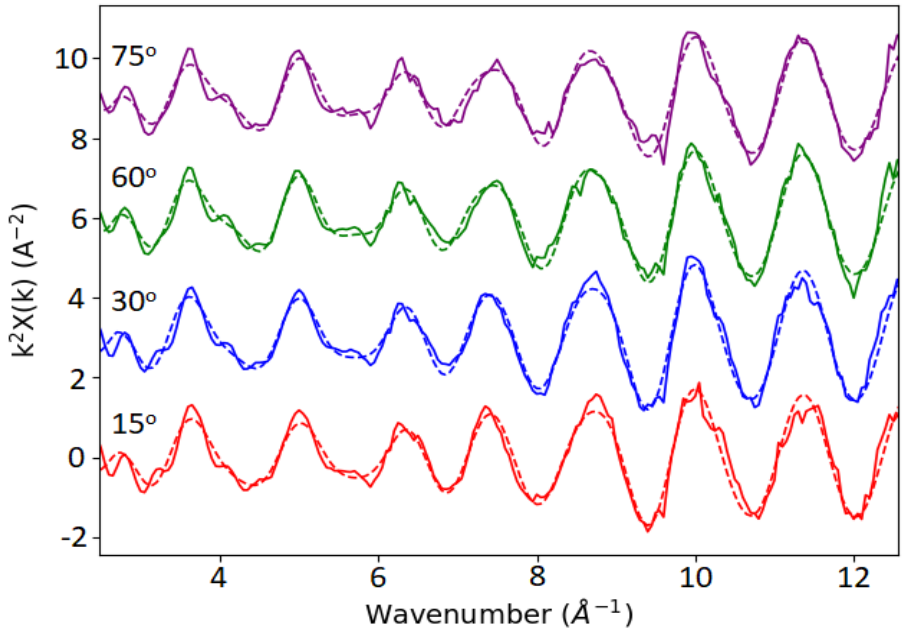

(b)

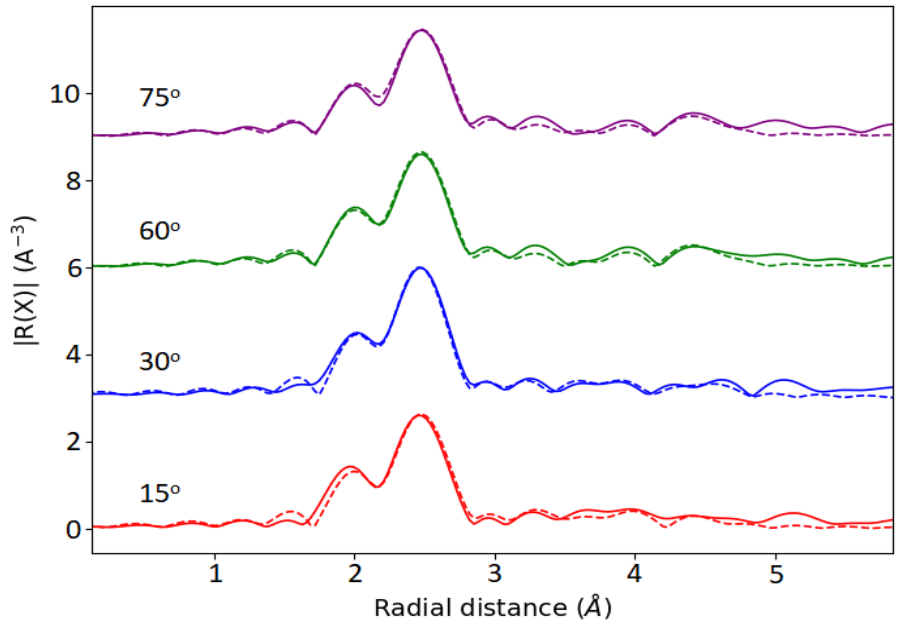

Figure 6.4.28: a) EXAFS and b) FT-EXAFS fitting examples for $Ir_{1-x}Pt_xTe_2$ (Ir L_3-edge), $x = 0.05$ at 300K using 4 angles. The dashed lines indicate the fitting result.

(a)

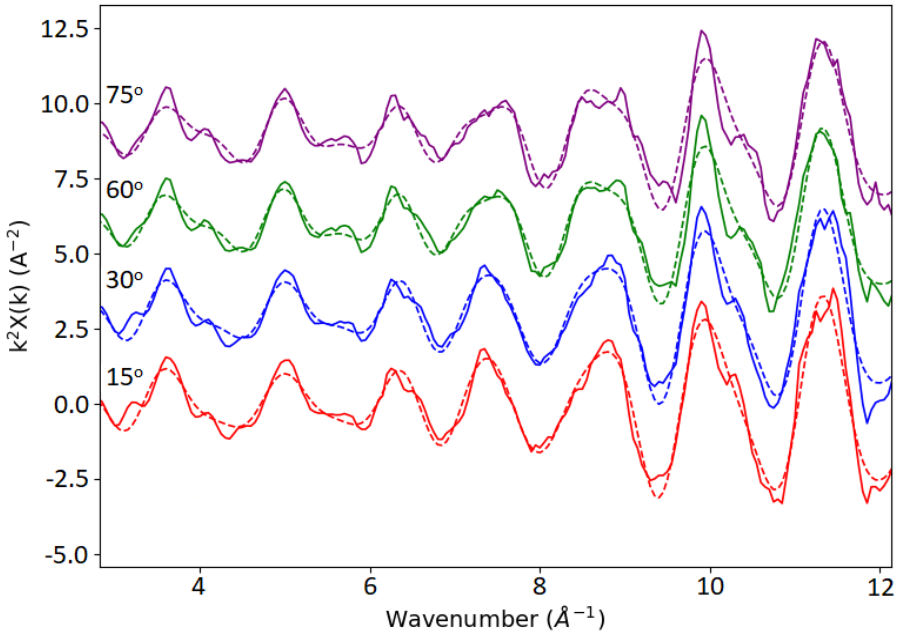

(b)

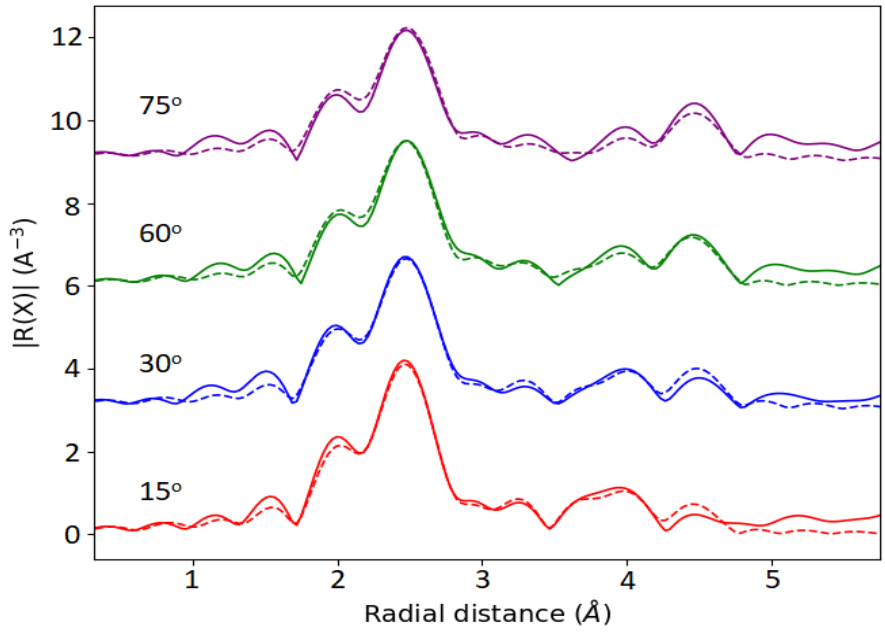

Figure 6.4.29: a) EXAFS and b) FT-EXAFS fitting examples for $Ir_{1-x}Pt_xTe_2$ (Ir L_3-edge), $x = 0.05$ at 55K using 4 angles. The dashed lines indicate the fitting result.

Parameters	300K	250K	200K	100K	55K
ΔE_0 (eV)	5.9±0.5	6.0±0.6	6.3±0.5	6.2±0.5	6.3±0.4
S_o^2 - (15^o)	0.82±0.04	0.85±0.04	0.87±0.04	0.84±0.03	0.86±0.03
S_o^2 - (30^o)	0.90±0.04	0.90±0.04	0.89±0.04	0.84±0.04	0.85±0.04
S_o^2 - (60^o)	0.93±0.04	0.94±0.05	0.95±0.05	0.90±0.04	0.91±0.04
S_o^2 - (75^o)	1.01±0.06	0.95±0.06	0.93±0.06	0.92±0.05	0.94±0.05
1^{st} Ir-Te R (Å)	2.640±0.001	2.640±0.002	2.640±0.002	2.641±0.001	2.641±0.001
1^{st} Ir-Te σ^2 ($Å^2$)	0.0028±0.0002	0.0021±0.0003	0.0016±0.0003	0.0008±0.0002	0.0007±0.0002
Ir-Ir Dimer (Ir_S) R (Å)	3.88±0.03	3.86±0.02	3.87±0.02	3.90±0.02	3.90±0.03
Ir-Ir Dimer (Ir_S) σ^2 ($Å^2$)	0.004±0.003	0.001±0.002	0.001±0.002	0.002±0.004	0.002±0.004
Ir-Ir (Ir_L) R (Å)	3.99±0.03	3.99±0.02	3.99±0.02	4.01±0.02	4.01±0.02
Ir-Ir (Ir_L) σ^2 ($Å^2$)	0.004±0.005	0.001±0.002	0.001±0.003	0.001±0.002	0.001±0.002
2^{nd} Ir-Te R (Å)	4.62±0.01	4.63±0.01	4.63±0.01	4.62±0.01	4.619±0.008
2^{nd} Ir-Te σ^2 ($Å^2$)	0.010±0.001	0.008±0.001	0.007±0.001	0.007±0.001	0.006±0.001
R-Factor	0.015	0.015	0.016	0.011	0.010
Independent points	64.0	62.2	62.9	59.4	62.5
Variables	16	16	16	16	16

Table 6.4.8: $Ir_{1-x}Pt_xTe_2$, $x = 0.02$: EXAFS fitting parameters for data between 300K-55K. Model 1: Ir-Ir dimers fitted along all Ir-Ir paths

Parameters	300K	250K	200K	100K	55K
ΔE_0 (eV)	5.9±0.5	5.9±0.6	6.2±0.7	6.2±0.5	6.3±0.5
S_o^2 - (15^o)	0.84±0.04	0.85±0.04	0.87±0.04	0.85±0.03	0.86±0.04
S_o^2 - (30^o)	0.91±0.04	0.91±0.04	0.89±0.04	0.84±0.04	0.85±0.04
S_o^2 - (60^o)	0.94±0.04	0.94±0.05	0.95±0.05	0.91±0.04	0.91±0.04
S_o^2 - (75^o)	1.02±0.05	0.95±0.06	0.92±0.06	0.93±0.05	0.93±0.05
1^{st} Ir-Te R (Å)	2.638±0.001	2.638±0.002	2.639±0.001	2.642±0.001	2.641±0.001
1^{st} Ir-Te σ^2 ($Å^2$)	0.0029±0.0002	0.0021±0.0003	0.0016±0.0003	0.0008±0.0002	0.0007±0.0002
Ir-Ir Dimer (Ir_S) R (Å)	3.91±0.01	3.84±0.02	3.84±0.01	3.88±0.03	3.88±0.03
Ir-Ir Dimer (Ir_S) σ^2 ($Å^2$)	0.01±0.01	-0.001±0.002	-0.001±0.002	0.001±0.004	0.001±0.004
Ir-Ir (Ir_L) R (Å)	3.93±0.02	3.97±0.01	3.97±0.01	3.99±0.01	3.99±0.01
Ir-Ir (Ir_L) σ^2 ($Å^2$)	0.005±0.002	0.001±0.002	0.001±0.001	0.001±0.002	0.001±0.002
2^{nd} Ir-Te R (Å)	4.62±0.01	4.62±0.01	4.63±0.01	4.620±0.009	4.620±0.008
2^{nd} Ir-Te σ^2 ($Å^2$)	0.010±0.001	0.008±0.001	0.007±0.001	0.007±0.001	0.006±0.001
R-Factor	0.016	0.015	0.016	0.011	0.010
Independent points	71.0	61.5	61.5	61.5	61.5
Variables	16	16	16	16	16

Table 6.4.9: $Ir_{1-x}Pt_xTe_2$, $x = 0.02$: EXAFS fitting parameters for data between 300K-55K. Model 2: Ir-Ir dimers fitted along one Ir-Ir path (a-axis)

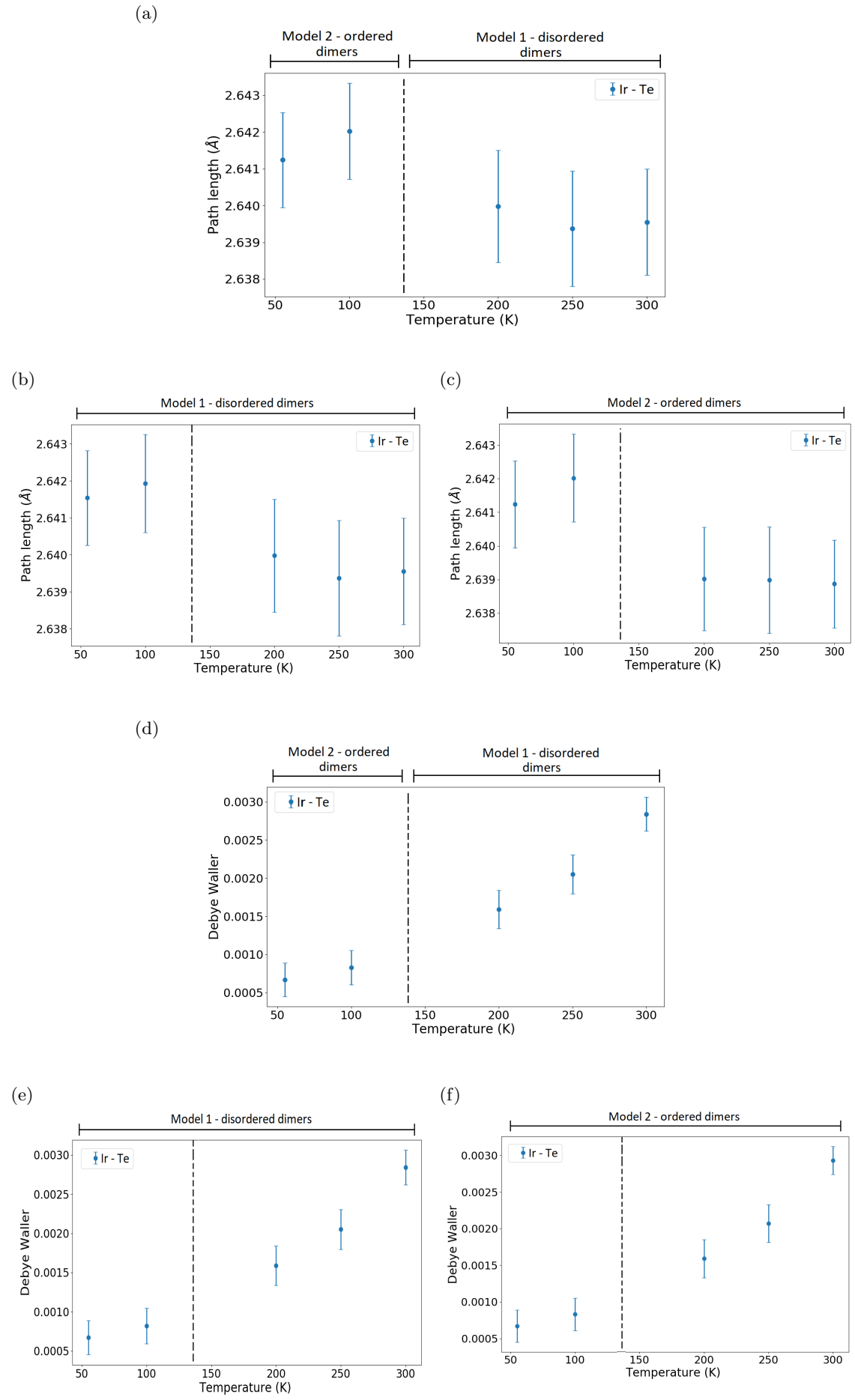

Figure 6.4.30: Fitting parameters for Ir-Te paths for $Ir_{1-x}Pt_xTe_2$ $x = 0.02$. (a)-(c) Path lengths, (d)-(f) Debye-Waller factors. (a)/(d) - model 1 applied to 280K and above, model 2 applied to below 280K. (b)/(e) - model 1 only, (c)/(f) - model 2 only. Dashed lines indicate transitions.

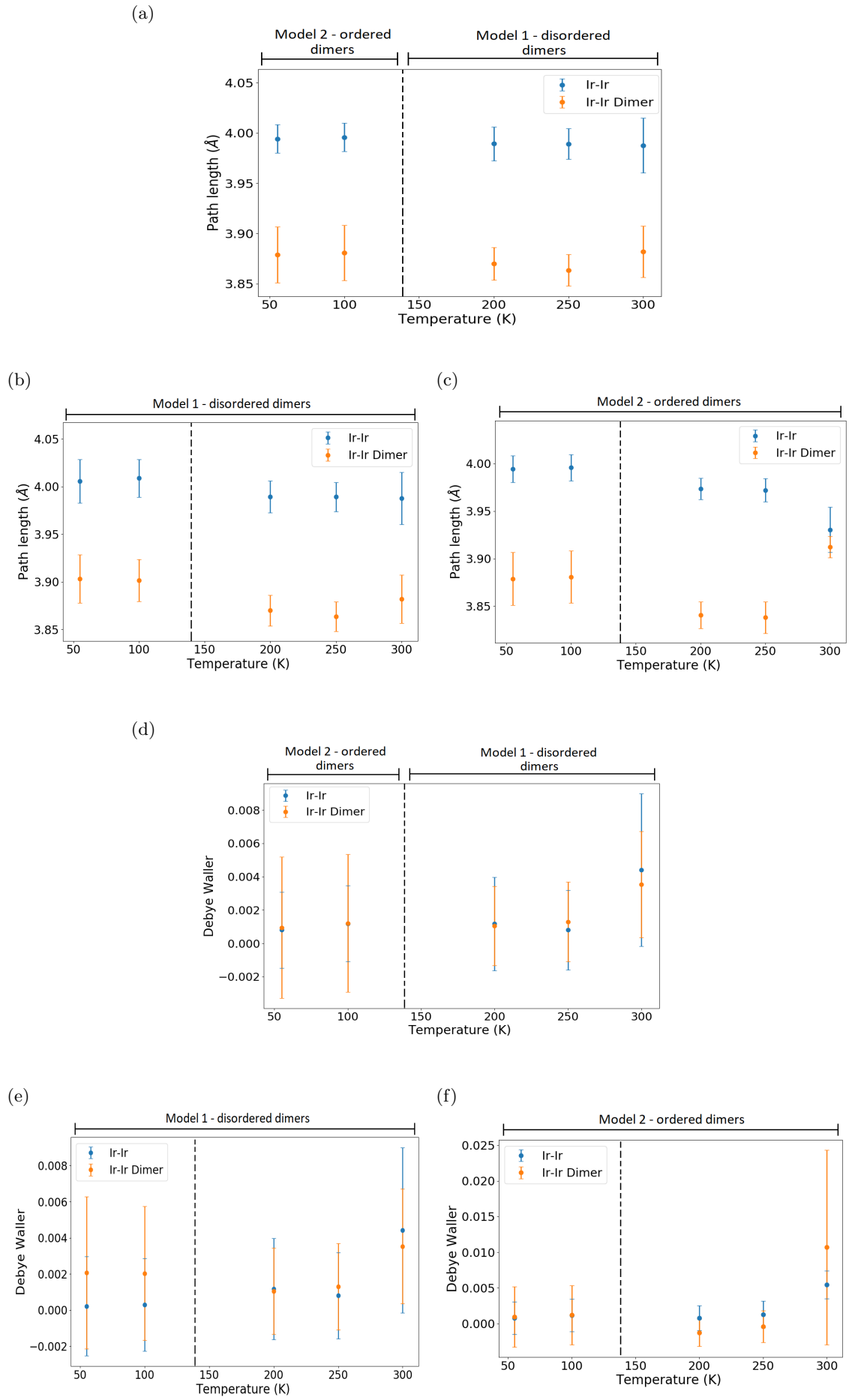

Figure 6.4.31: Fitting parameters for Ir-Ir paths (Ir$_L$ - blue, Ir$_S$ - orange) for $Ir_{1-x}Pt_xTe_2$ $x = 0.02$. (a)-(c) Path lengths, (d)-(f) Debye-Waller factors. (a)/(d) - model 1 applied to 280K and above, model 2 applied to below 280K. (b)/(e) - model 1 only, (c)/(f) - model 2 only. Dashed lines indicate transitions.

Parameters	300K	250K	200K	100K
ΔE_0 (eV)	6.1±0.5	6.3±0.5	5.7±0.6	6.1±0.6
S_o^2 - (15^o)	0.86±0.05	0.96±0.04	0.86±0.04	0.93±0.05
S_o^2 - (30^o)	0.99±0.05	-	-	0.95±0.05
S_o^2 - (60^o)	1.06±0.06	1.07±0.06	0.95±0.06	0.99±0.06
S_o^2 - (75^o)	1.01±0.05	-	-	0.99±0.06
1^{st} Ir-Te R (Å)	2.637±0.002	2.637±0.002	2.637±0.002	2.636±0.002
1^{st} Ir-Te σ^2 ($Å^2$)	0.0029±0.0002	0.0028±0.0003	0.0016±0.0003	0.0006±0.0003
Ir-Ir Dimer (Ir_S) R (Å)	3.85±0.01	3.84±0.02	3.85±0.02	3.86±0.02
Ir-Ir Dimer (Ir_S) σ^2 ($Å^2$)	0.002±0.002	0.005±0.004	0.002±0.003	0.002±0.003
Ir-Ir (Ir_L) R (Å)	3.98±0.02	3.97±0.01	3.98±0.01	3.99±0.02
Ir-Ir (Ir_L) σ^2 ($Å^2$)	0.002±0.003	0.001±0.002	0.001±0.002	0.001±0.002
2^{nd} Ir-Te R (Å)	4.59±0.01	4.59±0.02	4.61±0.02	4.613±0.007
2^{nd} Ir-Te σ^2 ($Å^2$)	0.013±0.002	0.012±0.002	0.012±0.003	0.004±0.007
R-Factor	0.015	0.007	0.009	0.014
Independent points	56.2	26.9	29.2	54.7
Variables	16	12	12	16

Table 6.4.10: $Ir_{1-x}Pt_xTe_2$, $x = 0.05$: EXAFS fitting parameters for data between 300K-55K. Model 1: Ir-Ir dimers fitted along all Ir-Ir paths. Dashed marks (-) indicate no available data.

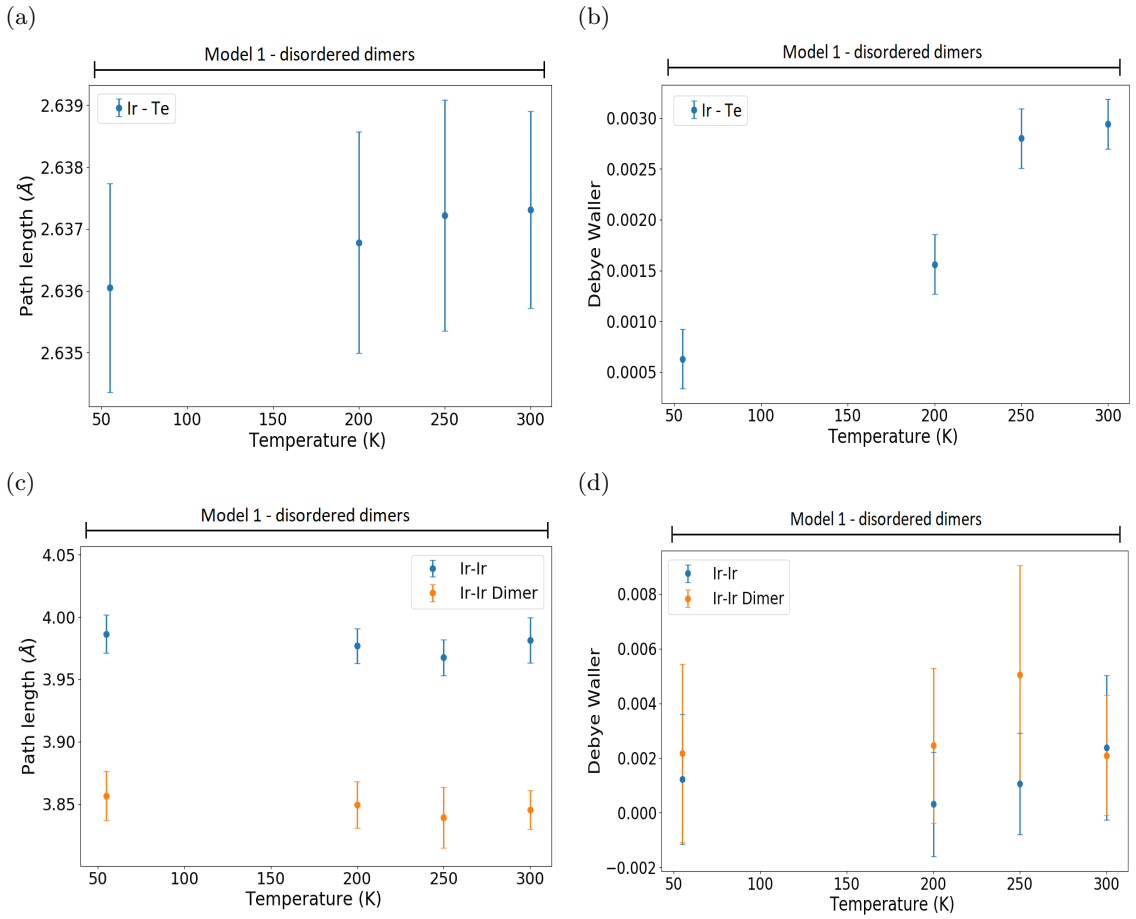

Figure 6.4.32: Fitting parameters for $Ir_{1-x}Pt_xTe_2$ $x = 0.05$. (a)-(b) Ir-Te path lengths and Debye-Waller factors. (c)-(d) Ir-Ir (Ir_L - blue, Ir_S - orange) path lengths and Debye-Waller factors.

6.4.4 DFT simulations

First-principle calculations have been carried out to address the XANES post-edge region on the high and low temperature $IrTe_2$ parent material. 3 structures have been simulated. A high temperature structure for comparison with the literature to confirm suitable parameters (no dimers). Two low temperature structures simulating the ordered dimers and Te octahedra are also shown. While it is not possible to fully separate the two changes, the structures used allows for the identification of the changes that are responsible for the XANES structure. Specific details of these simulations are given below, with the Exciting package described in section 3.5.1. To give further insight into the electronic changes that result in the intensity increase of certain features across the transition, the L_2 spectra, band structure and density of states have been produced. The reported HT phase based on the initial structure used for the EXAFS analysis (Table 6.4.4) gives a suitable reference model to compare the two major structural changes below the transition. It should be noted that it was not possible to model the high temperature structure with disordered dimers. The reason for this is that both FDMNES and Exciting require an inputted structure of the unit cell which is then repeated to form a super-lattice. To model disorder the unit cell would need to be very large and hence the calculation would become extremely computationally expensive. It would be possible to run this calculation via a cluster model. However this technique is outside the scope of this thesis. The ordering of the Ir dimers has been modelled using the structural data from the fitting analysis where $Ir_L = 3.973$Å and $Ir_S = 3.810$Å. There is one dimerized path for every five undistorted paths, representing the $Q_{1/5}$ structure. The compression of the Te octahedra has been modelled separately and based of the reported path lengths given in [214]: two opposite Ir-Te paths have been shortened to 2.638Å and 4 have effectively been elongated to 2.688Å (Ir-Te path length). The structures have been built in Material Studios [228] with a coarse geometrical optimization using CASTEP [229] to ensure a reasonable structure. The structures for $IrCl_3$, IrO_2 and both LT $IrTe_2$ are given in section B.2.

The groundstate calculations for each structure have been kept consistent to ensure that a comparison can be made. A generalized gradient approximation (GGA), Perdew-Burke-Ernzerhof (PBE) [121] exchange-correlation functional has been used. While a local density approximation (LDA), Perdew-Wang (PW) [120] has been tested, it was unable to reproduce the band separation around the Fermi level when compared to the literature on similar simulations. Due to the large atomic numbers of the elements in this compound, the spin-orbit coupling has also be considered. A k-grid of 5x5x5[6] has been used to sample the Brillouin zone and $R_{MT}G_{max}$, which determines the number of augmented planewaves, has been converged to 8.0. To ensure an accurate groundstate, the total energy and effective potential have been converged within a set of limits during the self-consistent cycles. The convergence limit for the absolute change in total energy was set to 1×10^{-4} (compared to the previous iteration). The convergence limit for the root mean squared change in effective potential was set to 1×10^{-5} (compared to the previous iteration). The density of states has been calculated using a k-grid size of 15x15x15[7] to ensure a sufficient sampling to map the partial density of states (PDOS).

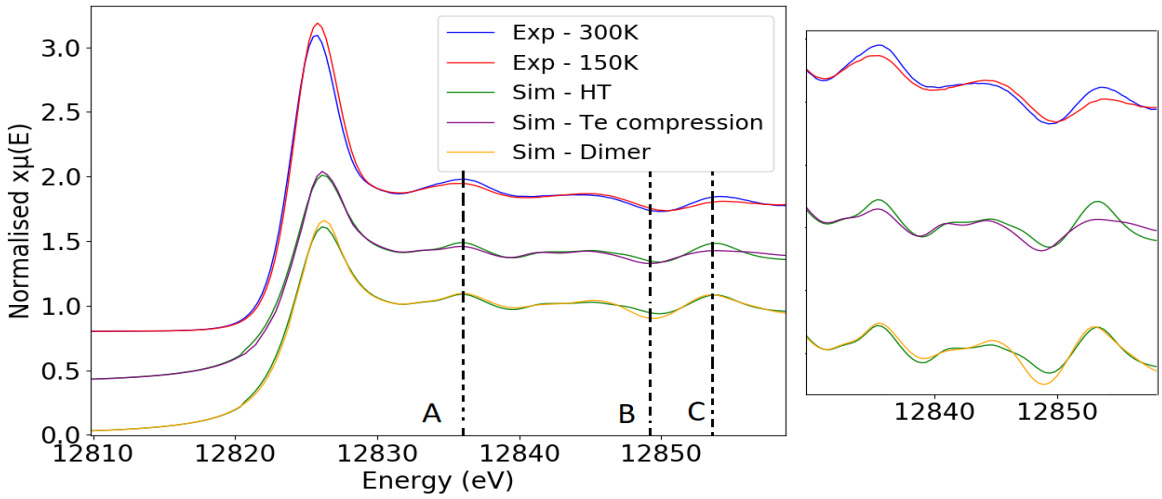

Figure 6.4.33: $IrTe_2$ Simulated spectra (Ir L_2-edge), shown at 0^o along the ab-plane, with close up of features after peak.

[6]Note: k-grid is represented along the basis vector directions (a, b, c), with the sampling points evenly spread.
[7]Please see footnote 6

The calculated XANES spectra for the 3 models and the experimental data are shown in figure 6.4.33 alongside a close up view of the features after the whiteline. All spectra have been normalized and both the Te compression and dimer structure are shown with the simulated high temperature phase. Features defined as A and C show a small reduction in intensity when the Te is compressed which is in good agreement with the experimental data. However this is not the case with the dimer structure which shows very little change. There is a difference between the simulated Te compressed structure and the simulated HT structure, shown as feature B, which is not seen in the experimental spectra. This disagreement has not been accounted for. The whiteline feature shows a stable position in both cases. However there is an intensity increase relative to the high temperature simulated structure for the ordered dimers. The results suggests that the changes seen after the whiteline are driven by the Te compression while the whiteline change is related to the dimer ordering.

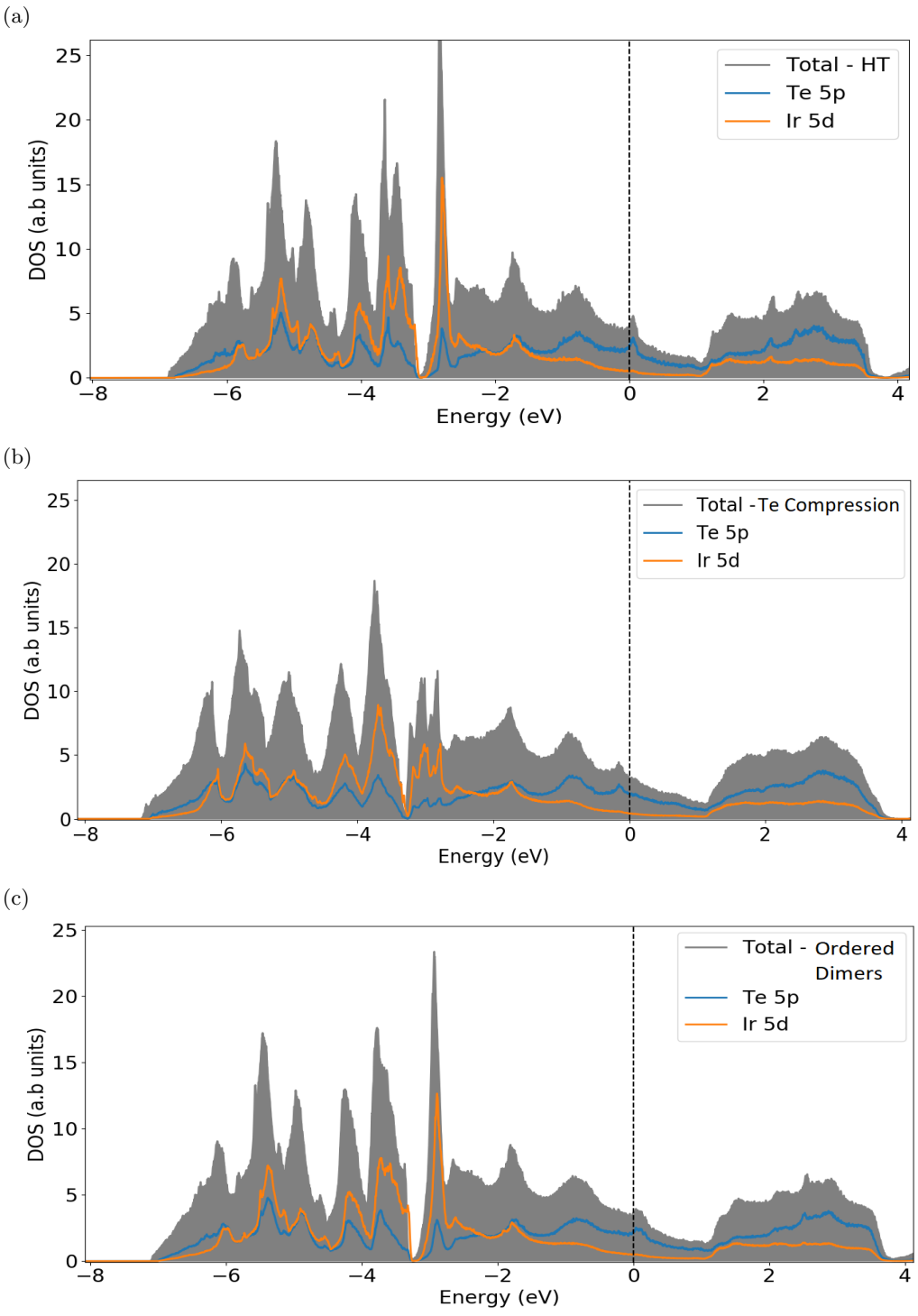

Figure 6.4.34: Density of states with Ir d and Te p orbital partial states for $IrTe_2$ structure. a) high temperature phase, b) Te compression, c) Dimer structure

Figure 6.4.34 shows the calculated density of states for the high temperature, Te compression and ordered dimer structures. In all cases the overall density is shown in grey, with both the Te 5p and Ir 5d partial states shown. Comparison between the high temperature phase and the ordered dimer system shows very little difference, especially around E_F. It indicates that the ordering of the dimers has very little effect on the overall density of states and that this is most likely not the mechanism for the transition. Comparison with the structure in which the Te is compressed however does show significant differences. There are some changes below E_F in both the Ir and Te orbitals. Around the Fermi energy the changes are more subtle however may indicate a mechanism for the transition. The Te 5p orbitals show a redistribution of charge across the E_F, indicated by a small feature at the E_F in the high temperature phase which is shifted to a lower energy in the Te compressed system. This result is similar to the literature, in particular to [16] in which it is suggested that the increase below E_F in the Te 5p orbitals would have the result of decreasing the kinetic energy of the electrons and this could be a driving force for the transition.

The calculated band structures for the simulated structures are shown in figure 6.4.35, where both the Te *p* and Ir *d* character has been plotted. The ordered dimer structure shows very little difference when compared to the high temperature phase similar to the density of states. Comparison between the Te compressed structure and high temperature phase reveal that the changes are mostly related to sections of bands which are dominated by Te character. For example, along the Γ-M direction at approximately 2.6eV there is a clear separation of bands, which can also be seen at the H point at the same energy. The overall structure in both case shows highly dispersive bands in all directions. Considering two adjacent layers (i.e Γ-M-K-Γ and A-L-H-A) and between the layers (i.e. Γ-A) the highly dispersive nature of all the bands suggests a very three dimensional electronic structure, which as noted in [211] is not favourable in the case of nesting and therefore separates $IrTe_2$ from CDW materials like $NbSe_2$.

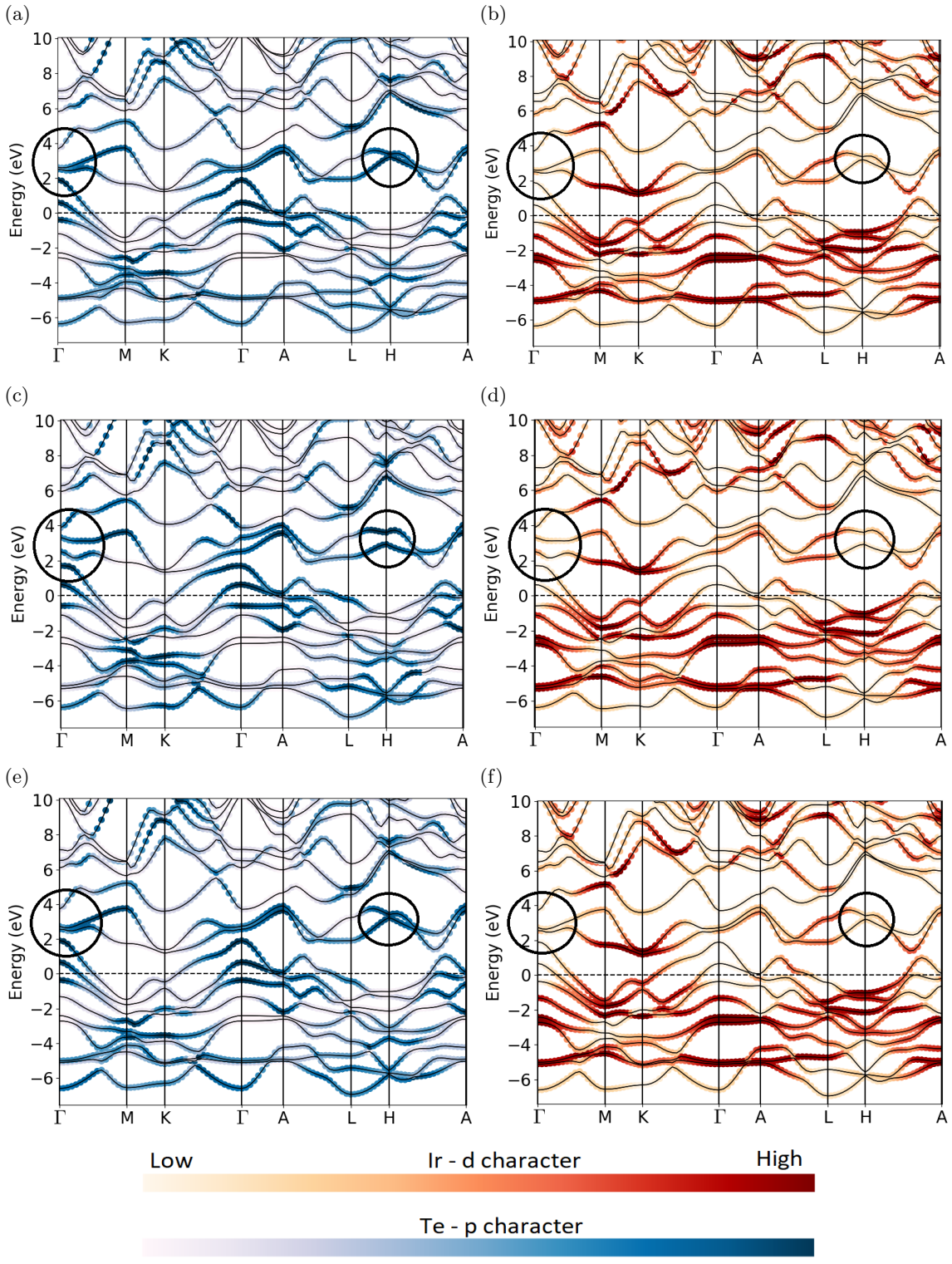

Figure 6.4.35: Calculated band structures for $IrTe_2$ with p and d character shown. a/b) high temperature phase, c/d) Te compression and e/f) dimer structure. Examples of the changes in the band structure due to the different phases have been highlighted.

6.5 Discussion

One of the key aims of this research has been to understand the Ir-Ir dimers in this system across the first order transition. This will be addressed first with respect to the $IrTe_2$ parent material. The back Fourier transform (beat effect) confirms that both Ir_L and Ir_S paths are present above and below both transitions and suggests a difference of approximately 0.16±0.01Å. To further understand if the Ir_S paths undergo an ordering transition, two models have been used. The results show that there is a change in the properties of the dimerized Ir paths. This can been seen when only one model is applied to the data, the fitting parameters drastically change across the transition at 280K. Model 1 which represents a system with disordered dimers shows realistic values for the path lengths and Debye-Waller factors above the transition. However, below the transition the Debye-Waller factors become significantly larger with errors which suggest this model is not correct for the low temperature phase. The difference between the Ir_L and Ir_S paths lengths (≈0.15Å) is in good agreement with the value calculated from the beat effect, further suggesting this model is applicable. The fitting parameters from model 2 which represented the order dimers along the *a*-axis, where 1 in 5 Ir-Ir paths are dimerized, is more realistic below the transition at 280K. The path lengths are consistent and while the Debye-Waller values have larger errors for the Ir_S paths compared to Ir_L, the values are reasonable. The increase in the error is a consequence of the Ir_S paths contribution to the signal being significantly weaker than the other paths. It is also important to note that some of the Debye-Waller values can be negative within the error. While this may indicate an unreliable fitting parameter, the most likely cause is again due to the weaker contribution of the Ir_S paths compared to the Ir_L paths. Again the difference in the paths is comparable to the beat effect values. The analysis of the structure shows that the dimerized Ir-Ir paths are present above and below the transition and suggests that this is an order-disorder like transition, which differs from the majority of the literature where diffraction data suggests dimers only form below the transition.

In interpreting these results it is important to understand the nature of the dimers. It has been generally accepted that there is a competition between lowering the internal energy upon the formation of dimers vs the vibration entropy which destabilizes the dimers at higher temperatures. It should also be noted that it has been previously shown that the Te atoms directly influence the dimers and stops the system from becoming fully dimerized. As diffraction data only detected dimers in the low temperature phase, it has been argued that the transition temperature is high enough to completely destroy the dimers. The results presented here show that this is not the case, that in fact the higher symmetry allows the internal energy gain to be favourable if the dimers are in a disordered state, within the *ab*-planes. This would suggest that the formation of dimers is not the mechanism involved in causing the transition, instead it seems to correlate to the ordering of those dimers. It has been suggested that below the 180K transition, the system undergoes a further ordering, where the wave vector changes to (1/8, 0, 1/8). Due to this transition being significantly weaker than the 280K transition it has been difficult to confirm if this data shows any differences between the low temperature phases through these measurements. However it does confirm that dimers are also present below 180K.

It has been suggested that the formation of the dimers causes a partial oxidation state change in the Ir, which pushes away nearby Te atoms. This causes the lattice deformation and it is a type of charge transfer mechanism that causes the less metallic system. The XANES data collected from a range of absorption edges and emission lines shows that there is no signature of an oxidation state change or any significant effect on the Ir valence (5d) electronic structure across either transition. When compared to the reference samples (IrO_2 and $IrCl_3$) it appears that the Ir is most likely in a +3 state. The branching ratio also shows no changes and a value of 0.73 is in line with a +3 Ir state. The valence-to-core spectra also confirms that the electronic structure of the Ir species is stable across both transitions. These results also confirm that the bonding interaction between the Ir and Te atoms does not undergo a significant change. This is important to note, as it suggests that the Te interaction with the Ir-Ir dimers is not responsible for the ordering effect below the transition. There is a small change seen in the intensity of the whiteline, which is preferential along the *ab*-plane. Given that the structural analysis shows a change in the Ir dimers, the most plausible explanation for this intensity increase is as a result from the ordering of the dimers, where Ir orbitals become slightly more localized due to an increase in the interactions within the Ir dimer chains. This has been consistent with the DFT simulations, which also indicate that the intensity change is a result from the ordering of the dimers.

The research presented in this thesis supports a scenario in which changes in the electronic structure of the Te are responsible for the transition at 280K[8]. While measurements have not been carried out on the Te species directly, due to a strong hybridization between the Te 5p and Ir 5d

[8]This may also be the mechanism for the second transition at 180K, however there is not sufficient information to address this.

orbitals, an insight in to the role of the Te can be given. After the whileline several features are seen to change across transition at 280K, which are within the XANES region. There is a decrease in the intensity of two features which are consistent across angles and edges and cannot be accounted for by the temperature variation. DFT simulations have been carried out on 3 structures, representing the different structural changes. The simulated XANES spectra show that the changes seen after the whiteline are a direct result for the compression of the Te octahedra rather than the ordering of the dimers and the magnitude of these changes are in very good agreement with the experimental data. The density of states show that the compression causes a change in the available tellurium states near the Fermi level, with a redistribution to lower energies. The bandstructure shows significant dispersion which rules out the possibility of a CDW mechanism and shows how changes within the bands are governed by the Te electronic structure rather than the Ir. The DFT results suggest that it is the Te structural changes that causes the most significant changes in the electronic structures and it is most likely this change that drives the transitions.

When the system is doped with Pt, the temperature of the transition is suppressed and at approximately 4% the transition is lost. The analysis of the atomic structure in the $Ir_{1-x}Pt_xTe_2$, $x = 0.02$ sample shows that the Ir dimers are present above and below the transition. The difference between these paths, calculated from the beat effect, is approximately 0.15Å which is confirmed from the fits. The fits show the same results as the pure sample where the most reasonable parameters come from fits where above the transition the Ir_S dimerized paths are disordered and below they are ordered along the a-axis. The $x = 0.05$ sample in which the transition is fully suppressed also shows dimerized paths in all temperatures measurement and the disordered dimer model is the most appropriate.

The dopant appears to have little effect on the electronic structure of the Ir species. The XANES analysis shows that the Ir is most likely in a 3+ state in both compositions and the small intensity change in the whiteline across the transition is seen in the $x = 0.02$ sample. Along with this, the changes seen after the whiteline are also present with the transition. This result shows that the mechanism responsible for the transition is the same as the pure system and that Ir dimers are present in all compositions and at all temperatures measured.

One area that has not been addressed with this research is the mechanism for the reduction and suppression of the first order transition once doped. The nature of this transition is the same when compared to the pure system, which suggests that it is not a change in Ir-Ir dimers or the Te compression which modulates the transition temperature. It has already been noted that as the level of dopant increases, so does the length of the a-axis. Given that this research has shown it is most likely the Te compression that drives the transition, it is important to consider the correlation between the a-axis lattice length and the Te-Te bonding. It was shown that the transition temperature increases when the $IrTe_2$ is doped with Se, which undergoes the opposite effect compared to the Pt dopant, where the increase in dopant reduces the size of the a-axis [230]. This suggests that the intralayer Te-Te bonding is an important factor. In the case of the Pt doping, the increase in the a-axis leads to a weakening of these bonds resulting in the lower transition temperature. This also suggests that the destabilization of the intralayer Te-Te bonding is the mechanism which drives the compression of the Te octahedra.

6.6 Conclusion

The structural analysis of the $IrTe_2$ sample shows that above and below both transitions, Ir-Ir dimers are present. The analysis suggests that in terms of the dimers, this is a structural order-disorder type of transition, where above 280K the dimers are in a disorder state within the ab-plane, between 280K-180K they become ordered along the a-axis where 1-5 Ir-Ir paths are dimerized and finally below 180K there is a further modulation where the dimers still persist. The XANES data reveals that there is no significant change in the electronic structure of the Ir species. From this research it would appear that the Ir species is not the driving force of the first order transition. With DFT simulations showing that the reported changes in the Te octahedra causes the most significant changes in the overall electronic structure. It suggests that the redistribution and reduction in the kinetic energy of the associated electrons is responsible for the reduction in conductivity.

When the system is doped, the analysis indicates that the Ir-Ir dimers are still present above and below the transition in the $x = 0.02$ composition, where the transition temperature is reduced. It is also found that the same type of order-disorder transition occurs, with little changes seen in the XANES. This suggests that the transition occurs through the same mechanism as in the pure sample. When the transition is fully suppressed in the $x = 0.05$ compound, the dimers are still present (at least above the superconducting phase).

Chapter 7

Ca_2RuO_4: study of the first order Mott transition

Two scenarios have previously been suggested for the metal to insulator (MI) transition in the 4d Ca_2RuO_4 system. These scenarios suggest different mechanisms for the Mott-type insulator, involving different orbital occupations. While experiments have shown a significant change in the structure in this compound, the electronic transition is not yet fully resolved. In this chapter XAS measurements track both the electronic and atomic changes across the MI transition. It is shown that along with a compression of the octahedra, there is a charge transfer between the non-degenerate d_{xy} and $d_{xz,yz}$ states. By lightly doping with lanthanum (on the calcium sites), the MI transition is suppressed while the original lattice structure is retained. The research shows how the structural and electronic transitions are strongly linked, but suggests that it is the structural transition that leads the electronic change.

7.1 Introduction

$Ca_{2-x}La_xRuO_4$ belongs to a complex family of layered ruthenate materials [231, 232], and is specifically a member of the alkaline earth-ruthenium Ruddlesden-Popper series [233]. Ca_2RuO_4 is a compound isostructural with the Sr_2RuO_4 superconductor [234], but shows severe distortions due to the smaller ionic radius of Ca. Both materials show a perovskite structure, where the RuO_2 bilayers are typically responsible for the conductivity [235, 236]. These materials display a wide range of properties and electronic orders including superconductivity, Mott transitions and charged order states [237, 238, 239, 240, 241]. This is due to the close proximity of the energy scales driving these properties, which can be easily unbalanced by small distortions. In transition metals the competition between the intra-atomic Coulomb interaction, U, and the bandwidth, W, often drive the groundstate properties. In many 4d compounds the systems are closely balanced near a metal to non-metal boundary with $U/W \approx 1$ [242]. Small distortions can lead to a narrowing of the bandwidth and hence a metal to insulator transition can occur [243]. The spin-orbit interaction within the 4d shell of ruthenium is substantial and may play a key role in the formation of these properties. The importance of this interaction for the development of charge order is linked to its role as a driving force for new quantum orders [201, 244].

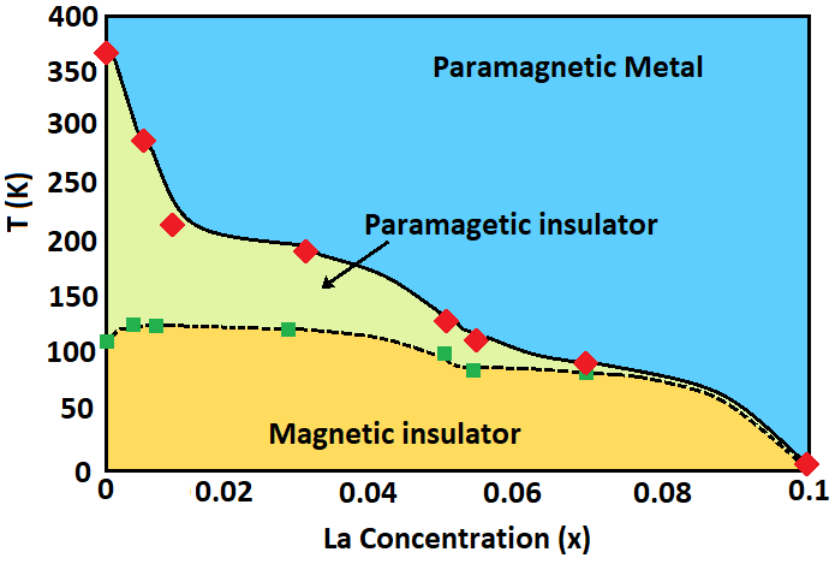

Figure 7.1.1: $Ca_{2-x}La_xRuO_4$ phase diagram. Red diamonds - Metal-insulator transition, green squares - magnetic transition. Reproduced from [27]

$Ca_{2-x}La_xRuO_4$ shows a rich phase diagram, figure 7.1.1, displaying a metal to insulator transition as a function of lanthanum doping. The parent compound ($x = 0$) undergoes a metal to insulator transition at $T_{MI} = 360K$ and a magnetic transition from paramagnetic to antiferromagnetic at $T_N = 110K$ [22]. The nature of the metal to insulator transition and the role played by the orbital degree of freedom is unclear. While it is clear that a Mott - type mechanism makes the 2/3 filled t_{2g} band insulating, two scenarios have been proposed [25]. Since both scenarios have differing orbital occupations (n =(n_{xy}, $n_{xz} + n_{yz}$)) and polarization (p ≡ n_{xy} - ($n_{xz} + n_{yz}$)/2) [245], it allows these scenarios to be probed by XAS techniques. One suggests that the transition is orbital selective and it only affects the *xy* band which becomes metallic, where n and p goes from (1,3) and -1/2 in the metal state to (2,2) and 1 in the insulating phase [24, 25]. The second scenario suggests that the transition is assisted by the crystal field splitting, $\Delta = \varepsilon_{xz/yz} - \varepsilon_{xy} > 0$, similar to the case of $3d^1$ perovskites where P > 0 in all phases [26, 246, 247]. While both scenarios can be supported by some experimental data, it is unclear which mechanism is driving the transition since both appear to be inconclusive.

The interplay between the electronic and atomic structure in this compound is complex. Accompanying the electronic transitions, the material undergoes significant structural changes. As a layered perovskite, above 360K Ca_2RuO_4 is made of RuO_2 layers built up of corner sharing RuO_6 octahedra, with a space group Pbca [23]. In the metallic phase the compound is characterized by a long *c*-axis (L-Pbca) with the octahedra slightly elongated along the *c*-axis and a lattice ratio of c/a = 3.25. In the insulating phase the *c*-axis is shorter (S-Pbca) and the octahedra are flattened in the *ab*-plane, with a lattice ratio of c/a = 3.10 [22]. It has been reported that the crystal field splitting effect in the Ru 4d orbitals is on the order of 10Dq which leads to a splitting of the 4d states [26]. A simple representation of this effect, the Jahn-Teller distortion, is shown in figure 7.1.2. In the elongated state, the degeneracy of the levels is broken by the stabilization of the orbitals with a z-component, which are lowered in energy. The orbitals without a z-component become destabilized in which they become higher in energy. This is a result of the d_{xy} and $d_{x^2-y^2}$ orbitals having a greater overlap with the ligand orbitals. In the compressed state this situation is opposite, where the degeneracy is broken by the stabilization of the orbitals without z-components and the remaining orbitals becoming destabilized.

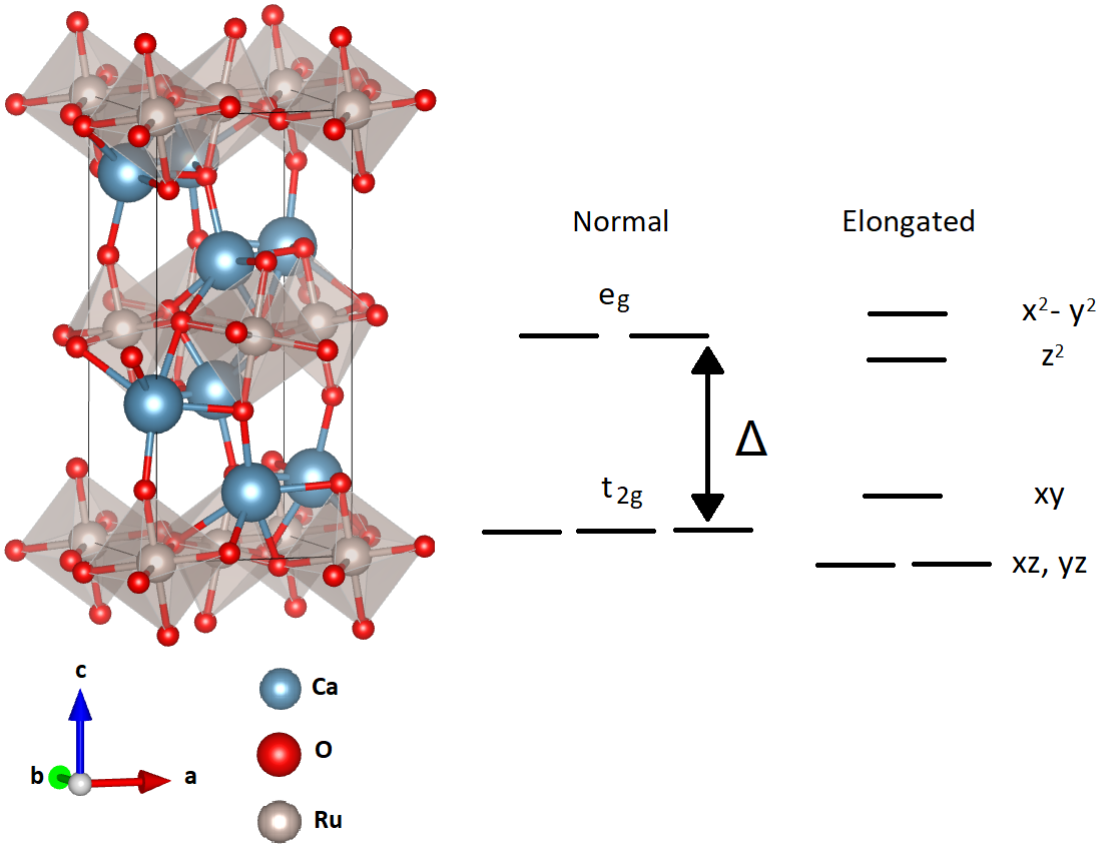

Figure 7.1.2: Left: Ca_2RuO_4 crystal structure. Right: Jahn-Teller distortion example (elongated).

Additional to the Jahn-Teller distortion, the octahedra are rotated around the c-axis and shows a tilt around the b-axis. Research on the effect of these distortions has shown that they may play a critical role in the formation of the insulating phase. The tilting about the c-axis increases when the system is cooled, which causes the e_g bandwidth to decrease and the Ca-O bond length to change [74]. While the rotation about the b-axis undergoes a very small change across the T_{MI} transition (about a degree), it has been suggested that this rotation causes a severe modification to the d_{xy} orbital while both d_{xz} and d_{yz} orbitals are unaffected [248]. It is also clear that both structural distortions are necessary to minimize the total energy of the system [240].

While the structural changes and the general electronic structure in this material has been been well characterized, the interplay between these and the driving factor for the T_{MI} transition is complex and not fully understood. Unravelling how the different effects are linked together is a major challenge and is the focus of this chapter. To aid this research on the parent compound, the substitution of lanthanum onto the calcium sites provides a direct route to explore the interplay between the atomic and electronic structures across T_{MI}. Lanthanum, which has a slightly larger ionic radius (La^{3+} $r = 1.22$Å and Ca^{2+} $r = 1.18$Å), offers the advantage of retaining the original lattice structure and Coulomb interaction [27, 79]. The slight substitution is believed to effectively increase the t_{2g} bandwidth by lowering the highly distorted Ru-O-Ru bond angle (151^o) and simultaneously filling the t_{2g} orbitals with the electron added by the La ion. While the bandwidth control and filling control are common in perovskite-like oxides, the drastic and distinct effects in Ca_2RuO_4 is rarely seen, making a study of the La doping an interesting topic in its own right [28, 29]. It is also important to note that the tilt of the octahedra decreases as a function of dopant [249]. The change in the tilt is reported to go from approximately 11^o when x=0.0, to 7.7^o when x=0.13. The change in the tilting of the octahedra is linked to the lowering of the Ru-O-Ru bond angle, and a consequence of the doping. The transport properties of Ca_2RuO_4 as a function of La dopant and temperature have been well documented, shown in figure 7.1.3.

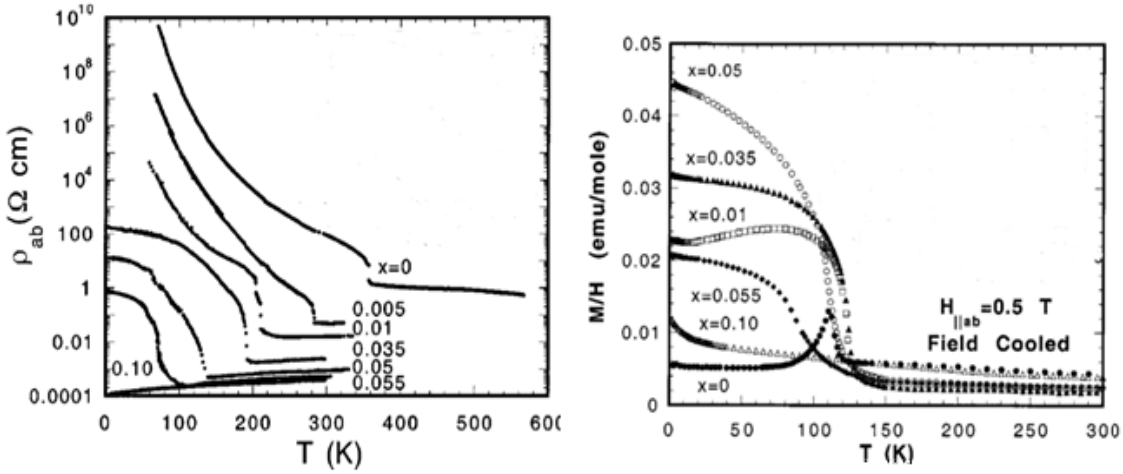

Figure 7.1.3: Resistivity and magnetic susceptibility measurements $Ca_{2-x}La_xRuO_4$ [27]

The introduction of La into the system causes the T_{MI} to reduce in temperature; upon heavy substitution the transition is completely suppressed. The resistivity measurements show that when $x = 0$ there is an abrupt first order transition from a nearly fully metallic high temperature phase to a low temperature insulating phase at $T_{MI} = 360$K, which is simultaneous with the major structural change where the very elongated octahedra compresses to a nearly regular structure. Upon doping, both ρ_{ab} and T_{MI} decrease dramatically. For $x = 0.005$ the T_{MI} drops to approximately 280K and ρ_{ab} decrease by more than 2 orders of magnitude. At approximately $x = 0.1$ the metallic phase is retained down to at least 2K and the ρ_{ab} decrease to $10^{-4}\Omega cm$. The behaviour of the resistivity for $x < 0.01$ and $x > 0.035$ is fundamentally different. There is a deviation in the conduction process from a variable range hopping-Efros-Shklovshii mechanism to an excitation to extended states, which is characterized by a much weaker temperature dependence [27, 250]. The conductivity O ($1/\rho$) extrapolated to T = 0 exhibits an abrupt rise around $x = 0.035$ suggesting that the electrons start to populate extended states in the upper Hubbard band and the system accordingly approaches a delocalised state. A distinct change in the low temperature resistivity is rare and unambiguously defines a continuos transition from a strictly insulating phase to a regime with low, yet finite, conductivity [251]. The magnetic transition is not the focus of this research. However it is important to note that in the parent compound the system goes from paramagnetic

to antiferromagnetic at approximately 110K. Doping the system does not affect the temperature of this transition, however as x approaches 0.1, it becomes suppressed [27].

In this chapter the $Ca_{2-x}La_xRuO_4$ is studied with polarization dependent XAS to track both the atomic and electronic structure as a function of temperature and dopant. By using polarization dependent measurements it may be possible to track changes in different crystallographic planes and due to the system being highly anisotropic, provide further information regarding the mechanisms involved in the metal to insulator transition.

7.2 Sample preparation and characterization

The samples used in this research have been grown by R. Perry, using a growth method presented in S. Ricco thesis [252]. A brief overview of this method is given here. Equation (59) gives the chemical reaction used to grow the crystals and allows the determination of the correct ratios for different doping levels.

$$(2-x)CaCO_3 + \frac{x}{2}X_2O_3 + yRuO_2 \rightarrow Ca_{2-x}X_xRu_yO_4 + (2-x)CO_2 \tag{59}$$

The samples have been grown using a floating zone technique, using a commercial four-mirror image furnace. Using equation (59), appropriate ratios of $CaCO_3$, RuO_2 and La_2O_3 were mixed together. The resultant mixture was dried, due to the $CaCO_3$ being hygroscopic, at 600^oC for 18 hours. This was then pressed into pellets of a diameter of approximately 2cm and height of 5mm. These pellets were then placed onto a Pt plate, with a thinner bedding pellet used to prevent contamination through the following steps. This was then baked in air at 1100^oC for an additional 18 hours, which allows the solid-state reaction to occur. The resultant melt was then grounded, placed inside a narrow cylindrical balloon, which was also placed in a straw and pressed in water using an isostatic press. Once removed from the straw, the rod was then sintered in air at 1200^oC for 2 hours. This constitutes the feed rod. Suspended in the centre of the mirror stage of the furnace this rod was vertically aligned with the seed rod held from below. The FZ method requires the melting of the bottom of the feed rod. The hot spot was focused at the centre of the four-mirror stage, reaching a maximum temperature of 2200^oC. As the seed and feed rods were lowered at different speeds, new material containing single crystals was grown from the molten zone on top of the seed rod. To track the changes as a function of dopant, 3 compositions have been used, $x = 0.0$, 0.05 and 0.15 where the T_{MI} is approximately 360K, 150K respectively for the first two compositions and suppressed when $x = 0.15$.

7.2.1 Characterization measurements (SEM/EDX)

Due to the anisotropic nature of these samples and the requirements of the polarization dependent measurements, it was important to confirm that the samples used in the XAS measurements were single crystals. Figures 7.2.1- 7.2.3 show the SEM images and EDX results on each composition. The details of these techniques are given in section 3.4.1. The SEM shows in all cases that the samples were homogeneous single crystals, with a constant contrast across the surface, while in some cases it was possible to see the different layers, there is no indication that different domains have formed. The EDX results confirm that the samples are pure with Ca, Ru and O in the appropriate ratios, suggesting high quality. Additionally, the doped crystals show the presence of La in the 2 compositions. While it is difficult to obtain accurate molecular weighting from this technique, the relative level of doping to the Ca species were: 0.05 ± 0.02 for the $x = 0.05$ composition and 0.14 ± 0.02 for $x = 0.15$, suggesting appropriate levels of doping in each case.

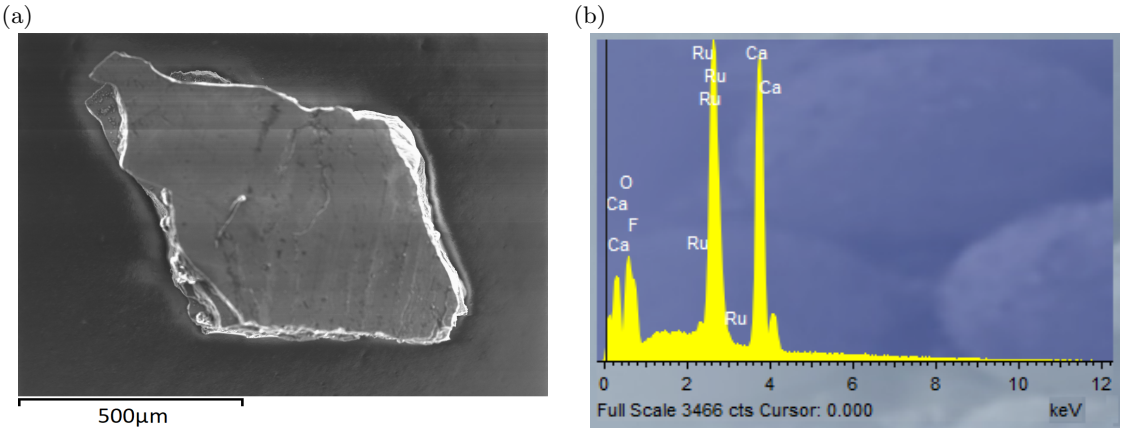

Figure 7.2.1: a) SEM images and b) EDX measurements on $Ca_{2-x}La_xRuO_4$ ($x = 0.0$).

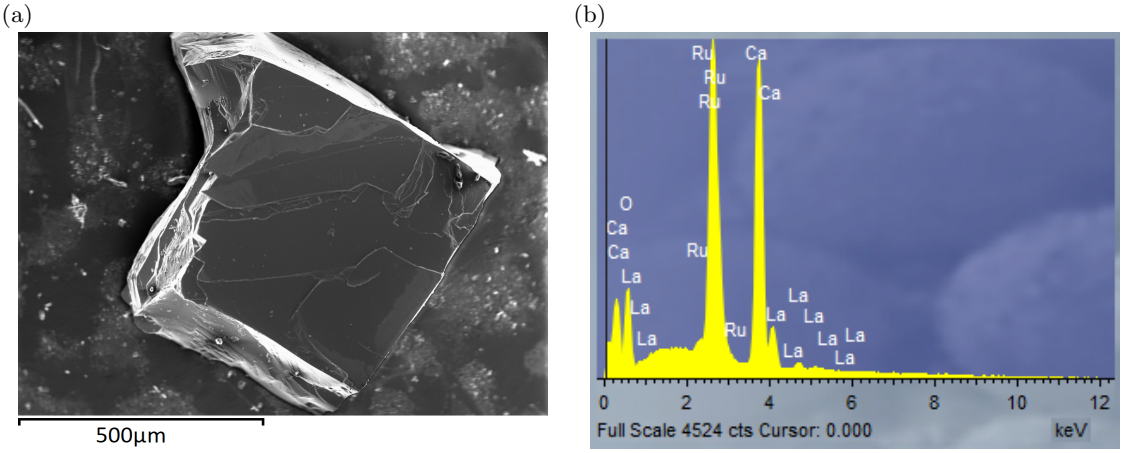

Figure 7.2.2: a) SEM images and b) EDX measurements on $Ca_{2-x}La_xRuO_4$ ($x = 0.05$).

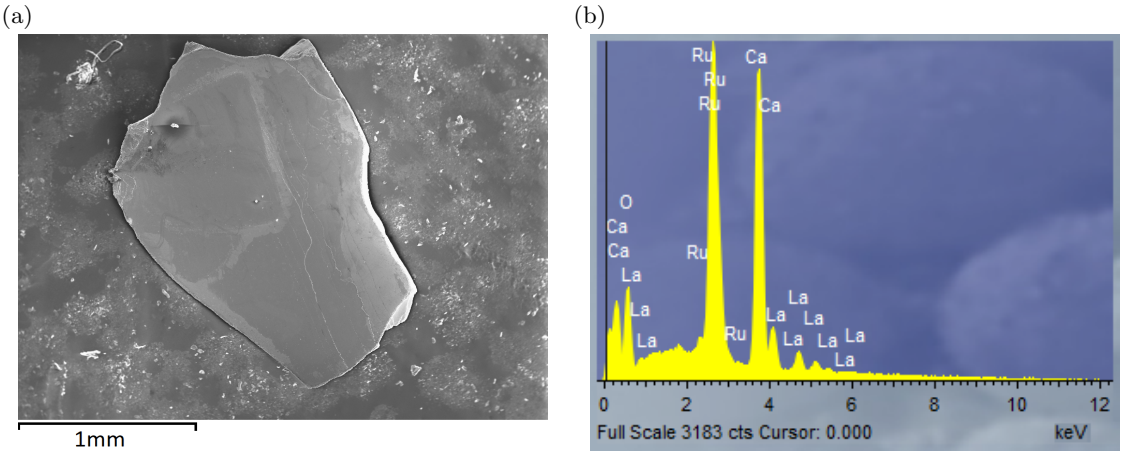

Figure 7.2.3: a) SEM images and b) EDX measurements on $Ca_{2-x}La_xRuO_4$ ($x = 0.15$).

7.3 Experimental set up

Due to the complex interplay between the atomic and electronic structure, both XANES and EXAFS measurements have been carried out on the different compositions. The aim of these measurements was to confirm the structural changes in the pure compound and compare with the behaviour of the doped compositions. Using the polarization dependent XANES, it is possible to track how the t_{2g} and e_g orbitals change across T_{MI} and obtain further information with respect to the mechanism driving this transition. The XANES measurements were performed at the XMas beamline (ESRF)

with details of the beamline in section 3.2.1. For the XMas beamtime the following co-workers assisted with the running of the beamline and collecting data: Dr Silvia Ramos (University of Kent), Dr Giannantonio Cibin (Diamond light source) and Dr Sinead Rowe. The EXAFS data has been collected on the B18 beamline at Diamond, with further details given in section 3.2.2. For the B18 experiment, the following co-workers assisted with the running of the beamlines and collecting data: Dr Silvia Ramos (University of Kent), Dr Giannantonio Cibin (Diamond light source), Dr Shusaku Hayama (Diamond light source) and Dr Sofia Diaz-Moreno (Diamond light source).

7.3.1 Sample environment and geometry

The L_2/L_3 XANES measurements at the XMas beamline were carried out using an ARS DE202G cryofurnace with an available temperature range of 600K-10K. A vortex Si drift diode detector was placed at 45^o to the sample to allow for the collection of the fluorescence signal. To allow for polarization dependent measurements, the sample environment was mounted on a Huber diffractometer enabling the rotation of the samples relative to the beam. The samples were oriented so that in all data sets 0^o refers to the beam polarization being parallel with the ab-plane, and 90^o indicates the beam polarization being parallel with c-axis.

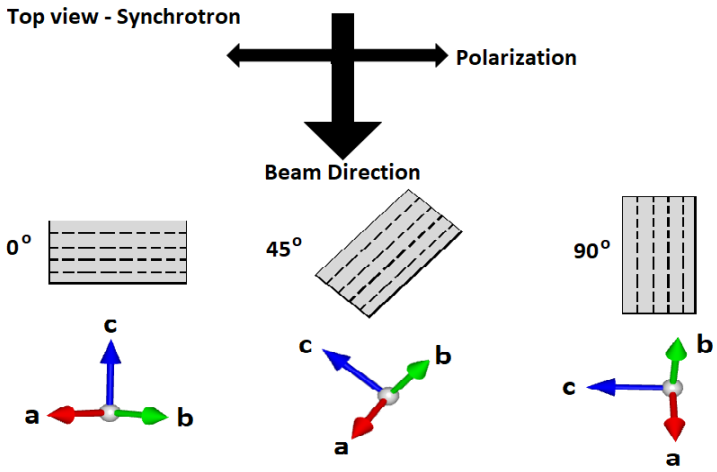

Figure 7.3.1: $Ca_{2-x}La_xRuO_4$ sample alignment relative to the beam.

The K-edge EXAFS were carried out at B18 with two different sample environments. This was due to the data being collected over two different sessions and depended on the availability of the environments: a helium pulse tube cryostat with a temperature range of 400K - 1.5K and a cryo-jet with a temperature range of 300K - 85K. In both experiments a 36 element Ge detector was place at 90^o to the direction of the beam and fluorescence was collected. In both cases, shown in figure 7.3.1 the sample were aligned so that the angles refer to the same orientation with respect to the XMas data sets.

7.3.2 Measurements

Due to the high absorption of the single crystals samples, all of the following measurements were carried out in fluorescence mode. Measurements have been performed on the Ru L_2-, L_3- and K-edges and the transitions considered are shown in figure 7.3.2.

Polarization dependent XAS measurements on the XMas beamline, focusing on the XANES region, have been collected on the 3 compositions ($x = 0.0, 0.05, 0.15$). The L_2- and L_3-edges were used. The L_2-edge at an energy of 2967eV probes the $2p_{1/2} \rightarrow 4d$ unoccupied states, where the dominant emission line is the Lβ_1 which corresponds to the $3d_{3/2} \rightarrow 2p_{1/2}$ transitions. While the L_3 at an energy of 2838eV probes the $2p_{3/2} \rightarrow 4d$ states. The dominant emission lines are the Lα_1 and Lα_2 which corresponds to the $3d_{5/2} \rightarrow 2p_{3/2}$ and $3d_{3/2} \rightarrow 2p_{3/2}$ transitions. The L_2-edge data was collected using a energy step of 0.25eV with ≈2s per point over the edge and an energy step of 1eV with ≈2s per point post-edge. The L_3 pre-edge data used 0.5eV energy step, 0.25eV energy step over the edge and 0.5eV post-edge. In each region each point was collected for ≈2s. Both edges where calibrated using a ruthenium foil. These measurements not only give information regarding the electronic structure of the d orbitals, it also allow for the branching ratio to be calculated. It should be noted that the Ru L-edges are very close in energy, so only a limited range in energy is available and not suitable for EXAFS measurements. Additionally the adhesive used to secure

the sample to the holder contained chlorine which has an absorption edge at 2822eV. Some of the L_3 data sets show a small feature caused by this additional element since the adhesive overlapped the sample surface. The parent compound was measured at 400K, 300K, and 55K which not only tracked the changes across the T_{MI} transition but also confirm the electronic structure below the magnetic transition. The doped samples where measured at 300K and 55K. Due to the experimental set up it was possible to measure angles between 0^o and 90^o.

The B18 measurements aimed to collect the EXAFS data from the K-edge and used 3 compositions ($x = 0.0, 0.05, 0.15$). The K-edge at the energy of 22.117keV using both the Kα_1 and Kα_2 emission lines which correspond to the $2p_{3/2,1/2} \rightarrow 1s$ transitions, in fluorescence mode. The energy has been calibrated with Ru foil, each scan used an energy step of 0.5eV and ≈0.3s per point. While in principle it is possible to extract electronic information for the K-edge XANES, this has been carried out by another PhD student in the research group (S Rowe) and the results are presented in [253]. The overall conclusion from this work showed how the resolution of the K-edge spectra was not sufficient to determine orbital occupational changes, hence the L_2/L_3 measurements presented in this chapter. This is due to the core-hole lifetime broadening effects. In all compositions a range of temperatures has been measured between 400K and 55K, with focus on tracking the changes in the RuO_6 octahedra. The samples have been measured at 4 angles to allow the fitting process to take into account the polarization dependence on the structure.

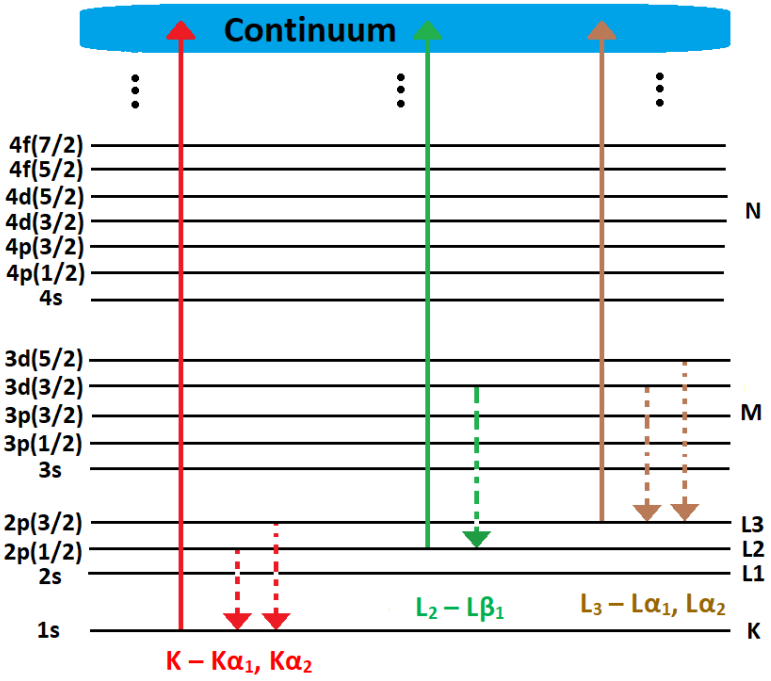

Figure 7.3.2: Electronic transitions considered in $Ca_{2-x}La_xRuO_4$ measurements. Dashed lines indicate fluorescence lines, and solid lines indicate absorption.

7.4 Data analysis and Results

The data analysis has been divided into the electronic and atomic structures, with a comprehensive discussion presented in the following section. Table 7.4.1 shows the parameters used for the self-absorption correction. Due to the short energy range collected for the L_2- and L_3-edges, a careful consideration of the self-absorption parameter after the edge was needed, since oscillations would still be present. To account for this a straight line function was fitted to the data after the edge and the average value was used for the correction. The data processing parameters for each set of data is given in table 7.4.2. A pre-edge subtracting, post-edge normalization and background subtraction have been applied to all data sets. It will be shown that the XANES L_2/L_3 data includes a double-peaked whiteline. The higher energy feature can be shown to arise from the Ru e_g bands [254] and since these are unoccupied above and below the transition it is this feature that has been used as a guide for the normalization.

	$\mu_{tot}(E_f)$	$\mu_b(E)$	$\mu_0(E_{ae})$	$\mu_0(E_{be})$
K x = 0.0	244.94	26.75	775.06	136.08
K x = 0.05	254.59	33.38	775.06	136.08
K x = 0.15	273.91	44.68	775.06	136.08
L_2 x = 0.0	8253.66	819.08	24304.07	18283.74
L_3 x = 0.0	9320.57	897.15	18843.740	6000.82
L_2 x = 0.05	8709.40	1101.81	24304.07	18283.74
L_3 x = 0.05	9842.21	1208.74	18843.74	6000.82
L_2 x = 0.15	9620.88	1667.24	24304.07	18283.74
L_3 x = 0.15	10885.51	1816.86	18843.74	6000.82

Table 7.4.1: Self-absorption correction parameters for $Ca_{2-x}La_xRuO_4$ for all edges. All values in cm^{-1}.

	E0 (eV)	**Pre-edge (eV)**		**Post-edge (eV)**		**Rbkg (Å)**
		Min	Max	Min	Max	
K - All compositions	See text	-150.0	-60.0	150.0	964.6	1.3
L_2 - All compositions	2971.89±0.5	-21.5	-11	37.1	59	-
L_3 - All compositions	2842.78±0.5	-40.24	-30	38.5	60	-

Table 7.4.2: Data processing parameters for $Ca_{2-x}La_xRuO_4$. Pre-edge and post-edge values relative to E_0.

7.4.1 XANES

Ca_2RuO_4

In figure 7.4.1, the L_2 and L_3 spectra are shown for the Ca_2RuO_4 sample. 3 angles are given to track possible changes in different crystallographic planes and 3 temperatures are given to track the transition (above the MI transition at 400K, just below at 300K and finally below the magnetic transition at 55K). In addition the first derivative is also given to allow a clear comparison of the peak positions. It has been shown in the literature that the two main features in the L_2/L_3 XANES related to the t_{2g} and e_g orbitals [255]. The most intense feature centred at approximately 2973eV and 2844eV for the L_2 and L_3 edges respectively relate to the e_g states. The lower energy feature centred at approximately 2970eV and 2841eV for the L_2 and L_3 edges respectively relate to the t_{2g} states. In the literature it is also noted that in the Ru $L_{2,3}$-edges multiplet effects can distort the two peak ratio from the expected theoretical values [254]. This is due to the combined effects of spin-orbit coupling and interelectronic Coulomb interaction. This makes it difficult to determine the exact orbital occupation of the states. However it is still possible to understand if the occupation is changing [254]. In the groundstate the Ru species is expected to have an electronic configuration of $4d^4$ where the 4 electrons are located in the t_{2g} orbitals and the e_g states are completely empty. This suggests that the e_g intensity should be stable across the transitions, which is confirmed by the data. The reason that the e_g orbitals remain empty is due to the local structure around the Ru which keeps the separation between the t_{2g} and e_g too large for the electrons to move to the upper energy levels. It should also be noted that the spectra is noisy especially, in the 400K data sets, and this is a limiting factor in interpreting the data.

It should be noted that the full spectra collected are shown in the appendix, and that the L_2-edge data with respect to the 0^o and 15^o were not usable. The L_2 and L_3 spectra both show two resolved main features as expected. The first derivative shows that the peak positions do not vary by any significant amount across the transition and that the edge position is comparable with the expected oxidation state in the compound [254]. Due to the octahedral crystal structure, the

polarization dependency of the XANES data will reflect different orbitals. With consideration of the orientation of the samples in these measurements relative to the beam polarization, the 90^o data will have significant contributions from orbitals with z components (i.e. $d_{xz,yz}$), while the 0^o will have contributions from orbitals without z components (i.e. d_{xy}). Across the data sets the e_g feature does not undergo any significant changes in its shape or intensity, which is expected. Focusing on the lower energy t_{2g} feature, there are some notable changes with respect to both angle and temperature. Firstly across the MI transition the feature changes from a shoulder in the 400K to a more defined peak at both 300K and 55K. This is clear in the 90^o data however is also seen in the other angles to a lesser extent. The reason for this is related to the structural changes later discussed, where a compression of the oxygen octahedra leads to a narrowing of the bandwidths, W, and the electrons become more localized. It is important to note that the features seen in the spectra relate to empty states. The layered structure leads to the *xz*, *yz* bandwidth being about half that of the *xy* bandwidth, which explains why the 90^o shows a clear peak since the bandwidth is smaller [25]. Figure 7.4.2 shows the t_{2g} and e_g peak ratio for both edges and the 3 angles. In monitoring this ratio, the relative occupation of these states across the transitions can be tracked. In both the L_2 and L_3 data the smaller angles (L_3 - 0^o and L_2 - 30^o) show a decrease in this ratio across the transition, while the 45^o shows a relative stable ratio and the 90^o shows an increase in the ratio value. This is clearly seen in the L_3 data, but also indicated in the L_2 data, however the increase in the noise does distort this slightly. In the simplest interpretation of this feature with respect to angular dependency, it suggests that the occupation of the $d_{xz,yz}$ (90^o) is decreasing, while the d_{xy} (0^o) is increasing.

It is important to note the conclusions presented by S. Rowe [253] with regards to the K-edge XANES. It was shown that the E_0 position shifts as function of temperature and this shift is greater in the *ab*-plane than the *c*-axis. This result is confirmed with the K-edge data collected for this thesis, where the edge position for the 300K data relative to the 400K data at 15^o shifts approximately -0.6eV while 75^o for the same temperatures shift by +0.1eV. It was suggested that this indicates a greater occupation change in the *xy* band than the bands with z components. However it was not possible from these measurements to determine which scenario is most likely to be the driving force for the transition. This is due to the low resolution of these measurements caused by the core-hole broadening. Additionally, as the K-edge probes the *s* to *p* transitions, it is indirectly probing the Ru 4d orbitals due to the hybridization between these and the O 2p orbitals [256]. It is also important to note that while the quadrupole transition to the d states should be present, there are no pre-edge features seen in the K-edge measurements. This suggests that the symmetry of the system does not allow for quadrupole transitions.

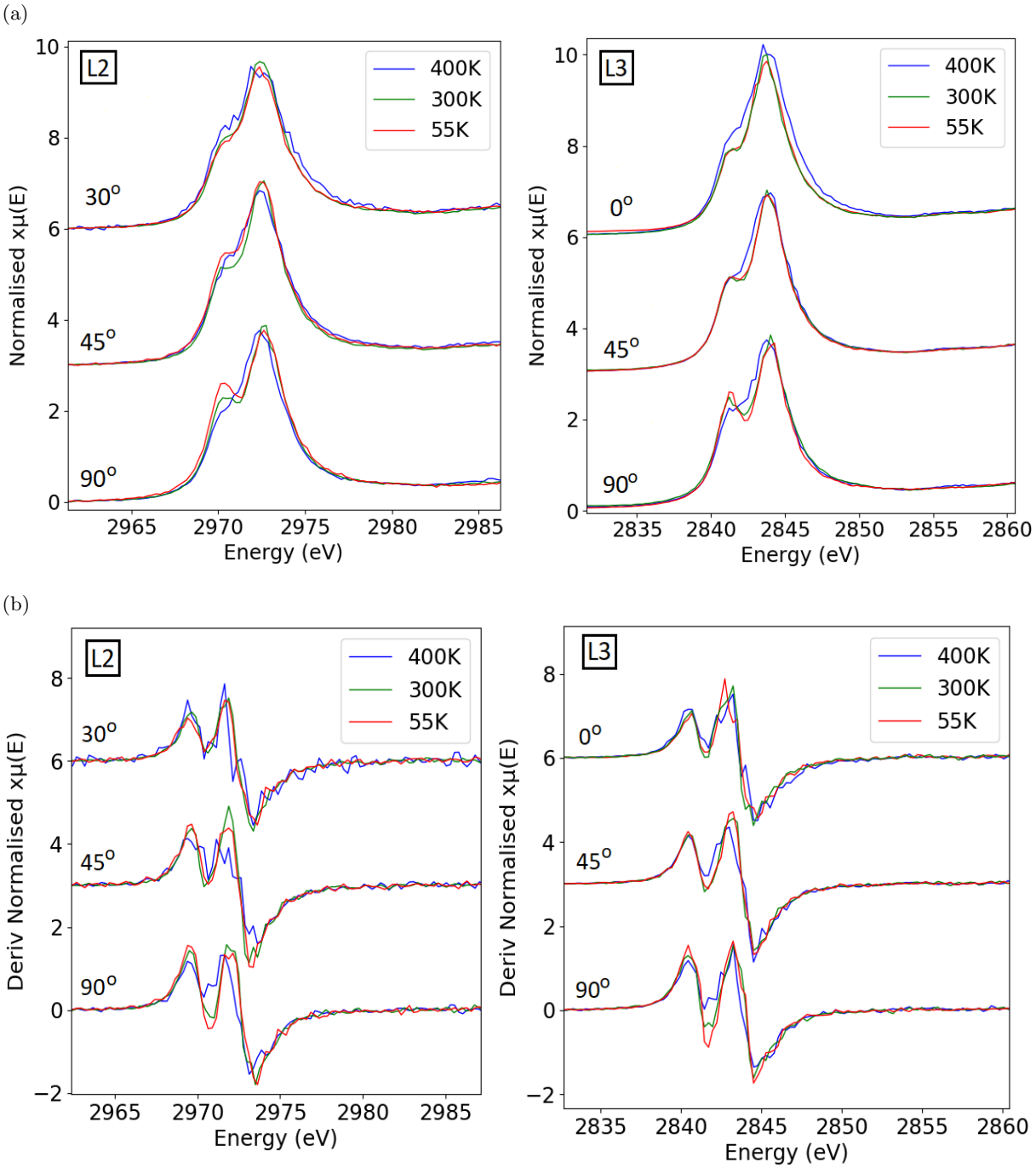

Figure 7.4.1: XANES: a) normalized spectra for the Ru L_2 and L_3 edges. b) normalized first derivative for the Ru L_2 and L_3. Ca_2RuO_4 for 3 angles and 3 temperatures.

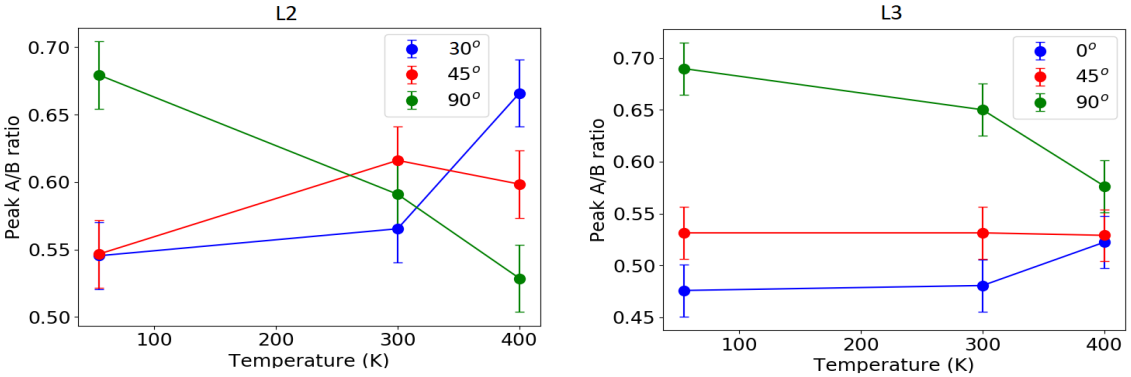

Figure 7.4.2: t_{2g} and e_g peak ratio for Ca_2RuO_4 across temperatures and angles

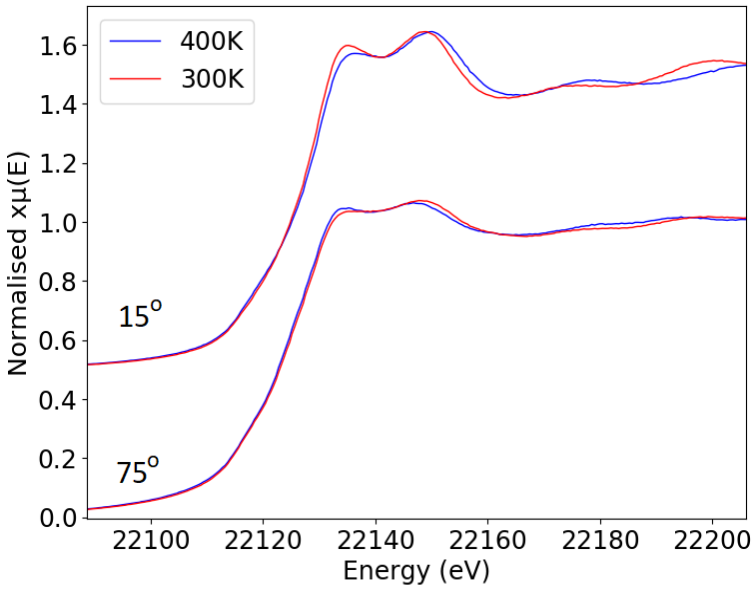

Figure 7.4.3: Ca_2RuO_4 Ru K-edge measurements for two angles across the MI transition.

$Ca_{2-x}La_xRuO_4$, $x = 0.05$ and 0.15

Using the same interpretation as the pure compound, figures 7.4.4 and 7.4.5 show the t_{2g} to e_g peak ratio for the L2 and L3 edges, while figures 7.4.6 and 7.4.7 show the XANES spectra and first derivative. In the $x = 0.05$ composition the MI transition is reduced to between 200K-150K, while in the $x = 0.15$ the transition is completely suppressed. The XANES spectra for the $x = 0.05$ composition shows similar changes in both the angles and temperatures when compared to the pure compound. The addition of La atoms to the system introduces an additional electron per atom and it is suggested that the t_{2g} bandwidth increases as a result of lowering the highly distorted Ru-O-Ru bond angle [27, 79]. Comparing the same angle across the transition shows how there is a change in the t_{2g} feature from a shoulder to a clear peak in the 90^o data, while in the 0^o data this is not as clear. Due to the increase in the bandwidth, as a result of the dopant, it is more difficult to fully separate the t_{2g} and e_g states. The peak positions for both the L_2 and L_3 data sets is comparable with the pure compound, suggesting that due to the relatively low concentration of the La there is not an overall change in the oxidation state of Ru. The peak ratios indicate the same type of occupation change when compared to the pure compound. While it is less clear in the L_2 data, due to the 0^o data quality, the L_3 clearly shows the 0^o intensity decreasing while the 90^o intensity increased. This suggests the same type of mechanism occurring in both the pure and doped compounds. When the transition is fully suppressed, across both edges there is no changes in either feature. This further highlights that the structural change is a critical factor in the MI transition.

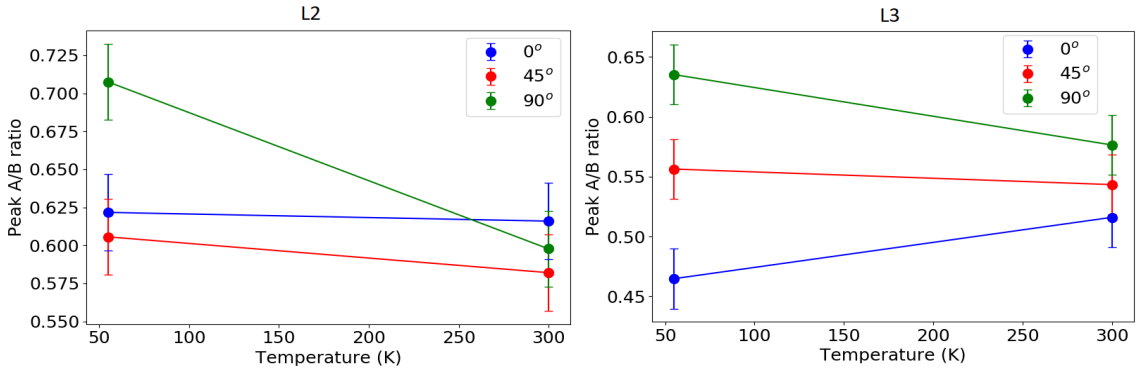

Figure 7.4.4: t_{2g} and e_g peak ratio for $Ca_{2-x}La_xRuO_4$, $x = 0.05$ across temperatures and angles

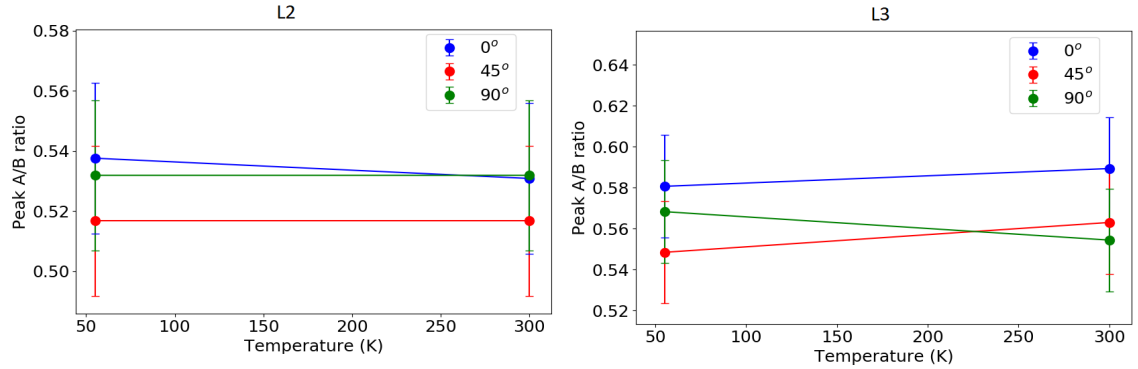

Figure 7.4.5: t_{2g} and e_g peak ratio for $Ca_{2-x}La_xRuO_4$, $x = 0.15$ across temperatures and angles

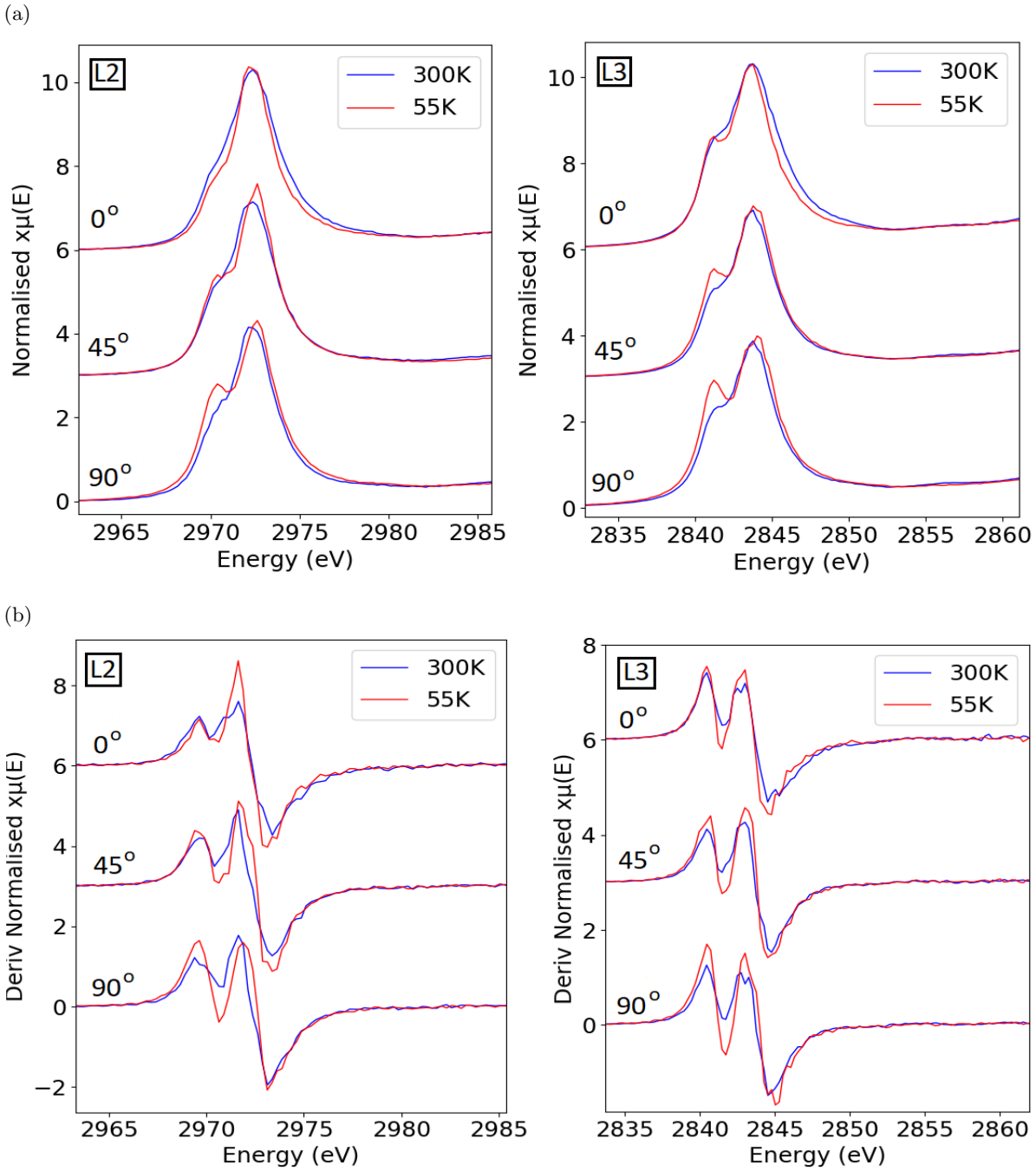

Figure 7.4.6: XANES: a) normalized spectra for the Ru L_2 and L_3 edges. b) normalized first derivative for the Ru L_2 and L_3. $Ca_{2-x}La_xRuO_4$, $x = 0.05$ for 3 angles and 3 temperatures.

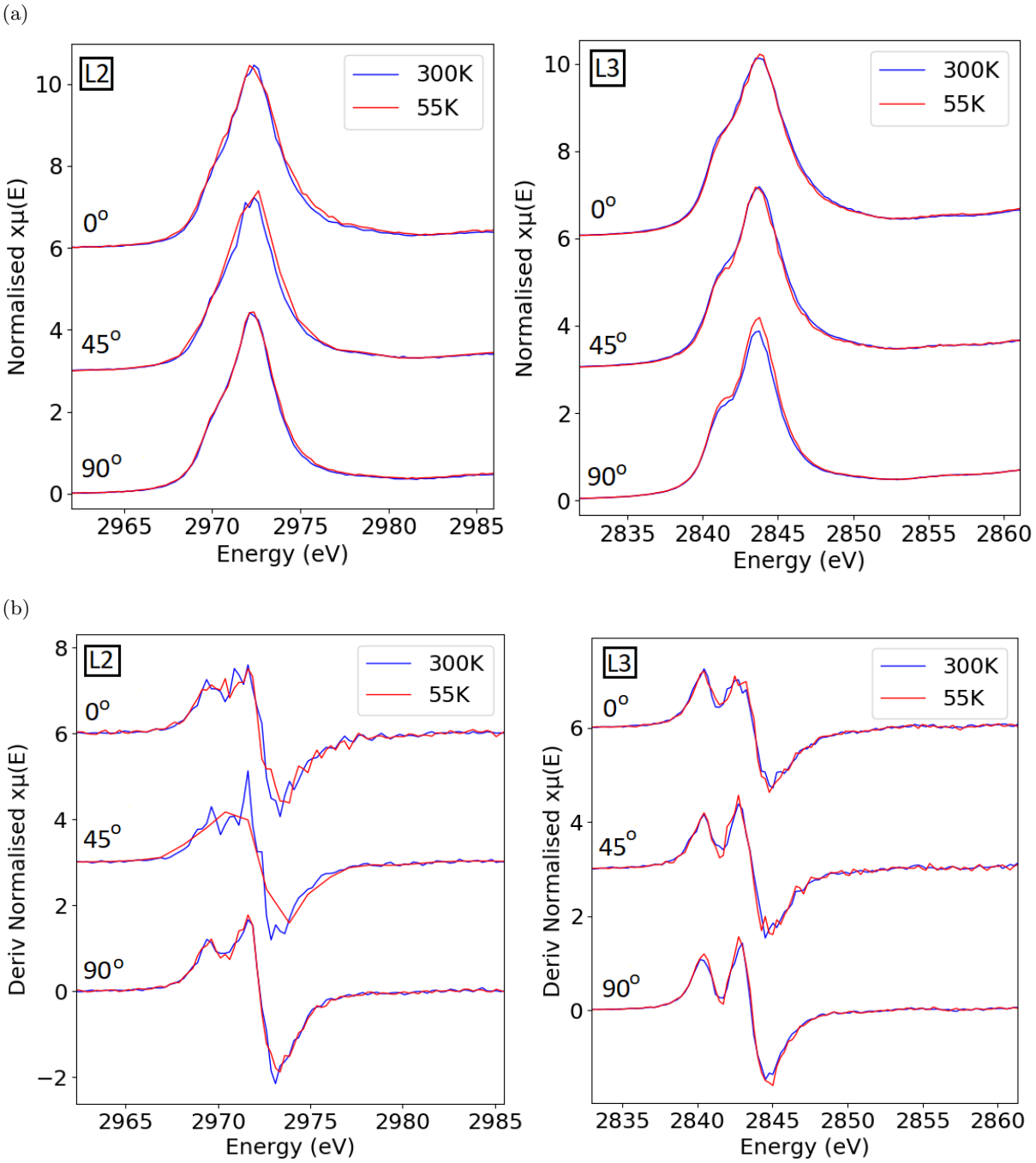

Figure 7.4.7: XANES: a) normalized spectra for the Ru L_2 and L_3 edges. b) normalized first derivative for the Ru L_2 and L_3. $Ca_{2-x}La_xRuO_4$, $x = 0.15$ for 3 angles and 3 temperatures.

7.4.2 Branching ratio

Due to the possible competition between the strong spin-orbit coupling and the crystal field in these compounds, a comparison across temperatures and angles for the L_3/L_2 branching ratio may provide further information. This may provide an understanding if there are significant changes in the spin-orbit and crystal field effects across the transition. The branching ratio theory is outlined in section 4.4, both peaks have been considered when calculating the area under the whiteline. The average value for all compositions shown in figure 7.4.8 is between 0.67 - 0.75 for the normalized BR (not normalized: 2.03 - 2.68) and this is comparable with literature on similar ruthenate compounds [75, 257]. While the spin-orbit coupling is significant in these materials, confirmed by the divergence of this average value from the suggested statistical BR ratio of 2:1, it does suggest that the spin-orbit is comparable to other Ru^{+4} compounds. There is no change across the transition in the branching ratio, clearly seen in the pure compound. There are small changes in the doped compound and the difference appears to increase as a function of dopant. However due to the quality of data and the limited number of temperatures measured it is not possible to confirm if there is a real change. Across the angles in the pure compound the values seem to oscillate with two minima at 15^o and 75^o. It could be suggested that this is caused by the slightly tilted octahedra structure, where the branching ratio is reflecting a greater interaction along the Ru-O bonds. This effect is not consistent in the other compositions, although that could be explained as a result of the decrease of the anisotropy of the electronic structure due to the La doping reducing the Ru-O-Ru bond angle. This again however cannot be confirmed due to the limited data points available.

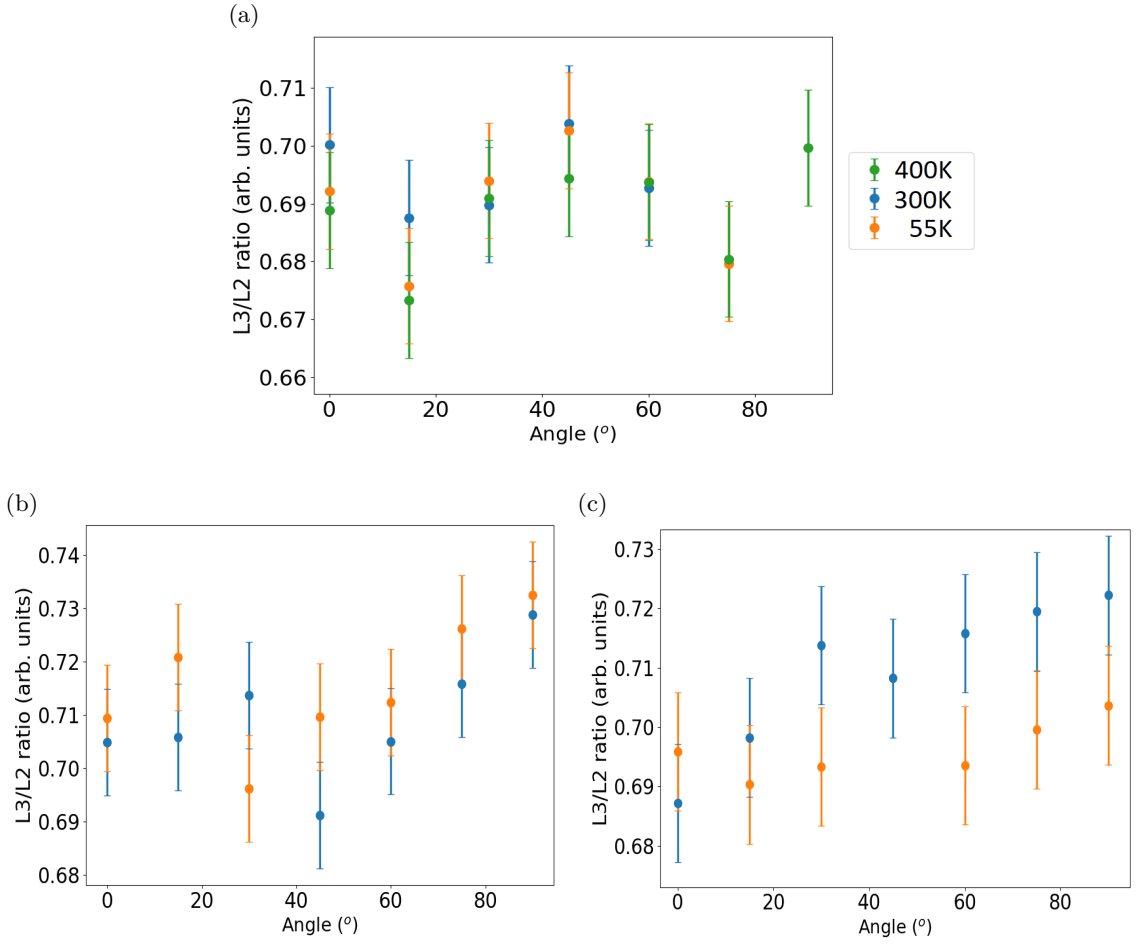

Figure 7.4.8: $Ca_{2-x}La_xRuO_4$, a) $x = 0.0$, b) $x = 0.05$, c) $x = 0.15$ Ru L_2/L_3 branching ratio.

7.4.3 EXAFS analysis

To track the structural changes across the transitions in all compositions, EXAFS data has been collected at a range of temperatures using the K absorption edge. Figure 7.4.9 shows the relative position and intensity of the single scattering paths[9], along with an example of the experimental data for reference. The first feature centred at 1.6Å has contributions from the Ru-O paths. Due to the octahedral structure the original degeneracy of 6 is split in to a set of 2 paths close to the c-axis and 4 paths in the ab-plane. There are several features seen after the main peak, which are formed from 5 major Ru-Ca paths at varying lengths and relative orientations. Table 7.4.3 shows the path lengths, degeneracies and relative angles of the path with respect to the ab-plane (ϕ_A) and c-axis (θ_A).

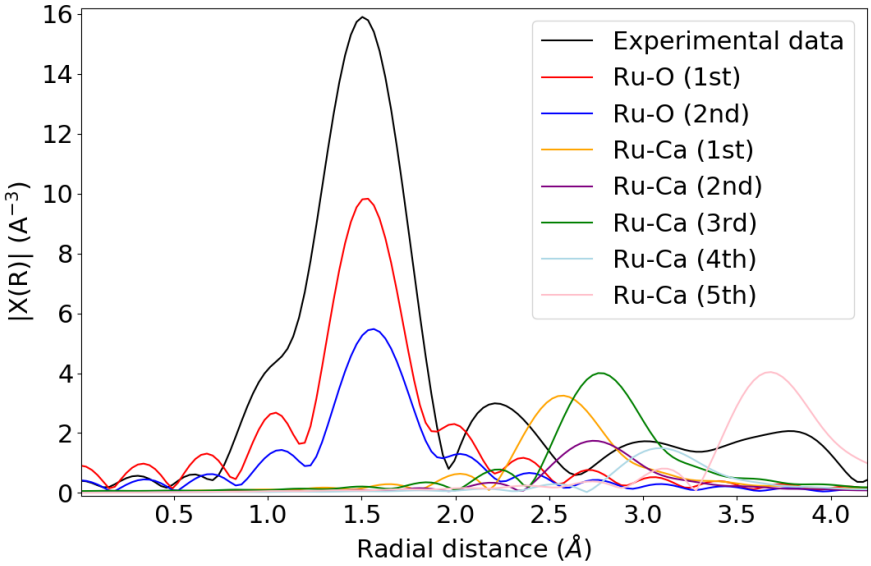

Figure 7.4.9: $Ca_{2-x}La_xRuO_4$ single scattering path contributions to EXAFS, plotted in R-space. $IrTe_2$ spectra (400K, 30^o) shown for reference.

Ca_2RuO_4

Figures 7.4.10 and 7.4.11 show the EXAFS and FT-EXAFS for the Ca_2RuO_4 compound, comparing the angular and temperature dependence. The data and fits shown here have been extracted from the K-edge spectra. The EXAFS have been plotted with a k-weighting of 2, and the Fourier transform is extracted from a k-range of 3Å^{-1} - 11.5Å^{-1}. The EXAFS shown in figures 7.4.10 indicates reasonable data quality up to approximately 12Å^{-1}. There are very clear differences seen across both angles and the two temperatures. These changes show that these measurements are sensitive to the structure across different crystallographic planes because of the octahedral environment around the Ru. It should be noted that the 400K data shows a loss of strong oscillations from approximately 10Å when compared to the 55K data set, which is expected due to the temperature difference. The FT-EXAFS spectra shows a well defined feature at approximately 1.5Å. In the 400K data the features after this peak show significant distortion however there are some clear changes across the angles. In the 55K data there are 3 well defined features between 2Å and 4Å with a consistent intensity decrease between the 15^o and 75^o angles. This data has not been shown with a phase shift, hence the difference in the position of the Ru-O bonds compared to the values shown in table 7.4.3. Figure 7.4.11 shows the 15^o data across all temperatures measured. The EXAFS data shows that there is a significant difference between the 400K and other temperatures, suggesting a large structural change between these temperatures. There are some subtle changes between the remaining temperatures however this is seen more clearly in the FT-EXAFS. There is a small change in the Ru-O path feature peak (at approximately 1.5Å), which shifts slightly to higher R values as the temperature increases suggesting the path length is increasing. The features between 2Å and 4Å, which relate to the Ru-Ca paths show significant differences, not only related to thermal effects. Firstly there is clear difference between the 400K and 340K data, with shifts in the peaks positions

[9]Additional paths have been included in the fitting process, however these have a weaker contribution than the paths shown in figure 7.4.9

suggesting that these paths also undergo changes across the MI transition. There is also a change between the 300K and 250K data, with the peaks becoming more defined and more intense. While the intensity change is most likely related to thermal effects, the difference suggests that this system undergoes structural changes across a significant temperature range. These changes indicate that the Ca cage around the Ru expands as the temperature decreases. However due to the number of paths around this length it is difficult to be more specific regarding the nature of the changes.

(a)

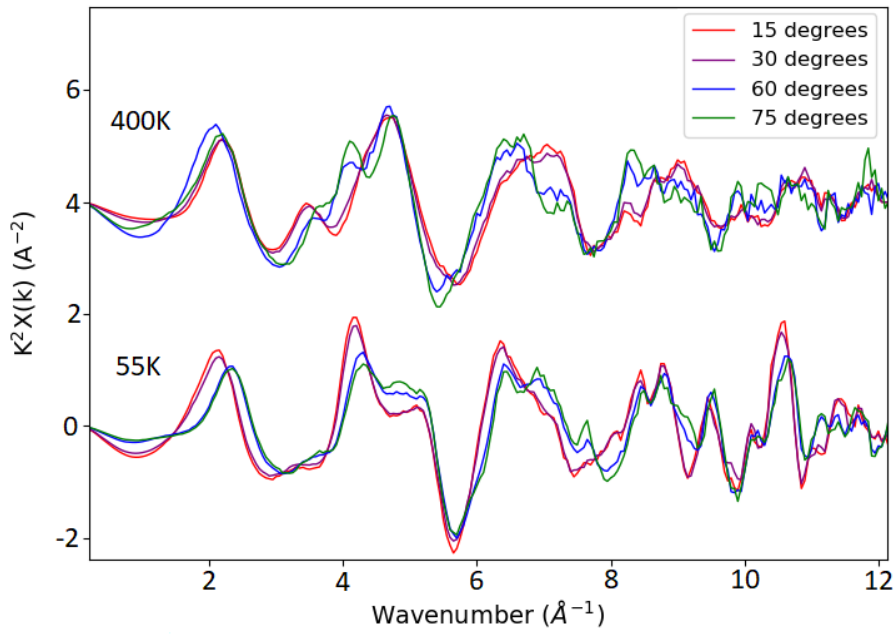

(b)

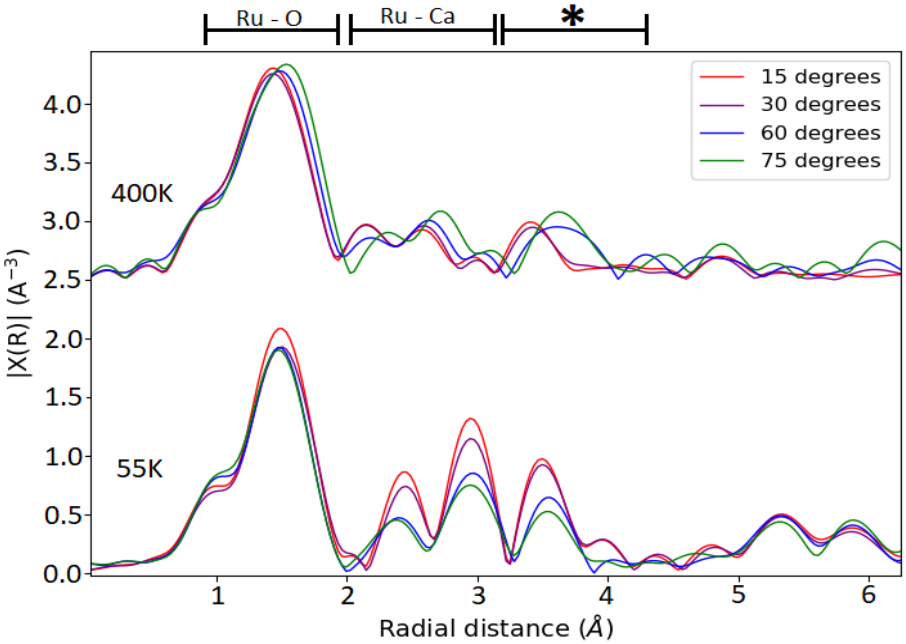

Figure 7.4.10: a) EXAFS and b) FT-EXAFS for Ca_2RuO_4 (Ru K-edge). Showing the angular dependence of these measurements at both 400K and 55K. Also indicated are the two main regions of interest, identifying the first Ru-O and Ru-Ca regions in the FT-EXAFS, * indicates a region of mixed scattering paths.

(a)

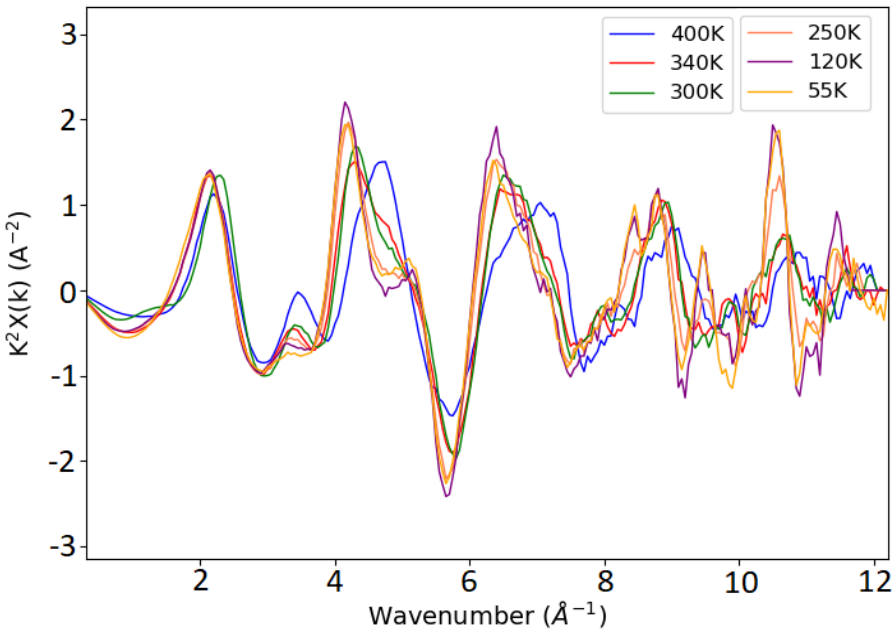

(b)

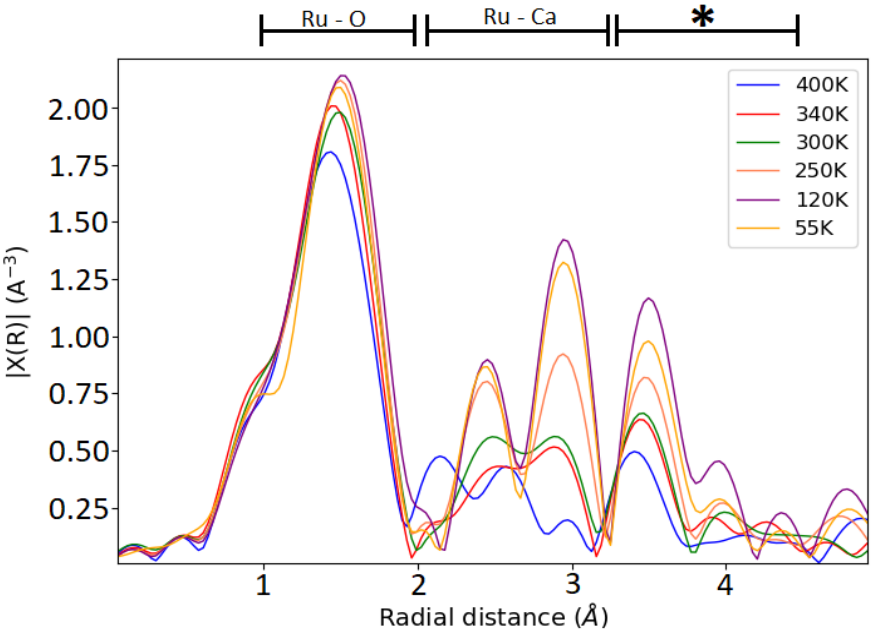

Figure 7.4.11: a) EXAFS and b) FT-EXAFS for Ca_2RuO_4 (Ru K-edge). Showing the 15^o measurements across all temperatures. Also indicated are the two main regions of interest, identifying the first Ru-O and Ru-Ca regions in the FT-EXAFS, * indicates a region of mixed scattering paths.

Fitting Ca_2RuO_4

To track the changes in the structure across the temperature range measured, the EXAFS data has been fitted. Table 7.4.3 shows the original structure used to build the theoretical EXAFS model, along with the angles considered to calculate the weighting factor for each path. This fit has been carried out in R-space to allow peak by peak fitting. Due to the complicated mixture of paths after the Ru-O feature, a multiple scattering path was needed to allow a reasonable fit; details of how this is treated are given in section 2.2.3. Additional information regarding the fitting procedure and parameters used are given in section 4.5.

Path	**Path length (Å**	**Degeneracy**	$\theta_A(^o)$	$\phi_A(^o)$
1^{st} Ru-O	1.970	2	11.20	198.59
2^{nd} Ru-O	2.011	2	81.08	57.96
”	”	”	98.92	145.90
1^{st} Ru-Ca	3.033	2	55.08	269.45
2^{nd} Ru-Ca	3.204	2	57.18	173.44
3^{rd} Ru-Ca	3.242	2	57.61	6.57
4^{th} Ru-Ca	3.565	2	60.85	90.42
Ru-Ru	3.888	2	90.00	46.07
”	”	”	90.00	133.93
Ru-O-Ru	3.955	4	81.08	57.96
”	”	”	98.92	145.90
5^{th} Ru-Ca	4.158	2	4.33	85.86
3^{rd} Ru-O	4.022	2	80.07	57.96
”	”	”	98.89	145.90
4^{th} Ru-O	4.054	2	118.58	51.38
”	”	”	61.42	51.38

Table 7.4.3: Ca_2RuO_4 scattering paths details for fitting.

Figures 7.4.13 and 7.4.14 show examples of the fits for both 400K and 55K, across the 4 angles used and plotted in both k and R-space. The fitting parameters are given in table 7.4.4. In addition, the Ru-O path lengths and Debye-Waller factors are plotted in figure 7.4.12. The fits were carried out in R-space within a range of 1.5Å - 3.4Å, with the data extracted from a k-range between 3Å^{-1} - 11.5Å^{-1} using k-weighting of 1, 2 and 3. The fitting examples for both temperatures show very good agreement between the experimental and theoretical EXAFS. The FT-EXAFS also shows good agreement between the experiment and theoretical spectra, the Ru-O feature is fitted well. The region which includes the Ru-Ca paths shows some differences, especially from 3.5Å in the 400K data, caused by the smaller available range of data used.

The number of independent points for each data set ranges between 75 and 110, with the number of variables between 48 and 70. The background has been also been fitted. The number of variables used reflects that a significant number of Ru-Ca paths have been consider after the Ru-O feature. The resultant R-factor ranges between 0.016 and 0.030, which shows good agreement across the fitting range. The value for S_o^2 is a global parameter that takes into account a number of factors that affect the amplitude of the signal. The values are close to 1, suggesting that the model is appropriate. This also reflects that both the self-absorption and weighting factor considerations have been treated correctly. The E_0 position, which gives the shift in the data compared to the theoretical model, show fairly stable values across temperatures and angles. This parameter was not fixed across the data sets to allow potential small differences due to the angular dependence of these measurements to be taken into account, similar to the effects in the XANES measurements. Due to the number of paths being considered between 2Å - 3.8Å and the considerable overlap of these paths, the reliability of the results of the fitting is not certain. To produce a reliable fit, a multiple scattering path has been included as it has a comparable intensity contribution when compared to the single scattering paths in the region considered. While other multiple scattering paths are present, these have not been fitted since their contribution is significantly lower. This may have an impact on the reliability of the Debye-Waller values for paths above 3Å. The Debye-Waller values for all these paths are reasonable further suggesting that the model is appropriate. In general the

1^{st} and 2^{nd} Ru-Ca paths show a small decrease with decreasing temperature, the 4^{th} and 5^{th} paths show an increase and the 3^{th} path is stable. This suggests that across the temperature range there are small distortions in the Ca cage, which may be a result of the overall structure responding to changes in the octahedra. It is important to also note that the Ru-Ru paths show a general increase in line with the crystal lattice changing below the transition. The lattice parameters change from $a/b = 5.44$Å to $a = 5.35$Å and $b = 5.58$Å [23]. This research focuses on the Ru-O paths and figure 7.4.12 shows the path lengths and Debye-Waller factors for the in-plane and apical oxygens. The path lengths show a significant change between 400K and 200K. In considering the shape of the octahedra, across the MI transition there is a sudden contraction from an elongated state to a more regular structure. Between 350K and 250K the structure goes from a slightly elongated octahedra through to a slightly compressed one. After 250K the path lengths appear to remain stable in a compressed state. This has significant ramifications for the ordering of the 4d energy levels, which will be discussed in the follow sections. The Debye-Waller factor are fairly consistent across the temperature range and shows reasonable values for both paths.

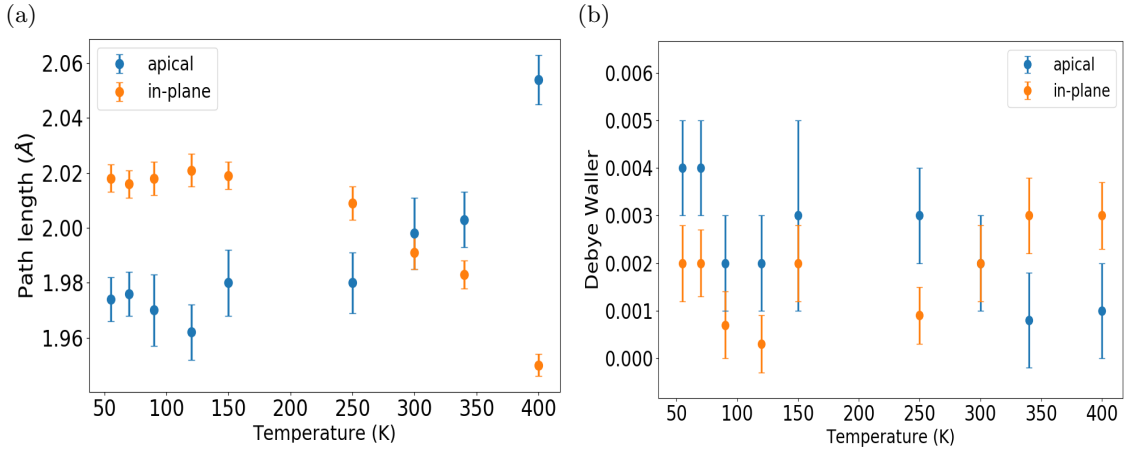

Figure 7.4.12: Oxygen path lengths and Debye-Waller factors for Ca_2RuO_4, across the measured temperature range.

(a)

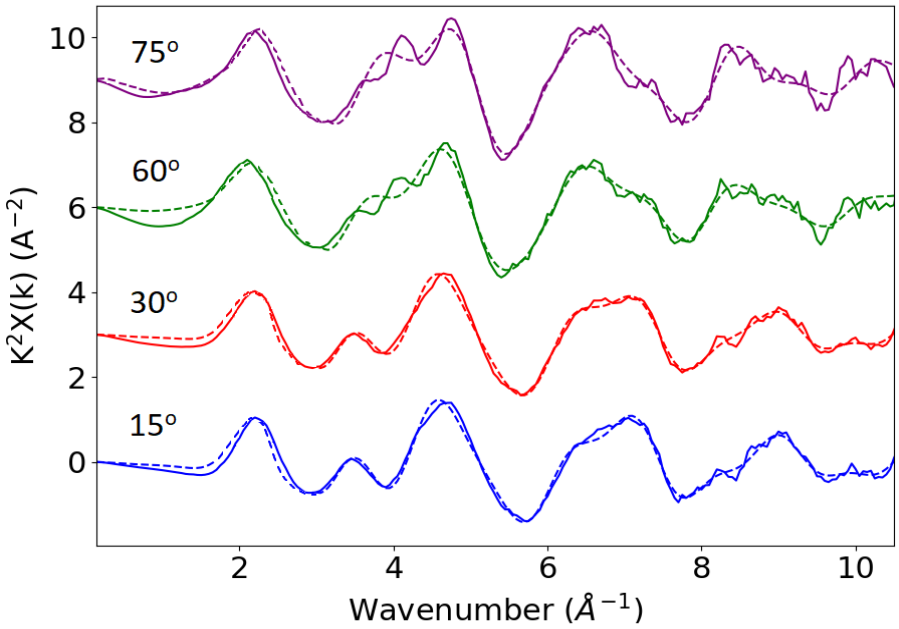

(b)

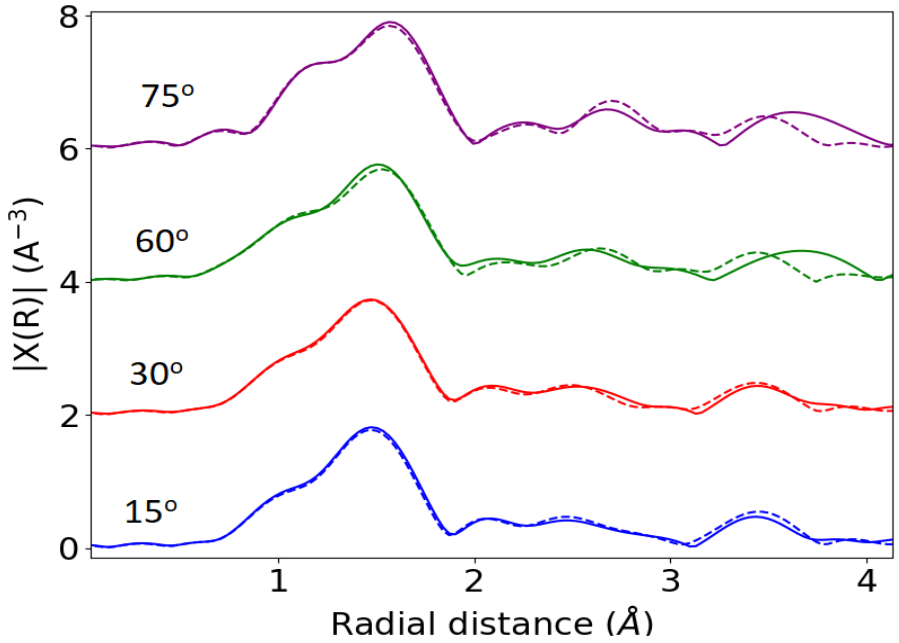

Figure 7.4.13: a) EXAFS and b) FT-EXAFS fitting examples for Ca_2RuO_4 (Ru K-edge) at 400K using 4 angles. The dashed lines indicate the fitting result.

(a)

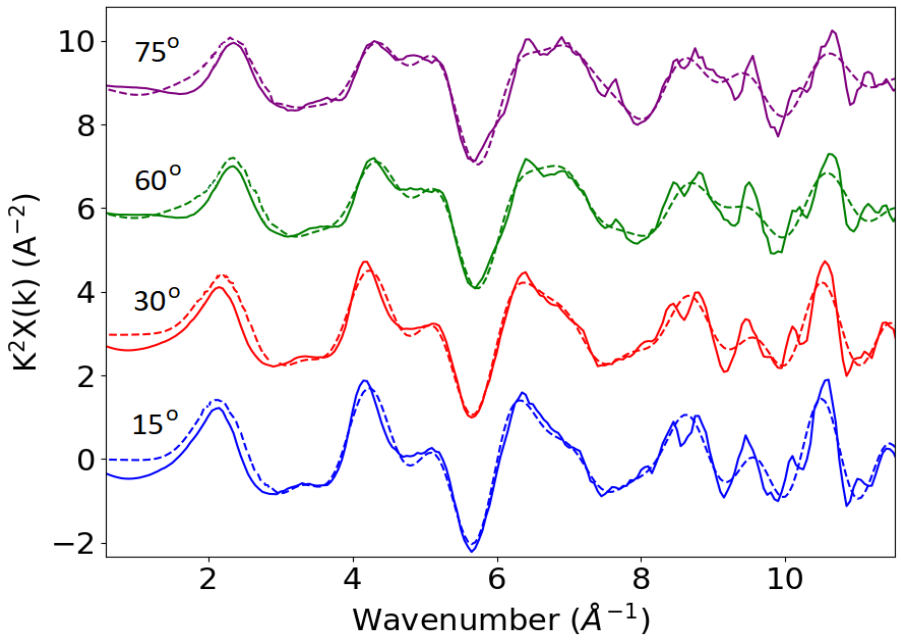

(b)

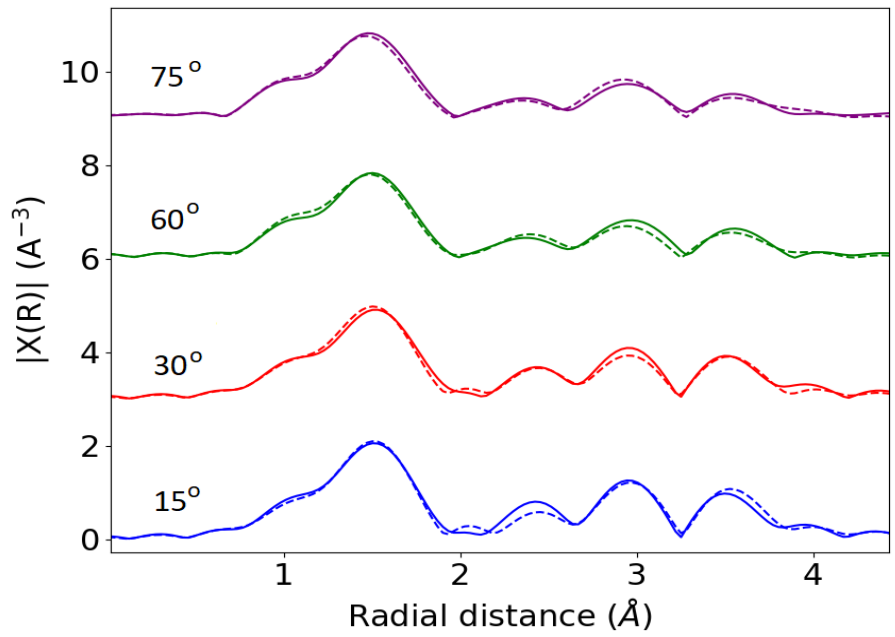

Figure 7.4.14: a) EXAFS and b) FT-EXAFS fitting examples for Ca_2RuO_4 (Ru K-edge) at 55K using 4 angles. The dashed lines indicate the fitting result.

Parameters	400K	340K	300K	250K	150K	120K	90K	70K	55K
ΔE_0 (eV) - (15^o)	-3.7±0.7	-5.3±0.8	-3±1	-5±1	-3.0±0.9	-5±1	-5±1	-5.4±0.9	-5.7±0.9
ΔE_0 (eV) - (30^o)	-3.9±0.7	-3.1±0.8	-2.7±0.9	-4.6±0.9	-4.7±0.8	-4.7±0.9	-5.1±0.9	-5.1±0.8	-5.1±0.7
ΔE_0 (eV) - (45^o)	-	-	-2±1	-3±1	-	-4±1	-	-3.6±0.9	-
ΔE_0 (eV) - (60^o)	-3±1	-1±2	1±2	-2±1	-	-4±1	-	-3±1	-1±1
ΔE_0 (eV) - (75^o)	-2±2	-1±2	-	-	-2±2	-3±2	-2±2	-2±1	-1±1
S_o^2 - (15^o)	0.93±0.07	1.01±0.08	0.91±0.07	0.93±0.06	1.0±0.1	0.98±0.09	1.01±0.09	1.00±0.08	0.98±0.08
S_o^2 - (30^o)	0.95±0.07	0.94±0.06	1.00±0.07	0.97±0.06	0.98±0.09	0.96±0.05	0.97±0.07	0.96±0.07	0.96±0.06
S_o^2 - (45^o)	-	-	1.00±0.07	1.03±0.07	-	0.98±0.09	-	0.99±0.08	-
S_o^2 - (60^o)	1.0±0.1	0.97±0.09	1.0±0.1	0.98±0.09	-	1.0±0.1	-	0.93±0.08	0.96±0.08
S_o^2 - (75^o)	1.0±0.1	1.0±0.1	-	-	1.0±0.2	1.0±0.1	-2±2	1.0±0.1	0.96±0.09
1^{st} Ru-O R (Å)	2.054±0.009	2.00±0.01	1.99±0.01	1.98±0.01	1.98±0.01	1.96±0.01	1.97±0.01	1.976±0.008	1.974±0.008
1^{st} Ru-O σ^2 ($Å^2$)	0.001±0.001	0.001±0.001	0.002±0.001	0.003±0.001	0.003±0.002	0.002±0.001	0.002±0.001	0.004±0.001	0.004±0.001
2^{nd} Ru-O R (Å)	1.950±0.004	1.983±0.005	1.991±0.006	2.009±0.006	2.019±0.005	2.021±0.006	2.018±0.006	2.016±0.005	2.018±0.005
2^{nd} Ru-O σ^2 ($Å^2$)	0.0030±0.0007	0.0030±0.0008	0.0020±0.0008	0.0009±0.0006	0.0020±0.0008	0.0003±0.0006	0.0007±0.0007	0.0020±0.0007	0.0020±0.0008
1^{st} Ru-Ca R (Å)	3.27±0.03	3.15±0.03	3.15±0.02	3.08±0.01	3.08±0.01	3.07±0.01	3.06±0.01	3.076±0.009	3.08±0.01
1^{st} Ru-Ca σ^2 ($Å^2$)	0.012±0.003	0.009±0.004	0.010±0.003	0.004±0.001	0.004±0.001	0.003±0.001	0.002±0.001	0.005±0.001	0.004±0.001
2^{nd} Ru-Ca R (Å)	3.36±0.03	3.09±0.02	3.06±0.03	3.10±0.06	3.22±0.04	3.16±0.09	3.22±0.04	3.23±0.03	3.24±0.03
2^{nd} Ru-Ca σ^2 ($Å^2$)	0.008±0.005	0.006±0.003	0.003±0.005	0.003±0.007	0.002±0.004	0.002±0.001	0.001±0.003	0.002±0.004	0.001±0.004
3^{rd} Ru-Ca R (Å)	3.23±0.01	3.33±0.04	3.4±0.2	3.259±0.009	3.26±0.02	3.26±0.01	3.25±0.01	3.262±0.009	3.26±0.01
3^{rd} Ru-Ca σ^2 ($Å^2$)	0.011±0.003	0.02±0.02	0.04±0.04	0.0005±0.0005	0.001±0.001	0.0001±0.0002	0.0001±0.0005	0.0001±0.0002	0.0001±0.0005
4^{th} Ru-Ca R (Å)	3.42±0.03	3.33±0.05	3.6±0.2	3.61±0.06	3.64±0.04	3.63±0.07	3.64±0.05	3.62±0.02	3.62±0.03
4^{th} Ru-Ca σ^2 ($Å^2$)	0.0003±0.0003	0.002±0.006	0.02±0.03	0.005±0.006	0.004±0.001	0.003±0.001	0.002±0.001	0.0010±0.0001	0.0010±0.0002
Ru-Ru R (Å)	3.86±0.02	3.90±0.01	3.90±0.01	3.908±0.007	3.93±0.01	3.91±0.02	3.92±0.02	3.93±0.01	3.92±0.01
Ru-Ru σ^2 ($Å^2$)	0.008±0.002	0.005±0.001	0.005±0.001	0.0020±0.0008	0.003±0.001	0.0020±0.0008	0.0010±0.0008	0.002±0.001	0.002±0.001
Ru-O-Ru R (Å)	3.93±0.02	3.96±0.01	3.97±0.01	3.975±0.001	4.00±0.01	3.98±0.02	3.98±0.02	4.00±0.01	3.99±0.01
Ru-O-Ru σ^2 ($Å^2$)	0.014±0.002	0.011±0.001	0.008±0.001	0.0040±0.0008	0.007±0.001	0.0020±0.0009	0.0020±0.0008	0.006±0.001	0.006±0.001
5^{th} Ru-Ca R (Å)	4.01±0.03	4.38±0.03	4.37±0.02	4.328±0.007	4.30±0.07	4.28±0.06	4.29±0.08	4.30±0.03	4.30±0.03
5^{th} Ru-Ca σ^2 ($Å^2$)	0.007±0.003	0.003±0.003	0.001±0.002	0.010±0.007	0.01±0.01	0.009±0.006	0.01±0.01	0.009±0.004	0.009±0.004
3^{rd} Ru-O R (Å)	3.973±0.004	3.994±0.004	4.002±0.006	4.019±0.006	4.029±0.005	4.031±0.006	4.029±0.005	4.027±0.005	4.029±0.005
3^{rd} Ru-O σ^2 ($Å^2$)	0.0030±0.0007	0.0020±0.0008	0.0020±0.0008	0.0010±0.0006	0.0020±0.0008	0.0003±0.0006	0.0007±0.0007	0.0020±0.0007	0.0020±0.0008
4^{th} Ru-O R (Å)	4.01±0.03	4.06±0.01	4.07±0.01	4.074±0.001	4.06±0.01	4.08±0.02	4.08±0.02	4.09±0.01	4.09±0.01
4^{th} Ru-O σ^2 ($Å^2$)	0.008±0.002	0.005±0.001	0.005±0.001	0.0020±0.0008	0.003±0.001	0.0020±0.0008	0.0010±0.0009	0.002±0.001	0.002±0.001
R-Factor	0.028	0.021	0.019	0.016	0.023	0.035	0.030	0.022	0.017
Independent points	92	92	92	96	79	106	75	110	89
Variables	60	61	60	60	55	61	48	70	59

Table 7.4.4: Ca_2RuO_4 Fitting parameters. Note that (-) indicates the data set was not usable.

EXAFS: $Ca_{2-x}La_xRuO_4$, x = 0.05, 0.15

Due to the low level of doping in this system the same fitting strategy has been used for both doped compositions with the assumption that the small distortions due to the doping will be taken into account by the fitting parameters. Figures 7.4.15 and 7.4.16 show the EXAFS and FT-EXAFS for the two compositions across different angles. For the sample with $x = 0.05$, the k-space data shows similar changes in the 300K data when compared to the pure compound. However only small changes are seen in the 50K when compared to the pure compound. Due to an increase in the vibration caused by the cryo-jet used for some of the temperatures, some of the spectra show weaker oscillations and more systematic noise. The following temperatures were measured whilst using the cryo-jet and the R-factors for the fitting analysis later shown reflect the increase in vibration; $x = 0.00$: 150K, 120K, 90K. $x = 0.05$: 300K, 217K, 170K, 120K. $x = 0.15$: 300K, 150K. The FT-EXAFS data shows a clear first feature at 1.6Å related to the Ru-O paths, and further features are seen between 2Å - 4Å which are related mainly to the Ru-Ca paths. The angular dependency of these data sets can be seen at both temperatures, for example small changes in the Ru-O path intensity and position. If compared to the pure compound, the changes appear to be weaker, which may be due to more distortion in the data and a smaller k-range available to extract the R-space data. The temperature related effects in the 30^o data for the $x = 0.05$ composition is shown in figure 7.4.17. In both the EXAFS and FT-EXAFS data there are changes in certain features between 217K and 180K, which is consistent with the main structural transition being suppressed. For example in the EXAFS between 4 - 5Å^{-1} and in the FT-EXAFS at 3Å. It is difficult to determine changes in the Ru-O paths, however there is a very small shift in the peak position. There is a clear change in Ru-Ca region at 2.8Å. This also indicates significant intensity differences due to the thermal effects.

In the $x = 0.15$ composition the MI transition should be completely suppressed along with the structural transition. Figure 7.4.16 shows the angular dependence of the EXAFS and FT-EXAFS data for this composition across two temperatures. While there is a dependence of the features with respect to the angles measured, there is no significant difference in the data across the temperature range. This confirms that the structural transition is suppressed to at least below 50K. The data quality shown is comparable to that of the pure sample, and shows strong signal up to approximately 9Å^{-1} in k-space and 4Å in R-space.

(a)

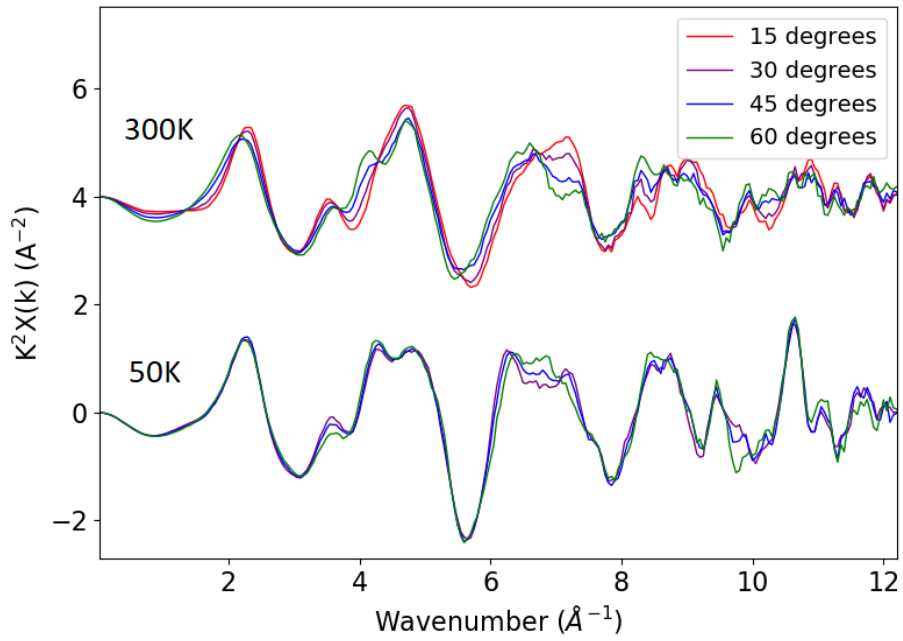

(b)

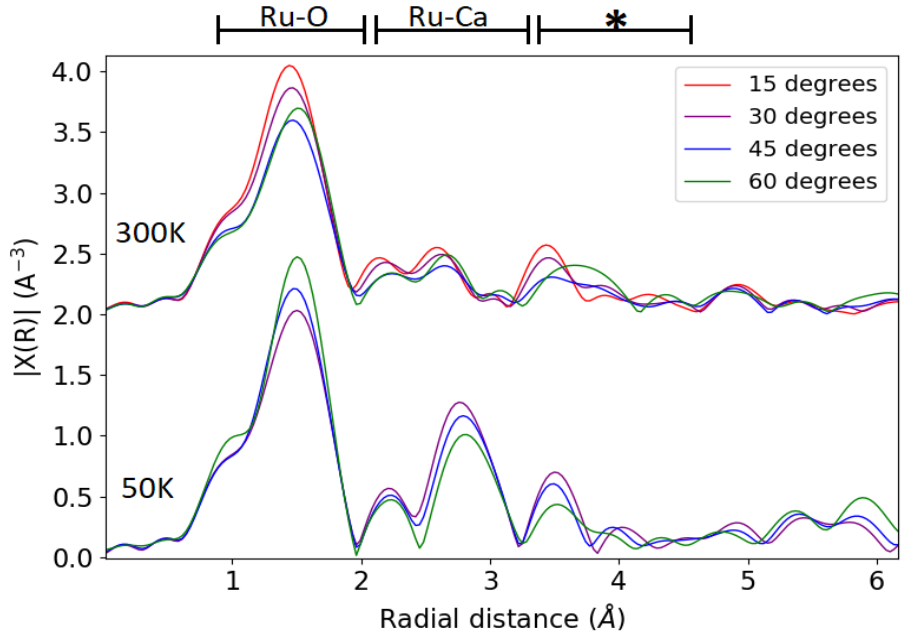

Figure 7.4.15: a) EXAFS and b) FT-EXAFS for $Ca_{2-x}La_xRuO_4$ (Ru K-edge), $x = 0.05$. Showing the angular dependence of these measurements at both 300K and 50K. Also indicated are the two main regions of interest, identifying the first Ru-O and Ru-Ca regions in the FT-EXAFS, * indicates a region of mixed scattering paths.

(a)

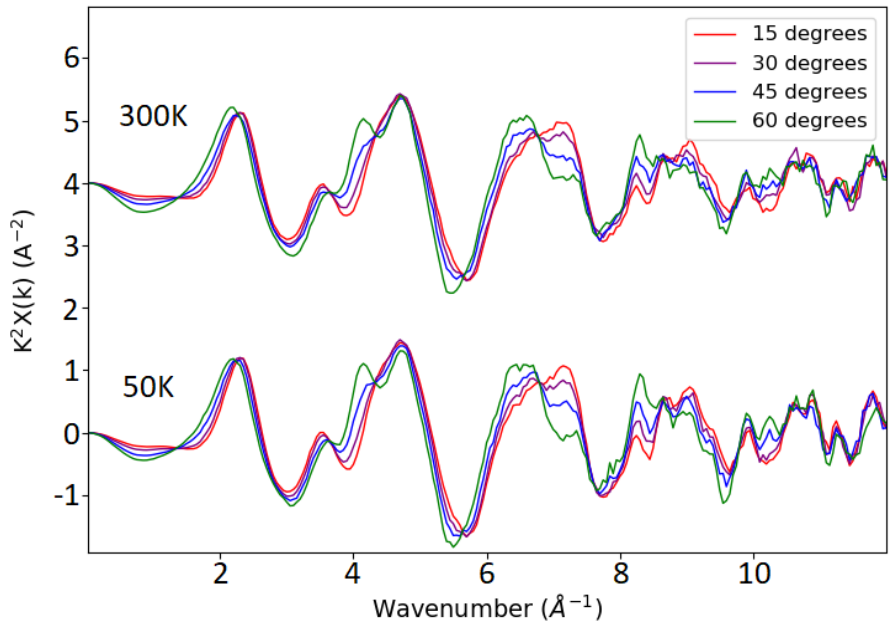

(b)

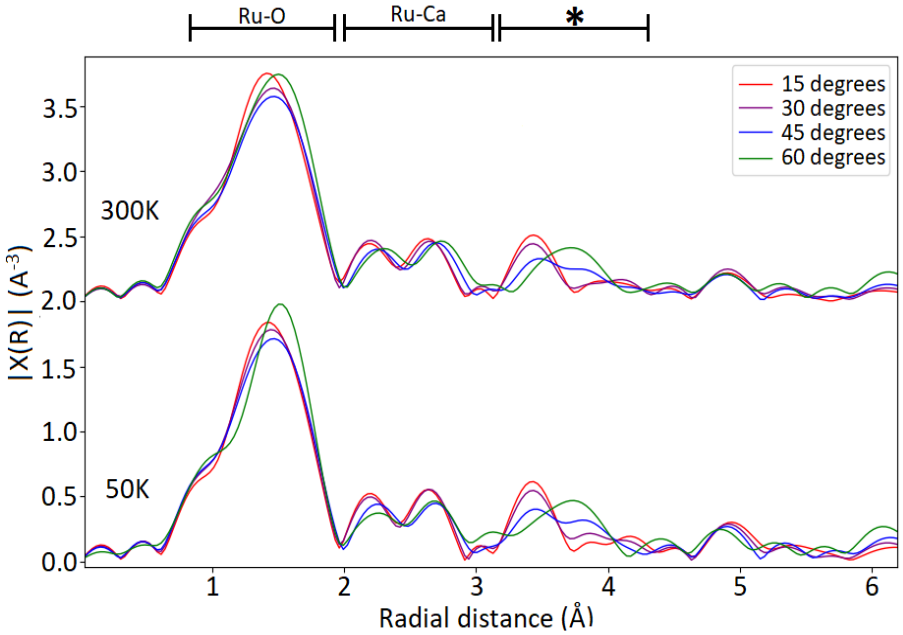

Figure 7.4.16: a) EXAFS and b) FT-EXAFS for $Ca_{2-x}La_xRuO_4$ (Ru K-edge), $x = 0.15$. Showing the angular dependence of these measurements at both 300K and 50K. Also indicated are the two main regions of interest, identifying the first Ru-O and Ru-Ca regions in the FT-EXAFS, * indicates a region of mixed scattering paths.

(a)

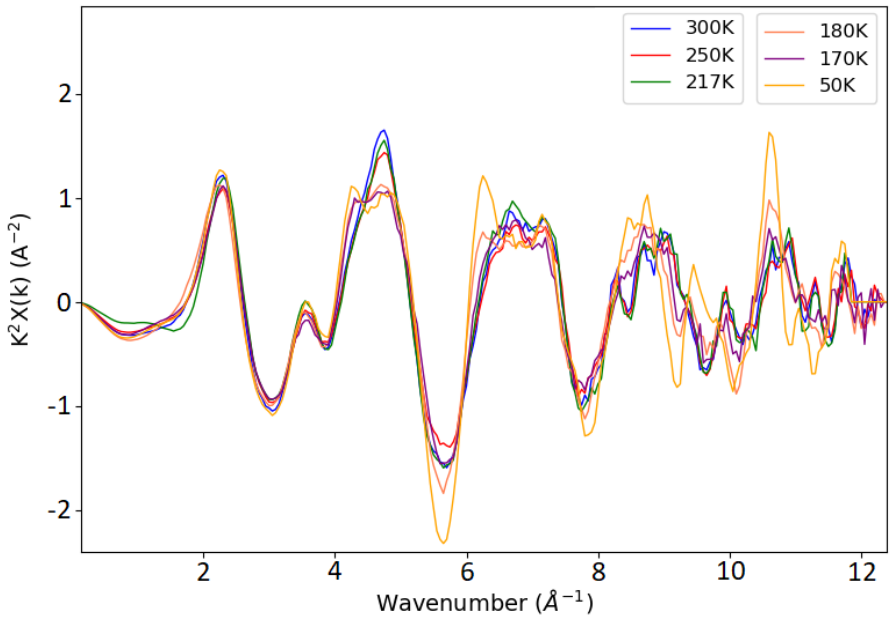

(b)

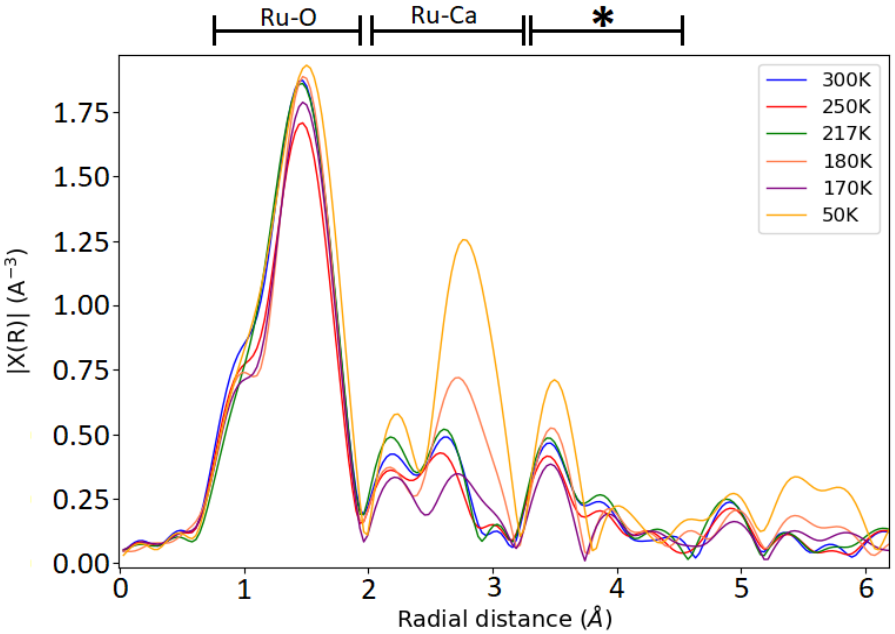

Figure 7.4.17: a) EXAFS and b) FT-EXAFS for $Ca_{2-x}La_xRuO_4$ (Ru K-edge), $x = 0.05$. Showing the 30^o measurements across all temperature. Also indicated are the two main regions of interest, identifying the first Ru-O and Ru-Ca regions in the FT-EXAFS, * indicates a region of mixed scattering paths.

Fitting: $Ca_{2-x}La_xRuO_4$, $x = 0.05$, 0.15

Example fits for the $x = 0.05$ composition are shown in figures 7.4.20 and 7.4.21, the fitting parameters are shown in table 7.4.5. These fits have been carried out using the same structure and procedure as for the pure compound. The fitting has been carried out in R-space over a range of 1.3Å - 3.5Å, where a k-range between 3Å^{-1} - 11.5Å^{-1} using k-weighting of 1, 2 and 3. The example fits show good agreement between the experimental and theoretical data in both k- and R-space for the two different temperatures. There are some small differences seen in the 300K data from approximately 3.2Å, however as this is at the end of the fitting window it suggests there may be additional paths in this region that are not considered in the fits.

The number of independent points for each data set varies between 72 - 105, with the number of variables used between 50-68. The R-factor for these fits is between 0.008 and 0.029, suggesting very good agreement between the experimental and theoretical spectra within the fitting window. The E_0 values are comparable with the pure sample and fairly consistent across angles and temperature. This parameter was left as a variable across the temperatures and angles due to the small changes seen in the edge position in the XANES region. The S_o^2 global parameters is generally close to 1, however in a couple of cases this raises to a maximum of 1.037 which may be a result from the overall distortion introduced by the dopant and that only one multiple scattering path has been included. The S_o^2 parameter has also been left as a variable across temperatures and angles, this has been done so that the angular dependence and self absorption correction for each data set can be check since this parameter is correlated to these effects. Similar to the pure compound, the Ru-Ca path lengths undergo small changes across the main structural transition. The 1^{st} and 2^{nd} path decrease, the 3^{rd} path is stable and the 4^{th} and 5^{th} paths increase. This suggests that similar distortions in the Ca cage are occurring in the doped compound over this transition. The Ru-Ru paths also see a small increase, in line with a small increase in the crystal lattice parameters below the transition, similar to the pure composition. The Debye-Waller factors are consistent with the pure compound results, however the errors for some paths are large, where the values could be negative. While this suggests some of the paths are not fitted well, the overall result is consistent with the pure compound and the Debye-Waller factor may indicate a significant level of distortion in the crystal structure. The in-plane and apical Ru-O path lengths are shown in figure 7.4.18. In considering the structure of the octahedra, above 200K the system is in a significantly elongated state. Between 220K and 160K the structure compresses but still remains elongated. Finally after approximately 160K the structure appears to be a regular octahedra, differing from the pure sample which enters a compressed state. The Debye-Waller factors for these paths are reasonable and show no consistent change across the temperature range measured.

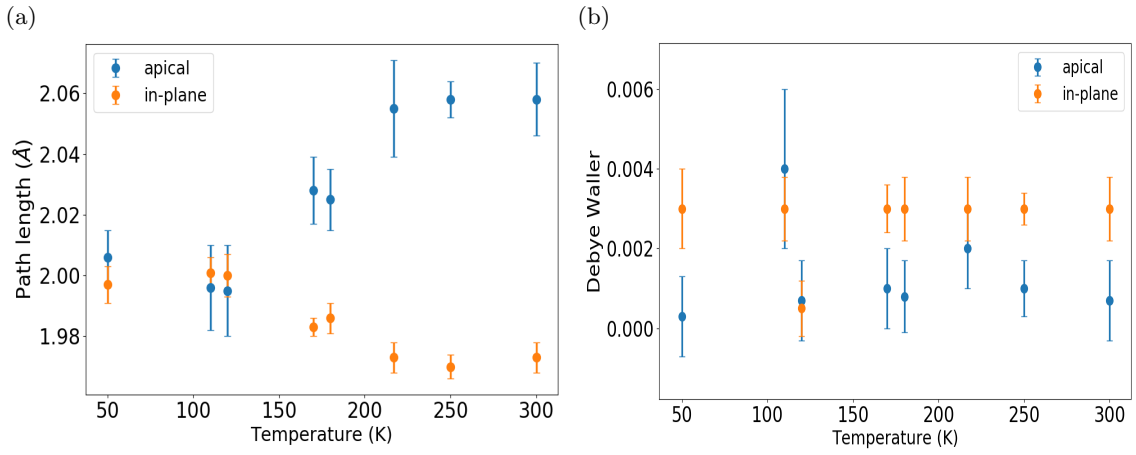

Figure 7.4.18: Oxygen path lengths and Debye-Waller factors for $Ca_{2-x}La_xRuO_4$, $x = 0.05$, across the temperature range measured.

The XANES data for the $x = 0.15$ compositions indicated that the MI transition has been fully suppressed, hence any changes seen in the structure would not be related to the transition. Figure 7.4.22 shows the example fit for this data, while table 7.4.6 shows the fitting parameter for a range of temperatures to track any changes in the structure. The fits have been carried out using the same procedure and ranges as the $x = 0.05$ compound. The example fits show good agreement between the experimental and theoretical data in the fitting range for both k- and R-space.

The E_0 parameters for these fits are consistent with the other compounds and are reasonable across the temperatures and angles. The S_o^2 parameter is close to 1 for all fits, and suggest that

even at this level of dopant the model is still applicable. The number of independent points ranges between 68-96 for the data sets, with the number of used variables between 48-60. The R-factor is significantly higher in these fits ranging from 0.025-0.036, which suggests slightly worst agreement with the theoretical data when compared to the other samples. The range however still suggests a reasonable fit. The Ru-Ca path lengths and Debye-Waller factors show some variation which is not consistent when compared to the pure material. Some of the errors are significant for these paths, this suggests that the quality of the fits in this region is affected by an increase in distortion in the EXAFS signal, caused by an increase in the crystal structure distortion due to the doping. The Ru-Ru path is consistent across the measured temperatures indicating that the lattice change seen in the samples with the MI transition does not occur in this sample. The in-plane and apical Ru-O paths are shown in figure 7.4.19. Unlike the other two samples, both paths are consistent across all temperatures, with reasonable (slightly higher) Debye-Waller factors. It confirms that the octahedra compression is linked to the MI transition.

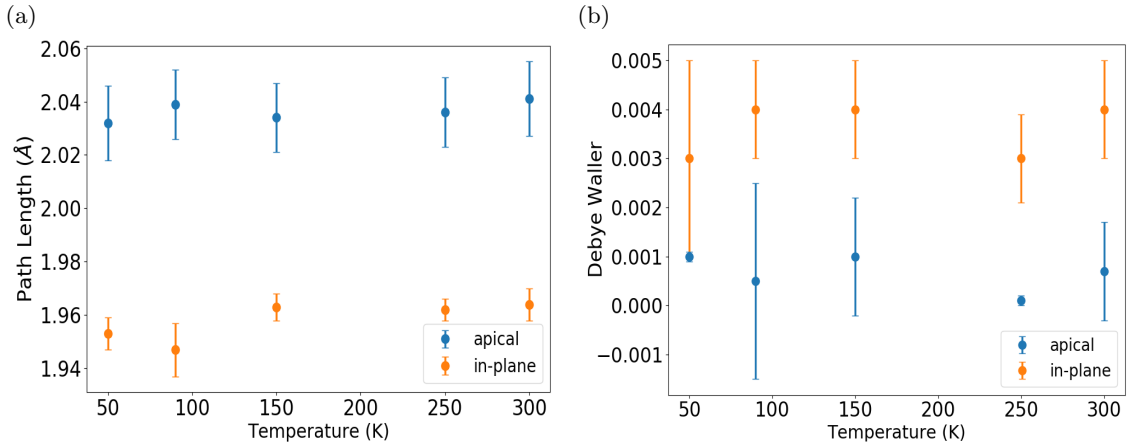

Figure 7.4.19: Oxygen path lengths and Debye-Waller factors for $Ca_{2-x}La_xRuO_4$, $x = 0.15$, across the temperature range measured.

(a)

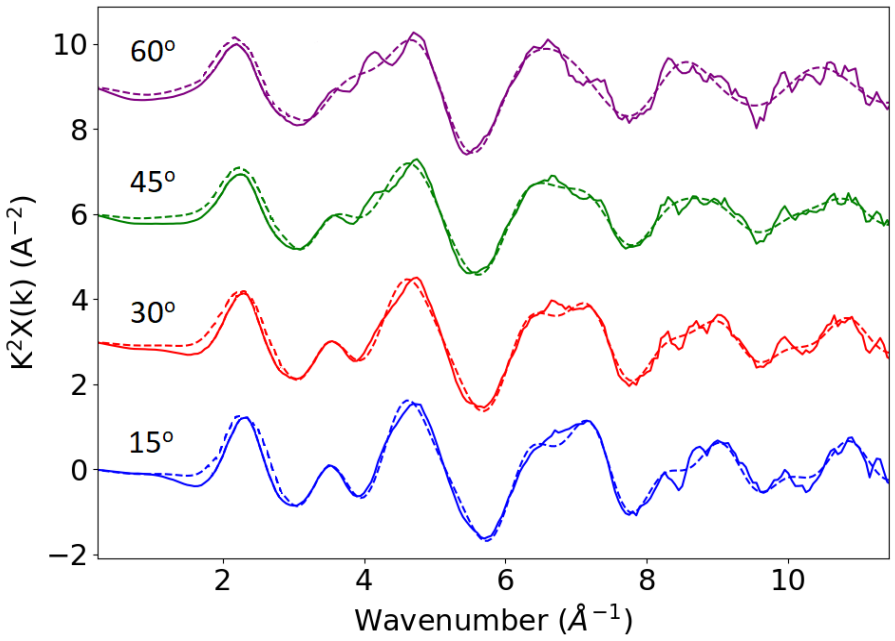

(b)

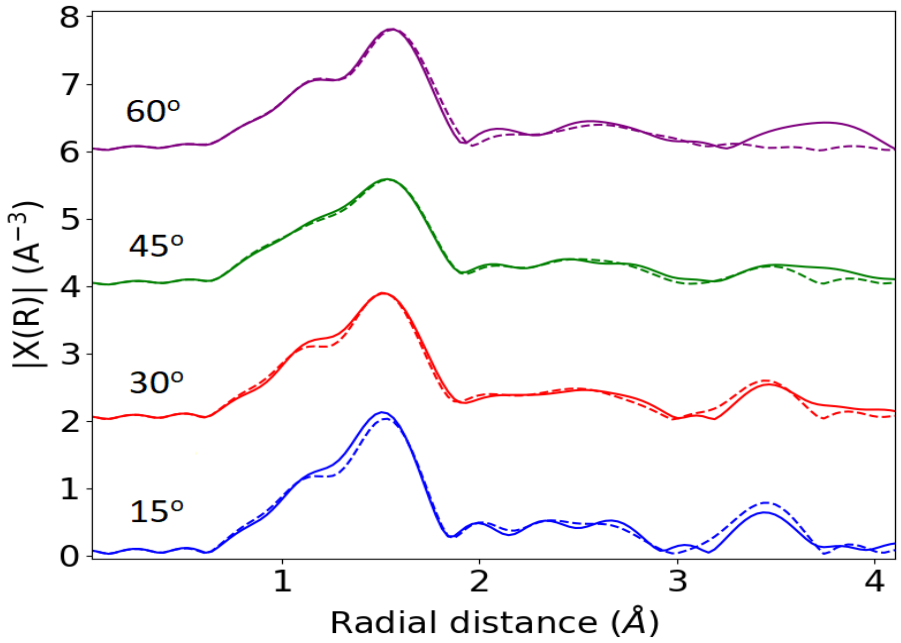

Figure 7.4.20: a) EXAFS and b) FT-EXAFS fitting examples for $Ca_{2-x}La_xRuO_4$ (Ru K-edge), $x = 0.05$ at 300K using 4 angles. The dashed lines indicate the fitting result.

(a)

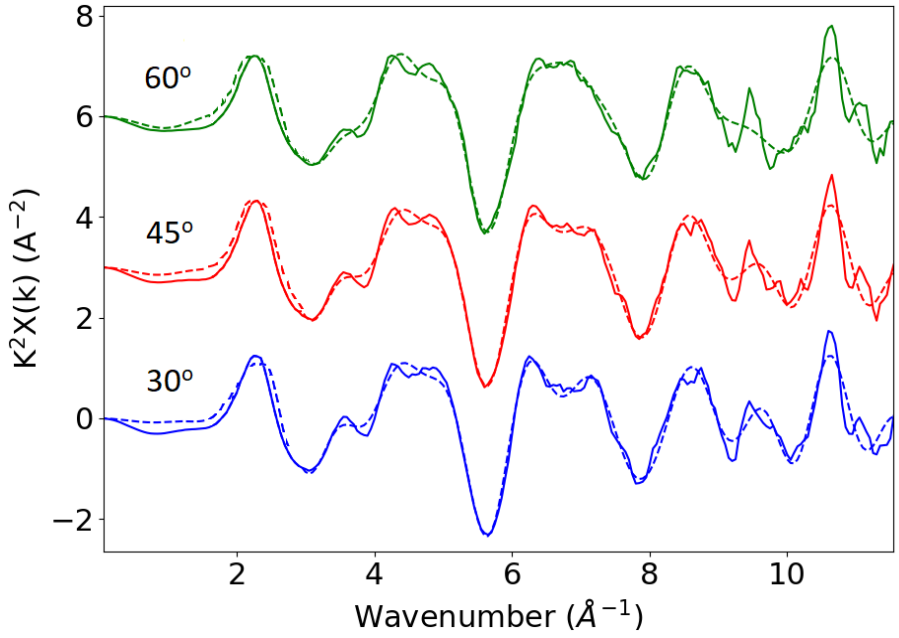

(b)

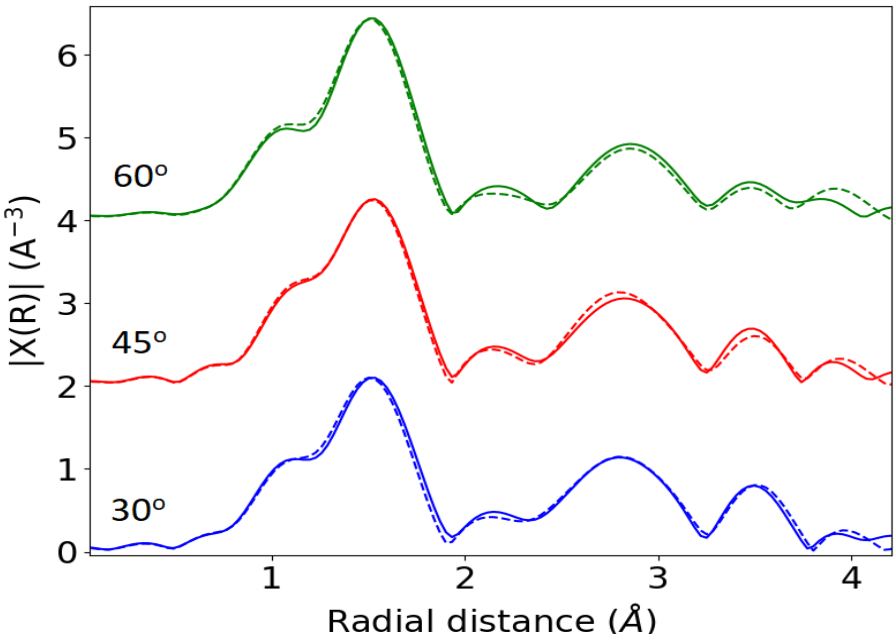

Figure 7.4.21: a) EXAFS and b) FT-EXAFS fitting examples for $Ca_{2-x}La_xRuO_4$ (Ru K-edge), $x = 0.05$ at 50K using 3 angles. The dashed lines indicate the fitting result.

Parameters	300K	250K	217K	180K	170K	120K	110K	50K
ΔE_0 (eV) - (15^o)	-2.4±0.8	-2.0±0.7	-1.7±0.8	-	-5.7±0.6	-	-	-
ΔE_0 (eV) - (30^o)	-2.9±0.9	-2.2±0.7	-2.1±0.9	-3.8±0.8	-3.1±0.7	-3±1	-3.6±0.8	-2.8±0.8
ΔE_0 (eV) - (45^o)	-2±1	-1.1±0.7	-2±1	-2.7±0.8	-1.8±0.9	-2±1	-3.5±0.8	-1.5±0.8
ΔE_0 (eV) - (60^o)	0±2	-1.1±0.7	-1±2	0±1	0±1	-2±1	-1±1	0±1
S_o^2 - (15^o)	1.04±0.09	0.95±0.05	1.0±0.1	-	0.95±0.06	-	-	-
S_o^2 - (30^o)	1.03±0.09	1.02±0.06	1.0±0.1	1.00±0.07	0.94±0.06	1.00±0.07	1.05±0.07	1.00±0.07
S_o^2 - (45^o)	0.95±0.09	1.02±0.06	1.0±0.1	1.01±0.07	0.97±0.07	0.98±0.07	1.00±0.07	1.01±0.06
S_o^2 - (60^o)	1.0±0.1	0.98±0.07	1.0±0.2	0.97±0.08	1.0±0.1	1.0±0.1	1.0±0.1	0.99±0.07
1^{st} Ru-O R (Å)	2.06±0.01	2.058±0.006	2.06±0.02	2.03±0.01	2.03±0.01	1.99±0.02	1.99±0.01	2.006±0.009
1^{st} Ru-O σ^2 ($Å^2$)	0.001±0.001	0.0010±0.0007	0.002±0.001	0.0008±0.0009	0.001±0.001	0.001±0.001	0.004±0.002	0.001±0.001
2^{nd} Ru-O R (Å)	1.973±0.005	1.970±0.004	1.973±0.005	1.986±0.005	1.983±0.003	2.000±0.007	2.001±0.005	1.997±0.006
2^{nd} Ru-O σ^2 ($Å^2$)	0.0030±0.0008	0.0030±0.0004	0.0030±0.0008	0.0030±0.0008	0.0030±0.0006	0.0005±0.0007	0.0030±0.0008	0.003±0.001
1^{st} Ru-Ca R (Å)	3.23±0.02	3.28±0.03	3.15±0.07	3.08±0.03	3.09±0.02	3.12±0.05	3.11±0.02	3.07±0.03
1^{st} Ru-Ca σ^2 ($Å^2$)	0.02±0.05	0.013±0.005	0.008±0.007	0.007±0.005	0.007±0.003	0.002±0.005	0.006±0.004	0.001±0.004
2^{nd} Ru-Ca R (Å)	3.35±0.05	3.38±0.02	3.23±0.06	3.13±0.04	3.18±0.04	3.18±0.05	3.08±0.02	3.12±0.04
2^{nd} Ru-Ca σ^2 ($Å^2$)	0.009±0.006	0.001±0.002	0.02±0.02	0.008±0.005	0.013±0.007	0.001±0.004	0.005±0.002	0.002±0.003
3^{rd} Ru-Ca R (Å)	3.22±0.03	3.23±0.01	3.30±0.05	3.264±0.007	3.27±0.02	3.26±0.01	3.264±0.007	3.255±0.007
3^{rd} Ru-Ca σ^2 ($Å^2$)	0.011±0.003	0.007±0.002	0.009±0.005	0.0060±0.0008	0.007±0.002	0.002±0.001	0.0070±0.0009	0.0020±0.0007
4^{th} Ru-Ca R (Å)	3.36±0.02	3.81±0.01	3.34±0.02	3.58±0.05	3.44±0.02	3.53±0.01	3.62±0.04	3.55±0.01
4^{th} Ru-Ca σ^2 ($Å^2$)	0.006±0.006	0.005±0.001	0.01±0.03	0.003±0.006	0.006±0.003	0.01±0.03	0.002±0.004	0.02±0.03
Ru-Ru R (Å)	3.84±0.01	3.80±0.02	3.84±0.01	3.89±0.01	3.885±0.008	3.89±0.02	3.99±0.02	3.92±0.01
Ru-Ru σ^2 ($Å^2$)	0.007±0.001	0.009±0.001	0.006±0.001	0.006±0.001	0.0070±0.0008	0.0020±0.0009	0.010±0.001	0.004±0.001
Ru-O-Ru R (Å)	3.91±0.01	3.86±0.02	3.91±0.01	3.96±0.01	3.952±0.008	3.95±0.02	3.99±0.02	3.99±0.01
Ru-O-Ru σ^2 ($Å^2$)	0.013±0.004	0.016±0.001	0.011±0.004	0.011±0.005	0.013±0.004	0.003±0.003	0.016±0.002	0.009±0.002
5^{th} Ru-Ca R (Å)	3.93±0.03	4.02±0.01	3.93±0.03	3.87±0.03	3.92±0.03	4.37±0.03	4.39±0.02	4.37±0.02
5^{th} Ru-Ca σ^2 ($Å^2$)	0.010±0.004	0.005±0.001	0.009±0.004	0.013±0.006	0.012±0.004	0.003±0.003	0.004±0.002	0.006±0.003
3^{rd} Ru-O R (Å)	3.984±0.005	3.981±0.004	3.984±0.005	3.997±0.005	3.994±0.003	4.011±0.007	4.012±0.005	4.008±0.006
3^{rd} Ru-O σ^2 ($Å^2$)	0.0030±0.0008	0.0030±0.0004	0.0030±0.0008	0.0030±0.0008	0.0030±0.0005	0.0005±0.0007	0.0030±0.0008	0.003±0.001
4^{th} Ru-O R (Å)	4.01±0.01	3.96±0.02	4.01±0.01	4.06±0.01	4.051±0.008	4.05±0.02	4.08±0.02	4.09±0.01
4^{th} Ru-O σ^2 ($Å^2$)	0.007±0.001	0.009±0.001	0.006±0.001	0.006±0.001	0.0070±0.0007	0.0020±0.0008	0.010±0.002	0.004±0.001
R-Factor	0.029	0.016	0.037	0.011	0.024	0.022	0.015	0.008
Independent points	105	105	105	79	105	79	81	72
Variables	68	68	68	56	68	50	56	50

Table 7.4.5: $Ca_{2-x}La_xRuO_4$, $x = 0.05$ fitting parameters. Note that (-) indicates the data set was not usable.

(a)

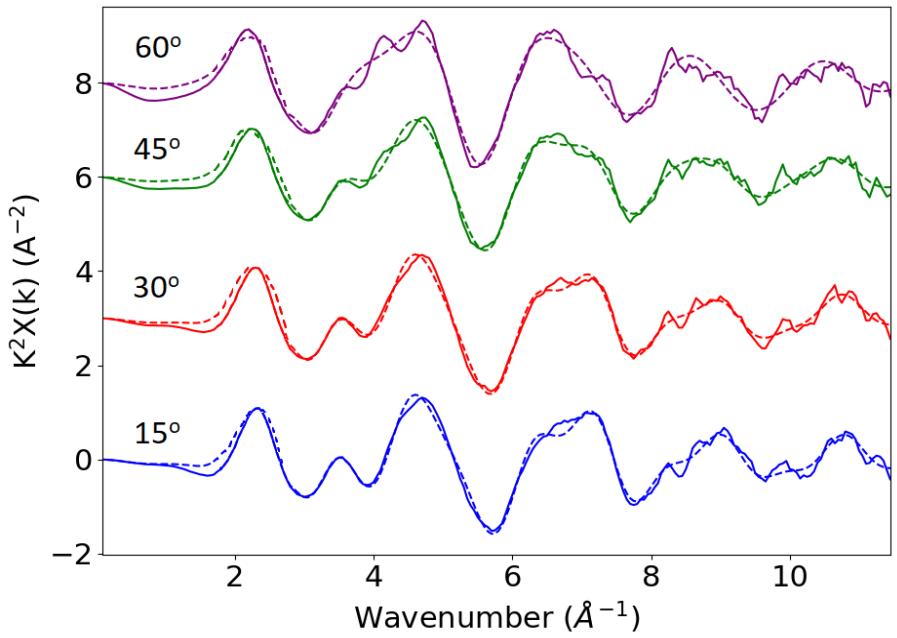

(b)

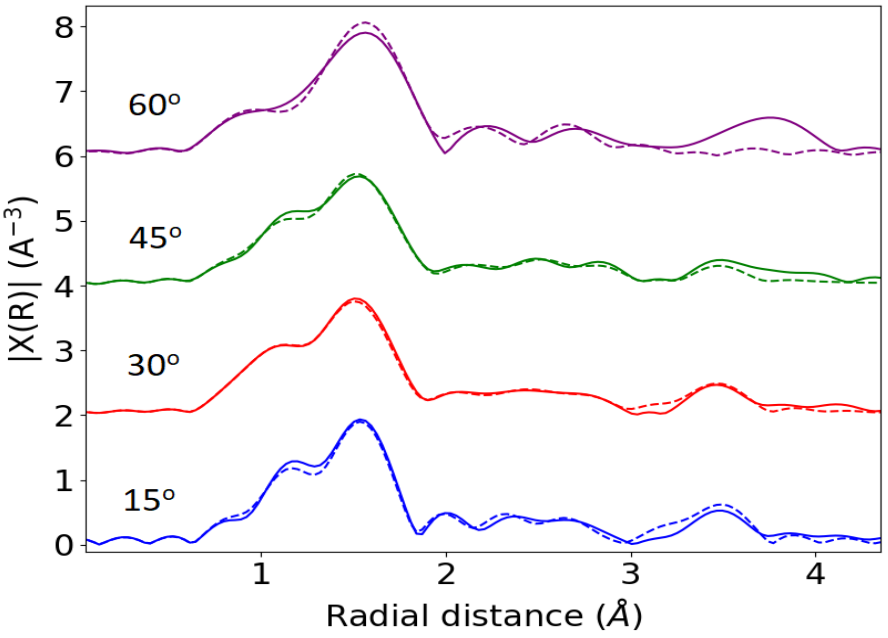

Figure 7.4.22: a) EXAFS and b) FT-EXAFS fitting examples for $Ca_{2-x}La_xRuO_4$ (Ru K-edge), $x = 0.15$ at 300K using 4 angles. The dashed lines indicate the fitting result.

Parameters	300K	250K	150K	90K	50K
ΔE_0 (eV) - (15^o)	-3.2±0.9	-3.7±0.8	-3.6±0.9	-	-
ΔE_0 (eV) - (30^o)	-3.4±0.9	-3.8±0.9	-4±1	-5±1	-4±1
ΔE_0 (eV) - (45^o)	-3±1	-4±1	-4±1	-4±1	-4±1
ΔE_0 (eV) - (60^o)	-4±2	-4±2	-6±2	-	-4±2
ΔE_0 (eV) - (75^o)	-	-	-	0±2	-2±3
S_o^2 - (15^o)	1.0±0.1	1.00±0.09	1.0±0.1	-	-
S_o^2 - (30^o)	1.00±0.09	0.99±0.08	1.0±0.1	0.9±0.1	1.0±0.2
S_o^2 - (45^o)	0.98±0.09	0.99±0.08	0.99±0.09	1.0±0.1	0.9±0.1
S_o^2 - (60^o)	1.0±0.1	1.02±0.08	1.0±0.1	-	0.94±0.09
S_o^2 - (75^o)	-	-	-	1.0±0.2	1.0±0.1
1^{st} Ru-O R ($\AA$)	2.04±0.01	2.04±0.01	2.03±0.01	2.04±0.01	2.03±0.01
1^{st} Ru-O σ^2 ($\AA^2$)	0.001±0.001	0.0001±0.0001	0.001±0.001	0.001±0.002	0.0010±0.0001
2^{nd} Ru-O R ($\AA$)	1.964±0.006	1.962±0.004	1.963±0.005	1.95±0.01	1.953±0.006
2^{nd} Ru-O σ^2 ($\AA^2$)	0.004±0.001	0.0030±0.0009	0.004±0.001	0.004±0.001	0.003±0.002
1^{st} Ru-Ca R ($\AA$)	3.23±0.07	3.22±0.09	3.19±0.05	3.24±0.04	3.20±0.04
1^{st} Ru-Ca σ^2 ($\AA^2$)	0.006±0.008	0.01±0.02	0.002±0.006	0.001±0.004	0.002±0.005
2^{nd} Ru-Ca R ($\AA$)	3.19±0.06	3.14±0.09	3.20±0.08	3.12±0.09	3.12±0.05
2^{nd} Ru-Ca σ^2 ($\AA^2$)	0.02±0.01	0.01±0.03	0.02±0.01	0.01±0.01	0.002±0.006
3^{rd} Ru-Ca R ($\AA$)	3.29±0.04	3.18±0.04	3.28±0.02	3.15±0.02	3.17±0.01
3^{rd} Ru-Ca σ^2 ($\AA^2$)	0.011±0.006	0.009±0.005	0.010±0.005	0.011±0.002	0.008±0.003
4^{th} Ru-Ca R ($\AA$)	3.28±0.02	3.33±0.03	3.23±0.08	3.43±0.03	3.42±0.02
4^{th} Ru-Ca σ^2 ($\AA^2$)	0.006±0.005	0.008±0.005	0.002±0.006	0.001±0.004	0.001±0.001
Ru-Ru R ($\AA$)	3.86±0.02	3.85±0.01	3.85±0.01	3.84±0.03	3.84±0.02
Ru-Ru σ^2 ($\AA^2$)	0.008±0.002	0.008±0.005	0.006±0.002	0.005±0.002	0.006±0.002
Ru-O-Ru R ($\AA$)	3.93±0.02	3.92±0.01	3.91±0.01	3.90±0.03	3.90±0.02
Ru-O-Ru σ^2 ($\AA^2$)	0.016±0.009	0.015±0.008	0.013±0.008	0.01±0.01	0.01±0.01
5^{th} Ru-Ca R ($\AA$)	3.91±0.05	3.91±0.05	3.91±0.05	3.86±0.09	3.85±0.07
5^{th} Ru-Ca σ^2 ($\AA^2$)	0.015±0.008	0.015±0.008	0.015±0.008	0.02±0.01	0.02±0.01
3^{rd} Ru-O R ($\AA$)	3.976±0.006	3.973±0.005	3.974±0.006	3.96±0.01	3.965±0.007
3^{rd} Ru-O σ^2 ($\AA^2$)	0.004±0.004	0.0030±0.0009	0.004±0.001	0.004±0.001	0.003±0.002
4^{th} Ru-O R ($\AA$)	4.03±0.02	4.02±0.01	4.01±0.01	4.00±0.02	4.00±0.02
4^{th} Ru-O σ^2 ($\AA^2$)	0.009±0.001	0.008±0.005	0.006±0.001	0.005±0.002	0.006±0.002
R-Factor	0.035	0.031	0.036	0.035	0.025
Independent points	96	96	96	68	81
Variables	60	60	60	48	58

Table 7.4.6: $Ca_{2-x}La_xRuO_4$, $x = 0.15$ fitting parameters. Note that (-) indicates the data set was not usable.

7.5 Discussion

The aim of this research was to track both the atomic and electronic structures in Ca_2RuO_4 across the metal to insulator transition. It has been previously suggested that the orbital occupation of the Ru t_{2g} states will change in a particular way across the MI transition. The two scenarios that have been tested in this chapter will affect the orbital occupations in different ways. In one scenario, the orbital occupation (n =(n_{xy}, n_{xz} + n_{yz})) goes from (2,2) in the insulating phase to (1,3) in the metal phase. In the other scenario the d_{xy} and $d_{xz,yz}$ energy difference is significantly affected by crystal field splitting. Additionally, the octahedral structural changes are suggested to be closely linked with the electronic structure. The XAS measurements presented in this chapter track both the electronic and atomic structure in both the pure composition and when doped with La.

The structure of the parent compound has been fully resolved by previous experiments. However to be confident that the electronic changes in the Ru are linked to certain structural changes, the EXAFS data has been collected to track the structure as a function of temperature. The results show that directly above the MI transition the oxygen octahedra around the Ru are in an elongate state along the *c*-axis. The octahedral structure undergoes a significant compression across the transition, where the distance between the in-plane oxygens lengthens and the apical oxygens contracts. Between 350K and 250K this octahedra further compresses until the in-plane oxygen paths are longer than the apical oxygen paths. Structurally, the octahedra goes from an slightly elongated state to a slightly compressed state. This is classed as a full Jahn-Teller distortion, and it is linked to a significant effect on the Ru energy levels. To determine if there is a strong interplay between these structural changes and the electronic state of this system, measurements have also been taken once the system is chemically doped with La. The La dopant retains the original lattice structure. However due to an increase in the t_{2g} bandwidth, caused by decreasing the highly distorted Ru-O-Ru bond angle (151^o when $x = 0$), the MI transition temperature is reduced. When the doping level reaches approximately $x = 0.1$, the MI transition is completely suppressed. The results for the $x = 0.05$ composition show that the MI transition temperature has been reduced to approximately 200K. Both the electronic and atomic structures show the same changes across this transition when compared to the pure sample. Interestingly the system does not undergo a further change which is seen in the parent compound and remains in a more regular octahedra. In the case where the MI transition is fully suppressed, there is no change in the octahedra structure. These results clearly suggest that the contraction of the octahedra is an important factor with relation to the MI transition. The doped material results suggest that the continued reduction of the distortion in the Ru-O-Ru bond angle may stabilize the system and prevent the octahedra from changing. It is important to also note that there are small changes in the Ca cage in this system, which also appear to be consequence on the MI transition since it is likely that they do not occur in the $x = 0.15$ system. It is reasonable to suggest that the change in the Ca cage is a result of the system reacting to the compression of the octahedra, however due to the quality of the data and the number of paths contributing to the region in R-space where the Ru-Ca path contributions are found, it is difficult to fully confirm.

The XANES L_2 and L_3 data tracks the electronic structure of Ru across the MI transitions and the magnetic transition in the parent compound. There are 2 well defined features in the absorption edge, which correspond to the lower energy t_{2g} states and higher e_g states. It is seen in the literature that in Ru structures the L_2- and L_3-edge features can not be fully separated due to the spin-orbit coupling and strong interelectronic Coulomb interaction, which leads to a transfer of intensity between these states [254]. This coupling can make it difficult to completely separate the different orbitals to accurately determine the occupation. However, by monitoring the changes in the relative intensities of the different features, it is possible to gain an understanding of the changes in the orbital occupations across the MI transition. Due to the electronic configuration, the e_g states are fully unoccupied. Across the MI transition the t_{2g} feature generally becomes more defined as a separate peak. This is a result of the compression of the octahedra which reduces the bandwidth of the two states. The difference across the angles due to this effect shows that in the lower angles the t_{2g} feature is less defined than in the higher angles. In considering the crystal structure and the relative orientation of the x-ray beam, it is expected that the lower angles show a high contribution of the d_{xy} orbital, while the higher angles represent the $d_{xz,yz}$ orbitals. It has been reported that due to the layered structure of this material, the *xz*, *yz* bandwidth is about half of that of the *xy* bands [25]. The difference in the bandwidths of the different states explains why the t_{2g} feature becomes more defined at the higher angles. It is interesting to compare the same angles across the different temperatures. In the 90^o spectra the t_{2g} peak intensity increases, while in the 0^o data it slightly decreases. While there may be a small effect from the bandwidth change, which may increase the localization of the electrons, the fact that one feature is increasing and one is decreasing suggests a different interpretation. The result indicate that there is charge transfer

between d_{xy} and $d_{xz,yz}$, where there is an increase in the number of electrons in the d_{xy} orbitals. This result is further confirmed by the XANES spectra of the doped samples. In the slightly doped sample, the same effect is seen in the t_{2g} orbitals however no change is seen on the fully doped sample. It suggests that the electronic and structural changes are closely linked.

While it is difficult to determine the exact occupation of the different orbitals, the results do suggest a system where the occupation (n =(n_{xy}, n_{xz} + n_{yz})) changes from close to (2,2) in the metal state to (1,3) in the insulating state. Due to the significant elongation of the octahedra, the t_{2g} orbitals should be split in energy, and the occupation suggests a possible Mott type insulator. It should be noted at this point that recent ARPES measurements and DFT calculations have indicated that all 3 bands are metallic in the metal state. [258]. While the Jahn-Teller distortion would suggest that the ordering of the two states should switch as the octahedra goes from the elongated to compressed state, it has been shown that due to the highly disordered nature of the Ru-O-Ru bond angle this is not the case [25, 26, 79, 248]. Due to the resolution of these measurements, it is difficult to determine the ordering of the orbitals and whether this changes across the transition. The results however do suggest a change in occupation across the transition. The doped system shows that by reducing the distortion in the Ru-O-Ru bond angles by doping with La, the t_{2g} bandwidth is slightly increased. This effect is most likely the reason that the MI transition temperature is reduced/suppressed.

One of the issues not addressed in the research so far is whether the structural transition is the driving force of the MI electronic transition. While from the parent compound it is not possible to answer this question, the doped system may indicate if this is the case. It suggests that the distortion in the structure, linked to the Ru-O-Ru bond angle, plays a critical role is stabilizing the system. If the system is highly distorted then it is favourable for the transition to occur. However when this distortion is reduced the system remains in the high temperature structure. While this may suggest that the structural transition is the driving mechanism, since the resultant changes in the energy levels causes the system to become an insulator, it is unclear from these results as to the effect of the additional electron that is added to the system from the La (per atom).

7.6 Conclusion

This chapter has presented XANES and EXAFS data on the Ca_2RuO_4 system to track both the electronic and atomic structures across the metal to insulator transition. The structural analysis confirms the previously reported octahedra compression across this transition, along with small distortions of the Ca cage. When the system is doped with La, the structural transition is suppressed. It has been suggested that due to the dopant reducing the distortion in the Ru-O-Ru bond angle, the system can remain in the high temperature state. The XANES analysis indicates that there is a charge transfer between the non-degenerate d_{xy} and $d_{xz,yz}$ states, along with a narrowing of the bandwidths. This narrowing pushes the system to a state where the on-site Coulomb interaction causes the electrons to become localized and the system to be in an insulating state since the d_{xy} is full. The doped system confirms that the atomic and electronic transitions are closely linked and it is most likely that the compression of the octahedra is the mechanism which drives the MI transition.

Chapter 8

Study of the nematic phase transition in $NaFe_{1-x}Co_xAs$

The role of the spin and orbital degrees of freedom in the iron pnictide superconductors remains unclear in the recently discovered nematic state. While both the low temperature structural and magnetic phase transitions have been fully resolved, experimental data has not confirmed if the preceding nematic state is of static or fluctuating order and what is driving the emergence of this state. The original aim of this research was to use polarization dependent XAS and vtc-XES measurements to probe the system once doped with Co, where a bulk superconducting state emerges. These samples are highly sensitive in air and due to contamination with moisture, this experiment was unsuccessful in determining the electronic and atomic structural changes in this region. It was confirmed however that the $[FeAs_4]^{-1}$ structure is an important factor for the different states that can exist in this system. Small distortions in this structure can suppress these transitions.

8.1 Introduction

Since its discovery, understanding compounds which display superconducting properties has been a significant challenge in condensed matter physics. A diverse range of materials have emerged over the decades which typically fall in a select group of families, including pure elements [259], cuprates [30] and iron-based superconductors (SC) [260]. Characterized by FeAs or FeSe layers, iron based superconductors have proven to be an abundant class of materials in which unconventional superconductivity has been discovered with transition temperatures as high as $T_c = 50K$ [261]. The tuning of the electronic and atomic structures in these compounds often lead to significantly higher T_c than the parent compound. Chemical doping for instance can suppress structural and magnetic transitions which can lead to the appearance of the SC phase [33]. It can also affect the local electronic and magnetic correlations and shift the Fermi energy by changing the number of electron or hole carries [36, 38]. It is typical to find a number of different unusual electronic states that precede the onset of a SC phase, making it difficult to untangle the correlations between the different degrees of freedom present in the system.

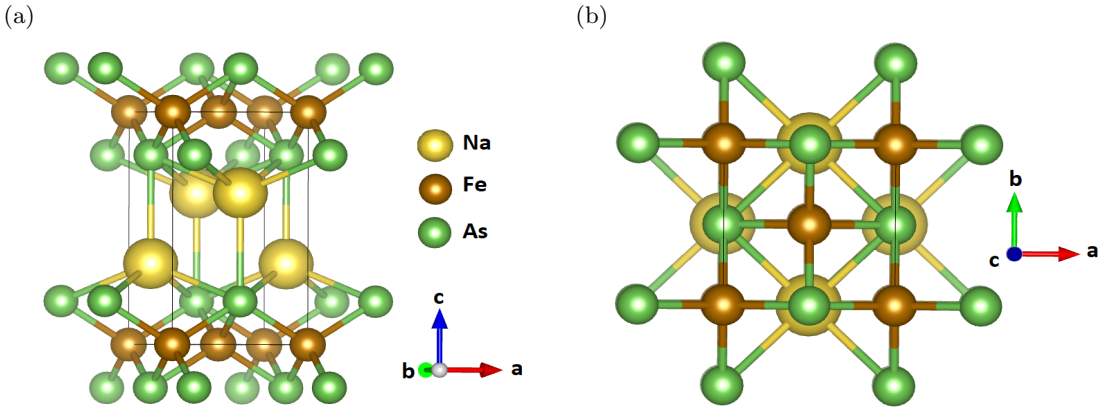

Figure 8.1.1: NaFeAs crystal structure. a) side view, b) top view.

The discovery of iron pnictide compounds in 2008 [262] has generated significant interest since these compounds may lead to new theories of unconventional superconductivity, as they are fundamentally very different from the cuprates, in which most high temperature SC's are found. There are 3 main families of iron base superconductors: (1:1:1) (Li,Na)FeAs, (1:2:2) (Ba, Sr, Ca)Fe_2As_2

and (1:1:1:1) RFe(As, P)O (where R=rare earth elements) [31]. In each case the structural properties are similar, where two-dimensional Fe-As layers form face sharing $FeAs_4$ tetrahedra [263]. With strong electronic correlations, the parent compounds show long-range magnetic ordering and when doped, superconductivity [33]. The normal states of these compounds often show strong anisotropy and breaking of the 4-fold rotation (C_4) symmetry [35]. Studies also suggest that there might be a small degree of overlap between the AF magnetic and SC phase [32, 38]. Due to the relatively simple structures and synthesis processes [263], these materials have become an important testing ground for understanding the interplay between the different driving forces behind the transitions and the fundamental physics involved.

The (1:1:1) NaFeAs system with an anti-PbFCl structure type (figure 8.1.1), shows a structural transition (T_s=54K) well above the magnetic transition at 42K (T_N) and is a filamentary superconductor (T_c≈10K). Upon doping the Fe site with Co, bulk superconductivity can emerge where a maximum transition temperature of 21K has been achieved [38]. Similar to the other iron pnictides, in the high temperature phase the parent compound is formed of Fe-As layers with face sharing $FeAs_4$ tetrahedra and is in a paramagnetic metallic state (p4/nmm, a = 3.947Å, c = 7.039Å). Upon cooling it undergoes a transition at approximately T_{Nem}=90K into a nematic state. At T_S=54K a structural transition from tetragonal to orthorhombic phase is seen, where the Fe(Co)As bond length decreases, and the volume of the cell is dominated by a c-lattice contraction. Finally at T_N=42K the system becomes anti-ferromagnetic. While both the structural and magnetic transitions have been fully resolved [31, 32], the preceding orbital/spin nematic state is still unclear. The electronic nematic phase in NaFeAs is characterized as an electronic order that breaks the rotation symmetries without changing the translational symmetry of the underlying lattice [264, 265, 266, 267]. The origin of the transition has been theoretically linked to both the spin and orbital degrees of freedom but it is still unclear from experimental results as to what is the critical driving factor and whether it is caused by a static or fluctuating order [34, 35, 36, 37, 38]. It has been suggested that the spin nematicity can be understood as a direct consequence of orbital order, potentially involving an incommensurate state on the Fe $d_{xy/yz}$ orbitals [33, 34], but there is not a sufficient amount of experimental data to confirm this. It has become critical to understand this issue as it is believed that the interaction and coupling of these states may be responsible for the high temperature SC [38, 268].

Additionally, upon doping with Co, which contributes an additional electron per doping atom, all three transitions reduce in temperature and are eventually suppressed and superconducting phase appears between x = 0.025-0.07, shown in figure 8.1.2. In its normal state, Fe is in a $3d^6$ state where the Co doping pushes this towards $3d^7$ [36]. It has been suggested that the electron count is a critical factor in these compounds with regards to the SC temperature, where upon doping the Fermi level is increased. It is also important to consider the hybridization between the Fe d and As p orbitals, which is expected to be significant as the As sites are close to the Fe planes. While the SC phase is not the focus of this research, the literature suggests that the electron-phonon coupling in this system is too weak for conventional SC [269], and it is for this reason that these materials have attracted interest.

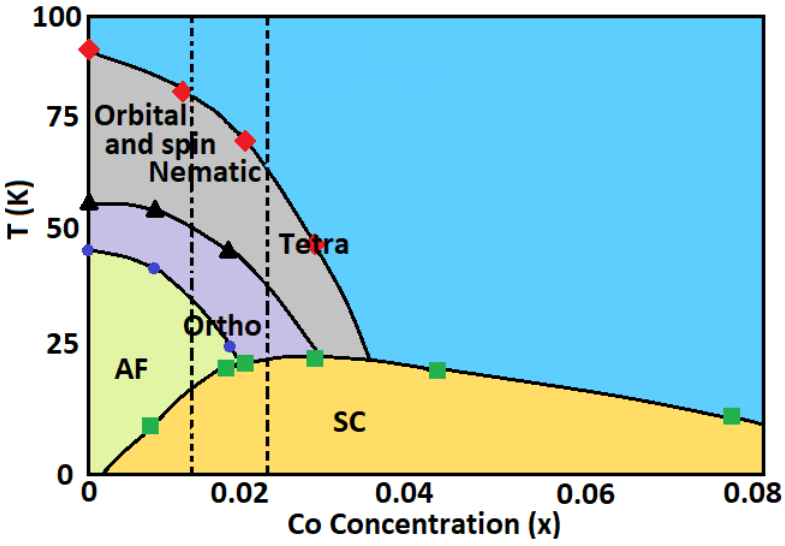

Figure 8.1.2: $NaFe_{1-x}Co_xAs$ Phase diagram [34]. The dashed lines indicate the compositions used in this research.

The NaFeAs compound is known to be very air and moisture sensitive and it is expected that this will also be the case in the doped system. While the exact time scale of the effect is debated, in some cases 24hr in others 2/3 weeks, it is clear that decomposition starts to occur immediately once exposed [270, 271]. A slow oxidative deintercalation of Na^+ results in the gradual contraction of the unit cell and a transformation in to $NaFe_2As_2$. The nature of the final product is not well studied, however it has been shown in the literature that it does not exhibit a SC phase and the antiferromagnetic phase appears at a much higher temperature (≈140K) and above this phase small structural distortions are observed [270]. Interestingly, on initial exposure the SC temperature increases, which may be related to an increase in internal strain, but with further exposure it decreases again [272].

Understanding the phases that can emerge before the SC is critical and this research focuses on the nematic phase transition once the system is doped with Co. It is strongly suggested that both the lattice and magnetic transitions are driven by (local) electronic reconstruction rather than a Fermi surface nesting, XAS/XES are suitable techniques to study these aspects. Using polarization-dependent HERFD-XAS and valence-to-core XES, single crystal samples ($x = 0.014$ and 0.023) have been investigated with the aim to provide evidence as to whether or not this transition is driven by orbital degrees of freedom. Further to this, measurements have also been taken across the other phases to understand how the interplay between the electronic and structural properties result in the different characteristic observed.

Due to the possible effects from decomposition due to exposure to moisture, care was taken to limit the exposure of the samples used in these measurements. To avoid air contact, the samples were stored in a argon filled container until the spectroscopy measurements. Initially, the samples used in the experiments were exposed to air for a short period whilst loading in the cryostat. However the effect for the decomposition on both the structural and magnetic phases is not well understood. Due to this, a second sample was loaded in to the cryostat within a He environment to reduce the overall exposure. It was important to identify any decomposition signatures when analysing the results obtained to understand the possible effects of decomposition on the different phases. After the spectroscopy experiments the samples were stored in an air tight container until it was possible to carry out characterization measurements to understand the level of decomposition.

8.2 Sample preparation and characterization

Single crystal samples of varying doping levels have been supplied and originally characterized using x-ray diffraction and magnetic susceptibility measurements by *Dr. Huiqian Luo*[10] at the Chinese Academy of sciences in Beijing. The samples were transported in a sealed argon filled container. It was decided that due to the sensitivity of the samples, additional characterization would be carried out after the spectroscopy measurements to reduce possible exposure. Two different compositions have been measured during these experiments and treated in different ways due to their air sensitivity. Initially, a sample of $NaFe_{0.986}Co_{0.014}As$ was loaded on to the sample cryostat in air and exposure was less than 10 minutes, assuming that decomposition would not affect the nematic phase on this time scale. In this composition $T_{Nem} \approx 80$K, $T_S \approx 53$K, $T_N \approx 35$K and $T_{SC} \approx 16$K. The second sample with $x = 0.023$ was loaded in the cryostat in an atmosphere flushed with He gas in an attempt to further reduce exposure. In this composition the transition temperatures are approximately $T_{Nem} \approx 64$K, $T_S \approx 40$K and $T_{SC} \approx 21$K, where the AFM state has been suppressed. Once the samples were loaded in the cryostat, the sample space was kept under vacuum till the end of the experiment.

8.2.1 Characterization measurements (SEM/EDX)

Characterization measurements have been carried out at the University of Kent approximately 1 year after the experiment due to restrictions on the use of the SEM/EDX during the COVID19 pandemic. The samples were stored in a moisture free environment to stop further exposure. SEM and EDX measurements have been carried out to check the sample quality and composition. Although these measurements are only surface sensitive, while the XAS/XES technique probe the bulk sample, the indicators of decomposition should be visible. These measurements allows an understanding of whether the results are relevant for the investigation presented in this chapter. It has been shown previously that two signs of significant decomposition can be detected with this technique [271]. Firstly, if conversion to the $NaFe_2As_2$ has started to take place, visual appearance of the reaction product may be detectable. In addition, it is expected that before a complete conversion occurs, stripes may appear indicating different domains. SEM and EDX data are shown on both compositions used and an additional composition ($x = 0.016$) as a reference. The reference sample

[10] Institute of Physics, Chinese Academy of Sciences, Beijing National Laboratory of Condensed Matter Physics

should not have been exposed during the experiment, remaining in the transport sample container until the SEM/EDX measurements with a minimal exposure time, therefore if it also show signs of exposure then it may point towards contamination before the main experiments.

The results from the SEM/EDX measurements are shown in figures 8.2.2-8.2.4. The SEM images for both compositions measured by x-rays ($x = 0.014$ and 0.023) show an uneven crystal surface, indicated by the varying contrast across the sample surface. This suggests that the samples are decomposed and are not homogeneous single phase crystals. The EDX measurements further suggest that these samples have been significantly contaminated by moisture due to the high concentration of oxygen present. It should be noted that due to the relatively low dopant levels, the Co was not detectable. The reference sample ($x = 0.016$) was not exposed to air during the experiment. However the SEM and EDX measurements also show similar effects when compared to the other samples. This suggests that the contamination either occurred before the XAS/XES experiments or the sample containers were not air tight during the transportation.

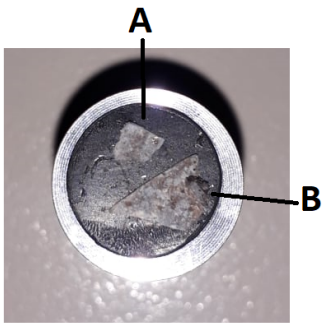

Figure 8.2.1: Example image of the $NaFe_{1-x}Co_xAs$ samples a) $x = 0.014$, b) $x = 0.0223$.

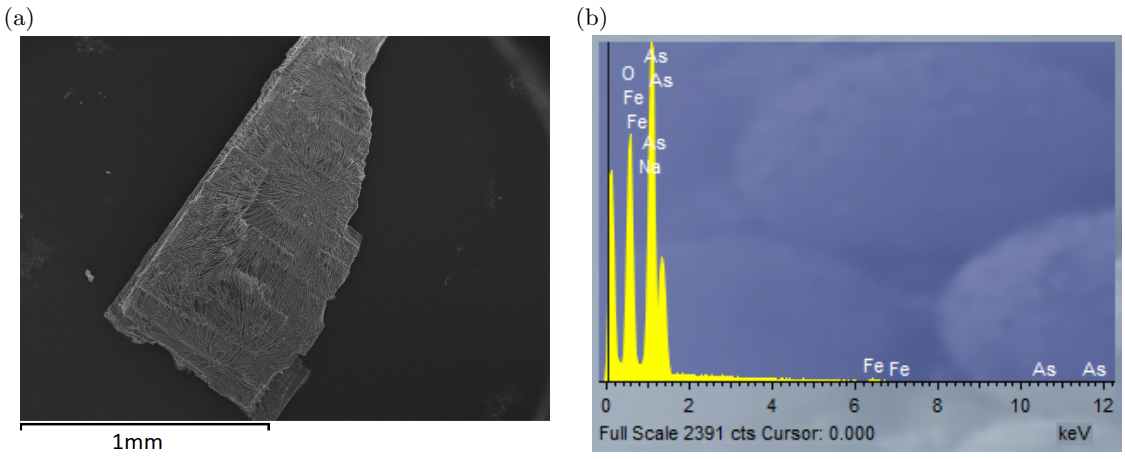

Figure 8.2.2: a) SEM images and b) EDX measurements on $NaFe_{1-x}Co_xAs$ ($x = 0.014$).

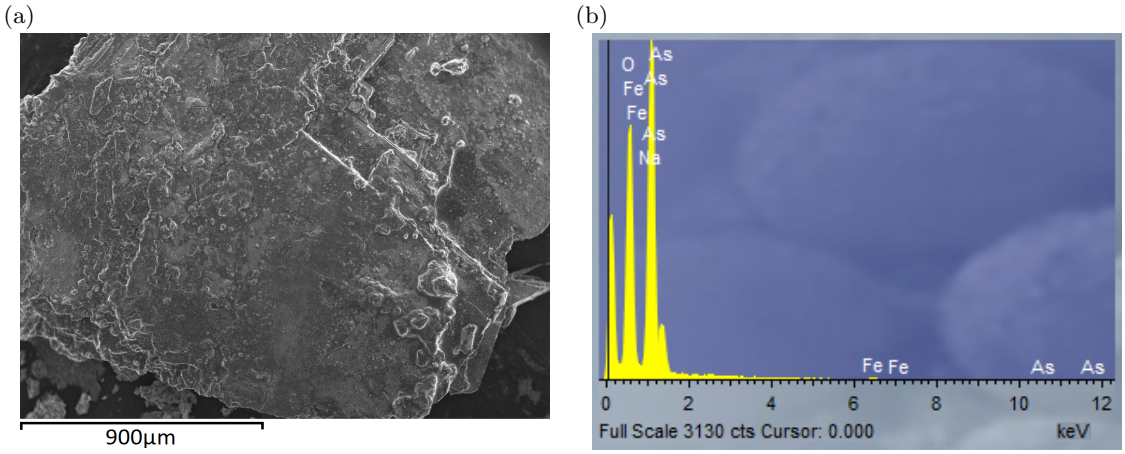

Figure 8.2.3: a) SEM images and b) EDX measurements on $NaFe_{1-x}Co_xAs$ ($x = 0.023$).

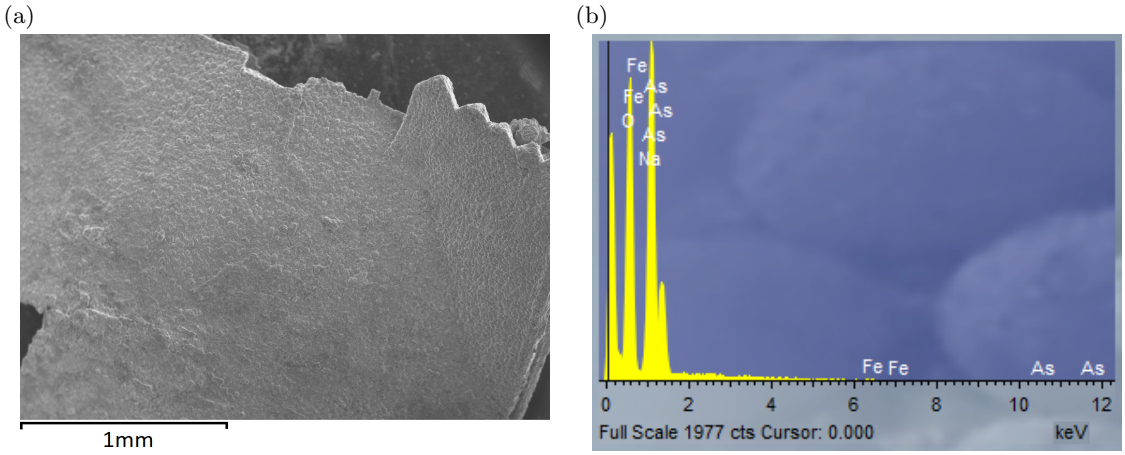

Figure 8.2.4: a) SEM images and b) EDX measurements on $NaFe_{1-x}Co_xAs$ ($x = 0.016$).

8.3 Experimental set-up and measurements

Both the HERFD-XAS and vtc-XES have been carried out on the I20-scanning beamline, Diamond Light Source U.K, with details of the beamline given in section 3.2.3. For this experiment the following co-workers assisted with the running of the beamlines and collecting data: Dr Silvia Ramos (University of Kent), Dr Shusaku Hayama (Diamond light source) and Dr Sofia Diaz-Moreno (Diamond light source). The measurements were made using the XES spectrometer to allow the selection of specific emission lines, giving greater spectral resolution within the XANES region. To achieve the low temperatures required, a closed-cycle He cryostat (Stinger), with a temperature range of 400K-5K, has been used (shown in figure 8.3.1). Due to the suspected highly anisotropy characteristic of the nematic phase, polarization dependent measurement gives the ability to track changes in both the electronic and atomic structures along different crystallographic planes. Using single crystal samples which have been cleaved between the Fe-As layers, the c-axis has been aligned parallel to the direction of the beam and rotated towards the ab-plane, which is in an unknown orientation. Shown in figure 8.3.1, all data sets in this chapter have been labelled so that 0^o refers to the beam polarization being parallel with the ab-plane and 90^o indicates that the beam polarization is parallel with the c-axis.

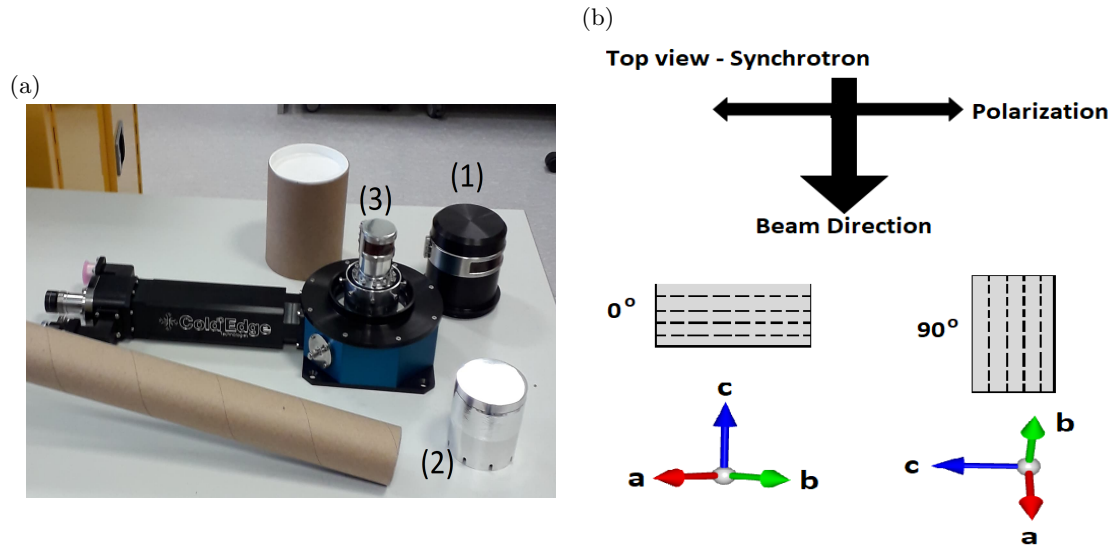

Figure 8.3.1: a) Stinger cryostat with the outer window (1), radiation shield (2) and cooling space (3) shown, b) sample alignment

The HERFD-XAS measurements were carried out using the Fe K-edge (7112eV) with the XES spectrometer (Si(440) crystals) monitoring the Kβ_1 and Kβ_3 emission lines while the incident energy is scanned over the absorption edge. The energy has been calibrated with an Fe foil at the K-edge. The scan parameters for each region were as follows: for the pre-edge region, an energy step of 5eV with 1s per point. Across the edge and XANES region an energy step of 0.3eV with 3s per point was used. Finally, for the EXAFS an energy step of ≈2eV with ≈5s per point was used, with each spectra repeated twice under the same conditions. These measurements probed the 1s→3d transitions to the unoccupied Fe states, where the emission spectrometer monitored the peak of the Kβ_1/Kβ_3[11] at 7057eV which corresponds to the 3p→1s transitions. For both compositions, 4 angles were measured (15^o, 30^o, 60^o, 75^o) to track changes across different crystallographic planes and across each transition. For $x = 0.014$ the temperatures measured where: 110K, 65K, 38K, 23K. For $x = 0.023$ these were 300K, 110K, 51K, 30K, 23K.

The vtc-XES measurements were carried out by setting the incident beam to an energy of 7500eV and scanning the emission spectrometer across the energy range between 7075eV-7124eV and using a energy step of 0.3eV, with 5s per data point. The transition involved are significantly weaker than the main emission line (Kα) (≈ 150x), and therefore the scans were repeated 3 times under the same conditions to improve the statistics. The measurements probe the valence bands of the ligands (As) and provide information regarding the metal-ligand bond lengths, oxidation state and metal-ligand interactions. The same angles and temperature as the HERFD-XAS have been collected.

Along with both compositions, measurements have been collected on Fe reference samples for both HERFD-XAS and vtc-XES. Fe_2O_3 with the Fe in a +3 state in a tetrahedral coordination and Fe_3O_4 which contains both Fe +2 and +3 states in both tetrahedral and octahedral coordination, have been measured to be able to compare the different oxidation states. The samples were mixed with cellulose to form diluted pellets to minimise the self-absorption effects and spectra have been collected at room temperature with the pellet at 45^o relative to the beam polarization.

8.4 Data analysis and Results

The data processing methods used for each spectra are outlined in chapter 4. In each case the data has had a pre-edge subtraction, background subtraction and post-edge normalization applied so a comparison between data sets can be carried out. A self-absorption correction has also been applied to extract the true absorption values. The method for this is given in section 4.2.1 and the relevant parameters used for the correction are: $\mu_{tot}(E_f) = 1076.3cm^{-1}$, $\mu_b(E) = 532.28cm^{-1}$, $\mu_0(E_{ae}) = 2655.81cm^{-1}$, $\mu_0(E_{be}) = 410.13cm^{-1}$. Further information specific to the XANES and EXAFS regions are given the relevant sections below.

[11] These emission lines are too close together to separate with the spectrometer.

8.4.1 XANES

Shown in figure 8.4.1 is a comparison across both samples in the nematic phase, along with the XANES data for the reference samples. The reference samples show a clear pre-edge feature and main absorption edge. Both the pre-edge (1s→3d) and absorption peak centred at approximately 7132eV (1s→4p) show a splitting of the features in the Fe_2O_3 sample compared to the other sample, which can be attributed to a splitting in the d states driven by the change in the coordination geometry of the different samples. There is a clear intensity difference in the pre-edge features going from Fe_2O_3 to Fe_3O_4. This could indicate an increase in holes in the 3d orbitals [273, 274, 275], as the pre-edge intensity can relate to an oxidation state. However, it is important to note that the pre-edge feature is mainly due to the geometry of the system. If there is a distortion in the system, which is the case with the two references, the pre-edge will become partially dipole and the intensity much higher.

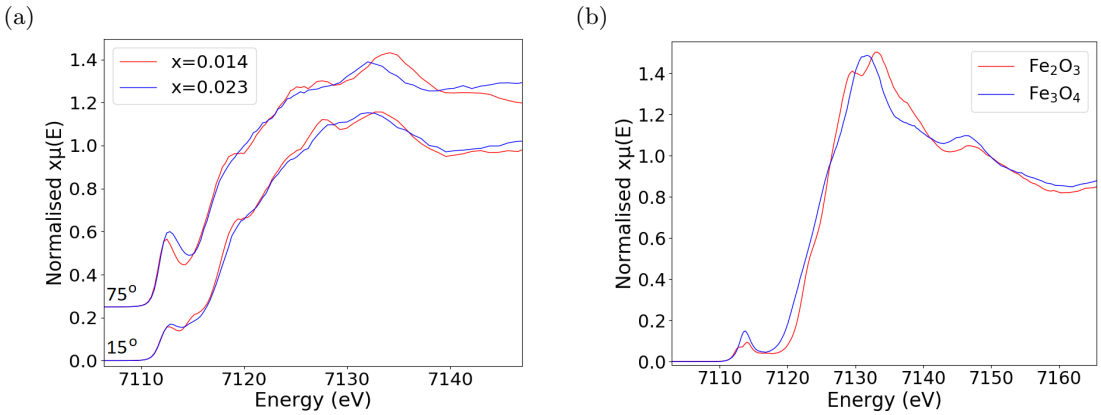

Figure 8.4.1: a) Comparison between both $NaFe_{1-x}Co_xAs$ samples at two angles (Fe K-edge) in the reported nematic state (x = 0.014 - 65K, x = 0.023 - 51K). b) Comparison between reference samples at room temperature (45^o).

The comparison between the two different samples in the nematic phase is shown in figure 8.4.1. There are some significant differences between the samples and angles. At both angles the main feature above the edge between 7125-7138eV has a clear double peak feature in the $x = 0.014$. However, it is less broad in the other sample. The main absorption edge start at 7118eV and is consistent across the two samples but is again better defined in the lighter doped sample. The pre-edge feature, representing the 1s→3d transition due to the lack of inversion symmetry in the iron tetrahedron, shows an increase in intensity for the $x = 0.023$ sample. There is an additional shoulder at approximately 7120eV in the $x = 0.014$ compound. The different between the two samples suggests a significant difference in the electronic structure, which could be related to two different effects. Firstly this could be caused by an increase in the doping, which introduces an additional electron per doping atom. Secondly this could be related to an affect from the decomposition of the samples due to exposure to moisture. While it is unclear as to which effect may be causing the differences in the spectra, the $x = 0.014$ is closer to the Fe_2O_3 reference spectra and the $x = 0.023$ is closer to the Fe_3O_4 spectra. Since these samples should be in the same phase and the level of doping is small, it is more likely that the differences are caused by the decomposition.

The $NaFe_{0.986}Co_{0.014}As$ sample shown in figure 8.4.2 across all transitions and two angles indicates very little change. After the absorption edge (E_0 = 7117.69eV) the peak positions and intensities show no change other than statistical noise. The main absorption edge also shows very little differences apart from a small intensity change at approximately 7120eV. A similar change is seen in the pre-edge features suggesting that this is most likely a thermal effect as no consistent change is seen over a transition. The first derivative shows how the pre-edge feature and the absorption edge positions are consistent across all measurements. It is also clear that the shoulder feature after the pre-edge is clearly defined in the 15^o data. Shown in figure 8.4.3 is the XANES data for the $NaFe_{0.977}Co_{0.023}As$ sample, which also shows very little differences across the transitions. The absorption edge is consistent with an E_0 position of 7117.9eV, and the pre-edge feature shows very little changes in intensity. The first derivative shows that the shoulder feature after the pre-edge is present in this data set but is significantly less intense. Both samples indicate that there is very little change across the temperature range in the electronic structure and both samples appear not to undergo a transition which effects the electronic state.

(a)

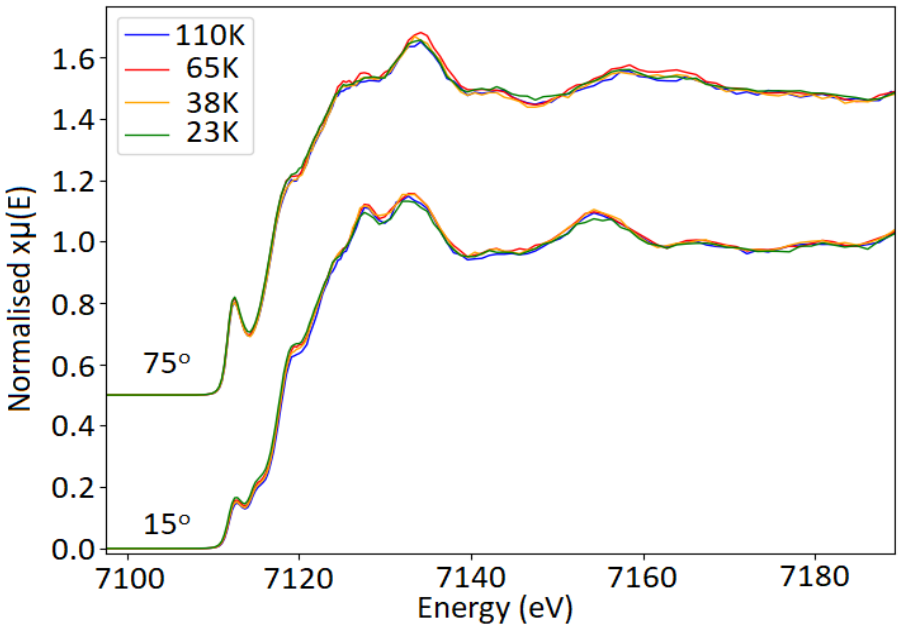

(b)

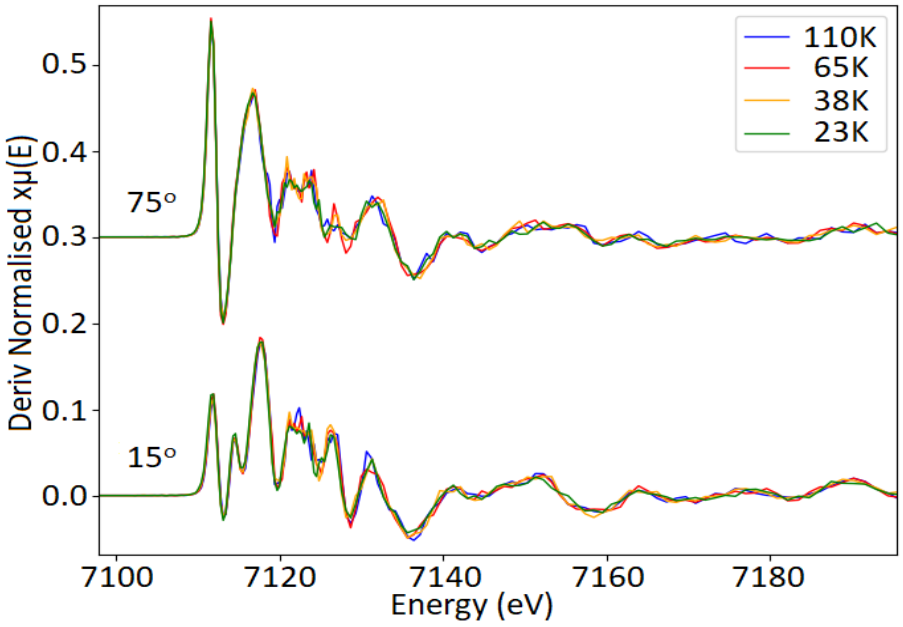

Figure 8.4.2: XANES: a) normalized spectra and b) normalized first derivative for the $NaFe_{1-x}Co_xAs$ ($x = 0.014$) Fe K-edge. Data is shown for 15^o and 75^o angle.

(a)

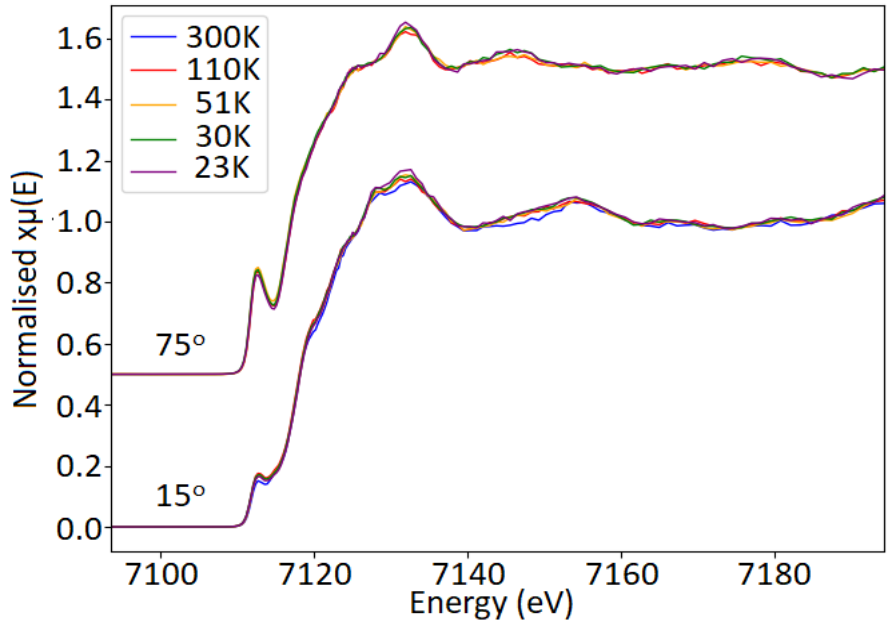

(b)

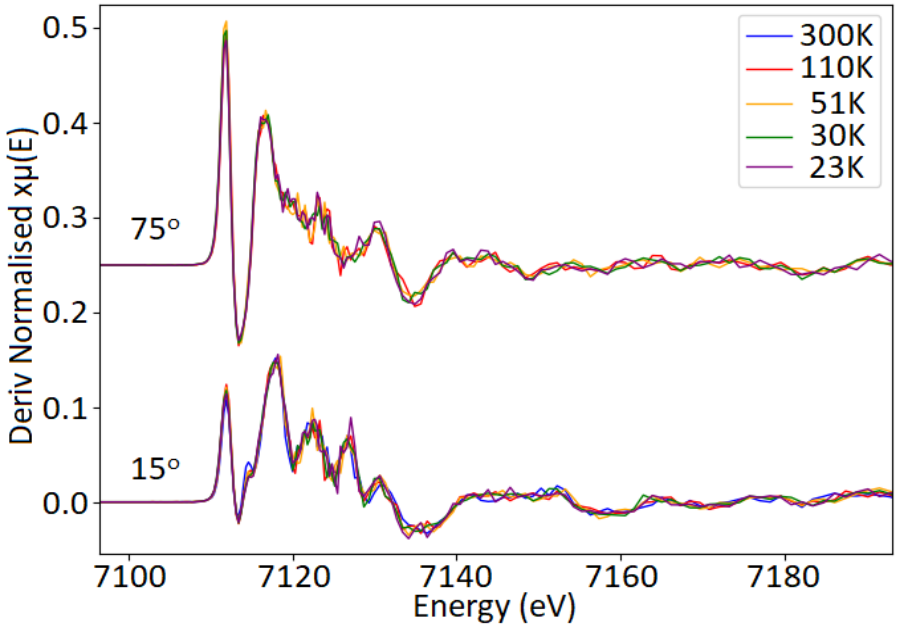

Figure 8.4.3: XANES: a) normalized spectra and b) normalized first derivative for the $NaFe_{1-x}Co_xAs$ ($x = 0.023$) Fe K-edge. Data is shown for 15^o and 75^o angle.

8.4.2 Valence-to-core XES

Given the range and type of transitions in the NaFeAs compound, vtc-XES is an important complementary technique to the HERFD-XAS, which probed the valence states of the As species. Using the Kβ emission line and measuring the Kβ'' and K$\beta_{2,5}$, 2 reference samples and both NaFeAs compounds were measured. The spectra were normalized using the method outlined in section 5.2 and the FDMNES simulations have been used to model the spectra, DOS and orbital overlap. Figure 8.4.4 shows the crystal structures for both reference samples. The Fe in Fe_2O_3 is in a +3 state and bounded to six O ligands where the Fe-O bond lengths are 1.96Å and 2.09Å [276]. The Fe_3O_4 compound contains both Fe +3 and +4 states where both single, double and triple bonds to oxygen are present. One site only has Fe^{3+} ion which is tetrahedrally coordinated to the oxygen while the other site has equal amounts of Fe^{3+} and Fe^{2+} in an octahedral coordination. The tetrahedral and octahedral Fe-O bonds lengths are 1.88Å and 2.07Å respectively [277].

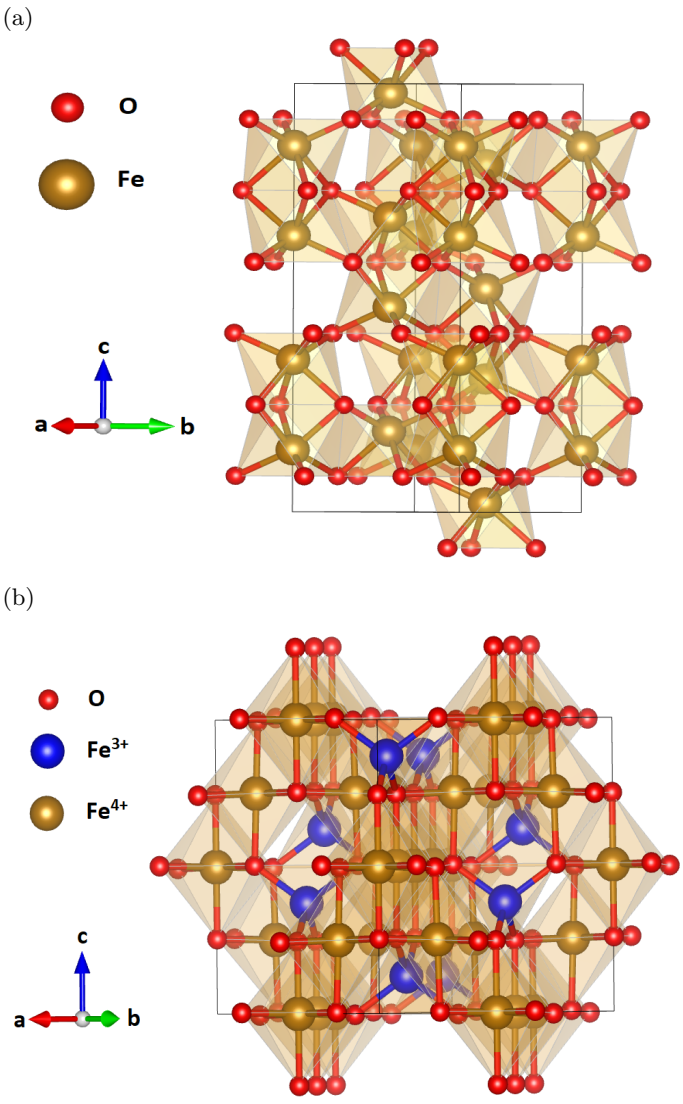

Figure 8.4.4: a) Fe_2O_3 [278] and b) Fe_3O_4 [279] structures.

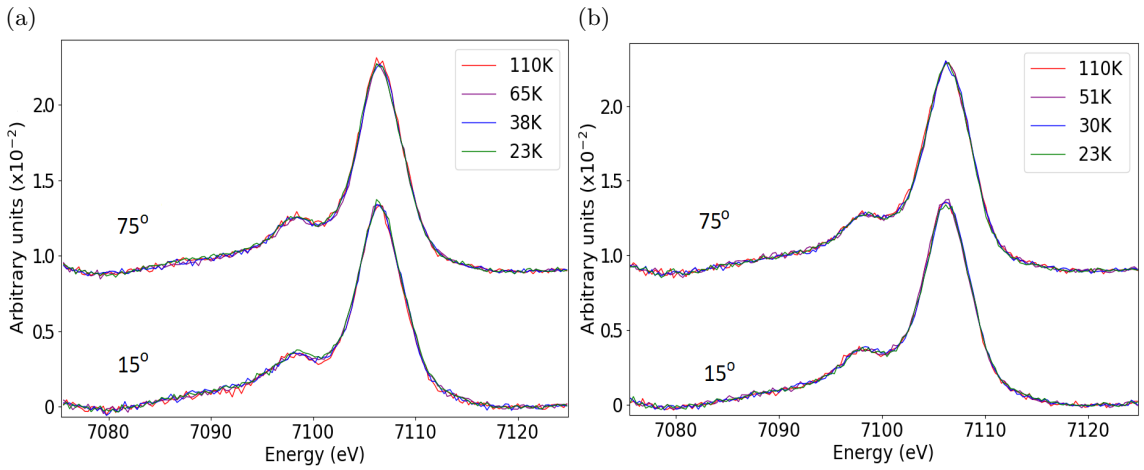

Figure 8.4.5: Fe K-edge: vtc-XES for a) $x = 0.014$ and b) $x = 0.023$, across the measured temperature range and 2 extreme angles

Figure 8.4.5 shows both $NaFe_{1-x}Co_xAs$ samples at the 15^o and 75^o, at a range of temperatures across the transitions. There are two well defined features at 7098eV and 7107eV. The intensity of the feature at 7098eV is approximately $0.4x10^{-2}$ arb. units and the feature at 7107eV is approximately $1.3x10^{-2}$ arb. units. In both samples no changes are seen in the intensity or position in either feature, across angle or temperature. Given the early results that suggest these samples have been contaminated by moisture, the lack of changes in the valence spectra is not surprising. For completion, FDMNES simulations have been carried out for all 3 compounds to confirm the origins of each feature and are shown in figures 8.4.6- 8.4.7. The simulations of the $NaFe_{1-x}Co_xAs$ have been carried out with $x = 0$. Also shown in figure 8.4.9 the suspected origins of each feature based on the earlier work in chapter 5 are given.

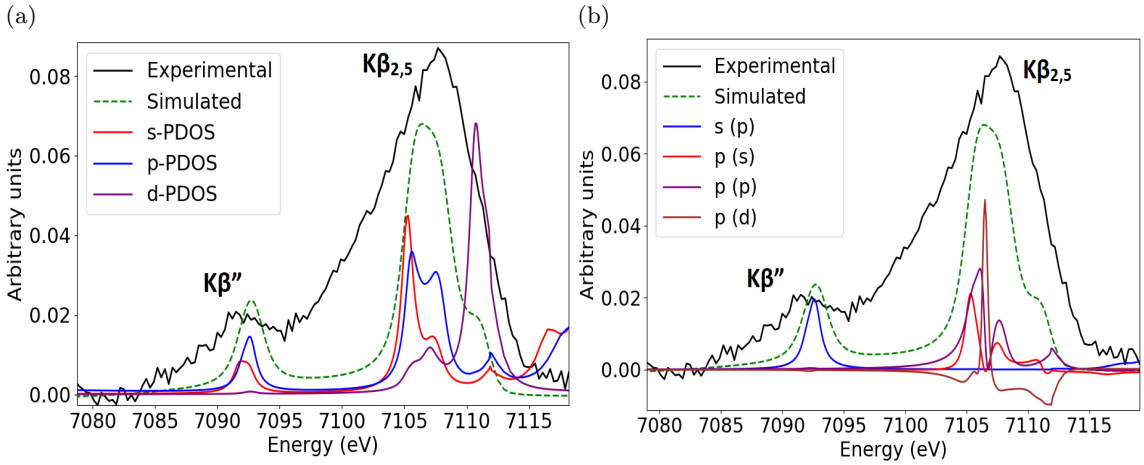

Figure 8.4.6: Fe K-edge: Fe_2O_3 vtc-XES. a) experiment vs simulated DOS, b) experiment vs simulated orbital overlap. Legend indicates (Ligand(Metal)) orbital overlap.

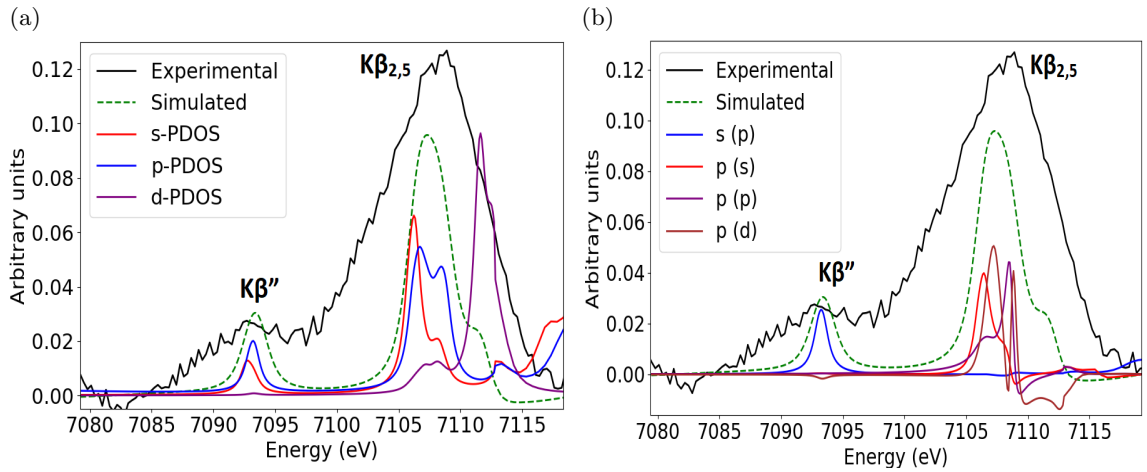

Figure 8.4.7: Fe K-edge: Fe_3O_4 vtc-XES. a) experiment vs simulated DOS, b) experiment vs simulated orbital overlap. Legend indicates (Ligand(Metal)) orbital overlap.

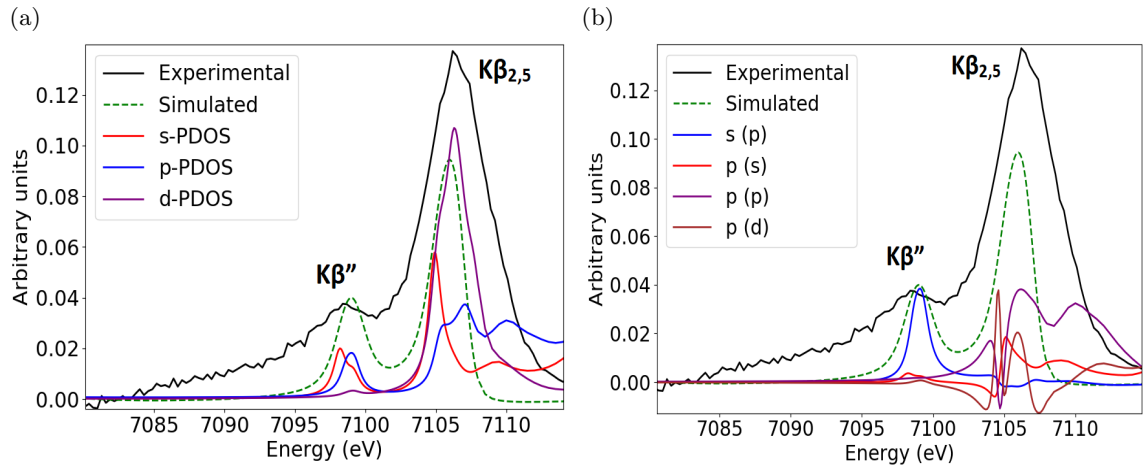

Figure 8.4.8: Fe K-edge: $NaFe_{0.977}Co_{0.023}As$ vtc-XES compared to NaFeAs simulation at 300K. a) experiment vs simulated DOS, b) experiment vs simulated orbital overlap. Legend indicates (Ligand(Metal)) orbital overlap.

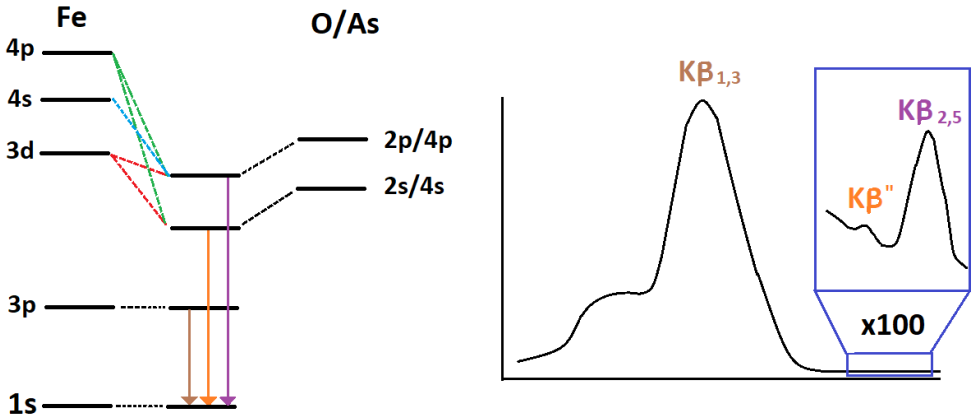

Figure 8.4.9: Fe Kβ XES spectrum and simplified molecular orbital (MO) diagram (Fe_2O_3, Fe_3O_4, $NaFe_{1-x}Co_xAs$)

In all cases the simulated spectra peak position and relative intensities are in good agreement with the experimental data. The DOS indicate that both features are centred around s and p orbitals and the higher energy feature also shows contributions from the d orbitals. It is interesting to note how the p orbitals in the $NaFe_{1-x}Co_xAs$ compound show high dispersion and the d orbital

are approximately 5eV lower than the two references. Due to the link between the metal and ligand orbitals, the orbital overlap provides information regarding which orbitals contribute to the spectral features, and changes in the overlap will also affect the intensity of these features [280]. The orbital overlap agrees with the proposed origins of the two features. The lower energy feature only shows overlap with the ligand s orbitals while the higher energy feature shows overlap with the ligand p orbitals. The notable change is seen in the energy position of the low energy feature. The two reference samples are at approximately 7093eV, with the Fe_3O_4 sample showing slightly higher intensity tail on the low energy side. This feature is at a significantly higher energy (7099eV) in the $NaFe_{1-x}Co_xAs$ compound. This change reflects that the bond between the metal and ligand is significantly stronger in this compound when compared to the reference sample. There is a difference between the intensities of the two reference sample, where the feature at 7093eV in Fe_2O_3 is approximately 0.025 arb. units while in Fe_3O_4 is approximate 0.03 arb. units. The second feature has an intensity in the Fe_2O_3 sample of approximately 0.086 arb. units while in Fe_3O_4 is approximate 0.12 arb. units. A comparison with the $NaFe_{1-x}Co_xAs$ spectra, shows that the intensity is similar to Fe_3O_4, suggesting it could be in a mixed valence state.

8.4.3 EXAFS analysis

It is expected that in both samples, without exposure to air, two structural transitions should be present. At T_s the system should undergo a tetrahedral to orthorhombic transition, and in the nematic phases it has been reported that fluctuations in the $FeAs_4$ tetrahedra are responsible for an orbital ordering transition [34, 37]. The positions and relative intensities of the single scattering paths are shown in figure 8.4.10, along with an example of the experimental data at 110K for reference. The first contributions come from the Fe-As scattering paths, with a degeneracy of 4 at 2.346Å; the second set comes from the Fe-Fe scattering within the layers at approximately 2.774Å with a degeneracy of 4 and the third originates from the Fe-Na across the layers with a scattering length of 3.107Å and a degeneracy of 4. In this short range there is no strong multiple scattering paths. While there are further defined features between approximately 3.5Å - 5.5Å, the intensity of these features across the different angles is relatively low and is difficult to fit accurately. Table 8.4.1 shows the path lengths, degeneracies and relative angles of the paths with respect to the *ab*-plane (ϕ_A) and *c*-axis (θ_A).

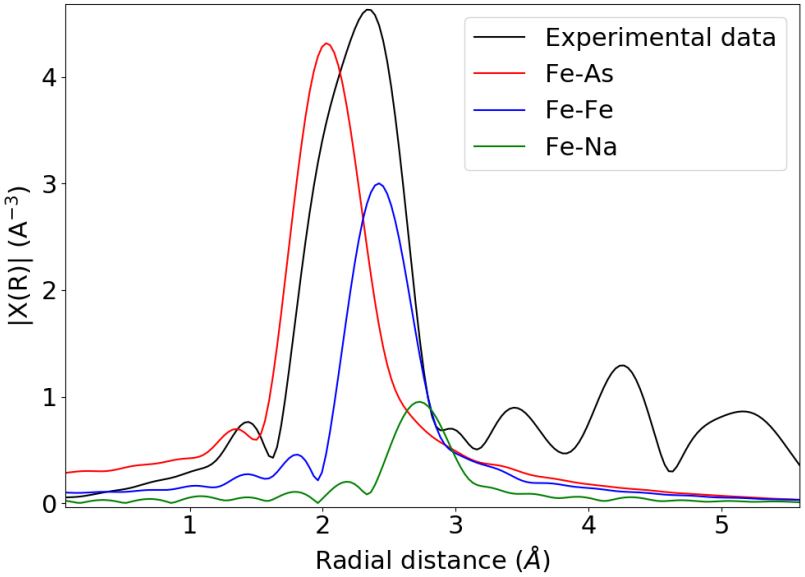

Figure 8.4.10: NaFeAs single scattering path contributions, along with an example $NaFe_{1-x}Co_xAs$ ($x = 0.014$, 110K, 30^o) spectra. Plotted in *R*-space.

Figures 8.4.11 and 8.4.12 show the EXAFS and FT-EXAFS for both samples measured across all temperatures and 2 angles. The Fourier transform has been extracted from a *k*-range of 3Å^{-1} - 11.5Å^{-1}, with the EXAFS data plotted using a *k*-weight of 2. Measuring EXAFS with the spectrometer is not very efficient, especially with the Kβ line, hence the reason for the limited range in *k*-space. The $NaFe_{0.986}Co_{0.014}As$ results plotted in *R*-space show a clear main feature between 1.6-2.8Å and a clear change across angles. However no change consistent with a structural transition is observed as a function of temperature. The 1^{st} peak has contributions from the Fe-As, Fe-Fe, Fe-Na scattering paths. The differences seen between the angles are a result of the 15^o and 75^o closely representing the *ab*-plane and *c*-axis polarization respectively. It is important to note that the experimental paths have not be phase corrected. The Fe-Fe paths have the greatest contribution in the 15^o at 2.4Å, while the Fe-As is strongest in the 75^o at 2Å. There are well defined features after 3Å and significant distortions in the 75^o. The *k*-space data shows consistent spectra across the transitions and good quality data up to 12Å, which has been aided by the very concentrated samples.

The second sample measured had $x = 0.021$ doping and shows differences when compared to the first sample. Shown in *R*-space the main feature in the 75^o data is narrower and does not show a shoulder at 2.6Å. The 15^o shows a slightly less intense main feature and the ratio between the peak and shoulder is less than in the other sample. The *k*-space data also confirms that there is no differences across any of the transition temperatures. While there are no changes that are related to a transition, the differences between the 2 samples is significant and is most likely linked to changes in the structure caused by the higher Co doping.

(a)

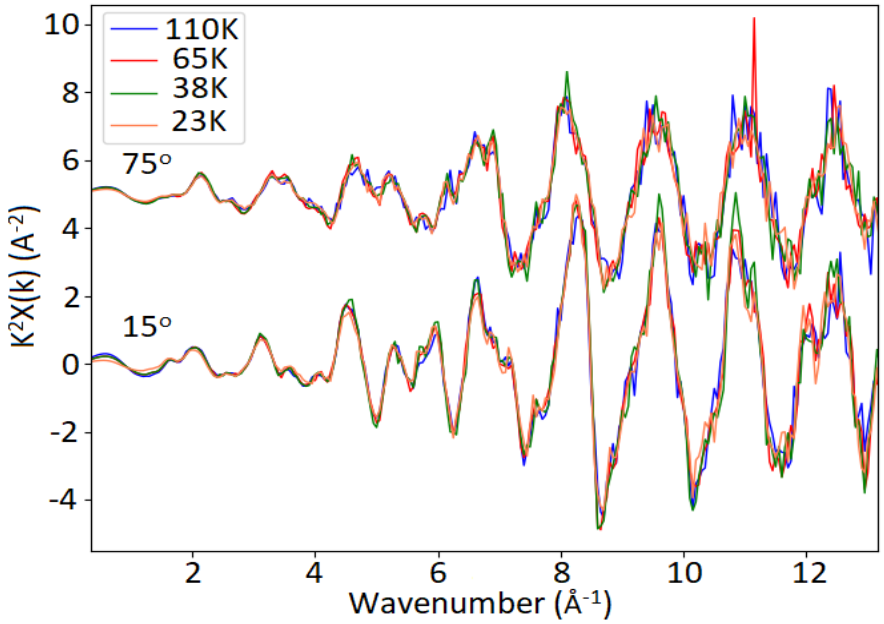

(b)

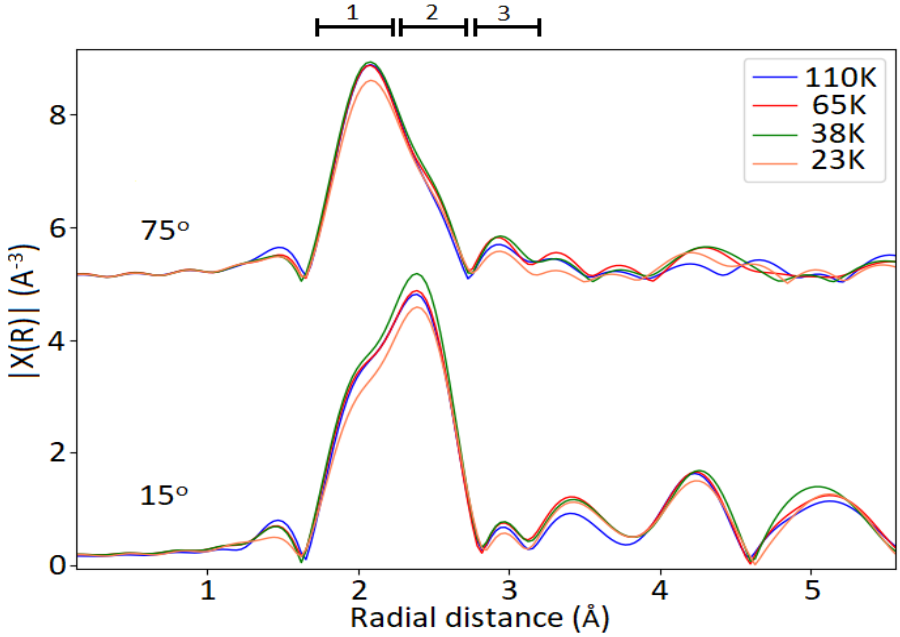

Figure 8.4.11: a) EXAFS and b) FT-EXAFS for $NaFe_{1-x}Co_xAs$ ($x = 0.014$) (Fe K-edge) for 2 angles and all temperatures. Different areas indicate the contributions from; 1: Fe - As, 2: Fe - Fe and 3: Fe - Na paths.

(a)

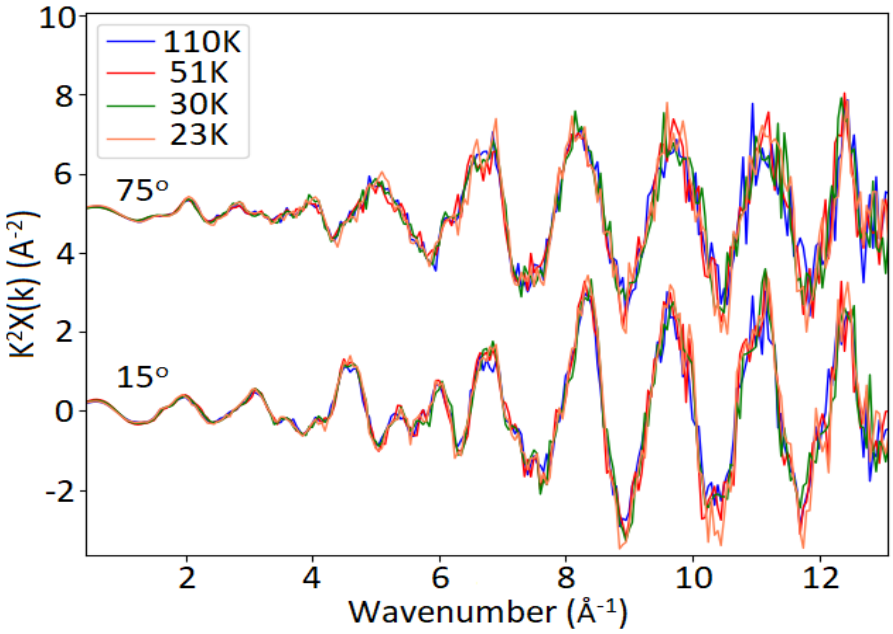

(b)

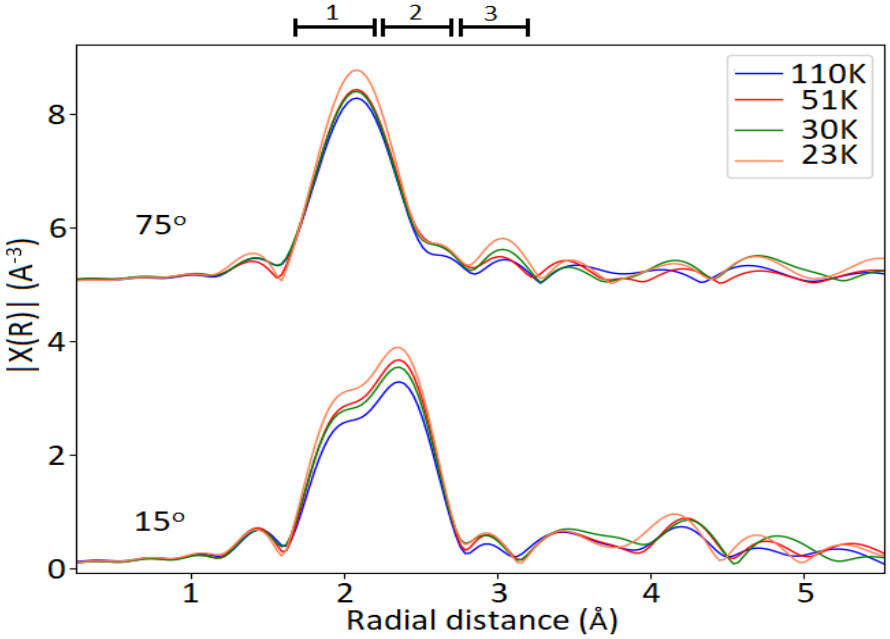

Figure 8.4.12: a) EXAFS and b) FT-EXAFS for $NaFe_{1-x}Co_xAs$ ($x = 0.023$) (Fe K-edge) for 2 angles and all temperatures. Different areas indicate the contributions from; 1: Fe - As, 2: Fe - Fe and 3: Fe - Na paths.

Fitting

Even though the changes seen in the data are more likely coming from thermal effects rather than related to a transition, the EXAFS data has also been fitted to the high temperature structure to confirm if any changes are present. The method of fitting is outlined in section 4.5, the initial structure used is given in table 8.4.1. While it is expected that the Co dopant will distort the structure, the low level of doping was assumed to be taken into account as disorder. Example fits are shown in figures 8.4.13 and 8.4.14 for both $x = 0.014$ and 0.021 at 110K and all angles. Tables 8.4.2 and 8.4.3 give the results of all the fitting parameters. The fitting was carried out in R-space over a range between 1.4Å - 3.2Å, and the data has been extracted from k-space between 3Å^{-1} - 11.7Å^{-1} for $x = 0.014$ and 3Å^{-1} - 11.4Å^{-1} for $x = 0.021$. The fits have been carried out as a function of 3 k-weighting (1, 2 and 3). The number of independent points available is 40 and 34 for $x = 0.014$ and $x = 0.021$ respectively, with 14 variables used in each fit. The R-factor, which gives an indication of the closeness of the fits, is between 0.005-0.01. The S_o^2 is a global parameter which takes into account factors that will affect the amplitude and is slightly below 1 for all data sets. The S_o^2 parameter has been left as a variable across the temperatures and angles since monitoring this value is important to confirm a realistic fit. Both the R-factor and S_o^2 values suggest that there is reasonably good agreement between the model and data. The E_0 value varies by several eV's across the angles but are similar (within error) across temperatures for a given angle. Due to the importance of tracking the oxidation state in these samples this parameter has been left as a variable across the temperatures and angles. While fixing the value would reduce the number of fitting parameters, it would also not allow the differences to be tracked. There is a consistent increase in this values across angles for the same temperature.

Path	**Path length (Å)**	**Degeneracy**	$\theta_A(^o)$	$\phi_A(^o)$
Fe-As	2.346	1	56.8	0.0
”	”	”	123.2	90.0
”	”	”	56.8	180.0
”	”	”	123.2	270.0
Fe-Fe	2.774	2	90.0	45.0
”	”	”	90.0	135.0
Fe-Na	3.107	1	140.9	0.0
”	”	”	39.2	90.0
”	”	”	140.9	180.0
”	”	”	39.2	270.0

Table 8.4.1: NaFeAs Scattering paths

For $NaFe_{0.986}Co_{0.014}As$, the Fe-As and Fe-Fe path lengths show a very small decrease across the 110K to 65K, and no further changes seen afterwards. The Debye-Waller factors are reasonable for these paths suggest a good fit. The change in the path lengths are more consistent with a temperature related effect. These paths were expected to show a change across the structural transition at 54K. However this signature is absent and the results indicate only a small thermal contraction. The Fe-Na path shows a contraction which, given that these path represent the differences between the Fe and Na layers, suggests a contraction mostly along the c-axis. The Debye-Waller factors and associated errors are significantly larger for these paths, however there are no changes across the structural transition.

The $NaFe_{0.979}Co_{0.021}As$ Fe-As and Fe-Fe path lengths show similar changes when compared to the $x = 0.014$ sample, with a small contraction across 110K to 51K. The Debye-Waller factors are consistent, which suggests the path values are realistic. These results suggest that the tetrahedral to orthorhombic transition is not present in this sample. The Fe-Na path lengths are shorter in this composition when compared to the $x = 0.014$ sample. Interestingly, these path lengths are closer to the reported $NaFe_2As_2$ path lengths, suggesting that the sample has undergone decomposition. The Debye-Waller factors are slightly larger, further suggesting there is additional distortion in the structure introduced by the dopant. The Fe-Na path lengths show a significant contraction when compared to the first sample. However also show large errors and Debye-Waller factors, which is most likely a result of an increase in the long range disorder caused by the decomposition. The EXAFS results shows that the transitions are not present in these samples. Additionally, the Fe-Na

path results suggest that the c-axis contraction is more significant in the $x = 0.021$ sample and these paths are more distorted, which is consistent with a highly decomposed system.

(a)

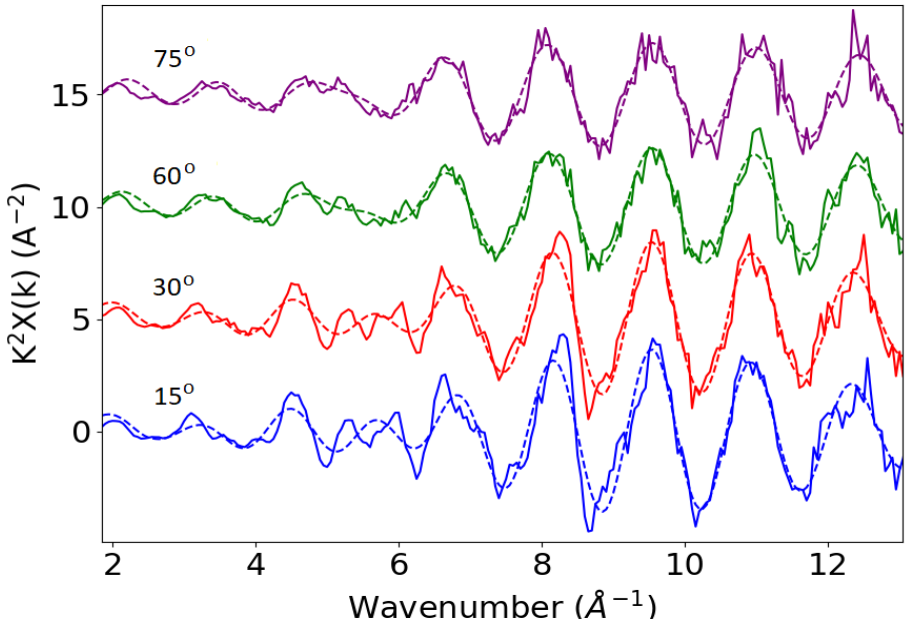

(b)

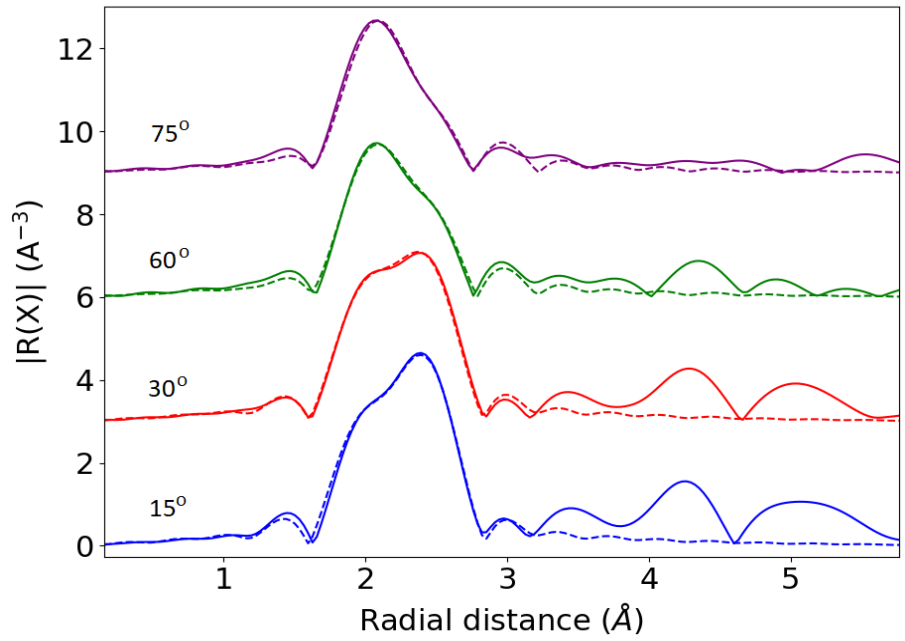

Figure 8.4.13: a) EXAFS and b) FT-EXAFS example fits for $NaFe_{1-x}Co_xAs$ ($x = 0.014$) (Fe K-edge) at 110K using 4 angles.

(a)

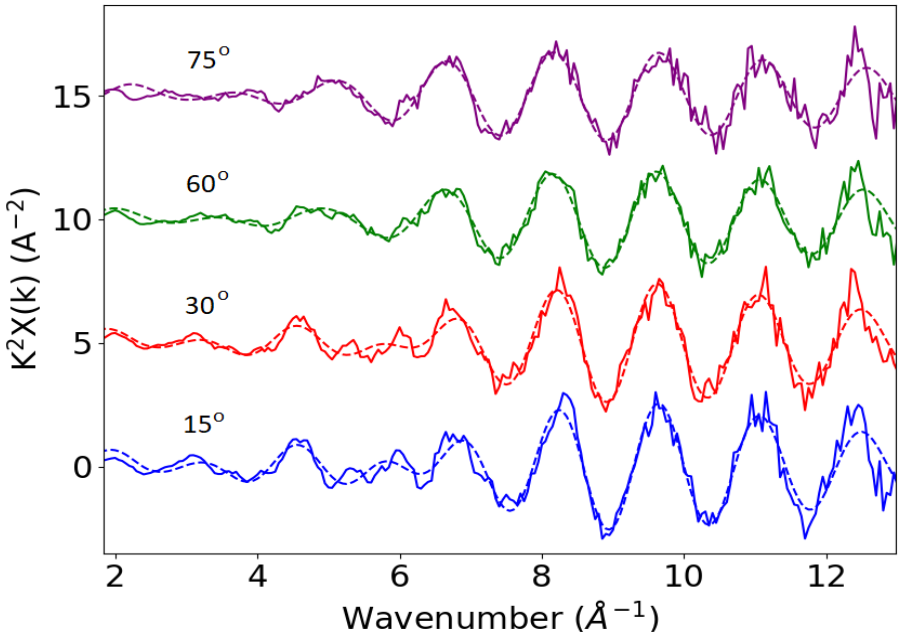

(b)

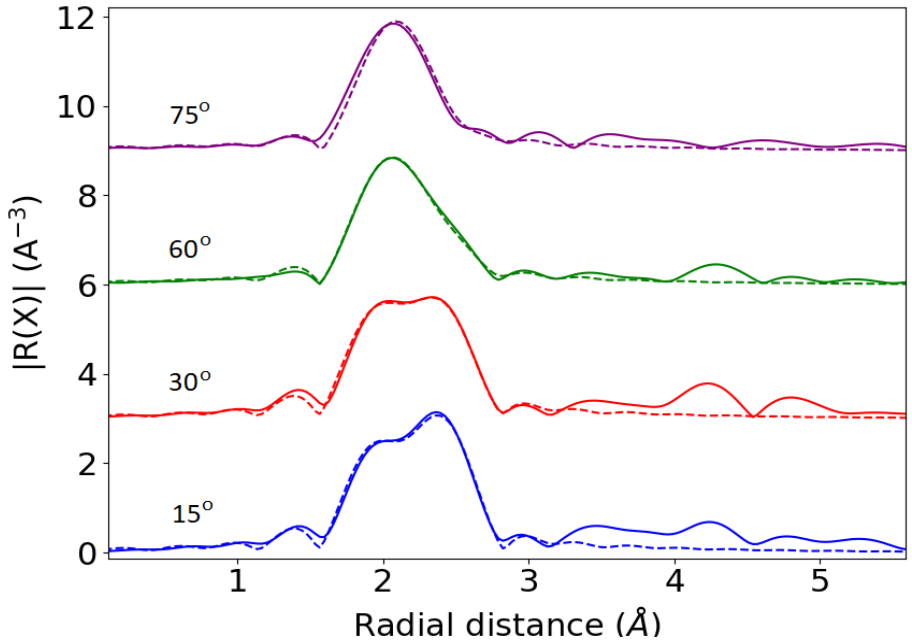

Figure 8.4.14: a) EXAFS and b) FT-EXAFS example fits for $NaFe_{1-x}Co_xAs$ ($x = 0.023$) (Fe K-edge) at 300K using 4 angles.

Parameters	110K	65K	38K	23K
ΔE_0 (eV) - (15^o)	3.1±0.7	2.0±0.6	1.6±0.9	2.5±0.9
ΔE_0 (eV) - (30^o)	3.5±0.8	3.2±0.7	3.0±0.9	3±1
ΔE_0 (eV) - (60^o)	5.0±0.9	3.5±0.7	4±1	4±1
ΔE_0 (eV) - (75^o)	6.0±0.9	4.1±0.8	5±1	4±1
S_o^2 - (15^o)	0.98±0.07	0.98±0.06	0.98±0.08	0.98±0.09
S_o^2 - (30^o)	0.99±0.07	0.99±0.06	0.98±0.08	0.98±0.09
S_o^2 - (60^o)	0.99±0.07	0.99±0.06	0.98±0.08	0.99±0.09
S_o^2 - (75^o)	0.99±0.08	0.99±0.07	0.99±0.08	1.03±0.09
Fe-As R (Å)	2.416±0.002	2.414±0.002	2.411±0.003	2.412±0.003
Fe-As σ^2 ($Å^2$)	0.0010±0.0003	0.0010±0.0003	0.0009±0.0004	0.0020±0.0004
Fe-Fe R (Å)	2.783±0.004	2.777±0.003	2.775±0.005	2.777±0.005
Fe-Fe σ^2 ($Å^2$)	0.0040±0.0005	0.004±0.004	0.0030±0.0006	0.0040±0.0007
Fe-Na R (Å)	3.25±0.03	3.22±0.02	3.22±0.02	3.23±0.03
Fe-Na σ^2 ($Å^2$)	0.018±0.004	0.015±0.003	0.014±0.003	0.021±0.005
R-Factor	0.0075	0.0049	0.0091	0.0114
Independent points	40	40	40	40
Variables	14	14	14	14

Table 8.4.2: Fitting parameters for $NaFe_{1-x}Co_xAs$ ($x = 0.014$)

Parameters	110K	51K	30K	23K
ΔE_0 (eV) - (15^o)	2.2±0.8	2.1±0.9	1.6±0.9	1.4±0.8
ΔE_0 (eV) - (30^o)	1.0±0.8	3±1	0.8±0.9	0.9±0.8
ΔE_0 (eV) - (60^o)	2.0±0.8	3.1±0.9	3±1	3.4±0.8
ΔE_0 (eV) - (75^o)	5.4±0.9	4.9±0.9	5±1	3.8±0.8
S_o^2 - (15^o)	0.99±0.07	0.98±0.07	0.97±0.07	0.97±0.07
S_o^2 - (30^o)	0.99±0.07	0.98±0.08	0.98±0.08	1.00±0.07
S_o^2 - (60^o)	1.00±0.07	0.99±0.07	1.00±0.08	1.00±0.07
S_o^2 - (75^o)	0.99±0.07	1.02±0.07	1.01±0.08	1.02±0.07
Fe-As R (Å)	2.393±0.002	2.389±0.003	2.386±0.003	2.395±0.004
Fe-As σ^2 ($Å^2$)	0.0020±0.0003	0.0020±0.0003	0.0020±0.0004	0.0010±0.0006
Fe-Fe R (Å)	2.745±0.004	2.741±0.005	2.735±0.005	2.750±0.008
Fe-Fe σ^2 ($Å^2$)	0.0070±0.0005	0.0060±0.0006	0.0060±0.0006	0.005±0.009
Fe-Na R (Å)	3.2±0.2	3.2±0.2	3.1±0.2	3.10±0.08
Fe-Na σ^2 ($Å^2$)	0.09±0.04	0.11±0.06	0.09±0.05	0.05±0.02
R-Factor	0.007	0.006	0.008	0.005
Independent points	34	34	34	34
Variables	14	14	14	14

Table 8.4.3: Fitting parameters for $NaFe_{1-x}Co_xAs$ ($x = 0.023$)

8.5 Discussion

The original aim of this research was to track the local electronic and atomic structures around Fe species across the nematic, structural, magnetic and SC transitions in $NaFe_{1-x}Co_xAs$ ($x = 0.014$, 0.021). The nature of nematic state in this system is unclear, however it has been theoretically linked to both spin and orbital degrees of freedom. While experimental data has not been able to confirm which mechanism is driving this state, it has recently been suggested that the spin nematicity can be understood as a direct consequence of orbital ordering involving the Fe $d_{xy/yz}$. The use of polarization dependent HERFD-XAS and vtc-XES measurements allows changes in both the electronic and atomic structure to be tracked across the transition within different crystallographic planes. These measurements aimed to provide further information as to the state of the Fe species in this compound in each phase. It has become clear early in the analysis that the two samples have been exposed to moisture and due to their sensitivity, have started a process of decomposition. The parent compound (NaFeAs) will eventually, over a prolonged exposure to moisture, decompose in to $NaFe_2As_2$ and it is expected that the doped system will undergo a similar change.

The XANES data (figures 8.4.2 and 8.4.3) shows significant differences between the two samples. In the suspected nematic state, the pre-edge feature, originating from 1s→3d transitions suggests, is more intense in the $x = 0.021$ composition, and there is a more defined double peak feature in the absorption edge for the $x = 0.014$ composition. The XANES analysis suggests that these differences are a result of a significant structural difference between the two compositions, which is most likely due to decomposition rather than an effect from the small difference in dopant. A comparison to the reference samples suggest that the $x = 0.014$ sample is closer to the Fe_2O_3 with the Fe in a +3 state, while the $x = 0.023$ sample is closer to a mixed valence state similar to the Fe_3O_4. A comparison of the spectra for each sample across the transitions shows that there are very little change in either sample, apart from thermal effects. The vtc-XES results (figure 8.4.5) also indicate no changes in either the Fe or As valence orbitals or their interactions. The electronic structures of both samples appear to be stable across the temperature range measured and suggests that due to the samples exposure to air, the electronic transitions are suppressed. The results of this research indicate that even a partial decomposition of the $NaFe_{1-x}Co_xAs$ suppresses the transitions being investigated.

The structural analysis for both compositions is given in tables 8.4.2 and 8.4.3. The results for the Fe-As and Fe-Fe path lengths across the temperature range suggest that apart from a very small contraction there is no signature of a structural transition. The Fe-Na path for both compositions shows a more significant contraction, which is largest in the $x = 0.021$ system. However there are also larger errors and large Debye-Waller factors associated with these paths indicates greater distortion due to the Co doping. It is expected that the decomposition will occur in patches and the changes in the structure will be most significant across the c-axis. Comparison of the Fe-As path lengths with the literature suggest that the Fe-As path (2.414Å) in $x = 0.014$ sample is similar to the parent compound at 2.417Å, while the the Fe-As path (2.393Å) in $x = 0.021$ sample is closer to the $NaFe_2As_2$ composition at 2.380Å. The structural results further confirm that the exposed doped system does not undergo any of the reported transitions.

8.6 Conclusion

Using polarization dependent HERFD-XAS and vtc-XES measurements, this research aimed to investigate the nematic phase in the $NaFe_{1-x}Co_xAs$ ($x = 0.014$, 0.021) system. Since it has been suggested that this phase is dominated by an orbital ordering on the $Fe_{xy/yz}$ site, by tracking the electronic and atomic structures across the difference phases it should be possible to confirm or otherwise this mechanism. However, due to exposure to moisture, the original aim of this research has not been accomplished. The characterization measurements, HERFD-XANES, vtc-XES and EXAFS results indicate that the $x = 0.014$ composition has had limited exposure and is close to the original structure, On the other hand, the $x = 0.021$ analysis indicates the sample has undergone significant decomposition and is closer to the $NaFe_2As_2$ system. The results indicate that the exposed doped system does not undergo any electronic or structural transition, which is most likely a result of the increase in the distortion within the structure. It is reasonable to suggest that the $FeAs_4$ structure is a critical factor with relation to the transitions and that small distortion in this structure can significantly affect these transitions.

Chapter 9

Conclusion

This thesis has presented research on the transition metal compounds: $IrTe_2$, Ca_2RuO_4 and NaFeAs. In addition, it has also developed further the Lβ vtc-XES technique and a new correction method for the self-absorption effects in fluorescence detection. In this chapter the key results for each section will be given, focusing on the new results.

In fluorescence detected XAS the self-absorption effect can severely suppress the XANES and EXAFS amplitudes, leading to incorrect coordination numbers and Debye-Waller factors. In chapter 4, a review of the current widely available correction methods shows how for the data used in this thesis, numerical instabilities near the absorption edge prevented a reasonable correction. It is suggested that the reason for this comes from the highly localized electrons in these systems which creates a significant intensity change at the absorption edge and this is not well modelled by the tabulated absorption coefficients used to provide a correction. To allow for a reasonable correction for the data in this thesis, a new correction procedure, which takes into account the background fluorescence intensity for the absorption edge, is presented. A comparison between transmission data, which does not suffer from the self-absorption effect, and the corrected data shows that in both the XANES and EXAFS regions this methods provides a suitable correction.

In chapter 5, a study of the Lβ emission valence-to-core XES has been presented, specifically using tungsten reference samples. The use of vtc-XES has been shown to be an important technique in the study of materials, as it is sensitive to the metal spin and oxidation state, as well as ligand identification, hybridization, protonation state and metal-ligand bond lengths. However, the current available literature focuses on the light metal/ligand system using the Kβ emission. By measuring a range of tungsten reference samples using the Lβ emission and calculating the corresponding density of states and orbital overlap, an interpretation of the sensitivity of this technique to changes in the electronic structure was shown to be possible. The Lβ emission line should be more sensitive to the d states since it probes the d states directly as the $d \rightarrow p$ is allowed, whereas for the Kβ emission the $d \rightarrow s$ transitions are not allowed. The key result from this work is that while the Lβ emission features are similar to the Kβ, probing the ligand ns and np orbitals, the achievable resolution may be a limiting factor, caused by the core-hole broadening. Small changes were seen across some of the references, for example the subtle oxidation state change between WO_2 and WO_3.

In chapter 6, the role of the Ir-Ir dimers and the electronic state of this species across the metal to partial insulator transition in $IrTe_2$ has been studied. The structural analysis has shown that unlike what is presented in the majority of the literature, dimers are present in this compound at temperatures above the known transitions. By tracking the fitting parameters (Debye-Waller factor) across the MI transition, it is proposed that this is a order to disorder like transition. Above the transition the dimers are in a disordered state throughout the ab-plane. However below the transition they become ordered along the a-axis. The XANES data collected on the L_1, L_2 and L_3 Ir edges, along with the vtc-XES measurements, suggest that the Ir does not undergo a significant electronic change across this transition. Further to this, DFT simulations show how the compression of the Te octahedra leads to the small changes seen after the absorption edge. Additional density of state simulations suggest that rather than the ordering of the Ir dimers, it is the Te change that causes a reconstruction across the Fermi level. Hence, it seems that it is the change in the Te structure that is the driving force for the change in the conductivity of this system and that the ordering of the dimers is an additional effect. When the system is doped with Pt, the MI transition is suppressed and a SC state can emerge. It was previously suggested that upon doping, the Ir dimers are absent in this system and lead to the possibility that a different symmetry breaking mechanism was driving the transitions. The study of two compositions, where the MI is slightly reduced and fully suppressed, suggests that dimers are present in these samples too and that the Ir electronic structure is the same with respect to the pure compound. The results show that the same mechanisms are driving the transition. Due to the increase in the lattice parameters as a function of

dopant, it seems that the effect on the MI is caused by the Te-Te interlayer bonding. As the a-axis lattice constant increases, the Te-Te weakens and the transition temperature is reduced.

The metal to insulator transition in Ca_2RuO_4 has been studied in chapter 7. The results confirm a significant structure change in the oxygen octahedra around the Ru, with smaller distortions in the Ca cage. The XANES analysis indicated that there is a charge transfer between the non-degenerate d_{xy} and $d_{xz,yz}$ states, along with a narrowing of the bandwidths. With measurements on the system once doped with La, where the MI transition is suppressed, the overall result shows that the structural and electronic changes are closely linked. Above the MI transition, the t_{2g} orbitals are split in energy due to the significant elongation of the octahedra. The 4th electron in the Ru is localized on to the $d_{xz,yz}$ orbitals, leaving the d_{xy} state only half-filled and conducting. Directly below the transition the octahedra compresses and due to this the bandwidth decreases but also the relative separation between the $d_{xz,yz}$ and d_{xy} states decreases. This effect allows the 4th electron to overcome the Coulomb repulsion and move to the d_{xy} state. This fills this band and the system becomes insulating. The transition/La doping changes the t_{2g} bandwidth and unbalances the U/W interaction resulting in a metallic state. While this research cannot address whether the structural transition is the only driving factor for the overall change, it does suggest that the distortion in the Ru-O-Ru bond angle is a critical factor in this material.

In chapter 8, the high temperature superconducting iron pnictide system is investigated. Originally, the aim of this research was to use XAS and vtc-XES techniques to probe the electronic and atomic structures near a nematic state. Literature has suggested that this state, which precedes both an atomic and magnetic transition, is related to both spin and orbital degrees of freedom, in which the Fe d_{xy} states may play a crucial role. Due to contamination with moisture, this research was not successful and it was not possible to probe this state, since the sample decomposes in to $NaFe_2As_2$ (which does not show an nematic state). The research however does highlight that even a small amount of contamination prevents the system from undergoing electronic or atomic transitions. It also suggests that the $FeAs_4$ structure is highly sensitive to small structural distortions.

The research presented in this thesis has used polarization dependent conventional XAS, HERFD-XAS and vtc-XES techniques, along with simulations, to probe the structural and electronic states in 3 compounds across different transitions. It has been shown that these techniques can provide the necessary information to understand what factors are driving the emergence of the different phases, including the interplay between the atomic and electronic structures. The use of simulations has also been shown to provide additional information regarding the origins of the different changes seen the experimental data. The HERFD-XAS and vtc-XES results additionally show that as synchrotrons and beamlines improve, the data processing techniques must also be re-evaluated. This is due to the assumptions used in the theory that describes the interactions of the x-rays with the samples.

Chapter 10

Future work

In this chapter a discussion is given with regards to the possible avenues of additional research that stems from the work presented in this thesis. In general this can be split into work with regards to the technique side of the thesis and the materials studied.

There have been two major developments to the techniques used in this work. In section 4.2.2 a new approach for making a correction for the self-absorption effect (in fluorescence mode) is given. It takes into account the numerical instabilities near the absorption edge that are encountered in the standard correction codes, specifically when correcting for L-edges with strong whiteline features typical for high-resolution measurements. It was shown that for the data sets in this thesis the new procedure provides a reasonable correction to both the XANES and EXAFS region. However it is unclear as to whether this is only applicable in certain situations. It was suggested that the reason for the instabilities is that the electrons in these compounds (specifically transition metals) are in a highly localized state. It would be desirable to test if the code is robust for a wider range of energies and absorption edges. Additionally, it is important that the limitations are identified, as this would allow for corrections to data that previously has been problematic. This is especially important for HERFD-XANES taken with XES and would also allow experiments to be done with high-concentrated samples. To be able to provide this verification, additional measurements are needed on a range of compounds, with varying absorption edges and with electrons in different states (localized/non-localized). By taking measurements in both fluorescence and transmission mode, it is possible to confirm if the correction is reasonable, since the transmission data does not suffer from self-absorption effects.

A significant study of the valence-to-core XES using Lβ emission lines was presented is chapter 5. While this provided some useful interpretation of the features that arise in the spectra, it is still unclear as to the achievable sensitivity of these measurements to changes in the electronic structure. To be able to take the technique further, careful consideration of additional reference sample measurements needs to be made. This technique is in theory sensitive to the oxidation state of both the metal and ligand, hybridization effects and the local chemical environment around the absorbing species. A further study comprising of a set of references which take into account these effects would allow for comparisons to be made across varying atomic and electronic structures to determine the situations for which this technique is suitable. It would also be useful to measure 4d compounds at lower energies which should have less spectral broadening. In addition, this technique is also very photon hungry and a further investigation into the concentration limits with the current instruments should also be carried out.

The study of $IrTe_2$ (chapter 6) revealed how the Ir-Ir dimers are present above and below the metal to partial insulator transition and that the electronic structure of the Ir species does not undergo any significant changes. When the system is doped with Pt, the nature of the transition is the same with respect to the parent compound and that the dimers persist close to the superconducting phase. Three further studies naturally present themselves from this research. Firstly these results point towards the Te species playing a critical role in the transition and it is likely that this species is responsible for the change in the conducting behaviour. To confirm if this is the case, the same techniques used for the Ir species would provide the relevant information to track the electronic changes in the Te species. While it is not possible to carry out these measurements with the I20 spectrometer, as the edge energy of Te is too low for this beamline, conventional XAS measurements using the Te L_2/L_3 absorption edges is already planned. Secondly, a fundamental property of the dimers is that they typically become destabilized at high temperatures. Since the dimers in this system are present in a disordered state above the metal to insulator transition, the question then is as to whether the destabilization of these dimers at high temperature results in a continuos transition (slow loss of dimer states) or a clear transition from a dimer to non-dimer state. By understanding the material at higher temperatures and providing a full phase diagram for the

dimer states, the underlying nature of the dimers in the system would be given and has important implications as to the role of the Ir-Ir dimers. Finally, in the doped compound the dimers persist down to at least 50K, however an important question to answer is whether the dimers survive in the SC phase. The research presented in this thesis shows that the techniques used are sensitive to dimers in different states and hence further measurements at low temperatures would be suitable. The possible realization of an entangled dimer/SC state in this system would be an important discovery in understanding the nature and mechanisms of the SC state.

In the case of Ca_2RuO_4 (chapter 7), the interaction between the Ru and O atoms plays a critical role in the stabilization of certain orbitals. Vtc-XES on the Ru species would be an ideal technique to probe the interaction between these atoms and may provide further information regarding the nature of the metal to insulator transition. If a sufficient resolution was achieved, changes in the energy levels due to the metal-ligand interaction should be detectable. Due to the octahedral structure in this material and the significant distortions occurring across the structural transition, this would also provide information with regards to the sensitivity of the polarization dependency of this technique which has not been possible to address in this thesis. While these measurements would not be possible with the I20 spectrometer as the edge energies are not achievable, it would be possible on the ID26 beamline at the ESRF [281].

In chapter 8, the iron pnictide superconductor (NaFeAs) has been probed to understand the structural and electronic changes that lead to a nematic phase. This research was not able to provide further information on the compound due to contamination of the samples with moisture. To be able to probe the different phases in this material with HERFD-XAS and vtc-XES techniques, further work would require a better system to avoid sample decomposition. This can be achieved by loading the samples on to the cryostat within a moisture-free environment and ensuring that they remain under vacuum during the measurements. It would be also important to characterize the samples directly before and after the spectroscopy experiments to ensure any decomposition is identified.

References

[1] Y. Wang, J. Li, and Z. Wei, "Transition-metal-oxide-based catalysts for the oxygen reduction reaction," *J. Mater. Chem. A*, vol. 6, pp. 8194–8209, 2018.

[2] V. Kumaravel, S. Mathew, J. Bartlett, and S. Pillai, "Photocatalytic hydrogen production using metal doped TiO_2: A review of recent advances," *Applied Catalysis B: Environmental*, vol. 244, pp. 1021–1064, 2019.

[3] H. Najafi-Ashtiani, B. Akhavan, F. Jing, and M. M. Bilek, "Transparent conductive dielectric metal dielectric structures for electrochromic applications fabricated by high power impulse magnetron sputtering," *ACS Applied Materials and Interfaces*, vol. 11, no. 16, pp. 14871–14881, 2019.

[4] D. I. Khomskii, "Transition metal compounds - Chapter: Localized and itinerant electrons in solids," *Cambridge University Press*, p. 1–24, 2014.

[5] E. H. Lieb, "Two theorems on the Hubbard model," *Phys. Rev. Lett.*, vol. 62, no. 10, pp. 1201–1204, 1989.

[6] M. Cyrot, "Theory of Mott transition : Applications to transition metal oxides," *J. Phys. France*, vol. 33, no. 1, pp. 125–134, 1972.

[7] D. I. Khomskii, "Transition metal compounds - Chapter: Isolated transition metal ions," *Cambridge University Press*, pp. 25–36, 2014.

[8] K. E. Hyde, "Methods for obtaining Russell-Saunders term symbols from electronic configurations," *Journal of Chemical Education*, vol. 52, no. 2, p. 87, 1975.

[9] J. Rubio and J. Perez, "Energy levels in the jj coupling scheme," *Journal of Chemical Education*, vol. 63, no. 6, p. 476, 1986.

[10] D. I. Khomskii, "Transition metal compounds - Chapter: Transition metal ions in crystals," *Cambridge University Press*, p. 37–93, 2014.

[11] M. C. M. O'Brien and C. C. Chancey, "The Jahn–Teller effect: An introduction and current review," *American Journal of Physics*, vol. 61, no. 8, pp. 688–697, 1993.

[12] D. I. Khomskii, "Transition metal compounds - Chapter: Charge ordering in transition metal compounds," *Cambridge University Press*, p. 238–268, 2014.

[13] J. J. Yang, Y. J. Choi, Y. S. Oh, A. Hogan, Y. Horibe, K. Kim, B. I. Min, and S.-W. Cheong, "Charge-orbital density wave and superconductivity in the strong spin-orbit coupled $IrTe_2$:Pd," *Phys. Rev. Lett.*, vol. 108, no. 11, p. 116402, 2012.

[14] M. J. Eom, K. Kim, Y. J. Jo, J. J. Yang, E. S. Choi, B. I. Min, J.-H. Park, S.-W. Cheong, and J. S. Kim, "Dimerization-induced fermi-surface reconstruction in $IrTe_2$," *Phys. Rev. Lett.*, vol. 113, no. 26, p. 266406, 2014.

[15] D. Ootsuki, S. Pyon, K. Kudo, M. Nohara, M. Horio, T. Yoshida, A. Fujimori, M. Arita, H. Anzai, H. Namatame, M. Taniguchi, N. L. Saini, and T. Mizokawa, "Electronic structure reconstruction by orbital symmetry breaking in $IrTe_2$," *Journal of the Physical Society of Japan*, vol. 82, no. 9, p. 093704, 2013.

[16] A. F. Fang, G. Xu, T. Dong, P. Zheng, and N. L. Wang, "Structural phase transition in $IrTe_2$: A combined study of optical spectroscopy and band structure calculations," *Scientific Reports*, vol. 3, no. 1, p. 1153, 2013.

[17] Y. S. Oh, J. J. Yang, Y. Horibe, and S.-W. Cheong, "Anionic depolymerization transition in $IrTe_2$," *Phys. Rev. Lett.*, vol. 110, no. 12, p. 127209, 2013.

[18] K. Kim, S. Kim, K.-T. Ko, H. Lee, J.-H. Park, J. J. Yang, S.-W. Cheong, and B. I. Min, "Origin of first-order-type electronic and structural transitions in $IrTe_2$," *Phys. Rev. Lett.*, vol. 114, no. 13, p. 136401, 2015.

[19] K.-T. Ko, H.-H. Lee, D.-H. Kim, J.-J. Yang, S.-W. Cheong, M. Eom, J. Kim, R. Gammag, K.-S. Kim, H.-S. Kim, T.-H. Kim, H.-W. Yeom, T.-Y. Koo, H.-D. Kim, and J.-H. Park, "Charge-ordering cascade with spin orbit Mott dimer states in metallic iridium ditelluride," *Nature Communications*, vol. 6, no. 1, p. 7342, 2015.

[20] D. Ootsuki, Y. Wakisaka, S. Pyon, K. Kudo, M. Nohara, M. Arita, H. Anzai, H. Namatame, M. Taniguchi, N. L. Saini, and T. Mizokawa, "Orbital degeneracy and Peierls instability in the triangular-lattice superconductor $Ir_{1-x}Pt_xTe_2$," *Phys. Rev. B*, vol. 86, no. 1, p. 014519, 2012.

[21] R. Yu, S. Banerjee, H. C. Lei, R. Sinclair, M. Abeykoon, H. D. Zhou, C. Petrovic, Z. Guguchia, and E. S. Bozin, "Absence of local fluctuating dimers in superconducting $Ir_{1-x}(Pt,Rh)_xTe_2$," *Phys. Rev. B*, vol. 97, no. 17, p. 174515, 2018.

[22] O. Friedt, M. Braden, G. André, P. Adelmann, S. Nakatsuji, and Y. Maeno, "Structural and magnetic aspects of the metal-insulator transition in $Ca_{2-x}Sr_xRuO_4$," *Phys. Rev. B*, vol. 63, no. 17, p. 174432, 2001.

[23] M. Braden, G. André, S. Nakatsuji, and Y. Maeno, "Crystal and magnetic structure of Ca_2RuO_4: Magnetoelastic coupling and the metal-insulator transition," *Phys. Rev. B*, vol. 58, no. 2, pp. 847–861, 1998.

[24] V. I. Anisimov, I. A. Nekrasov, D. E. Kondakov, T. M. Rice, and M. Sigrist, "Orbital-selective Mott-insulator transition in $Ca_{2-x}Sr_xRuO_4$," *The European Physical Journal B - Condensed Matter and Complex Systems*, vol. 25, no. 2, pp. 191–201, 2002.

[25] E. Gorelov, M. Karolak, T. O. Wehling, F. Lechermann, A. I. Lichtenstein, and E. Pavarini, "Nature of the Mott transition in Ca_2RuO_4," *Phys. Rev. Lett.*, vol. 104, no. 22, p. 226401, 2010.

[26] A. Liebsch and H. Ishida, "Subband filling and Mott transition in $Ca_{2-x}Sr_xRuO_4$," *Phys. Rev. Lett.*, vol. 98, no. 21, p. 216403, 2007.

[27] G. Cao, S. McCall, V. Dobrosavljevic, C. S. Alexander, J. E. Crow, and R. P. Guertin, "Ground-state instability of the Mott insulator Ca_2RuO_4: Impact of slight La doping on the metal-insulator transition and magnetic ordering," *Phys. Rev. B*, vol. 61, no. 8, pp. R5053–R5057, 2000.

[28] I. H. Inoue, O. Goto, H. Makino, N. E. Hussey, and M. Ishikawa, "Bandwidth control in a perovskite-type $3d^1$-correlated metal $Ca_{1-x}Sr_xVO_3$ i. evolution of the electronic properties and effective mass," *Phys. Rev. B*, vol. 58, no. 8, pp. 4372–4383, 1998.

[29] T. Katsufuji, Y. Taguchi, and Y. Tokura, "Transport and magnetic properties of a Mott-Hubbard system whose bandwidth and band filling are both controllable: $R_{1-x}Ca_xTiO_{(3+y/2)}$," *Phys. Rev. B*, vol. 56, no. 16, pp. 10145–10153, 1997.

[30] C. Ye, W. Ruan, P. Cai, X. Li, A. Wang, X. Chen, and Y. Wang, "Strong similarities between the local electronic structure of insulating iron pnictide and lightly doped cuprate," *Phys. Rev. X*, vol. 5, no. 2, p. 021013, 2015.

[31] S. Deng, J. Köhler, and A. Simon, "Electronic structure and lattice dynamics of NaFeAs," *Phys. Rev. B*, vol. 80, no. 21, p. 214508, 2009.

[32] D. R. Parker, M. J. Pitcher, P. J. Baker, I. Franke, T. Lancaster, S. J. Blundell, and S. J. Clarke, "Structure, antiferromagnetism and superconductivity of the layered iron arsenide NaFeAs," *Chem. Commun.*, no. 16, pp. 2189–2191, 2009.

[33] G. Tan, Y. Song, C. Zhang, L. Lin, Z. Xu, T. Hou, W. Tian, H. Cao, S. Li, S. Feng, and P. Dai, "Electron doping evolution of structural and antiferromagnetic phase transitions in $NaFe_{1-x}Co_xAs$ iron pnictides," *Phys. Rev. B*, vol. 94, no. 1, p. 014509, 2016.

[34] R. Zhou, L. Y. Xing, X. C. Wang, C. Q. Jin, and G.-Q. Zheng, "Orbital order and spin nematicity in the tetragonal phase of the electron-doped iron pnictides $NaFe_{1-x}Co_xAs$," *Phys. Rev. B*, vol. 93, no. 6, p. 060502, 2016.

[35] Y. Zhang, C. He, Z. R. Ye, J. Jiang, F. Chen, M. Xu, Q. Q. Ge, B. P. Xie, J. Wei, M. Aeschlimann, X. Y. Cui, M. Shi, J. P. Hu, and D. L. Feng, "Symmetry breaking via orbital-dependent reconstruction of electronic structure in detwinned NaFeAs," *Phys. Rev. B*, vol. 85, no. 8, p. 085121, 2012.

[36] J. Pelliciari, K. Ishii, L. Xing, X. Wang, C. Jin, and T. Schmitt, "Fluctuating magnetism of Co- and Cu-doped NaFeAs," *Applied Physics Letters*, vol. 118, no. 11, p. 112604, 2021.

[37] D. W. Tam, Z. Yin, Y. Xie, W. Wang, M. B. Stone, D. T. Adroja, H. C. Walker, M. Yi, and P. Dai, "Orbital selective spin waves in detwinned NaFeAs," *Phys. Rev. B*, vol. 102, no. 5, p. 054430, 2020.

[38] D. R. Parker, M. J. P. Smith, T. Lancaster, A. J. Steele, I. Franke, P. J. Baker, F. L. Pratt, M. J. Pitcher, S. J. Blundell, and S. J. Clarke, "Control of the competition between a magnetic phase and a superconducting phase in cobalt-doped and nickel-doped NaFeAs using electron count," *Phys. Rev. Lett.*, vol. 104, no. 5, p. 057007, 2010.

[39] I. G. Kaplan, "The Pauli exclusion principle and the problems of its experimental verification," *Symmetry*, vol. 12, no. 2, p. 320, 2020.

[40] J. M. O. Sǐpr, J. Vackář, "Finite lifetime broadening of calculated x-ray absorption spectra: possible artefacts close to the edge," *Journal of Synchrotron Radiation*, vol. 25, no. 2, pp. 523–528, 2018.

[41] D. F. Swinehart, "The Beer-Lambert law," *Journal of Chemical Education*, vol. 39, no. 7, p. 333, 1962.

[42] J. J. Sakurai, "Advanced quantum mechanics," *Pearson Education India*, 1967.

[43] N. Bouldi, N. J. Vollmers, C. G. Delpy-Laplanche, Y. Joly, A. Juhin, P. Sainctavit, C. Brouder, M. Calandra, L. Paulatto, F. Mauri, and U. Gerstmann, "X-ray magnetic and natural circular dichroism from first principles: Calculation of K- and L_1-edge spectra," *Phys. Rev. B*, vol. 96, no. 8, p. 085123, 2017.

[44] D. Haskel, "Local structural studies of oriented high temperature superconducting cuprates by polarized XAFS spectroscopy: Appendix B," *Thesis, University of Washington*, pp. 269–280, 1998.

[45] D. Harris and M. Bertolucci, *Symmetry and Spectroscopy: An Introduction to Vibrational and Electronic Spectroscopy*. Dover Books on Chemistry Series, Dover Publications, 1989.

[46] S. Bernadotte, A. J. Atkins, and C. R. Jacob, "Origin-independent calculation of quadrupole intensities in x-ray spectroscopy," *The Journal of Chemical Physics*, vol. 137, no. 20, p. 204106, 2012.

[47] F. Neese, B. Hedman, K. O. Hodgson, and E. I. Solomon, "Relationship between the dipole strength of ligand pre edge transitions and metal ligand covalency," *Inorganic Chemistry*, vol. 38, no. 21, pp. 4854–4860, 1999.

[48] M. Bauer, "HERFD-XAS and valence-to-core-XES: new tools to push the limits in research with hard x-rays," *Phys. Chem. Chem. Phys.*, vol. 16, no. 27, pp. 13827–13837, 2014.

[49] P.-E. Petit, F. Farges, M. Wilke, and V. A. Solé, "Determination of the iron oxidation state in earth materials using XANES pre-edge information," *Journal of Synchrotron Radiation*, vol. 8, no. 2, pp. 952–954, 2001.

[50] A. Boubnov, H. Lichtenberg, S. Mangold, and J.-D. Grunwaldt, "Identification of the iron oxidation state and coordination geometry in iron oxide and zeolite based catalysts using pre edge XAS analysis," *Journal of Synchrotron Radiation*, vol. 22, no. 2, pp. 410–426, 2015.

[51] S. Calvin, *XAFS for Everyone - Part II*. Taylor & Francis, 2013.

[52] C. A. Ashley and S. Doniach, "Theory of extended x-ray absorption edge fine structure (EXAFS) in crystalline solids," *Phys. Rev. B*, vol. 11, no. 4, pp. 1279–1288, 1975.

[53] E. A. Stern, "Theory of the extended x-ray-absorption fine structure," *Phys. Rev. B*, vol. 10, no. 8, pp. 3027–3037, 1974.

[54] P. A. Lee and J. B. Pendry, "Theory of the extended x-ray absorption fine structure," *Phys. Rev. B*, vol. 11, no. 8, pp. 2795–2811, 1975.

[55] J. J. Rehr and R. C. Albers, "Scattering-matrix formulation of curved-wave multiple-scattering theory: Application to x-ray-absorption fine structure," *Phys. Rev. B*, vol. 41, no. 12, pp. 8139–8149, 1990.

[56] J. J. Rehr, R. C. Albers, C. R. Natoli, and E. A. Stern, "New high-energy approximation for x-ray-absorption near-edge structure," *Phys. Rev. B*, vol. 34, no. 6, pp. 4350–4353, 1986.

[57] J. Mustre de Leon, J. J. Rehr, S. I. Zabinsky, and R. C. Albers, "Ab initio curved-wave x-ray-absorption fine structure," *Phys. Rev. B*, vol. 44, no. 9, pp. 4146–4156, 1991.

[58] M. Roy and S. J. Gurman, "Amplitude reduction in EXAFS," *Journal of Synchrotron Radiation*, vol. 6, no. 3, pp. 228–230, 1999.

[59] P. A. Lee and G. Beni, "New method for the calculation of atomic phase shifts: Application to extended x-ray absorption fine structure (EXAFS) in molecules and crystals," *Phys. Rev. B*, vol. 15, no. 6, pp. 2862–2883, 1977.

[60] J. J. Rehr, J. J. Kas, F. D. Vila, M. P. Prange, and K. Jorissen, "Parameter-free calculations of x-ray spectra with FEFF9," *Phys. Chem. Chem. Phys.*, vol. 12, no. 21, pp. 5503–5513, 2010.

[61] J. J. Rehr, J. J. Kas, M. P. Prange, A. P. Sorini, Y. Takimoto, and F. Vila, "Ab initio theory and calculations of x-ray spectra," *Comptes Rendus Physique*, vol. 10, no. 6, pp. 548–559, 2009.

[62] B. K. Teo and P. A. Lee, "Ab initio calculations of amplitude and phase functions for extended x-ray absorption fine structure spectroscopy," *Journal of the American Chemical Society*, vol. 79, pp. 2815–32, 1979.

[63] J. J. Rehr, E. A. Stern, R. L. Martin, and E. R. Davidson, "Extended x-ray-absorption fine-structure amplitudes-wave-function relaxation and chemical effects," *Phys. Rev. B*, vol. 17, no. 2, pp. 560–565, 1978.

[64] J. J. Rehr, R. C. Albers, and S. I. Zabinsky, "High-order multiple-scattering calculations of x-ray-absorption fine structure," *Phys. Rev. Lett.*, vol. 69, no. 23, pp. 3397–3400, 1992.

[65] S. J. Gurman, N. Binsted, and I. Ross, "A rapid, exact, curved-wave theory for EXAFS calculations. II. the multiple-scattering contributions," *Journal of Physics C: Solid State Physics*, vol. 19, no. 11, pp. 1845–1861, 1986.

[66] B.-K. Teo, "Novel method for angle determinations by EXAFS via a new multiple-scattering formalism," *Journal of the American Chemical Society*, vol. 103, no. 14, pp. 3990–4001, 1981.

[67] S. I. Zabinsky, J. J. Rehr, A. Ankudinov, R. C. Albers, and M. J. Eller, "Multiple-scattering calculations of x-ray-absorption spectra," *Phys. Rev. B*, vol. 52, no. 4, pp. 2995–3009, 1995.

[68] A. Ankudinov and J. J. Rehr, "Sum rules for polarization-dependent x-ray absorption," *Phys. Rev. B*, vol. 51, no. 2, pp. 1282–1285, 1995.

[69] C. Brouder, "Angular dependence of x-ray absorption spectra," *Journal of Physics: Condensed Matter*, vol. 2, no. 3, pp. 701–738, 1990.

[70] S. M. Heald and E. A. Stern, "Anisotropic x-ray absorption in layered compounds," *Phys. Rev. B*, vol. 16, no. 12, pp. 5549–5559, 1977.

[71] J. Stŏhr and R. Jaeger, "Polarization-dependent phase and amplitude interference effects in the L2,3 surface extended x-ray absorption fine structure," *Phys. Rev. B*, vol. 27, no. 8, pp. 5146–5149, 1983.

[72] P. H. Citrin, "Bond lengths and coordination numbers from L2,3-edge versus K-edge surface extended x-ray-absorption fine structure," *Phys. Rev. B*, vol. 31, no. 2, pp. 700–721, 1985.

[73] K. B. Teo and P. A. Lee, "Ab initio calculations of amplitude and phase functions for extended x-ray absorption fine structure spectroscopy," *Journal of the American Chemical Society*, vol. 101, p. 2815, 1979.

[74] T. Mizokawa, L. H. Tjeng, G. A. Sawatzky, G. Ghiringhelli, O. Tjernberg, N. B. Brookes, H. Fukazawa, S. Nakatsuji, and Y. Maeno, "Spin-orbit coupling in the Mott insulator Ca_2RuO_4," *Phys. Rev. Lett.*, vol. 87, no. 7, p. 077202, 2001.

[75] D. H. Pearson, C. C. Ahn, and B. Fultz, "White lines and d-electron occupancies for the 3d and 4d transition metals," *Phys. Rev. B*, vol. 47, no. 14, pp. 8471–8478, 1993.

[76] J. Fraxedas, Y. J. Lee, I. Jiménez, R. Gago, R. M. Nieminen, P. Ordejón, and E. Canadell, "Characterization of the unoccupied and partially occupied states of TTF-TCNQ by XANES and first-principles calculations," *Phys. Rev. B*, vol. 68, no. 19, p. 195115, 2003.

[77] J.-H. Park, L. H. Tjeng, A. Tanaka, J. W. Allen, C. T. Chen, P. Metcalf, J. M. Honig, F. M. F. de Groot, and G. A. Sawatzky, "Spin and orbital occupation and phase transitions in V_2O_3," *Phys. Rev. B*, vol. 61, no. 17, pp. 11506–11509, 2000.

[78] T. Mizokawa, L. H. Tjeng, H.-J. Lin, C. T. Chen, S. Schuppler, S. Nakatsuji, H. Fukazawa, and Y. Maeno, "Orbital state and metal-insulator transition in $Ca_{2-x}Sr_xRuO_4$ (x=0.0 and 0.09) studied by x-ray absorption spectroscopy," *Phys. Rev. B*, vol. 69, no. 13, p. 132410, 2004.

[79] D. Pincini, L. S. I. Veiga, C. D. Dashwood, F. Forte, M. Cuoco, R. S. Perry, P. Bencok, A. T. Boothroyd, and D. F. McMorrow, "Tuning of the Ru^{4+} ground-state orbital population in the $4d^4$ Mott insulator Ca_2RuO_4 achieved by La doping," *Phys. Rev. B*, vol. 99, no. 7, p. 075125, 2019.

[80] H. Yavas, M. Sundermann, K. Chen, A. Amorese, A. Severing, H. Gretarsson, M. W. Haverkort, and L. H. Tjeng, "Direct imaging of orbitals in quantum materials," *Nature Physics*, vol. 15, no. 6, p. 559, 2019.

[81] A. G. McKale, B. W. Veal, A. P. Paulikas, S. K. Chan, and G. S. Knapp, "Improved ab initio calculations of amplitude and phase functions for extended x-ray absorption fine structure spectroscopy," *Journal of the American Chemical Society*, vol. 110, no. 12, pp. 3763–3768, 1988.

[82] P. H. Citrin, P. Eisenberger, and R. C. Hewitt, "Extended x-ray-absorption fine structure of surface atoms on single-crystal substrates: Iodine adsorbed on Ag(111)," *Phys. Rev. Lett.*, vol. 41, no. 5, pp. 309–312, 1978.

[83] P. H. Citrin, P. Eisenberger, and R. C. Hewitt, "Adsorption sites and bond lengths of Iodine on Cu(111) and Cu(100) from surface extended x-ray-absorption fine structure," *Phys. Rev. Lett.*, vol. 45, no. 24, pp. 1948–1951, 1980.

[84] P. Zimmermann, S. Peredkov, P. M. Abdala, S. DeBeer, M. Tromp, C. Müller, and J. A. van Bokhoven, "Modern x-ray spectroscopy: XAS and XES in the laboratory," *Coordination Chemistry Reviews*, vol. 423, p. 213466, 2020.

[85] P. G. U. Bergmann, "X-ray emission spectroscopy," *Photosynthesis research*, vol. 102, no. 2, p. 11, 2009.

[86] J. D. Wadey and N. A. Besley, "Quantum chemical calculations of x-ray emission spectroscopy," *Journal of Chemical Theory and Computation*, vol. 10, no. 10, pp. 4557–4564, 2014.

[87] E. Gallo and P. Glatzel, "Valence to core x-ray emission spectroscopy," *Advanced Materials*, vol. 26, no. 46, pp. 7730–7746, 2014.

[88] F. de Groot, "High-resolution x-ray emission and x-ray absorption spectroscopy," *Chemical Reviews*, vol. 101, no. 6, pp. 1779–1808, 2001.

[89] V. I. Veksler, "A new method of acceleration of relativistic particles," *J. Phys. USSR*, vol. 9, no. 3, pp. 153–158, 1945.

[90] E. M. McMillan, "The synchrotron - a proposed high energy particle accelerator," *Phys. Rev.*, vol. 68, no. 5-6, pp. 143–144, 1945.

[91] F. R. Elder, A. M. Gurewitsch, R. V. Langmuir, and H. C. Pollock, "Radiation from electrons in a synchrotron," *Phys. Rev.*, vol. 71, no. 11, pp. 829–830, 1947.

[92] H. C. Pollock, "The discovery of synchrotron radiation," *American Journal of Physics*, vol. 51, no. 3, pp. 278–280, 1983.

[93] C. W. Roberson and P. Sprangle, "A review of free-electron lasers," *Physics of Fluids B: Plasma Physics*, vol. 1, no. 1, pp. 3–42, 1989.

[94] A. Singer and I. A. Vartanyants, "Coherence properties of focused x-ray beams at high-brilliance synchrotron sources," *Journal of Synchrotron Radiation*, vol. 21, no. 1, pp. 5–15, 2014.

[95] D. M. Mills, J. R. Helliwell, A. Kvick, T. Ohta, I. A. Robinson, and A. Authier, "Report of the working group on synchrotron radiation nomenclature - brightness, spectral brightness or brilliance?," *Journal of Synchrotron Radiation*, vol. 12, no. 3, p. 385, 2005.

[96] H. Winick, "Synchrotron radiation sources- present capabilities and future directions," *Journal of Synchrotron Radiation*, vol. 5, no. 3, pp. 168–175, 1998.

[97] J. M. Byrd and M. Georgsson, "Lifetime increase using passive harmonic cavities in synchrotron light sources," *Phys. Rev. ST Accel. Beams*, vol. 4, no. 3, p. 030701, 2001.

[98] "http://archive.synchrotron.org.au/synchrotron-science/ how-is-synchrotron-light-created," *Australian Synchrotron, Accessed 02-03-2021*, 2021.

[99] G. Bunker, "Introduction to XAFS: A practical guide to x-ray absorption fine structure spectroscopy, chapter 3.2/3.3," *Cambridge University Press.*, 2010.

[100] S. Hayama, G. Duller, J. P. Sutter, M. Amboage, R. Boada, A. Freeman, L. Keenan, B. Nutter, L. Cahill, P. Leicester, B. Kemp, N. Rubies, and S. Diaz-Moreno, "The scanning four-bounce monochromator for beamline I20 at the Diamond Light Source," *Journal of Synchrotron Radiation*, vol. 25, no. 5, pp. 1556–1564, 2018.

[101] S. D. Brown, L. Bouchenoire, D. Bowyer, J. Kervin, D. Laundy, M. J. Longfield, D. Mannix, D. F. Paul, A. Stunault, P. Thompson, M. J. Cooper, C. A. Lucas, and W. G. Stirling, "The XMaS beamline at ESRF: instrumental developments and high-resolution diffraction studies," *Journal of Synchrotron Radiation*, vol. 8, no. 6, pp. 1172–1181, 2001.

[102] "https://warwick.ac.uk/fac/crossfac/xmas/xmasbeamline/description/," *Xmas Beamline - ESRF - Accessed: 04-03-2021*, 2021.

[103] A. J. Dent, G. Cibin, S. Ramos, A. D. Smith, S. M. Scott, L. Varandas, M. R. Pearson, N. A. Krumpa, C. P. Jones, and P. E. Robbins, "B18: A core XAS spectroscopy beamline for diamond," *Journal of Physics: Conference Series*, vol. 190, p. 012039, 2009.

[104] "https://www.diamond.ac.uk/ instruments/spectroscopy/b18/specification.html," *B18 beamline - Diamond Light Source - Accessed: 06-03-2021*, 2021.

[105] S. Diaz-Moreno, S. Hayama, M. Amboage, A. Freeman, J. Sutter, and G. Duller, "I20 the versatile x-ray absorption spectroscopy beamline at Diamond Light Source," *Journal of Physics: Conference Series*, vol. 190, p. 012038, 2009.

[106] G. Bunker, "Introduction to XAFS: A practical guide to x-ray absorption fine structure spectroscopy, chapter 3.5," *Cambridge University Press.*, 2010.

[107] G. Barbiellini, E. Castelli, R. Giacomoch, G. Kidric, A. Penzo, F. Tomasini, L. Tromba, A. (Andreucci, and A. Schenone, *Topics On Biomedical Physics - Proceedings Of The 6th National Congress Of The Italian Association Of Biomedical Physics (Pages 79-100)*. World Scientific Publishing Company, 1992.

[108] S. Hayama, R. Boada, J. Chaboy, A. Birt, G. Duller, L. Cahill, A. Freeman, M. Amboage, L. Keenan, and S. Diaz-Moreno, "Photon-in/photon-out spectroscopy at the I20-scanning beamline at diamond light source," *Journal of Physics: Condensed Matter*, 2021.

[109] nanoScience instruments, "https://www.nanoscience.com/techniques/scanning-electron-microscopy/," *Accessed: 10-03-2021*, 2021.

[110] M. Abd Mutalib, M. Rahman, M. Othman, A. Ismail, and J. Jaafar, "Chapter 9 - scanning electron microscopy (SEM) and energy-dispersive x-ray (EDX) spectroscopy," in *Membrane Characterization* (N. Hilal, A. F. Ismail, T. Matsuura, and D. Oatley-Radcliffe, eds.), pp. 161–179, Elsevier, 2017.

[111] M. Buchner, K. Höfler, B. Henne, V. Ney, and A. Ney, "Tutorial: Basic principles, limits of detection, and pitfalls of highly sensitive SQUID magnetometry for nanomagnetism and spintronics," *Journal of Applied Physics*, vol. 124, no. 16, p. 161101, 2018.

[112] U. von Barth, "Basic density-functional theory an overview," *Physica Scripta*, vol. T109, p. 9, 2004.

[113] O. Bunău and Y. Joly, "Self-consistent aspects of x-ray absorption calculations," *Journal of Physics: Condensed Matter*, vol. 21, no. 34, p. 345501, 2009.

[114] Y. Joly, O. Bunău, J. E. Lorenzo, R. M. Galéra, S. Grenier, and B. Thompson, "Self-consistency, spin-orbit and other advances in the FDMNES code to simulate XANES and RXD experiments," *Journal of Physics: Conference Series*, vol. 190, p. 012007, 2009.

[115] A. Gulans, S. Kontur, C. Meisenbichler, D. Nabok, P. Pavone, S. Rigamonti, S. Sagmeister, U. Werner, and C. Draxl, "Exciting: a full-potential all-electron package implementing density-functional theory and many-body perturbation theory," *Journal of Physics: Condensed Matter*, vol. 26, no. 36, p. 363202, 2014.

[116] R. Woolley and B. Sutcliffe, "Molecular structure and the Born—Oppenheimer approximation," *Chemical Physics Letters*, vol. 45, no. 2, pp. 393–398, 1977.

[117] W. Koch and M. C. Holthausen, *A chemist's guide to density functional theory*. John Wiley & Sons, 2015.

[118] A. Seidl, A. Görling, P. Vogl, J. A. Majewski, and M. Levy, "Generalized Kohn-Sham schemes and the band-gap problem," *Phys. Rev. B*, vol. 53, no. 7, pp. 3764–3774, 1996.

[119] F. A. Hamprecht, A. J. Cohen, D. J. Tozer, and N. C. Handy, "Development and assessment of new exchange-correlation functionals," *The Journal of Chemical Physics*, vol. 109, no. 15, pp. 6264–6271, 1998.

[120] J. P. Perdew and Y. Wang, "Accurate and simple analytic representation of the electron-gas correlation energy," *Phys. Rev. B*, vol. 45, no. 23, pp. 13244–13249, 1992.

[121] J. P. Perdew, K. Burke, and M. Ernzerhof, "Generalized gradient approximation made simple," *Phys. Rev. Lett.*, vol. 77, no. 18, pp. 3865–3868, 1996.

[122] F. Jensen, *Introduction to computational chemistry*. John wiley & sons, 2017.

[123] D. J. Singh and L. Nordstrom, "Planewaves, pseudopotentials, and the LAPW method," *Springer Science & Business Media*, pp. 23–36, 2006.

[124] K. Hatada, K. Hayakawa, M. Benfatto, and C. R. Natoli, "Full-potential multiple scattering for x-ray spectroscopies," *Phys. Rev. B*, vol. 76, no. 6, p. 060102(R), 2007.

[125] O. K. Andersen, "Linear methods in band theory," *Phys. Rev. B*, vol. 12, no. 8, pp. 3060–3083, 1975.

[126] E. Sjöstedt, L. Nordström, and D. Singh, "An alternative way of linearizing the augmented plane-wave method," *Solid State Communications*, vol. 114, no. 1, pp. 15–20, 2000.

[127] J. M. Soler and A. R. Williams, "Simple formula for the atomic forces in the augmented-plane-wave method," *Phys. Rev. B*, vol. 40, pp. 1560–1564, 1989.

[128] D. Singh, "Ground-state properties of lanthanum: Treatment of extended-core states," *Phys. Rev. B*, vol. 43, pp. 6388–6392, 1991.

[129] G. K. H. Madsen, P. Blaha, K. Schwarz, E. Sjöstedt, and L. Nordström, "Efficient linearization of the augmented plane-wave method," *Phys. Rev. B*, vol. 64, p. 195134, 2001.

[130] J. Schwitalla and H. Ebert, "Electron core-hole interaction in the x-ray absorption spectroscopy of 3d transition metals," *Phys. Rev. Lett.*, vol. 80, no. 20, pp. 4586–4589, 1998.

[131] A. L. Ankudinov, Y. Takimoto, and J. J. Rehr, "Combined Bethe-Saltpeter equations and time-dependent density-functional theory approach for x-ray absorption calculations," *Phys. Rev. B*, vol. 71, no. 16, p. 165110, 2005.

[132] O. Bunău and Y. Joly, "Time-dependent density functional theory applied to x-ray absorption spectroscopy," *Phys. Rev. B*, vol. 85, no. 15, p. 155121, 2012.

[133] G. Onida, L. Reining, and A. Rubio, "Electronic excitations: density-functional versus many-body Green's-function approaches," *Rev. Mod. Phys.*, vol. 74, no. 2, pp. 601–659, 2002.

[134] J. Vinson, J. J. Rehr, J. J. Kas, and E. L. Shirley, "Bethe-Salpeter equation calculations of core excitation spectra," *Phys. Rev. B*, vol. 83, p. 115106, Mar 2011.

[135] J. Vinson and J. J. Rehr, "Ab initio Bethe-Salpeter calculations of the x-ray absorption spectra of transition metals at the L-shell edges," *Phys. Rev. B*, vol. 86, no. 19, p. 195135, 2012.

[136] M. Rohlfing and S. G. Louie, "Electron-hole excitations and optical spectra from first principles," *Phys. Rev. B*, vol. 62, no. 8, pp. 4927–4944, 2000.

[137] A. S. C. Friedrich, "Many-body perturbation theory: The GW approximation," *Computational Nanoscience: do it yourself!*, 2006.

[138] D. J. Singh and L. Nordstrom, *Planewaves, Pseudopotentials, and the LAPW method - Chapter: 5.16.* Springer Science & Business Media, 2006.

[139] C. Brouder and J. Kappler, "Prolegomena to magnetic circular dichroism in x-ray absorption spectroscopy," *Magnetism and Synchrotron Radiation*, pp. 19–32, 1997.

[140] C. R. Natoli, D. K. Misemer, S. Doniach, and F. W. Kutzler, "First-principles calculation of x-ray absorption-edge structure in molecular clusters," *Phys. Rev. A*, vol. 22, no. 3, pp. 1104–1108, 1980.

[141] A. Rusanu, "Computational methods in metallic alloys within multiple scattering theory," *Thesis, Florida Atlantic University*, 2005.

[142] M. Hölzer, "Lattice dynamics from first principles," *Thesis, Martin-Luther-Universität Halle-Wittenberg*, pp. 37–46, 2015.

[143] T. A. Tyson, K. O. Hodgson, C. R. Natoli, and M. Benfatto, "General multiple-scattering scheme for the computation and interpretation of x-ray-absorption fine structure in atomic clusters with applications to SF_6, $GeCl_4$ and Br_2 and molecules," *Phys. Rev. B*, vol. 46, no. 10, pp. 5997–6019, 1992.

[144] L. Hedin and B. I. Lundqvist, "Explicit local exchange-correlation potentials," *Journal of Physics C: Solid State Physics*, vol. 4, no. 14, pp. 2064–2083, 1971.

[145] J. C. Slater, "A simplification of the Hartree-Fock method," *Phys. Rev.*, vol. 81, no. 3, pp. 385–390, 1951.

[146] B. Ravel and M. Newville, "*ATHENA*, *ARTEMIS*, *HEPHAESTUS*: data analysis for x-ray absorption spectroscopy using *IFEFFIT*," *Journal of Synchrotron Radiation*, vol. 12, no. 4, pp. 537–541, 2005.

[147] G. Bunker, "Introduction to XAFS: A practical guide to x-ray absorption fine structure spectroscopy, chapter 5," *Cambridge University Press.*, 2010.

[148] K. Bauchspieβ, "EXAFS background substraction using splines," *Physica B: Condensed Matter*, vol. 208-209, pp. 183–184, 1995.

[149] Z. Tan, J. I. Budnick, and S. M. Heald, "Structural parameter determination in fluorescence EXAFS of concentrated samples," *Review of Scientific Instruments*, vol. 60, no. 6, pp. 1021–1025, 1989.

[150] D. Haskel, "FLUO: Correcting XANES for self-absorption in fluorescence measurements," *Computer program and documentation [online]. Available from http://www.aps.anl.gov/xfd/people/haskel/fluo.html (accessed 17-02-2021)*, 1999.

[151] J. M. Ablett, J. C. Woicik, and C. C. Kao, "NEW correction procedure for x-ray spectroscopic fluorescence data: simulations and experiment," *International centre for diffraction data*, vol. 48, pp. 266–273, 2005.

[152] J. Goulon, C. Goulon-Ginet, R. Cortes, and J. Dubois, "On experimental attenuation factors of the amplitude of the EXAFS oscillations in absorption, reflectivity and luminescence measurements," *J. Phys. France*, vol. 43, no. 3, pp. 539–548, 1982.

[153] L. Tröger, D. Arvanitis, K. Baberschke, H. Michaelis, U. Grimm, and E. Zschech, "Full correction of the self-absorption in soft-fluorescence extended x-ray-absorption fine structure," *Phys. Rev. B*, vol. 46, no. 6, pp. 3283–3289, 1992.

[154] S. Eisebitt, T. Böske, J.-E. Rubensson, and W. Eberhardt, "Determination of absorption coefficients for concentrated samples by fluorescence detection," *Phys. Rev. B*, vol. 47, no. 21, pp. 14103–14109, 1993.

[155] A. Iida and T. Noma, "Correction of the self-absorption effect in fluorescence x-ray absorption fine structure," *Japanese Journal of Applied Physics*, vol. 32, no. Part 1, No. 6A, pp. 2899–2902, 1993.

[156] D. L. Brewe, D. M. Pease, and J. I. Budnick, "Corrections of residual fluorescence distortions for a glancing-emergence-angle x-ray-absorption technique," *Phys. Rev. B*, vol. 50, no. 13, pp. 9025–9030, 1994.

[157] P. Pfalzer, J.-P. Urbach, M. Klemm, S. Horn, M. L. DenBoer, A. I. Frenkel, and J. P. Kirkland, "Elimination of self-absorption in fluorescence hard-x-ray absorption spectra," *Phys. Rev. B*, vol. 60, no. 13, pp. 9335–9339, 1999.

[158] R. Carboni, S. Giovannini, G. Antonioli, and F. Boscherini, "Self-absorption correction strategy for fluorescence-yield soft x-ray near edge spectra," *Physica Scripta*, p. 986, 2005.

[159] C. H. Booth and F. Bridges, "Improved self-absorption correction for fluorescence measurements of extended x-ray absorption fine-structure," *Physica Scripta*, p. 202, 2005.

[160] B. Ravel, "*ATOMS*: crystallography for the x-ray absorption spectroscopist," *Journal of Synchrotron Radiation*, vol. 8, no. 2, pp. 314–316, 2001.

[161] K. V. Klementiev, "XANES dactyloscope for windows," *Freeware [online]. Available from www.cells.es/Beamlines/CLAESS/software/xanda.html (accessed 17-02-2021)*, 2013.

[162] R. D. Leapman and L. A. Grunes, "Anomalous L3/L2 white-line ratios in the 3d transition metals," *Phys. Rev. Lett.*, vol. 45, no. 5, pp. 397–401, 1980.

[163] B. T. Thole and G. van der Laan, "Branching ratio in x-ray absorption spectroscopy," *Phys. Rev. B*, vol. 38, no. 5, pp. 3158–3171, 1988.

[164] J. T. Lau, J. Rittmann, V. Zamudio-Bayer, M. Vogel, K. Hirsch, P. Klar, F. Lofink, T. Möller, and B. V. Issendorff, "Size dependence of L2,3 branching ratio and 2p core-hole screening in x-ray absorption of metal clusters," *Phys. Rev. Lett.*, vol. 101, no. 15, p. 153401, 2008.

[165] A. L. Ankudinov, A. I. Nesvizhskii, and J. J. Rehr, "Dynamic screening effects in x-ray absorption spectra," *Phys. Rev. B*, vol. 67, no. 11, p. 115120, 2003.

[166] R. Laskowski and P. Blaha, "Understanding the L2,3 x-ray absorption spectra of early 3d transition elements," *Phys. Rev. B*, vol. 82, no. 20, p. 205104, 2010.

[167] P. A. van Aken, B. V. Liebscher, and J. Styrsa, "Quantitative determination of iron oxidation states in minerals using Fe L2,3-edge electron energy-loss near-edge structure spectroscopy," *Physics and Chemistry of Minerals*, vol. 25, no. 5, pp. 323–327, 1998.

[168] C. H. Booth and Y.-J. Hu, "Confirmation of standard error analysis techniques applied to EXAFS using simulations," *Journal of Physics: Conference Series*, vol. 190, p. 012028, 2009.

[169] G. Martens, P. Rabe, N. Schwentner, and A. Werner, "Extended x-ray-absorbtion fine-structure beats: A new method to determine differences in bond lengths," *Phys. Rev. Lett.*, vol. 39, no. 22, pp. 1411–1414, 1977.

[170] G. Vankó, T. Neisius, G. Molnár, F. Renz, S. Kárpáti, A. Shukla, and F. M. F. de Groot, "Probing the 3d spin momentum with x-ray emission spectroscopy: The case of molecular-spin transitions," *The Journal of Physical Chemistry B*, vol. 110, no. 24, pp. 11647–11653, 2006.

[171] J. A. Bearden and C. H. Shaw, "Shapes and wavelengths of K series lines of elements Ti 22 to Ge 32," *Phys. Rev.*, vol. 48, no. 1, pp. 18–30, 1935.

[172] W. W. Beeman and H. Friedman, "The x-ray K absorption edges of the elements Fe (26) to Ge (32)," *Phys. Rev.*, vol. 56, no. 5, pp. 392–405, 1939.

[173] U. Bergmann, C. Horne, T. Collins, J. Workman, and S. Cramer, "Chemical dependence of interatomic x-ray transition energies and intensities – a study of Mn Kβ" and Kβ2,5 spectra," *Chemical Physics Letters*, vol. 302, no. 1, pp. 119–124, 1999.

[174] E. Gallo and P. Glatzel, "Valence to core x-ray emission spectroscopy," *Advanced Materials*, vol. 26, no. 46, pp. 7730–7746, 2014.

[175] M. A. Beckwith, M. Roemelt, M.-N. Collomb, C. DuBoc, T.-C. Weng, U. Bergmann, P. Glatzel, F. Neese, and S. DeBeer, "Manganese Kβ x-ray emission spectroscopy as a probe of metal–ligand interactions," *Inorg. Chem.*, vol. 50, no. 17, p. 12, 2011.

[176] M. U. Delgado-Jaime, B. R. Dible, K. P. Chiang, W. W. Brennessel, U. Bergmann, P. L. Holland, and S. DeBeer, "Identification of a single light atom within a multinuclear metal cluster using valence-to-core x-ray emission spectroscopy," *Inorg. Chem.*, vol. 50, no. 21, p. 8, 2011.

[177] N. Lee, T. Petrenko, U. Bergmann, F. Neese, and S. DeBeer, "Probing valence orbital composition with iron Kβ x-ray emission spectroscopy," *J. Am. Chem. Soc.*, vol. 132, no. 28, p. 12, 2010.

[178] C. J. Pollock and S. DeBeer, "Valence-to-core x-ray emission spectroscopy: A sensitive probe of the nature of a bound ligand," *Journal of the American Chemical Society*, vol. 133, no. 14, pp. 5594–5601, 2011.

[179] S. G. Eeckhout, O. V. Safonova, G. Smolentsev, M. Biasioli, V. A. Safonov, L. N. Vykhodtseva, M. Sikora, and P. Glatzel, "Cr local environment by valence-to-core x-ray emission spectroscopy," *J. Anal. At. Spectrom.*, vol. 24, no. 2, pp. 215–223, 2009.

[180] G. E. Cutsail III, N. L. Gagnon, A. D. Spaeth, W. B. Tolman, and S. DeBeer, "Valence to core x-ray emission spectroscopy as a probe of O-O bond activation in Cu_2O_2 complexes," *Angewandte Chemie International Edition*, vol. 58, no. 27, pp. 9114–9119, 2019.

[181] C. J. Clarke, S. Hayama, A. Hawes, J. P. Hallett, T. W. Chamberlain, K. R. J. Lovelock, and N. A. Besley, "Zinc 1s valence-to-core x-ray emission spectroscopy of Halozincate complexes," *The Journal of Physical Chemistry A*, vol. 123, no. 44, pp. 9552–9559, 2019.

[182] C. J. Pollock, K. Grubel, P. L. Holland, and S. DeBeer, "Experimentally quantifying small-molecule bond activation using valence-to-core x-ray emission spectroscopy," *Journal of the American Chemical Society*, vol. 135, no. 32, pp. 11803–11808, 2013.

[183] C. J. Pollock and S. DeBeer, "Insights into the geometric and electronic structure of transition metal centers from valence-to-core x-ray emission spectroscopy," *Accounts of Chemical Research*, vol. 48, no. 11, pp. 2967–2975, 2015.

[184] A. Boubnov, H. W. P. Carvalho, D. E. Doronkin, T. Günter, E. Gallo, A. J. Atkins, C. R. Jacob, and J.-D. Grunwaldt, "Selective catalytic reduction of NO over Fe-ZSM-5: Mechanistic insights by operando HERFD-XANES and valence-to-core x-ray emission spectroscopy," *Journal of the American Chemical Society*, vol. 136, no. 37, pp. 13006–13015, 2014.

[185] F. K. Richtmyer and S. Kaufman, "X-ray satellites of high atomic number elements," *Phys. Rev.*, vol. 44, no. 8, pp. 605–609, 1933.

[186] R. D. Richtmyer, "The probability of KL ionization and x-ray satellites," *Phys. Rev.*, vol. 49, no. 1, pp. 1–8, 1936.

[187] F. R. Hirsh and F. K. Richtmyer, "The relative intensities of certain L-series x-ray satellites in cathode-ray and in fluorescence excitation," *Phys. Rev.*, vol. 44, no. 12, pp. 955–960, 1933.

[188] J. Chen, Y. Z. Finfrock, Z. Wang, and T.-K. Sham, "Strain and ligand effects in Pt-Ni alloys studied by valence-to-core x-ray emission spectroscopy," *Scientific Reports*, vol. 11, no. 1, p. 13698, 2021.

[189] C. Garino, E. Gallo, N. Smolentsev, P. Glatzel, R. Gobetto, C. Lamberti, P. J. Sadler, and L. Salassa, "Resonant x-ray emission spectroscopy reveals d–d ligand-field states involved in the self-assembly of a square-planar platinum complex," *Phys. Chem. Chem. Phys.*, vol. 14, no. 44, pp. 15278–15281, 2012.

[190] M. Rovezzi and P. Glatzel, "Hard x-ray emission spectroscopy: a powerful tool for the characterization of magnetic semiconductors," *Semiconductor Science and Technology*, vol. 29, no. 2, p. 023002, 2014.

[191] L. Mandić, S. Fazinić, and Jakšić, "Chemical effects on the Kβ'' and K$\beta_{2,5}$ x-ray lines of titanium and its compounds," *Phys. Rev. A*, vol. 80, no. 4, p. 042519, 2009.

[192] P. Glatzel, U. Bergmann, F. M. F. de Groot, and S. P. Cramer, "Multiple excitations in the K fluorescence emission of Mn, Fe and Ni compounds," *AIP Conference Proceedings*, vol. 652, no. 1, pp. 250–255, 2003.

[193] O. Bunău and Y. Joly, "Self-consistent aspects of x-ray absorption calculations," *Journal of Physics: Condensed Matter*, vol. 21, no. 34, p. 345501, 2009.

[194] T. L. Nicole, Petrenko, U. Bergmann, F. Neese, and S. DeBeer, "Probing valence orbital composition with iron Kβ x-ray emission spectroscopy," *Journal of the American Chemical Society*, vol. 132, no. 28, pp. 9715–9727, 2010.

[195] P. E. Best, "Electronic structure of the $MnO_4{}^-$, $CrO_4{}^{2-}$, and $VO_4{}^{3-}$ ions from the metal K x-ray spectra," *The Journal of Chemical Physics*, vol. 44, no. 9, pp. 3248–3253, 1966.

[196] M. A. Beckwith, M. Roemelt, M.-N. Collomb, C. DuBoc, T.-C. Weng, U. Bergmann, P. Glatzel, F. Neese, and S. DeBeer, "Manganese Kβ x-ray emission spectroscopy as a probe of metal–ligand interactions," *Inorganic Chemistry*, vol. 50, no. 17, pp. 8397–8409, 2011.

[197] J. C. Swarbrick, Y. Kvashnin, K. Schulte, K. Seenivasan, C. Lamberti, and P. Glatzel, "Ligand identification in titanium complexes using x-ray valence-to-core emission spectroscopy," *Inorganic Chemistry*, vol. 49, no. 18, pp. 8323–8332, 2010.

[198] V. A. Safonov, L. N. Vykhodtseva, Y. M. Polukarov, O. V. Safonova, G. Smolentsev, M. Sikora, S. G. Eeckhout, and P. Glatzel, "Valence-to-core x-ray emission spectroscopy identification of carbide compounds in nanocrystalline Cr coatings deposited from Cr(III) electrolytes containing organic substances," *The Journal of Physical Chemistry B*, vol. 110, no. 46, pp. 23192–23196, 2006.

[199] G. Smolentsev, A. V. Soldatov, J. Messinger, K. Merz, T. Weyhermüller, U. Bergmann, Y. Pushkar, J. Yano, V. K. Yachandra, and P. Glatzel, "X-ray emission spectroscopy to study ligand valence orbitals in Mn coordination complexes," *Journal of the American Chemical Society*, vol. 131, no. 36, pp. 13161–13167, 2009.

[200] D. I. Khomskii, *Transition Metal Compounds*. Cambridge University Press, 2014.

[201] B. J. Kim, H. Jin, S. J. Moon, J.-Y. Kim, B.-G. Park, C. S. Leem, J. Yu, T. W. Noh, C. Kim, S.-J. Oh, J.-H. Park, V. Durairaj, G. Cao, and E. Rotenberg, "Novel $J_{eff} = 1/2$ Mott state induced by relativistic spin-orbit coupling in Sr_2IrO_4," *Phys. Rev. Lett.*, vol. 101, no. 7, p. 076402, 2008.

[202] Y. Xia, D. Qian, D. Hsieh, L. Wray, A. Pal, H. Lin, A. Bansil, D. Grauer, Y. S. Hor, R. J. Cava, and M. Z. Hasan, "Observation of a large-gap topological-insulator class with a single Dirac cone on the surface," *Nature Physics*, vol. 5, no. 6, pp. 398–402, 2009.

[203] H. Zhang, C.-X. Liu, X.-L. Qi, X. Dai, Z. Fang, and S.-C. Zhang, "Topological insulators in Bi_2Se_3, Bi_2Te_3 and Sb_2Te_3 with a single Dirac cone on the surface," *Nature Physics*, vol. 5, no. 6, pp. 438–442, 2009.

[204] A. F. Kusmartseva, B. Sipos, H. Berger, L. Forró, and E. Tutiš, "Pressure induced superconductivity in pristine 1T-$TiSe_2$," *Phys. Rev. Lett.*, vol. 103, no. 23, p. 236401, 2009.

[205] A. Shitade, H. Katsura, J. Kuneš, X.-L. Qi, S.-C. Zhang, and N. Nagaosa, "Quantum spin hall effect in a transition metal oxide Na_2IrO_3," *Phys. Rev. Lett.*, vol. 102, no. 25, p. 256403, 2009.

[206] B. Sipos, A. F. Kusmartseva, A. Akrap, H. Berger, L. Forró, and E. Tutiš, "From Mott state to superconductivity in 1T-TaS_2," *Nature Materials*, vol. 7, no. 12, pp. 960–965, 2008.

[207] S. Nagata, N. Matsumoto, Y. Kato, T. Furubayashi, T. Matsumoto, J. P. Sanchez, and P. Vulliet, "Metal-insulator transition in the spinel-type $CuIr_2(S_{1-x}Se_x)_4$ system," *Phys. Rev. B*, vol. 58, no. 11, pp. 6844–6854, 1998.

[208] E. F. Hockings and J. G. White, "THE SYSTEM IRIDIUM-TELLURIUM," *Journal of physical Chemistry*, vol. 64, no. 8, pp. 1042–1045, 1960.

[209] S. Jobic, R. Brec, and J. Rouxel, "Occurrence and characterization of anionic bondings in transition metal dichalcogenides," *Journal of Alloys and Compounds*, vol. 178, no. 1, pp. 253–283, 1992.

[210] C.-S. Lee and G. J. Miller, "Vacancy ordering and bonding competition in the group 9 Tellurides M_xTe_2 (M = Rh, Ir; $0.75 \leq x \leq 2$): A theoretical study," *Inorganic Chemistry*, vol. 38, no. 22, pp. 5139–5150, 1999.

[211] H. Cao, B. C. Chakoumakos, X. Chen, J. Yan, M. A. McGuire, H. Yang, R. Custelcean, H. Zhou, D. J. Singh, and D. Mandrus, "Origin of the phase transition in $IrTe_2$: Structural modulation and local bonding instability," *Phys. Rev. B*, vol. 88, no. 11, p. 115122, 2013.

[212] T. Toriyama, M. Kobori, T. Konishi, Y. Ohta, K. Sugimoto, J. Kim, A. Fujiwara, S. Pyon, K. Kudo, and M. Nohara, "Switching of conducting planes by partial dimer formation in $IrTe_2$," *Journal of the Physical Society of Japan*, vol. 83, no. 3, p. 033701, 2014.

[213] G. L. Pascut, K. Haule, M. J. Gutmann, S. A. Barnett, A. Bombardi, S. Artyukhin, T. Birol, D. Vanderbilt, J. J. Yang, S.-W. Cheong, and V. Kiryukhin, "Dimerization-induced cross-layer quasi-two-dimensionality in metallic $IrTe_2$," *Phys. Rev. Lett.*, vol. 112, no. 8, p. 086402, 2014.

[214] B. Joseph, M. Bendele, L. Simonelli, L. Maugeri, S. Pyon, K. Kudo, M. Nohara, T. Mizokawa, and N. L. Saini, "Local structural displacements across the structural phase transition in $IrTe_2$: Order-disorder of dimers and role of Ir-Te correlations," *Phys. Rev. B*, vol. 88, no. 22, p. 224109, 2013.

[215] G. Jackeli and D. A. Ivanov, "Dimer phases in quantum antiferromagnets with orbital degeneracy," *Phys. Rev. B*, vol. 76, no. 13, p. 132407, 2007.

[216] N. Matsumoto, K. Taniguchi, R. Endoh, H. Takano, and S. Nagata, "Resistance and susceptibility anomalies in $IrTe_2$ and $CuIr_2Te_4$," *Journal of Low Temperature Physics*, vol. 117, no. 5, pp. 1129–1133, 1999.

[217] K. Takubo, R. Comin, D. Ootsuki, T. Mizokawa, H. Wadati, Y. Takahashi, G. Shibata, A. Fujimori, R. Sutarto, F. He, S. Pyon, K. Kudo, M. Nohara, G. Levy, I. S. Elfimov, G. A. Sawatzky, and A. Damascelli, "Bond order and the role of ligand states in stripe-modulated $IrTe_2$," *Phys. Rev. B*, vol. 90, no. 8, p. 081104, 2014.

[218] T. Qian, H. Miao, Z. J. Wang, X. Shi, Y. B. Huang, P. Zhang, N. Xu, L. K. Zeng, J. Z. Ma, P. Richard, M. Shi, G. Xu, X. Dai, Z. Fang, A. F. Fang, N. L. Wang, and H. Ding, "Structural phase transition associated with Van Hove singularity in 5d transition metal compound $IrTe_2$," *New Journal of Physics*, vol. 16, no. 12, p. 123038, 2014.

[219] J. Dai, K. Haule, J. J. Yang, Y. S. Oh, S.-W. Cheong, and W. Wu, "Hierarchical stripe phases in $IrTe_2$ driven by competition between Ir dimerization and Te bonding," *Phys. Rev. B*, vol. 90, no. 23, p. 235121, 2014.

[220] G. Saleh and S. Artyukhin, "First-principles theory of phase transitions in $IrTe_2$," *The Journal of Physical Chemistry Letters*, vol. 11, no. 6, pp. 2127–2132, 2020.

[221] T. Mochiku, Y. Matsushita, A. Sato, Y. Fujisawa, K. Igarashi, T. Machida, H. Sakata, and K. Hirata, "Crystal structure of Pt-doped $IrTe_2$ superconductor," *Physics Procedia*, vol. 58, pp. 90–93, 2014.

[222] D. Ootsuki, T. Toriyama, M. Kobayashi, S. Pyon, K. Kudo, M. Nohara, T. Sugimoto, T. Yoshida, M. Horio, A. Fujimori, M. Arita, H. Anzai, H. Namatame, M. Taniguchi, N. L. Saini, T. Konishi, Y. Ohta, and T. Mizokawa, "Important roles of Te 5p and Ir 5d spin–orbit interactions on the multi-band electronic structure of triangular lattice superconductor $Ir_{1-x}Pt_xTe_2$," *Journal of the Physical Society of Japan*, vol. 83, no. 3, p. 033704, 2014.

[223] S. Pyon, K. Kudo, and M. Nohara, "Emergence of superconductivity near the structural phase boundary in Pt-doped $IrTe_2$ single crystals," *Physica C: Superconductivity*, vol. 494, pp. 80–84, 2013.

[224] M. N. Wilson, T. Medina, T. J. Munsie, S. C. Cheung, B. A. Frandsen, L. Liu, J. Yan, D. Mandrus, Y. J. Uemura, and G. M. Luke, "μSR and magnetometry study of superconducting 5% Pt-doped $IrTe_2$," *Phys. Rev. B*, vol. 94, no. 18, p. 184504, 2016.

[225] D. J. Yu, F. Yang, L. Miao, C. Q. Han, M.-Y. Yao, F. Zhu, Y. R. Song, K. F. Zhang, J. F. Ge, X. Yao, Z. Q. Zou, Z. J. Li, B. F. Gao, C. Liu, D. D. Guan, C. L. Gao, D. Qian, and J.-F. Jia, "Fully gapped s-wave-like superconducting state and electronic structure in $Ir_{0.95}Pd_{0.05}Te_2$ single crystals with strong spin-orbital coupling," *Phys. Rev. B*, vol. 89, no. 10, p. 100501, 2014.

[226] B. T. Thole and G. van der Laan, "Branching ratio in x-ray absorption spectroscopy," *Phys. Rev. B*, vol. 38, no. 5, pp. 3158–3171, 1988.

[227] J. P. Clancy, N. Chen, C. Y. Kim, W. F. Chen, K. W. Plumb, B. C. Jeon, T. W. Noh, and Y.-J. Kim, "Spin-orbit coupling in iridium-based 5d compounds probed by x-ray absorption spectroscopy," *Phys. Rev. B*, vol. 86, no. 19, p. 195131, 2012.

[228] D. S. BIOVIA, *BIOVIA Material Studios*. 2018.

[229] J. Clark, M. D. Segall, C. J. Pickard, P. J. Hasnip, M. J. Probert, K. Refson, and M. C. Payne, "First principles methods using CASTEP," *Zeitschrift fuer Kristallographie*, vol. 220, no. (5-6), pp. 567–570, 2005.

[230] A. Glamazda, K.-Y. Choi, P. Lemmens, J. Yang, and S.-W. Cheong, "Proximity to a commensurate charge modulation in $IrTe_{(2-x)}Se_{(x)}$ (x=0 and 0.45) revealed by raman spectroscopy," *New journal of Physics*, vol. 16, no. 093061, 2014.

[231] T. R. Cummins, M. S. Schmidt, D. H. Lu, M. Buerk, S. Schuppler, F. Litchenburg, and J. G. Bednorz, "Occupied and unoccupied electronic states in a layered perovskite superconductor without copper: band dispersions, van Hove singularity, and hole states in Sr_2RuO_4," in *Spectroscopic Studies of Superconductors* (I. Bozovic and D. van der Marel, eds.), vol. 2696, pp. 533 – 543, International Society for Optics and Photonics, 1996.

[232] S. Nakatsuji, S. Ikeda, and Y. Maeno, "Ca_2RuO_4: New Mott insulators of layered ruthenate," *Journal of the Physical Society of Japan*, vol. 66, no. 7, pp. 1868–1871, 1997.

[233] S. N. Ruddlesden and P. Popper, "The compound $Sr_3Ti_2O_7$ and its structure," *Acta Crystallographica*, vol. 11, no. 1, pp. 54–55, 1958.

[234] Y. Maeno, H. Hashimoto, K. Yoshida, S. Nishizaki, T. Fujita, J. G. Bednorz, and F. Lichtenberg, "Superconductivity in a layered perovskite without copper," *Nature*, vol. 372, pp. 532–534, 1994.

[235] C. Lester, S. Ramos, R. S. Perry, T. P. Croft, M. Laver, R. I. Bewley, T. Guidi, A. Hiess, A. Wildes, E. M. Forgan, and S. M. Hayden, "Magnetic-field-controlled spin fluctuations and quantum criticality in $Sr_3Ru_2O_7$," *Nature Communications*, vol. 12, p. 5798, 2021.

[236] C. Lester, S. Ramos, R. S. Perry, T. P. Croft, R. I. Bewley, T. Guidi, P. Manuel, D. D. Khalyavin, E. M. Forgan, and S. M. Hayden, "Field-tunable spin-density-wave phases in $Sr_3Ru_2O_7$," *Nature Materials*, vol. 14, pp. 373–378, 2015.

[237] K. Ishida, H. Mukuda, Y. Kitaoka, Z. Q. Mao, Y. Mori, and Y. Maeno, "Anisotropic superconducting gap in the spin-triplet superconductor Sr_2RuO_4: Evidence from a Ru-NQR study," *Phys. Rev. Lett.*, vol. 84, pp. 5387–5390, 2000.

[238] S. Nakatsuji, D. Hall, L. Balicas, Z. Fisk, K. Sugahara, M. Yoshioka, and Y. Maeno, "Heavy-mass Fermi liquid near a ferromagnetic instability in layered ruthenates," *Phys. Rev. Lett.*, vol. 90, p. 137202, 2003.

[239] J. P. Carlo, T. Goko, I. M. Gat-Malureanu, P. L. Russo, A. T. Savici, A. A. Aczel, G. J. MacDougall, J. A. Rodriguez, T. J. Williams, G. M. Luke, C. R. Wiebe, Y. Yoshida, S. Nakatsuji, Y. Maeno, T. Taniguchi, and Y. J. Uemura, "New magnetic phase diagram of $(Sr,Ca)_2RuO_4$," *Nature Materials*, vol. 11, no. 4, pp. 323–328, 2012.

[240] C. S. Alexander, G. Cao, V. Dobrosavljevic, S. McCall, J. E. Crow, E. Lochner, and R. P. Guertin, "Destruction of the Mott insulating ground state of Ca_2RuO_4 by a structural transition," *Phys. Rev. B*, vol. 60, no. 12, pp. R8422–R8425, 1999.

[241] S. Nakatsuji and Y. Maeno, "Quasi-two-dimensional Mott transition system $Ca_{2-x}Sr_xRuO_4$," *Phys. Rev. Lett.*, vol. 84, pp. 2666–2669, 2000.

[242] Q. Han and A. Millis, "Lattice energetics and correlation-driven metal-insulator transitions: The case of Ca_2RuO_4," *Phys. Rev. Lett.*, vol. 121, no. 6, p. 067601, 2018.

[243] M. Cuoco, F. Forte, and C. Noce, "Interplay of coulomb interactions and c-axis octahedra distortions in single-layer ruthenates," *Phys. Rev. B*, vol. 74, no. 19, p. 195124, 2006.

[244] W. Witczak-Krempa, G. Chen, Y. B. Kim, and L. Balents, "Correlated quantum phenomena in the strong spin-orbit regime," *Annual Review of Condensed Matter Physics*, vol. 5, no. 1, pp. 57–82, 2014.

[245] A. T. Lee, H. Park, and S. Ismail-Beigi, "Origin of the orbital polarization of Co^{2+} in La_2CoTiO_6 and $(LaCoO_3)_1$ + $(LaTiO_3)_1$: A DFT + U and DFMT study," *Phys. Rev. B*, vol. 103, p. 125105, 2021.

[246] E. Pavarini, S. Biermann, A. Poteryaev, A. I. Lichtenstein, A. Georges, and O. K. Andersen, "Mott transition and suppression of orbital fluctuations in orthorhombic $3d^1$ perovskites," *Phys. Rev. Lett.*, vol. 92, no. 17, p. 176403, 2004.

[247] E. Pavarini, A. Yamasaki, J. Nuss, and O. K. Andersen, "How chemistry controls electron localization in $3d^1$ perovskites: a Wannier-function study," *New Journal of Physics*, vol. 7, pp. 188–188, 2005.

[248] E. Ko, B. J. Kim, C. Kim, and H. J. Choi, "Strong orbital-dependent d-band hybridization and Fermi-surface reconstruction in metallic $Ca_{2-x}Sr_xRuO_4$," *Phys. Rev. Lett.*, vol. 98, no. 22, p. 226401, 2007.

[249] A. Boothroyd, D. Pincini, S. Boseggia, R. Perry, M. Guttmann, S. Ricco, L. Veiga, C. Dashwood, S. Collins, G. Nisbet, A. Bombardi, D. Porter, F. Baumberger, and D. McMorrow, "Persistence of antiferromagnetic order upon la substitution in the 4d4 mott insulator ca2ruo4," *Physical Review B*, vol. 98, no. 1, 2018.

[250] A. Efros, N. Van Lien, and B. Shklovskii, "Variable range hopping in doped crystalline semiconductors," *Solid State Communications*, vol. 32, no. 10, pp. 851–854, 1979.

[251] M. Imada, A. Fujimori, and Y. Tokura, "Metal-insulator transitions," *Rev. Mod. Phys.*, vol. 70, no. 4, pp. 1039–1263, 1998.

[252] S.Ricco, "Angle-resolved photoemission studies of the metal-insulator transition in lightly rare earth doped Ca_2RuO_4," *Thesis, Universite de Geneve*, 2018.

[253] S. Rowe, "Study of the anisotropic electronic and atomic structures of novel layered materials using polarised x-ray absorption spectroscopy," *Thesis, University of Kent*, 2020.

[254] Z. Hu, H. von Lips, M. S. Golden, J. Fink, G. Kaindl, F. M. F. de Groot, S. Ebbinghaus, and A. Reller, "Multiplet effects in the Ru L2,3 x-ray-absorption spectra of Ru(IV) and Ru(V) compounds," *Phys. Rev. B*, vol. 61, no. 8, pp. 5262–5266, 2000.

[255] H. Gretarsson, H. Suzuki, H. Kim, K. Ueda, M. Krautloher, B. J. Kim, H. YavaS, G. Khaliullin, and B. Keimer, "Observation of spin-orbit excitations and Hund's multiplets in Ca_2RuO_4," *Phys. Rev. B*, vol. 100, p. 045123, 2019.

[256] J. L. Shay, B. Tell, H. M. Kasper, and L. M. Schiavone, "p - d hybridization of the valence bands of I-III-VI_2 compounds," *Phys. Rev. B*, vol. 5, pp. 5003–5005, 1972.

[257] D. H. Kiem, J.-H. Sim, H. Yoon, and M. J. Han, "First-principles-based calculation of branching ratio for 5d, 4d, and 3d transition metal systems," *Journal of Physics: Condensed Matter*, vol. 32, no. 24, p. 245501, 2020.

[258] A. Shimoyamada, K. Ishizaka, S. Tsuda, S. Nakatsuji, Y. Maeno, and S. Shin, "Strong mass renormalization at a local momentum space in multiorbital $Ca_{1.8}Sr_{0.2}RuO_4$," *Phys. Rev. Lett.*, vol. 102, no. 8, p. 086401, 2009.

[259] J. Eisenstein, "Superconducting elements," *Rev. Mod. Phys.*, vol. 26, no. 3, pp. 277–291, 1954.

[260] H. Hosono and K. Kuroki, "Iron-based superconductors: Current status of materials and pairing mechanism," *Physica C: Superconductivity and its Applications*, vol. 514, pp. 399–422, 2015.

[261] A. A. Kordyuk, "Iron-based superconductors: Magnetism, superconductivity, and electronic structure (review article)," *Low Temperature Physics*, vol. 38, no. 9, pp. 888–899, 2012.

[262] J. Dai, Q. Si, J.-X. Zhu, and E. Abrahams, "Iron pnictides as a new setting for quantum criticality," *Proceedings of the National Academy of Sciences*, vol. 106, no. 11, pp. 4118–4121, 2009.

[263] C. Chu, F. Chen, M. Gooch, A. Guloy, B. Lorenz, B. Lv, K. Sasmal, Z. J. Tang, J. Tapp, and Y. Y. Xue, "The synthesis and characterization of LiFeAs and NaFeAs," *Physica C: Superconductivity*, vol. 469, no. 9, pp. 326–331, 2009.

[264] E. Fradkin, S. A. Kivelson, M. J. Lawler, J. P. Eisenstein, and A. P. Mackenzie, "Nematic fermi fluids in condensed matter physics," *Annual Review of Condensed Matter Physics*, vol. 1, no. 1, pp. 153–178, 2010.

[265] C. Fang, H. Yao, W.-F. Tsai, J. Hu, and S. A. Kivelson, "Theory of electron nematic order in LaFeAsO," *Phys. Rev. B*, vol. 77, p. 224509, 2008.

[266] R. M. Fernanders, A. V. Chubukov, and J. Schmalian, "What drives nematic order in iron-based superconductors?," *Nature Physics*, vol. 10, pp. 97–104, 2014.

[267] S. Liang, A. Moreo, and E. Dagotto, "Nematic state of pnictides stabilized by interplay between spin, orbital, and lattice degrees of freedom," *Phys. Rev. Lett.*, vol. 111, p. 047004, 2013.

[268] C. He, Y. Zhang, B. P. Xie, X. F. Wang, L. X. Yang, B. Zhou, F. Chen, M. Arita, K. Shimada, H. Namatame, M. Taniguchi, X. H. Chen, J. P. Hu, and D. L. Feng, "Electronic-structure-driven magnetic and structure transitions in superconducting NaFeAs single crystals measured by angle-resolved photoemission spectroscopy," *Phys. Rev. Lett.*, vol. 105, p. 117002, 2010.

[269] H. M. Alyahyaei, R. A. Jishi, and I. Mazin, "Electronic and lattice dynamical properties of the iron-based superconductors LiFeAs and NaFeAs," *Advances in Condensed Matter Physics*, vol. 2010, p. 6, 2010.

[270] N. Spyrison, M. A. Tanatar, K. Cho, Y. Song, P. Dai, C. Zhang, and R. Prozorov, "Environmental stability and anisotropic resistivity of co-doped $Na_{1-d}Fe_{1-x}Co_xAs$," *Phys. Rev. B*, vol. 86, no. 14, p. 144528, 2012.

[271] M. A. Tanatar, N. Spyrison, K. Cho, E. C. Blomberg, G. Tan, P. Dai, C. Zhang, and R. Prozorov, "Evolution of normal and superconducting properties of single crystals of $Na_{1-d}FeAs$ upon interaction with environment," *Phys. Rev. B*, vol. 85, no. 1, p. 014510, 2012.

[272] I. Todorov, D. Y. Chung, H. Claus, C. D. Malliakas, A. P. Douvalis, T. Bakas, J. He, V. P. Dravid, and M. G. Kanatzidis, "Topotactic redox chemistry of NaFeAs in water and air and superconducting behavior with stoichiometry change," *Chemistry of Materials*, vol. 22, no. 13, pp. 3916–3925, 2010.

[273] E. Z. Kurmaev, J. A. McLeod, N. A. Skorikov, L. D. Finkelstein, A. Moewes, Y. A. Izyumov, and S. Clarke, "Identifying valence structure in LiFeAs and NaFeAs with core-level spectroscopy," *Journal of Physics: Condensed Matter*, vol. 21, no. 34, p. 345701, 2009.

[274] C. R. Randall, L. Shu, Y.-M. Chiou, K. S. Hagen, M. Ito, N. Kitajima, R. J. Lachicotte, Y. Zang, and L. Que, "X-ray absorption pre-edge studies of high-spin Iron(II) complexes," *Inorganic Chemistry*, vol. 34, no. 5, pp. 1036–1039, 1995.

[275] J. K. Kowalska, A. W. Hahn, A. Albers, C. E. Schiewer, R. Bjornsson, F. A. Lima, F. Meyer, and S. DeBeer, "X-ray absorption and emission spectroscopic studies of $[L_2Fe_2S_2]^n$ model complexes: Implications for the experimental evaluation of redox states in iron–sulfur clusters," *Inorganic Chemistry*, vol. 55, no. 9, pp. 4485–4497, 2016.

[276] E. Tronc, C. Chanéac, and J. Jolivet, "Structural and magnetic characterization of ϵ-Fe_2O_3," *Journal of Solid State Chemistry*, vol. 139, no. 1, pp. 93–104, 1998.

[277] L. R. Merte, P. A. T. Olsson, M. Shipilin, J. Gustafson, F. Bertram, C. Zhang, H. Grŏnbeck, and E. Lundgren, "Structure of two-dimensional Fe_3O_4," *The Journal of Chemical Physics*, vol. 152, no. 11, p. 114705, 2020.

[278] R. L. Blake, R. E. Hessevick, T. Zoltai, and L. W. Finger, "Refinement of the hematite structure," *American Mineralogist*, vol. 51, pp. 123–129, 02 1966.

[279] H. S. C. O'Neill and W. A. Dollase, "Crystal structures and cation distributions in simple spinels from powder XRD structural refinements: $MgCr_2O_4$, $ZnCr_2O_4$, Fe_3O_4 and the temperature dependence of the cation distribution in $ZnAl_2O_4$," *Physics and Chemistry of Minerals*, vol. 20, pp. 541–555, 1994.

[280] A. M. March, T. A. Assefa, C. Boemer, C. Bressler, A. Britz, M. Diez, G. Doumy, A. Galler, M. Harder, D. Khakhulin, Z. Németh, M. Pápai, S. Schulz, S. H. Southworth, H. Yavaş, L. Young, W. Gawelda, and G. Vankó, "Probing transient valence orbital changes with picosecond valence-to-core x-ray emission spectroscopy," *The Journal of Physical Chemistry C*, vol. 121, no. 5, pp. 2620–2626, 2017.

[281] P. Glatzel, A. Harris, P. Marion, M. Sikora, T.-C. Weng, C. Guilloud, S. Lafuerza, M. Rovezzi, B. Detlefs, and L. Ducotté, "The five-analyzer point-to-point scanning crystal spectrometer at ESRF ID26," *Journal of Synchrotron Radiation*, vol. 28, no. 1, pp. 362–371, 2021.

[282] W. H. McMaster, N. K. Del Grande, J. H. Mallett, and J. H. Hubbell, "COMPILATION OF X-RAY CROSS SECTIONS. no. ucrl-50174 (sec. 2)(rev. 1).," *California Univ., Livermore. Lawrence Radiation Lab*, 1969.

[283] G. Van Rossum and F. L. Drake, *Python 3 Reference Manual*. Scotts Valley, CA: CreateSpace, 2009.

Appendices

Self-absorption correction code

The self-absorption correction theory has been shown in section 4.2. The following code has been used to correct for the self-absorption effect, within the thickness limit, for all data sets presented in this thesis.

The code requires I(E)/I_o(E) spectra which has a pre-edge correction applied. It is important to ensure that the pre-edge correction properly subtracts the absorption coefficient before the absorption edge, but does not adversely affect the post-edge data. The atomic-like photoabsorption coefficients are available in x-ray data tables and the McMaster tables [282] have been used for this thesis. Coefficients are needed for each element at the fluorescence energy, post-edge region with minimal EXAFS oscillations and for the pre-edge region for the element of interest. This code has been written in Python (3.6) [283].

```
" " "
Self-Absorption correction code

Written by Steve Richards
" " "

# Standard packages needed to run the code #

import matplotlib.pyplot as plt
import pandas as pd
import numpy as np
import math

# Import data file. This is user specific, however must have energy (eV) and pre-edge subtracted data columns labelled as "ene" and "norm" respectively. #

IfIo = pd.read_fwf()
IfIo.columns = ['ene', 'norm']
NumRows = len(IfIo)

# Pre-set variables for correction but can be changed by user if needed. #

# Points used for average post-edge #

Post_edge_average = 20

# Starting point for post-edge average #

Post_edge_initial = NumRows - 30

# Accuracy of correction #

Accuracy = 0.0001

# unit size of increase in testing value #

Precision = 0.001

# Absorption coefficients for correction, given by user #
# FL = fluorescence, AE = after-edge, BE = before-edge #

# element of interest #

Element1_FL = 0
Element1_AE = 0
Element1_BE = 0

# Other elements #

Element2_FL = 0
Element2_AE = 0
```

```
Element3_FL = 0
Element3_AE = 0

Element4_FL = 0
Element4_AE = 0

# Angles Phi and Theta shown in figure 4.2.1, in degrees. And Delta for finite detector area. #

phi = 0
theta = 0
delta = 0

# Correction to the element of interest when using pre-edge corrected data #

Element1_AE = Element1_AE - Element1_BE

# Define variables used for self-absorption correction #
# TOT_FL = total at fluorescence, TOT_AE = Total after edge, Other_AE = All other elements after edge #
# All angles converted in to radians #

TOT_FL = Element1_FL + Element2_FL + Element3_FL + Element4_FL
TOT_AE = Element1_AE + Element2_AE + Element3_AE + Element4_AE
Other_AE = Element2_AE + Element3_AE + Element4_AE
Phi = math.radians(phi)
Theta = math.radians(theta)
Delta = math.radians(delta)

# Calculation for average value post-edge for calibration #

a = 0
for _ in range(Post_edge_average):
b = IfIo.loc[_+Post_edge_initial, 'norm']
a = a + b
Postedge_Value = a/Post_edge_average

# Calculating calibration constant #

i = TOT_AE + ((TOT_FL*math.sin(Phi))/(math.sin(Theta)*math.cos(Delta)))
j = i/Element1_AE
K_constant = Postedge_Value * j

# correction calculation #

result = np.zeros((NumRows, 2))
for _ in range(NumRows):
test = 1
coeff = 0
while test > Accuracy:
coeff = coeff + Precision
R_TOT_AE = coeff + Other_AE
c = coeff/(R_TOT_AE +((TOT_FL*math.sin(Phi))/(math.sin(Theta)*math.cos(Delta))))
trial = K_constant * c
test = IfIo.loc[_,'norm'] - trial
test = abs(test)
# Condition used to ensure code does not run away #
if coeff > 200000: test = 0.00001 result[_,0] = IfIo.loc[_,'ene']
result[_,1] = coeff

# Output for corrected data, plotted and saved to file #

plt.figure()
plt.title(Correction)
plt.plot(result[:,0], result[:,1], linewidth = 0.5)
plt.grid(b='on', axis='both')
plt.xlabel('Energy (EV)')
```

```
plt.ylabel('True absorption coefficient')
plt.savefig(Correction)

file1 = Selfabsorptioncorrection
open(file1, 'w')
np.savetxt(file1, result)
```

Reference sample crystal structures

The following structures have been used to model the experimental data collected on the different systems. The lattice parameters, lattice angles and atom coordinates are given. The atom positions are given in fractional coordinates, relative to the crystal parameters. All crystal structures are given in the P1 symmetry group, which is the most suitable structure for FDMNES and an acceptable structure for Exciting.

B.1 Tungsten structures

The following crystals structures have been used to model the tungsten reference samples used in section 5.4 for providing an understanding of the valence-to-core XES spectra using the Lβ emission, including the density of states and orbital overlap.

Lattice parameters	**a**	**b**	**c**
	4.8370	5.7989	6.4251
Lattice angles	**alpha**	**beta**	**gamma**
	124.0	90.0	90.0

Atom coordinates

Species	**x**	**y**	**z**
W	0.5000	0.4987	0.7488
”	0.0000	0.0013	0.7512
”	0.4999	0.5013	0.2512
”	0.9999	0.9987	0.2488
O	0.3016	0.2980	0.9015
”	0.8012	0.2019	0.5985
”	0.6985	0.7021	0.0985
”	0.1985	0.7979	0.4015
”	0.3029	0.2939	0.3981
”	0.1969	0.7940	0.8981
”	0.8029	0.2061	0.1019
”	0.6969	0.7059	0.6019

Table B.1.1: Crystal structure for WO_2, symmetry group P1. All distance are given in Å and the angles are given in degrees. The atom positions are given in fractional coordinates, relative to the crystal parameters.

Lattice parameters	**a**	**b**	**c**
	5.4403	5.4403	3.9081
Lattice angles	**alpha**	**beta**	**gamma**
	90.0	90.0	90.0

Atom coordinates

Species	**x**	**y**	**z**
W	0.0000	0.5000	0.9612
”	0.5000	0.0000	0.0387
O	0.0000	0.5000	0.4911
”	0.5000	0.0000	0.5088
”	0.2500	0.2500	0.0000
”	0.7500	0.2500	0.0000
”	0.7500	0.7500	0.0000
”	0.2500	0.7500	0.0000

Table B.1.2: Crystal structure for WO_3, symmetry group P1. All distance are given in Å and the angles are given in degrees. The atom positions are given in fractional coordinates, relative to the crystal parameters.

Lattice parameters	a	b	c
	2.9283	2.9283	2.8529
Lattice angles	**alpha**	**beta**	**gamma**
	90.0	90.0	120.0

Atom coordinates

Species	x	y	z
W	0.0000	0.0000	0.0000
C	0.6666	0.3333	0.5000

Table B.1.3: Crystal structure for WC, symmetry group P1. All distance are given in Å and the angles are given in degrees. The atom positions are given in fractional coordinates, relative to the crystal parameters.

Lattice parameters	a	b	c
	4.7563	5.2373	6.1110
Lattice angles	**alpha**	**beta**	**gamma**
	90.0	90.0	90.0

Atom coordinates

Species	x	y	z
W	0.2448	0.0812	0.8764
”	0.7448	0.9188	0.6236
”	0.2552	0.5812	0.6236
”	0.7552	0.4188	0.8764
”	0.2448	0.5812	0.1236
”	0.7448	0.4188	0.3764
”	0.2552	0.0812	0.3764
”	0.7552	0.9188	0.1236
C	0.5000	0.7500	0.8783
”	0.0000	0.2500	0.6218
”	0.5000	0.2500	0.1218
”	0.0000	0.7500	0.3783

Table B.1.4: Crystal structure for W_2C, symmetry group P1. All distance are given in Å and the angles are given in degrees. The atom positions are given in fractional coordinates, relative to the crystal parameters.

B.2 $IrTe_2$ and reference structures

The following crystals structures have been used to model the $IrTe_2$ system and reference samples used in chapter 6. The $IrTe_2$ structures have been used to model the bandstructure, density of states and L_2 XAS spectra, as shown in section 6.4.4. In addition, these structures have been used to model the valence-to-core XES spectra to allow the interpretation of the different features, including the density of states and orbital overlap.

Lattice parameters	**a**	**b**	**c**
	6.1424	6.1424	6.5152
Lattice angles	**alpha**	**beta**	**gamma**
	81.0	81.0	120.0

Atom coordinates

Species	**x**	**y**	**z**
Ir	0.1667	0.8333	0.0000
”	0.8333	0.1667	0.0000
Cl	0.4326	0.0786	0.2084
”	0.9214	0.5674	0.7916
”	0.2133	0.2133	0.7913
”	0.7866	0.7866	0.2087
”	0.0786	0.4326	0.2084
”	0.5674	0.9214	0.7916

Table B.2.1: Crystal structure for $IrCl_3$, symmetry group P1. All distance are given in Å and the angles are given in degrees. The atom positions are given in fractional coordinates, relative to the crystal parameters.

Lattice parameters	**a**	**b**	**c**
	4.5449	4.5449	3.1895
Lattice angles	**alpha**	**beta**	**gamma**
	90.0	90.0	90.0

Atom coordinates

Species	**x**	**y**	**z**
Ir	0.5000	0.5000	0.5000
”	0.0000	0.0000	0.0000
O	0.6916	0.6916	0.0000
”	0.1916	0.8084	0.5000
”	0.3084	0.3084	0.0000
”	0.8084	0.1916	0.5000

Table B.2.2: Crystal structure for IrO_2, symmetry group P1. All distance are given in Å and the angles are given in degrees. The atom positions are given in fractional coordinates, relative to the crystal parameters.

Lattice parameters	**a**	**b**	**c**
	3.930	3.930	5.393
Lattice angles	**alpha**	**beta**	**gamma**
	90.0	90.0	120.0

Atom coordinates

Species	**x**	**y**	**z**
Ir	0.0000	0.0000	0.0000
Te	0.3334	0.6667	0.2500
”	0.6667	0.3334	0.7500

Table B.2.3: Crystal structure for $IrTe_2$ in the high temperature phase without dimers, symmetry group P1. All distance are given in Å and the angles are given in degrees. The atom positions are given in fractional coordinates, relative to the crystal parameters.

Lattice parameters	a	b	c
	3.930	3.930	5.393

Lattice angles	alpha	beta	gamma
	90.0	90.0	120.0

Atom coordinates

Species	x	y	z
Ir	0.0000	0.0000	0.0000
Te	0.3334	0.6567	0.2462
”	0.6667	0.3432	0.7537

Table B.2.4: Crystal structure for $IrTe_2$ with a Te compression (no dimers), symmetry group P1. All distance are given in Å and the angles are given in degrees. The atom positions are given in fractional coordinates, relative to the crystal parameters.

Lattice parameters	a	b	c
	15.619	3.930	5.393

Lattice angles	alpha	beta	gamma
	90.0	90.0	120.0

Atom coordinates

Species	x	y	z
Ir	0.0000	0.0000	0.0000
”	0.2516	0.0000	0.0000
”	0.5032	0.0000	0.0000
”	0.7548	0.0000	0.0000
Te	0.0839	0.6667	0.2500
”	0.1677	0.3334	0.7500
”	0.3355	0.6667	0.2500
”	0.4193	0.3334	0.7500
”	0.5871	0.6667	0.2500
”	0.6710	0.3334	0.7500
”	0.8387	0.6667	0.2500
”	0.9225	0.3334	0.7500

Table B.2.5: Crystal structure for $IrTe_2$ with Ir-Ir ordered dimers (Q = 1/5), symmetry group P1. All distance are given in Å and the angles are given in degrees. The atom positions are given in fractional coordinates, relative to the crystal parameters.

B.3 $NaFe_{1-x}Co_xAs$ and reference structures

The following crystals structures have been used to model the NaFeAs system and reference samples used in chapter 8. These structures have been used to model the valence-to-core XES spectra to allow the interpretation of the different features, including the density of states and orbital overlap.

Lattice parameters	a	b	c
	5.1049	5.1048	5.4951
Lattice angles	**alpha**	**beta**	**gamma**
	118.0	90.0	120.0

	Atom coordinates		
Species	**x**	**y**	**z**
Fe	0.6458	0.2917	0.9375
”	0.3542	0.7085	0.0625
”	0.8542	0.7083	0.5625
”	0.1458	0.2917	0.4375
O	0.4451	0.1951	0.2499
”	0.5549	0.8048	0.7500
”	0.7499	0.8049	0.2500
”	0.2500	0.1951	0.7499
”	0.0549	0.5000	0.2499
”	0.9451	0.5000	0.7500

Table B.3.1: Crystal structure for Fe_2O_3, symmetry group P1. All distance are given in Å and the angles are given in degrees. The atom positions are given in fractional coordinates, relative to the crystal parameters.

Lattice parameters	a	b	c
	6.0209	6.0209	6.0471
Lattice angles	**alpha**	**beta**	**gamma**
	120.0	90.0	60.3

	Atom coordinates		
Species	**x**	**y**	**z**
Fe	0.5000	0.5000	0.5000
”	0.5000	0.5000	0.0000
”	0.0000	0.0000	0.5000
”	0.5000	0.0000	0.5000
”	0.1261	0.2522	0.1261
”	0.8739	0.7478	0.8739
O	0.7415	0.0046	0.2630
”	0.7369	0.5169	0.2585
”	0.2568	0.5135	0.2568
”	0.2630	0.4831	0.7415
”	0.2585	0.9954	0.2585
”	0.7432	0.4865	0.7432
”	0.2585	0.9954	0.7369
”	0.7415	0.0046	0.7415

Table B.3.2: Crystal structure for Fe_3O_4, symmetry group P1. All distance are given in Å and the angles are given in degrees. The atom positions are given in fractional coordinates, relative to the crystal parameters.

Lattice parameters	**a**	**b**	**c**
	3.9237	3.9237	6.9188
Lattice angles	**alpha**	**beta**	**gamma**
	90.0	90.0	90.0

Atom coordinates

Species	**x**	**y**	**z**
Na	0.0000	0.5000	0.3482
”	0.5000	0.0000	0.65175
Fe	0.0000	0.0000	0.0000
”	0.5000	0.5000	0.0000
As	0.5000	0.0000	0.1858
”	0.0000	0.5000	0.8142

Table B.3.3: Crystal structure for NaFeAs, symmetry group P1. All distance are given in Å and the angles are given in degrees. The atom positions are given in fractional coordinates, relative to the crystal parameters.

Ca_2RuO_4 Full XANES data

For completeness, all measured XANES spectra for the $Ca_{2-x}La_xRuO_4$ (x = 0.0, 0.05, 0.10, 0.15) samples are shown in this section. This is shown for all angles measured and all temperatures, for both the L_2 and L_3 Ru edges.

(a)

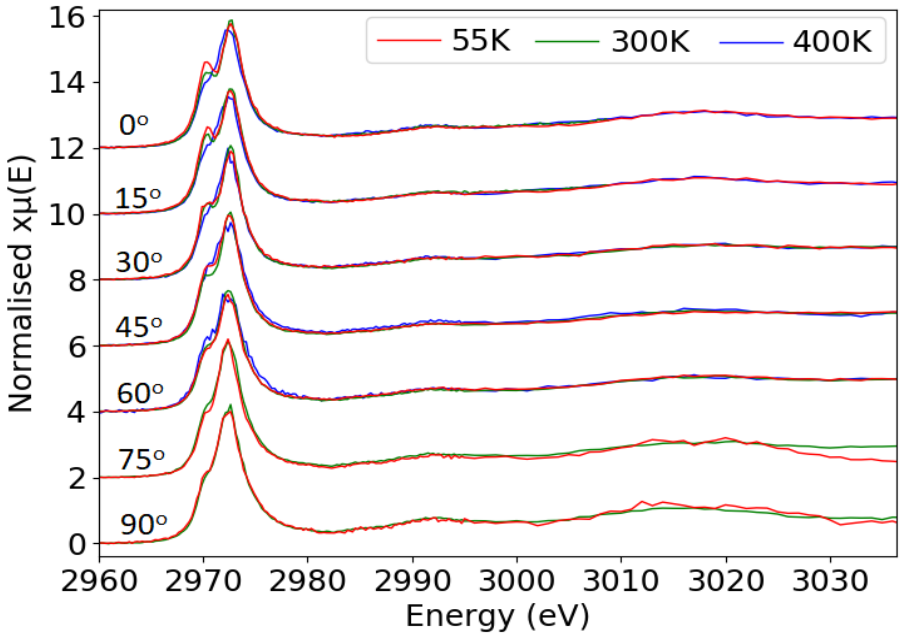

(b)

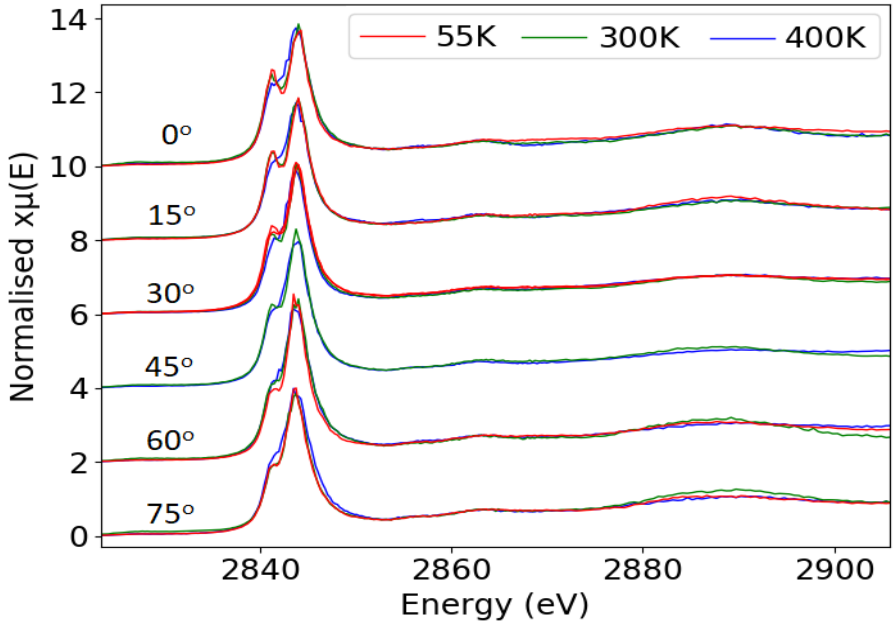

Figure C.0.1: XANES: a) L_2 ($L\beta_1$) normalized spectra, b) L_3 ($L\alpha_1$/$L\alpha_2$) normalized spectra for Ca_2RuO_4, for all angles and temperatures.

(a)

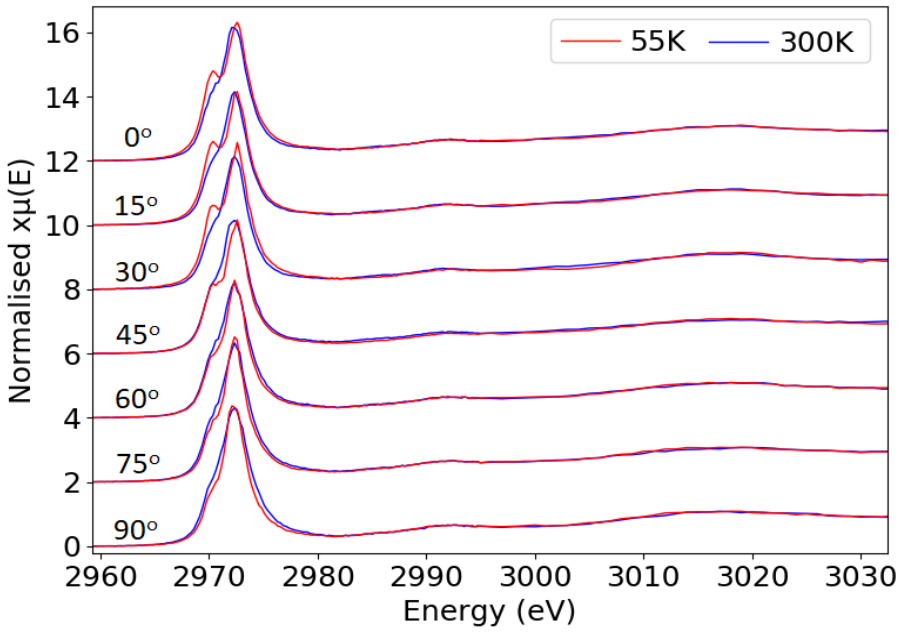

(b)

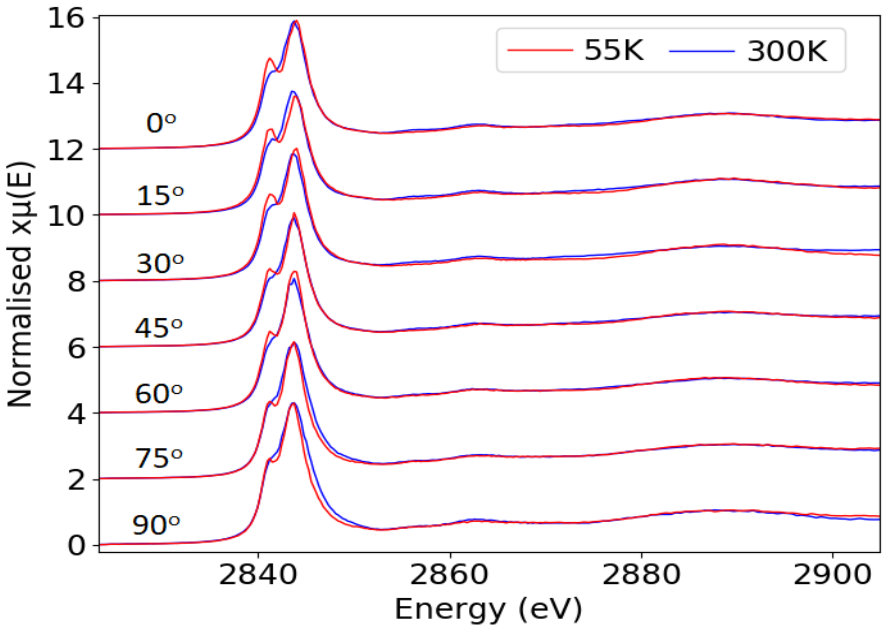

Figure C.0.2: XANES: a) L_2 ($L\beta_1$) normalized spectra, b) L_3 ($L\alpha_1/L\alpha_2$) normalized spectra for $Ca_{2-x}La_xRuO_4$ ($x = 0.05$), for all angles and temperatures.

(a)

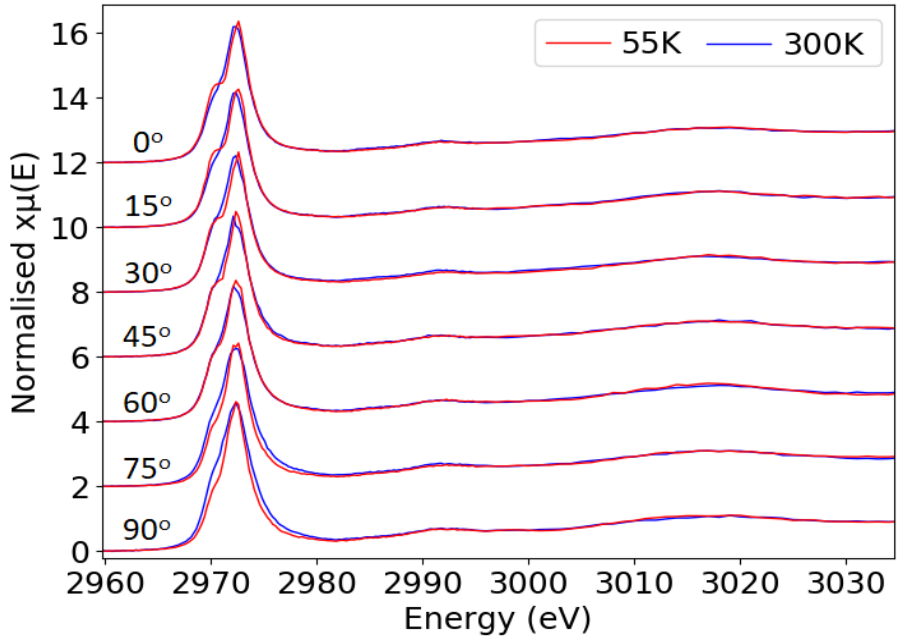

(b)

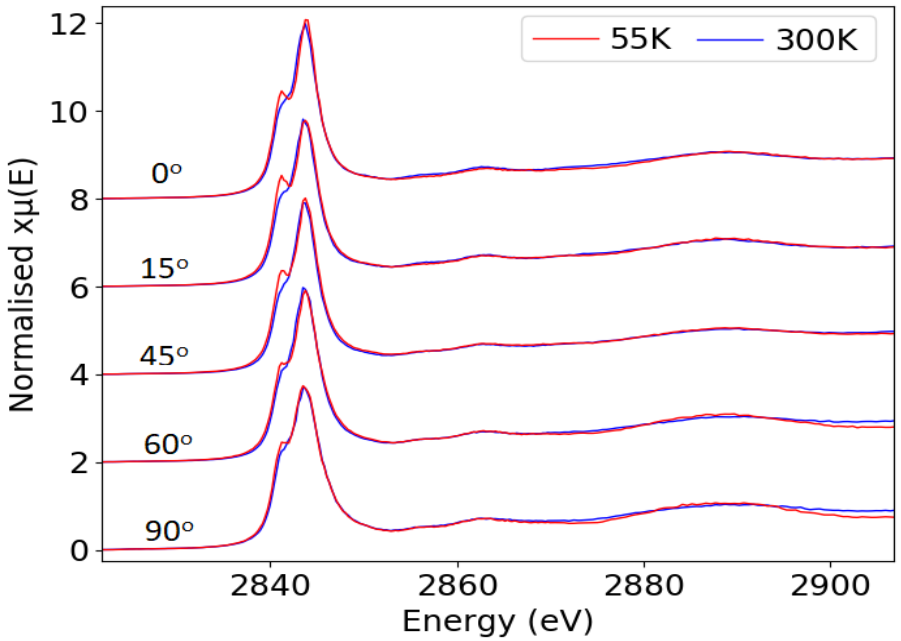

Figure C.0.3: XANES: a) L_2 ($L\beta_1$) normalized spectra, b) L_3 ($L\alpha_1$/$L\alpha_2$) normalized spectra for $Ca_{2-x}La_xRuO_4$ ($x = 0.10$), for all angles and temperatures.

(a)

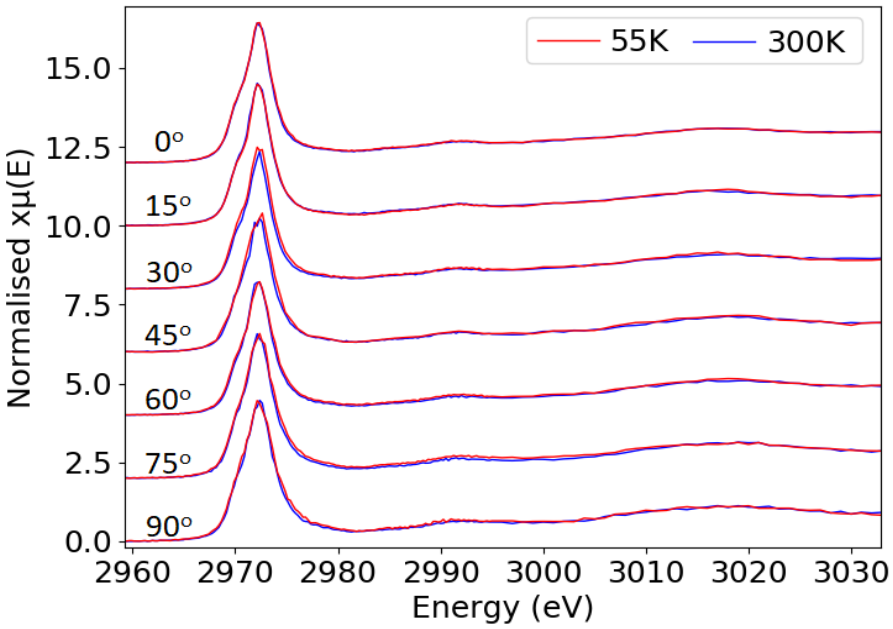

(b)

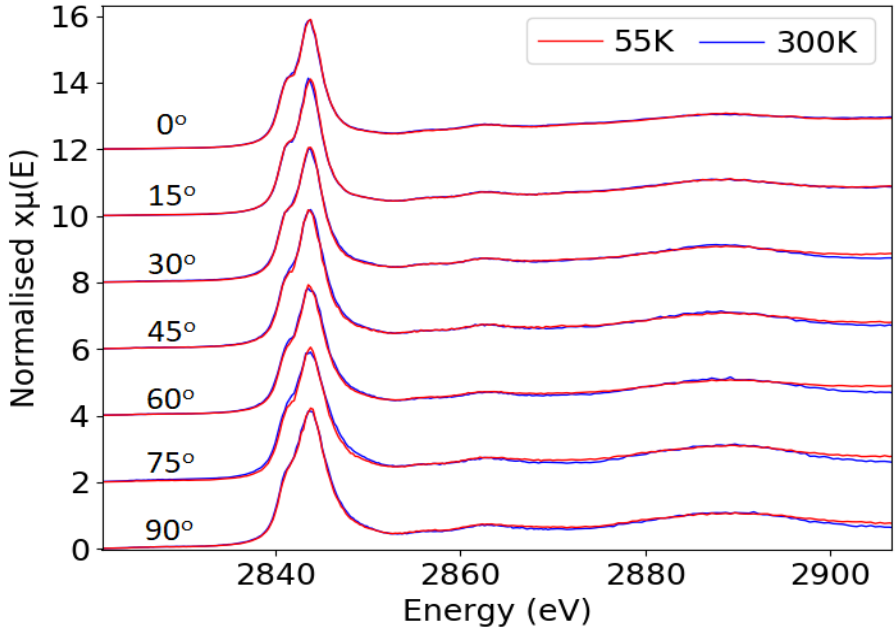

Figure C.0.4: XANES: a) L_2 ($L\beta_1$) normalized spectra, b) L_3 ($L\alpha_1/L\alpha_2$) normalized spectra for $Ca_{2-x}La_xRuO_4$ ($x = 0.15$), for all angles and temperatures.